Aalborg Universitet

ON THE ADHESIVE BEHAVIOUR OF MICRON-SIZED PARTICLES IN TURBULENT FLOW

A NUMERICAL STUDY COUPLING THE DISCRETE ELEMENT METHOD AND LARGE EDDY SIMULATIONS

BY
JAKOB HÆRVIG

DISSERTATION SUBMITTED 2017

AALBORG UNIVERSITY
DENMARK

On the Adhesive Behaviour of Micron-sized Particles in Turbulent Flow

A Numerical Study Coupling the Discrete Element Method and Large Eddy Simulations

Ph.D. Dissertation
Jakob Hærvig

Dissertation submitted October 2017

This dissertation is typeset using LaTeX 2$_\varepsilon$, plots are prepared using Ti*k*Z and drawings are included by combining vector graphics with LaTeX-overlay functionality.

Abstract

Small particles are commonly observed to stick to one another (typically denoted agglomerate) due to inter-particle attractive forces. When particles agglomerate their interaction with the surroundings is changed significantly. Particles with this behaviour are found in wide range of processes ranging from dust particles in space, that agglomerate to form early stages of planets, to soot particles emitted from various combustion processes on Earth that reduce the efficiency of various industrial processes by sticking to surfaces.

Most particles influenced by inter-particle attractive forces have diameters ranging from $d_{\mathrm{p}} = \mathcal{O}(0.1\,\text{μm})$ to $d_{\mathrm{p}} = \mathcal{O}(10\,\text{μm})$. Due to their small size, experimental investigations are limited to single particles colliding with a surface under well-controlled conditions. When adhesive particles interact in a turbulent flow, tracking individual particles in time becomes close to impossible. Due to the difficulties with tracking adhesive particles experimentally, computational methods with varying level of complexity have been developed over the last decades. Recent development within computational methods, such as the Discrete Element Method (DEM), allow more aspects of the agglomeration process to be resolved directly based on the properties of the particles. Despite the increase in computational power in the recent years, simulating the interaction of thousands, millions or even billions particles remains limited by the computational power of modern computers.

In this study, focus is first on how to analytically derive a criterion describing how to effectively speed up DEM simulations by altering the physical properties of the particles. For this purpose, simulations involving two particles colliding under various conditions are carried out to ensure the adhesive behaviour remains unchanged after applying the criterion. In conjunction with the criterion proposed, a relation describing the computational speed-up is proposed.

Secondly, focus is on applying the criterion to investigate how adhesive particles interact in a turbulent pipe flow by coupling Large Eddy Simulations (LES) of turbulent flow to the Discrete Element Method (DEM). Initially, simulations are done to verify the validity of the analytically-derived criterion. Next, simulations are done for a wide range of particle properties to get

a better understanding of how particle properties affect the agglomeration and deposition process.

Even though this dissertation is part of a project with focus on how soot particles agglomerate and deposit on heat exchanger surfaces, the work reported here is generally applicable to a much wider range of problems.

<div align="right">

Jakob Hærvig
Aalborg University

</div>

Resumé

Små partikler ses ofte klæbe sig til hinanden, hvilket kan forklares ved hjælp af tiltrækningskræfter, der virker mellem partiklerne. Når partikler klistrer sig til hinanden, ændrer det på måden, hvormed de interagerer med deres omgivelser. Partikler med denne adfærd kan observeres i en lang række tilfælde, som blandt andet inkluderer partikler i rummet, der danner tidlige stadier af nye planeter samt sodpartikler fra forbrændingsprocesser, som sætter sig på overflader og reducer virkningsgraden af en lang række industrielle processer.

Partikler med adfærd påvirket af tiltrækningskræfter er typisk i størrelsesordenen $d_\mathrm{p} = \mathcal{O}(0.1\ \mu\mathrm{m})$ til $d_\mathrm{p} = \mathcal{O}(10\ \mu\mathrm{m})$. Grundet den lille størrelse er der kun udført yderst velkontrollerede forsøg, som omhandler, hvordan enkelte partikler rammer en overflade. Hvis man ydermere er interesseret i at følge enkelte partikler i en turbulent strømning, er dette tæt på umuligt. Grundet vanskelighederne med at følge enkelte partikler er der gennem de sidste årtier blevet udviklet forskellige beregningsmetoder med varierende kompleksitet. Nylige beregningsmetoder inkluderer Discrete Element Metoden (DEM), som baserer sig direkte på partiklernes egenskaber for at opløse, hvordan partikler kolliderer. Af denne grund egner DEM sig til beregningsmæssigt at forudsige alle stadier af, hvordan partikler sætter sig sammen. På trods af en stigning i beregningskraft i de senere år, begrænses simuleringer af tusind, millioner eller milliarder af partikler dog stadig af beregningskraft.

I denne afhandling udledes der indledningsvist et analytisk udtryk for, hvordan beregningstiden kan nedbringes betydeligt ved at ændre på partiklernes egenskaber. I denne forbindelse simuleres først partikelkollisioner med to partikler under forskellige forhold for at sikre, at resultatet af kollisionen ikke ændrer sig, når det analytiske udtryk anvendes. Udover det analytiske udtryk udledes i afhandlingen et udtryk for, hvor meget beregningstiden kan nedbringes.

Derefter anvendes det udledte udtryk til numerisk at koble Large Eddy Simuleringer (LES) til Discrete Element Metoden (DEM) for at undersøge, hvordan partikler klæber til hinanden i turbulente strømninger. Først verifi-

ceres det, at udtrykket udledt i den første del er gældende. Dernæst bliver der udført simuleringer med en lang række partikler, der har til formål at give en bedre forståelse for, hvordan partiklernes egenskaber påvirker processen, hvorpå partikler klæber sig til hinanden.

Selvom denne afhandling er del af et projekt, hvor fokus er på, hvordan sodpartikler sætter sig på varmevekslerflader, er de rapporterede resultater generelt anvendelige i en lang række andre tilfælde.

Jakob Hærvig
Aalborg Universitet

Contents

Contents

Contents

Contents

Preface

This dissertation was prepared at the Department of Energy Technology at Aalborg University for the partial fulfilment of a PhD degree. The work presented in this dissertation has been carried out between September 2014 and October 2017. The work was financed by The Danish Council for Strategic Research under the programme "THERMCYC - Advanced thermodynamic cycles for low-temperature heat sources (No. 1305-00036B)". Travel grants to attend conferences and a stay abroad were provided by the Otto Mønsted Foundation, the Oticon Foundation and the PhD School at Aalborg University. Furthermore, a grant was provided by Aalborg University to use the DeiC National Abacus 2.0 cluster located at Southern University of Denmark. I would like to express my sincere gratitude to my supervisors Kim Sørensen and Thomas J. Condra for discussions, their direct form of communication and more importantly for giving me the freedom to structure and carry out the research I found most interesting. Additionally, I would like to thank the THERMCYC group, including the people at the Technical University of Denmark and Alfa Laval, for their valuable discussions and suggestions. Likewise, I would like to thank my colleagues, including Anna L. Jensen, Marie C. Pedersen and Anders S. Simonsen, for not complaining too much when I have kept talking about particles. Last but not least, I would like to thank Mads Boye at Aalborg University IT services for spending time and forcefully applying his admin rights to assist me in compiling OpenFOAM, LIGGGHTS and CFDEM and with setting up Open MPI and the Infiniband connection on the Fyrkat and later DeiC National Abacus 2.0 clusters.

Furthermore, I would like to thank all the people at the Institute of Energy Systems at the Technical University of Munich, including Wei Liu, Ulrich Kleinhans and Christoph Wieland for their kindness, time and inspiration during my three month stay there in Spring 2016. I would likewise like to thank the lovely family of Beatrice, Karl-Heinz and Charlotte for always being kind to me and for providing me with the perfect place to stay in Munich.

Finally, I would like to thank my family and girlfriend for their encouragement and willingness to accompany me in my search for adhesive particles when attending conferences on Hawaii.

Introduction to the Project

This PhD dissertation is part of the THERMCYC project. The THERMCYC project is a larger Danish research project with the overall goal of investigating how to effectively utilise low-temperature energy sources that are currently neither economically nor technically feasible to use due to their low temperatures. In the overall project, focus is on various thermodynamic cycles, such as the organic Rankine cycle (ORC), that convert energy from various low-temperature energy sources into electrical power through an expander.

Such low-temperature energy sources are available in a wide range of industries ranging from refrigeration industry, the dairy industry to hot exhaust gas from marine diesel engines to geothermal and solar energy. As these sources are available at different temperature intervals, a part of the project is focused on finding new organic fluids and mixtures suited for extracting energy at different specific temperature intervals.

Another part of the overall project is focused on components to be used in these thermodynamic cycles. These components include heat exchangers that are used to transfer energy from the low temperature heat source to the working fluid in the thermodynamic cycle.

As this project inevitably will be multi-disciplinary, some work related to working fluid selection for organic Rankine cycles and the heat transfer enhancing flow field in corrugated tube heat exchangers has been carried out as well. Despite the broad focus of the THERMCYC project, the main focus of this work has been to investigate the adhesive behaviour of micron-sized particles. Based on the main findings of this work, two papers have been published. These are attached in full in Part II.

Main Contributions of This Work

This dissertation is about the interaction between small adhesive particles in a turbulent fluid. Due to the small size of particles that exhibit this adhesive behaviour, experimental studies documenting the on-going process of agglomerates forming and breaking-up are few. Even simulating using state-of-the-art methods such as CFD coupled with DEM can be challenging due to high computational costs.

The purpose of this work is twofold. Firstly, a new method describing how to speed up DEM simulations of adhesive particles is presented. Secondly, using this new method, the fundamentals of how particle and fluid properties, such as adhesiveness and ability of follow local flow structures, affect the agglomeration and depositing mechanisms are investigated.

More details on the purpose of this dissertation and methodology used are given in Chapter 2 after the study is motivated in Chapter 1.

Paper-based Structure

This dissertation consists of two parts. Part I gives an introduction to the subject of adhesive particles, outlines the modelling framework briefly and summarises the results. Part II contains a collection of journal papers that have been published within the scope of this dissertation.

As the purpose of Part I is to only briefly summarise the modelling framework, the papers reprinted in Part II contain information that is not found in Part I. For the reader familiar with subjects such as adhesiveness of micronsized particles, JKR theory and particle-fluid interaction, the papers should be more or less self-explanatory. The papers are reprinted in full in Part II to help facilitate the reader. As these articles are published by Elsevier, general permission to reprint part of these articles or in full in the dissertation directly is given by Elsevier.

List of publications

This dissertation is based on a collection of papers, consisting of the following journal papers (reprinted in Part II):

A. J. Hærvig, U. Kleinhans, C. Wieland, H. Spliethoff, A.L. Jensen, K. Sørensen and T.J. Condra. *On the Adhesive JKR Contact and Rolling Models for Reduced Particle Stiffness Discrete Element Simulations*, Powder Technology, 319:472–482, 2017, http://dx.doi.org/10.1016/j.powtec.2017.07.006

B. J. Hærvig, K. Sørensen and T.J. Condra. *Early Stages of Agglomeration and Deposition Processes of Adhesive Micron-sized Particles in Fully-Developed Turbulent Pipe Flows*, Under peer-review

C. J. Hærvig, K. Sørensen and T.J. Condra. *On the Fully-Developed Heat Transfer Enhancing Flow Field in Sinusoidal Spirally Corrugated Tubes Using Computational Fluid Dynamics*, International Journal of Heat and Mass Transfer, 106:1051–1062, 2017, http://dx.doi.org/10.1016/j.ijheatmasstransfer.2016.10.080

D. J. Hærvig, K. Sørensen and T.J. Condra. *Guidelines for optimal selection of working fluid for an organic Rankine cycle in relation to waste heat recovery*, Energy, 96:592–602, 2016, http://dx.doi.org/10.1016/j.energy.2015.12.098

and the following conference papers (not included in the dissertation):

1. Jakob Hærvig, Thomas Condra and Kim Sørensen. *Numerical Investigation of Simultaneously Deposition and Re-Entrainment Fouling Processes in Corrugated Tubes by Coupling CFD and DEM*, Presented at The First Pacific Rim Thermal Engineering Conference, March 13-17, 2016, Hawaii's Big Island, USA (presented)

2. Jakob Hærvig, Thomas Condra and Kim Sørensen. *Numerical Investigation of the Fully-Developed Periodic Flow Field for Optimal Heat Transfer in Spirally Corrugated Tubes*, Presented at The First Pacific Rim Thermal Engineering Conference, March 13-17, 2016, Hawaii's Big Island, USA (presented)

3. Jakob Hærvig, Thomas Condra and Kim Sørensen. *Numerical Investigation of Single-phase Fully Developed Heat Transfer and Pressure Loss in Spirally Corrugated Tubes*, Presented at The 56th Conference on Simulation and Modelling, October 7-9, 2015, Linköping University, Sweden (presented)

Outside the scope of the dissertation, the following papers have been presented or co-authored (not included in the dissertation):

4. Jakob Hærvig, Anna L. Jensen, Marie C. Pedersen and Henrik Sørensen. *Numerical and Experimental Study of the Rotational Behaviour of Flat Plates Falling Freely with Periodic Oscillating Motion*, Presented at the ASME 2017 Fluids Engineering Division Summer Meeting, July 30-August 3, 2017, Hawaii's Big Island, USA (presented)

5. H. Sørensen, A.L. Jensen and J. Hærvig. *Flow structures generated by elongated plates settling in a water column*, 20th Australasian Fluid Mechanics Conference, December 5-8, 2016, Perth, Australia (co-authored)

6. Jakob Hærvig, Anna Lyhne Jensen, Marie Cecilie Pedersen and Henrik Sørensen. *General Observations of the Time-Dependent Flow Field Around Flat Plates in Free Fall*, Presented at the ASME-JSME-KSME Joint Fluids Engineering Conference, July 26-31, 2015, Seoul, Korea (presented)

Part I

Introduction

Chapter 1

Introduction to Adhesive Particles

Getting a better understanding of the motion and behaviour of small particles is important for a wide range of phenomena occurring in both nature and different industrial processes. When the particles considered are sufficiently small, short range adhesive forces acting between particles begin to play an important role in the overall description of their behaviour. That is, they begin to stick to one another or to surfaces, commonly denoted agglomeration and deposition respectively. This sticky behaviour causes particles to form long chains or more compact chunks of particles, which significantly alters the interaction between the particles and their surroundings. It is important to understand this interaction between particles and their surroundings in order to be able to both explain and model a wide range of phenomena. These phenomena can be anything ranging from important, fascinating to sometimes highly undesirable.

In short, the main subject of this dissertation is the adhesive behaviour of such particles and how phenomena, such as particle agglomeration in turbulent flows, can be predicted efficiently by numerical methods; namely the Discrete Element Method (DEM) coupled with Computational Fluid Dynamics (CFD).

1.1 Motivation

Dust in various forms are examples of sufficiently small size particles, where adhesive forces play an important role. An example of such dust include interstellar dust grains in the size range 5 Å to 2500 Å (Mathis et al., 1977) that collide and eventually agglomerate to form the very early stages of new
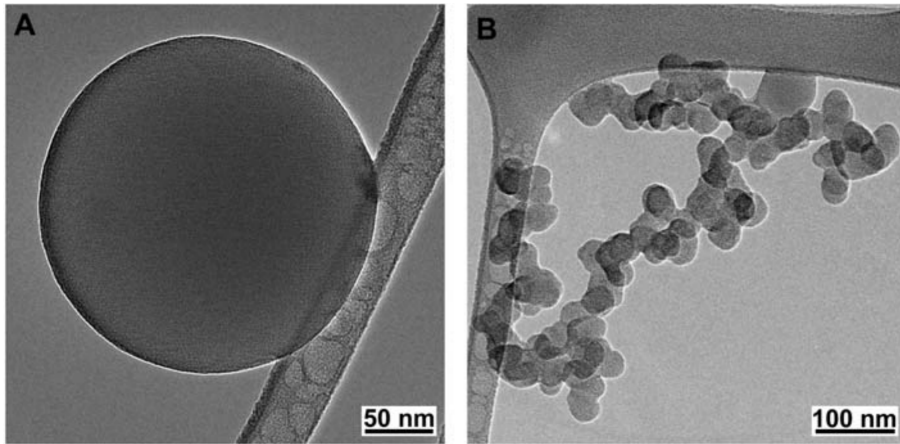
Figure 1.1: Transmission electron microscopy images showing: (A) Single soot particle; (B) Agglomerate consisting of numerous soot particles forming a longer chain-like structure. From "Brown Carbon Spheres in East Asian Outflow and Their Optical Properties" by Duncan T.L. Alexander, Peter A. Crozier and James R. Anderson, Science, vol. 321, pp. 833–836, 2008. Reprinted with permission from AAAS.

planets in space (Weidenschilling, 2000). Others examples include dusty environments such as the ones found on the Moon or on Mars, where the sticky behaviour of particles causes problems for both space equipment and for the astronauts that have to take numerous precautions not to inhale the dust. Such problems are commonly considered to be major obstacles towards populating these environments. On Earth, various industrial processes are designed in such a way that they utilise the adhesive behaviour of particles for various purposes. Such processes include separation processes, where agglomeration is used to increase the sedimentation velocity due to gravity by an increase in effective particle size. Other processes include filtration systems, where particles are brought in contact with fibres and stick due to adhesive contact forces.

One kind of particles that has a huge influence on both the environment, the health of humans and the equipment used to transport particle-laden gas streams, is soot particles. Soot particles are formed in fuel-rich regions of burning diesel flames through a series of sub-processes, that finally form primary soot particles that are close to spherical in shape, see figure 1.1(A) (Tree and Svensson, 2007; Alexander, 2008). Such soot particles are examples of particles of sufficiently small size where adhesive forces play a dominant role allowing longer chains or chunks of particles to form, see figure 1.1(B). As shown by Eggersdorfer and Pratsinis (2012), such agglomerates can be of different shape and either loosely packed chain-like structure as in figure 1.1(B) or more compactly packed as in figure 1.2.
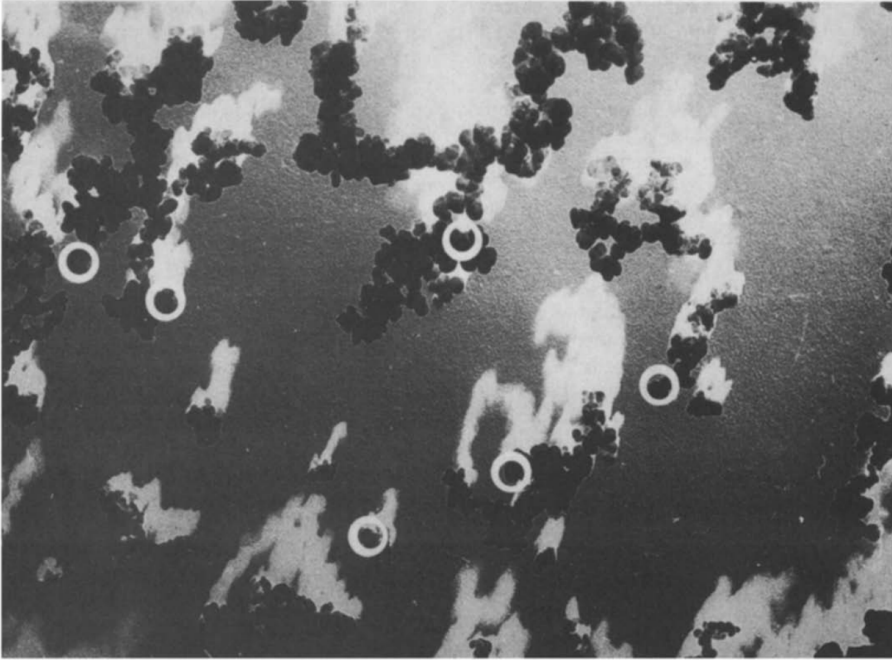
Figure 1.2: Micrograph of agglomerated soot particles with mean diameter $\hat{d}_p = 20$ nm. White circles show primary single soot particles and white shaded areas are shadows. Reprinted from "Soot Formation" by B.S. Haynes and H.Gg. Wagner published in Progress in Energy and Combustion Science, vol. 7, pp. 229–273, 1981, with permission from Elsevier.

In recent years, public awareness of how burning fossil fuels contributes to global warming has increased. Until recently, global warming was most commonly explained by increased concentrations of CO_2 and NO_x, whilst little attention was given to particulate emissions, such as black soot particles. However, the study by Bond et al. (2013) suggests that up to two-thirds of the global warming potential can be attributed black soot particles. Likewise, does the study by Shindell et al. (2012) suggests that the global rate of warming can be cut in half by aggressive actions on black soot and methane emissions.

Not only do soot particles affect the global climate, but research shows how particulate emissions can be linked directly to an increased risk of cardiovascular diseases, causing an excessive amount of premature deaths every year (Grahame and Schlesinger, 2010). Due to the small size of particulate emissions such as soot particles, these particles are able to travel far down into the human respiratory system where they finally deposit.

Due to the sticky behaviour of soot particles, they do as well cause problems for process equipment carrying the particle-laden exhaust gas from

combustion engines. When such particles are brought in contact with surfaces here, they tend to stick upon collision due to adhesive forces. Over time, the result is a layer of particles building up (commonly denoted particulate fouling) that gradually reduces the heat transfer performance of heat exchangers or at worst blocks up whole channels or pipes (Henry et al., 2012).

1.2 Modelling Approaches

Various approaches exist to simulate the transport, collision, agglomeration and deposition of particles. These methods vary significantly in terms of how the fluid and particles are treated numerically. The following sections give a brief overview of different methods commonly used to model the transport, collision and agglomeration of adhesive particles.

1.2.1 Particle-fluid interactions

Due to the high complexity of the flow around ever-changing agglomerate morphologies, different methods are used to model the interaction between particles and a fluid. These range from methods that resolve the flow around all particles directly, to methods where the particles are treated as a continuum.

Flow-resolving methods

To resolve the flow field around agglomerated particles directly, as schematically shown in figure 1.3, the Lattice-Boltzmann Method (LBM) and the Immersed Boundary Method (IBM) are commonly used. Even though such
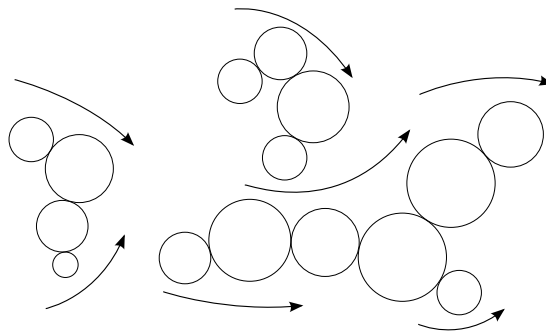
Figure 1.3: Schematic of flow field around agglomerates obtained by a flow-resolving method.

methods pose no restrictions on the level of details, resolving the flow fully simply makes these methods too computationally expensive for all but the

simplest problems even with modern computational resources (Crowe et al., 2011). As they pose no limitations on the level of details and handles complex geometries more easily without needing a boundary conforming computational mesh, they are typically used to investigate the fundamentals of a wide range of problems. As a result LBM has been used by numerous authors to investigate the flow field around different sphere arrangements. Such studies include Hill et al. (2001a,b), who used LBM to resolve the flow in random arrays of spheres and correlated particle drag with the Reynolds number and solid volume fraction. Other studies include Dietzel and Sommerfeld (2013) who resolved the flow around different randomly generated agglomerate morphologies to investigate the overall drag on agglomerates. However, as the agglomeration and deposition processes of interest here typically contain a higher number of particles, methods that resolve the flow around all particles fully are simply too computationally expensive for this study.

Therefore, focus is on methods that do not resolve the flow field around every particle but instead relies on correlations to describe the fluid force and torque acting on individual particles. These correlations are either obtained through experiments or detailed flow-resolving simulations as those mentioned above.

Non-resolving methods

Using traditional Lagrangian approaches, particles are typically represented by point-masses tracked in time by integrating Newtons equation of motion using correlations to describe the instantaneous fluid force and torque acting on particles. By representing the fluid force on particles by empirical correlations, the computational time can be significantly reduced, allowing for simulations that are not possible when all the flow field is resolved.

Even when all the detailed flow field around primary particles is not resolved, the computational time may, depending on the problem, still be too high for many problems. To overcome this limitation, various methods have been proposed. One such method is the Discrete Parcel Method (DPM) first proposed by Crowe et al. (1977), who suggested representing a set of primary particles by a single particle, commonly denoted a parcel, having a velocity equal to the average velocity of the constituting particles. This is schematically shown in figure 1.4. As each parcel can represent an arbitrary number of primary particles, the DPM approach can be used to model an infinitely high number of primary particles. However, as particle-particle interactions are not resolved directly using the DPM, the standard DPM formulation has some drawbacks when simulating agglomeration. As the agglomeration process is governed by collisions of primary particles, it is not trivial to predict the agglomeration process, as the primary particles are represented
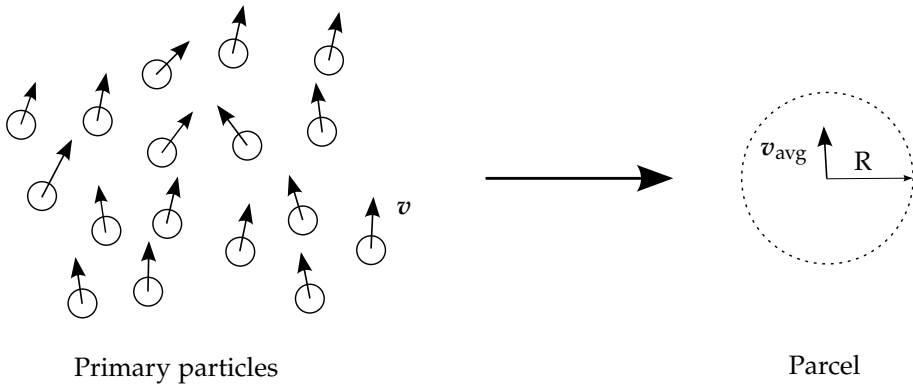
Figure 1.4: Schematic of the discrete parcel method (DPM) method where N particles are represented by a single parcel with the average velocity v_{avg} and parcel radius R.

by parcels using DPM. Numerous attempts have been made to extend the DPM method to take into account various processes, including turbulence dispersion by Zhou and Yao (1992) and collisions of primary particles by Sommerfeld (2001). Common for these attempts is that they correlate parcel properties v_{avg} and R to the flow field and information on the primary particles.

However, as noted by Marshall and Li (2014), DPM type models are not frequently used to model particle interactions involving adhesive particles. This is partly due to the complexity of handling collisions and more importantly the agglomerating behaviour of primary particles contained in different parcels. Therefore, the focus in this study is on methods that rely directly on the properties of the particles to resolve collisions directly.

1.2.2 Particle-particle interactions

The processes of particles colliding and forming agglomeration, as those depicted in figure 1.1(B) and figure 1.2, are highly dependent on the properties of the primary particles. Such particle properties include the Young's modulus, Poisson's ratio, density, particle shape, coefficient of restitution and in the case of adhesive particles, the surface energy density as well. Including the effect of all these parameters in methods relying on statistics to model particles agglomeration is not simple, and therefore an increasing amount of work is being done with methods that rely directly on all these properties. One such method proposed by Cundall and Strack (1979) is the Discrete Element Method (DEM) that relies on analytically-derived expressions for contact stresses in the particle material derived by Hertz (1882). When two particles collide, the contact region is slightly deformed as illustrated by a
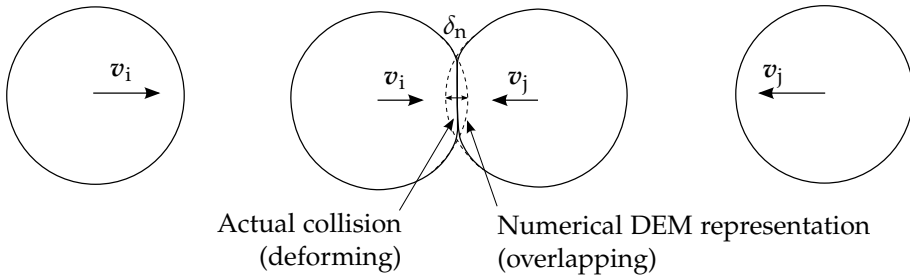
Figure 1.5: Schematic of a particle-particle collision handled by the soft-sphere discrete element method (DEM). The deformation in the contact region upon collision is handled in DEM by letting the particles overlap slightly by the distance δ_n. Note the overlap in the figure is highly exaggerated compared to collisions of common micron-sized particles.

solid line in figure 1.5. Numerically this is handled in the soft-sphere DEM approach by letting the particles overlap slightly upon collision as shown by the dashed line in figure 1.5. In the limiting case of perfectly rigid particles where only two particles collide at a time and particles do not stay in contact, the hard-sphere DEM approach can be used to significantly speed up simulations. Instead of resolving the particle collision over numerous time steps, the hard-sphere approach assumes particle collisions occur instantaneously and thus simple impulse equations can be used. However, as noted by Marshall and Li (2014), this is not convenient when modelling agglomeration and deposition as particles remain in contact over longer time intervals. Therefore, focus is on the soft-sphere approach, where the collision process is resolved over numerous time steps and thus does not pose any of the limitations of the hard-sphere DEM approach. As opposed to other typical Lagrangian approaches, the particles have a finite size in the computational domain using the DEM approach. Due to the natural way the collisions are handled, the DEM method is most commonly used to model processes where the particle volume fraction is high and particle interactions play an important role. One major disadvantage of the DEM approach, compared to other methods, is the computational cost. As all collisions are resolved over numerous time steps, the associated computational cost is high. However, as modern more powerful computational resources become available, an increasing amount of work is expected to be carried out with DEM in the future. Figure 1.6 gives an overview of the popularity of DEM visualised by the yearly number of citations. As figure 1.6 suggests, the popularity of the DEM approach seems to be increasing.

Depending on properties of the particles and surrounding fluid, the adhesive force causing particles to stick can be a result of different physical mechanisms. These are outlined briefly in the following.
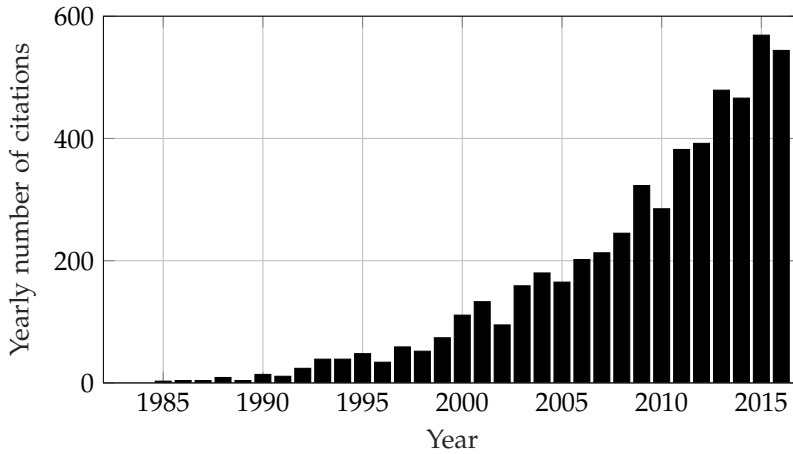
Figure 1.6: Yearly citations to the discrete element method (DEM) by Cundall and Strack (1979). Data extracted from Web of Science at the time of writing.

1.3 Types of Adhesive Forces

Depending on the surrounding environment, the particles and the properties of the particles, different distinct mechanisms cause the particles to stick to one another or to surfaces. The mechanisms are outlined briefly in the following.

All particles, independent of size, experience attraction caused by the van der Waals force. The van der Waals force is commonly described by various molecular scale effects that include dispersion, induction and orientation effects. For sufficiently large particles, typically diameters $d_p > 10\,\mu m$, these effects are negligible compared to other forces such as fluid and gravity forces. The result is collisions that behave as if the particles were non-adhesive. However, for sufficiently small particles, where the van der Waals force dominates fluid and gravity forces, the attractive van der Waals force alters or eventually causes particles to stick upon collision. As the van der Waals attractive force decays quickly with separation distance d ($F_{vdW} \propto d^{-5}$), one common modelling approach is to neglect van der Waals attraction until the particles come into physical contact. Details on how van der Waals attraction is accounted for in this work is given in section 4.3.

When small amounts of liquid content is added to an otherwise dry gaseous stream, a thin liquid film will form on the particle surfaces as shown in figure 1.7(A). When two particles come in close proximity, see figure 1.7(B), a liquid bridge is formed between the two particles. Due to surface tension forces in the liquid, the particles typically experience a strong attractive force that is important even for particles with diameters in the order of millimetres.

Figure 1.7: (A) Two initially separated particles surround by a thin liquid film; (B) A liquid bridge between the particles is formed, which results in an adhesive force due to surface tension forces in the fluid stretching between the particles.
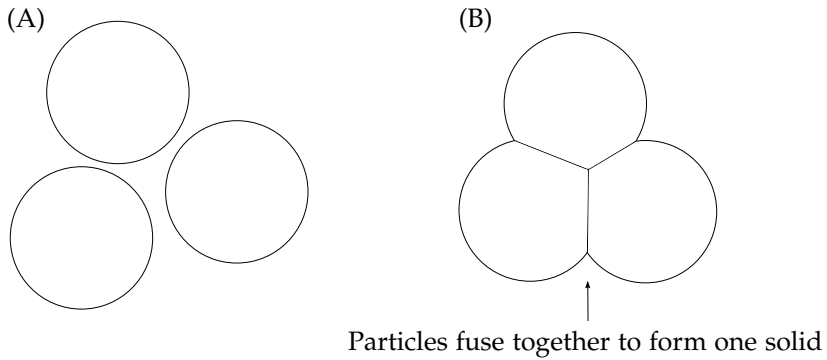
Figure 1.8: (A) Three initially separated particles; (B) A high temperature environment causes particle mass to diffuse between the particles creating one solid structure.

In high temperature environments, particles are commonly observed to form a solid layer after which the particles cannot simply be separated by applying a force. In this case, the particle material is transported between the particles, which ultimately results in one solid structure.

In this dissertation, focus is on particles agglomerating and depositing in a dry environment at low temperatures so that neither liquid bridges form nor particles fuse together due to high temperatures.

Chapter 1. Introduction to Adhesive Particles

Chapter 2

Research Questions and Dissertation Structure

2.1 Research Topics

The aim of this dissertation is to provide a better understanding of the early stages of agglomeration and deposition processes of small micron-sized particles in dry environments. By resolving all particle-particle collisions by the soft-sphere Discrete Element Method (DEM), no restrictions are imposed on the particulate phase. That is, at every time instant, the particle motion is governed by a force balance that directly governs all aspects of the agglomeration and deposition processes.

As agglomeration and deposition processes involve a large number of particles, the computational requirements are typically high. Therefore, part of this work is focused on developing new methods to effectively speed-up DEM simulations so that larger, more complex systems and with a higher particle count can be investigated. In this work, focus is on how to numerically replace the actual particles with softer particles to increase the collision duration and therefore allow for a higher time step size. The first research topic of interest is:

1. Propose a way to reduce the computational time of discrete element method simulations involving adhesive particles by introducing artificially softer particles

As the agglomeration and deposition processes are directly linked to the turbulent flow transporting the particles, focus is on flow-resolving methods that resolve the time-dependent anisotropic turbulent flow. However, as resolving all turbulence scales using direct numerical simulations is typically

too time consuming, part of this work is focused on the applicability of Large Eddy Simulations (LES) to predict particle transport and agglomeration:

2. Investigate the applicability of large eddy simulations to predict transport and the agglomerating behaviour of particles in fully-developed turbulent pipe flows

Depending on the application of interest, there could be a significant size difference between the particles and the geometry of interest. For example, the finest soot particles from diesel combustion have $d_\mathrm{p} = \mathcal{O}(0.1 \text{ nm})$ whilst most heat exchangers geometries have characteristic lengths $l_\mathrm{c} = \mathcal{O}(10^{-2} \text{ m})$. The result is significant difference in length scales and a high particle count for even a single layer of particles covering surfaces. For example, considering a 1 meter long pipe with inner diameter 1 cm, it takes $2 \cdot 10^{14}$ particles with $d_\mathrm{p} = 0.1$ nm to cover half the surface area of the tube with just a single layer of particles. Even for the largest particles with diameters $d_\mathrm{p} \approx 10$ µm, it takes $2 \cdot 10^8$ particles. As a consequence, part of this work is focused on how to increase the particle size numerically by employing scaling analyses and various dimensionless groups:

3. Investigate how to introduce larger particles by employing various non-dimensional groups

The last part of the work is focused on investigating how different particle characteristics, such as adhesiveness and ability to follow local flow structures, affect particles agglomeration and deposition processes. This is done by varying different non-dimensional groups governing the agglomeration and deposition processes systematically.

4. Vary different non-dimensional groups that govern how particles interact with the turbulent flow and the strength of adhesive forces acting between the particles to investigate how the agglomeration and deposition processes are affected

As already mentioned, this dissertation is part of the multi-disciplinary project THERMCYC. Therefore some work related to slightly different topics relevant to the THERMCYC project in general has been carried out as well. The additional work carried out in relation to the THERMCYC project is presented in paper C and paper D on page 163 and 197 respectively.

2.2   Dissertation Structure

This section gives the reader an overview of the structure of the dissertation. The following lists the contents of each chapter briefly (summarised graphically below):

- **Chapter 3** gives an introduction to particulate agglomeration and deposition phenomena. This includes a brief overview of the mechanisms that govern particles collisions and consequently agglomeration or surface deposition.

- **Chapter 4** gives an overview of the discrete element modelling framework along with various sub-models important to predict particle agglomeration and deposition of adhesive particles.

- **Chapter 5** deals with coupling between particles and the turbulent fluid modelled with the Discrete Element Method (DEM) and Large Eddy Simulations (LES) respectively.

- **Chapter 6** gives an overview of the results published in the papers

- **Chapter 7** contains a discussion, concluding remarks and ideas for how to continue in future studies.

Figure 2.1 gives a graphical overview of the structure along with an overview of how the papers concerned with adhesive particles reprinted in Part II are linked to the dissertation.

Particle phase | *Fluid phase including interaction with particles* | *Agglomeration and deposition*

Chapter 1
Introduction to adhesive particles

Chapter 2
Research outline and overview

Chapter 3
Introduction to particle deposition and agglomeration

Chapter 5
Interaction between fluid and particles

Paper B
Particle agglomeration in turbulent pipe flow by coupling LES and DEM

Chapter 4
The discrete element modelling framework

Chapter 6
Overview of contributions

Paper A
Criterion for reduced particle stiffness discrete element simulations

Chapter 7
Discussion, concluding remarks and perspectives

Figure 2.1: Graphical overview of the work carried out in relation to adhesive particles in the present work.

2.2.1 Brief overview of publications

The following gives the reader a brief overview of the journal papers published in relation to this dissertation. The results of the papers are outlined in Chapter 6.

- **Paper A: On the adhesive JKR contact and rolling models for reduced particle stiffness discrete element simulations:**
  Discrete element method simulations employing the soft-sphere approach are becoming increasingly more popular. However, the computational costs associated with the mechanistic models, where particle-particle collisions are resolved over numerous time steps, is still a major drawback.

  The focus of this paper is therefore to propose general analytically-derived guidelines for how to speed up such simulations by introducing particles with reduced particle stiffness based on the commonly used adhesive JKR model proposed by Johnson et al. (1971). The guidelines are validated by comparing simulations of particle-wall collisions with experiments found in literature. Lastly, limitations of the proposed criterion are given with the purpose of simulating the agglomerating and depositing behaviour of particles in a turbulent flow.
  The paper is reprinted in full in Part II on page 105.

- **Paper B: Early stages of agglomeration and deposition of adhesive micron-sized particles in fully-developed turbulent pipe flows:**
  The agglomerating and depositing mechanisms of micron-sized particles in a pipe flow will inherently be complex as they are typically governed by interactions with a turbulent flow. To impose no limitations on particle-particle interactions, the soft-sphere discrete element method is used. The turbulent flow field is solved using large eddy simulations.

  The purpose of this study is to first show that the criterion proposed in Paper A can be used to reduce the computational time without affecting the agglomerating behaviour. Next, simulations with various mesh resolutions are used to quantify the effect of using large eddy simulations instead of resolving all turbulence scales with direct numerical simulations. Lastly, the effect of various dimensionless groups on the agglomerating an depositing behaviour of particles is investigated in details.
  The paper is reprinted in full in Part II on page 133.

- **Paper C: On the fully-developed heat transfer enhancing flow field in sinusoidally, spirally corrugated tubes using computational fluid dynamics:**

Transferring heat through a straight tube is used in various processes. However, as the thermal boundary layer builds up, heat transfer is reduced drastically. To enhance the forced convection, different techniques are commonly used.

In this study, focus in on corrugated tubes that alter the flow field to enhance heat transfer. By representing the corrugated tube heat exchanger by a simple sinusoidal function, the corrugated tube is varied all the way from non-corrugated tubes to highly corrugated tubes. First, simulations of non-corrugated are validated by experimentally obtained heat transfer and pressure drop correlations found in literature. Next, parametric simulations are performed to investigate how the flow is affected by changes in corrugation. For a given Reynolds number, the Nusselt numbers and friction factors are mapped as function of corrugation height and length to ultimately propose guidelines on how to design corrugated tubes for various purposes.
The paper is reprinted in full in Part II on page 163.

- **Paper D: Guidelines for optimal selection of working fluid for an organic Rankine cycle in relation to waste heat recovery:**
  Waste heat is available at various temperatures from different sources found in nature and as a by-product from various industrial processes. One way to recover this waste energy is by the organic Rankine cycle that utilises different organic fluids as working fluid. As these fluids differ significantly in terms of thermodynamic properties, they are suited for extracting energy from sources at different temperatures.

  The purpose of this study is to come up with guidelines on how to link the performance of different fluids as working fluid candidates in the organic Rankine cycle to the temperature of the source available. To cover a wide range of temperature sources, sources in the temperature range 50°C to 280°C are investigated in intervals of 5 K. Based on the genetic optimisation algorithm (GA), design variables such as turbine inlet pressure and temperature, condensation pressure, hot source outlet temperature and mixture composition in the case of mixtures are chosen so that the maximum net work output. This optimisation is carried out for every temperature (intervals of 5 K) and working fluid candidate resulting in an extensive dataset of results from 1316 optimisations. Based on this dataset, a set of observations that link properties of the optimal working fluid candidate to the hot to the temperature of the source available are reported.
  The paper is reprinted in full in Part II on page 197.

Chapter 3

Introduction to Particulate Deposition

Particles sticking to heat exchanger surfaces will inherently take place and cause performance degradation in a wide range of industrial heat exchangers. Depending on the process stream of interest, the particles may be of different shape, size and of different molecular composition. Even the mechanism causing particles to deposit varies from gravity-dominated deposition, commonly denoted sedimentation, to deposition of smaller particles, where adhesive forces, such as van der Waals attraction, become important because of the small particle size. In the following, a brief overview of the different sub-processes governing the global particulate deposition process is given.

3.1 Particulate Deposition Sub-processes

The deposition process of particles depositing on a surface can be split into a combination of different distinct sub-processes. These are depicted in figure 3.1 along with different terms used throughout this study. When two particles collide, they may stick to each other and form a simple two-particle agglomerate. As these particles are adhered only due to adhesive forces, external forces may cause them to split up. Such external forces may result from collisions with other particles or agglomerates or due to high fluid forces acting to separate agglomerated particles in regions with high shear. These break-up mechanisms will be called "fluid-force-controlled agglomeration" and "collision-controlled agglomeration" in the rest of this work. As the break-up mechanism may vary significantly throughout the region of interest, agglomerates may range from only a few particles to several thousands as shown in figure 1.2 on page 5.
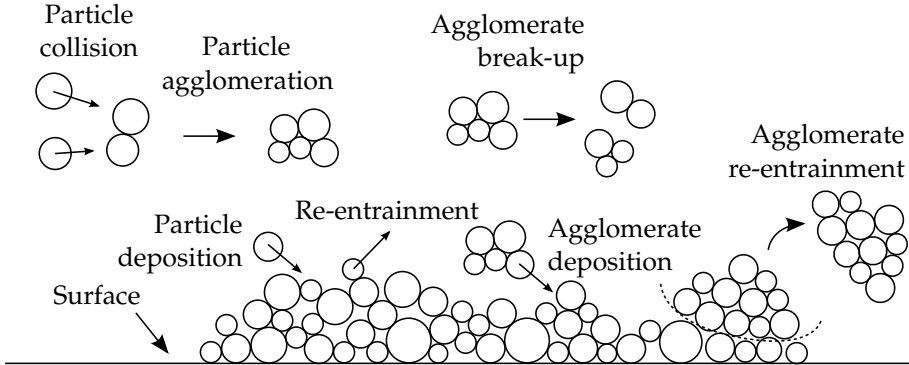
Figure 3.1: Overview of the various sub-processes that are implicitly accounted for when using the DEM approach.

As the agglomeration process is a result of particles colliding with one another, it is of prime importance to capture the different collision mechanisms using the CFD-DEM modelling framework. As a better understanding of the different collision mechanisms is of prime importance for a wide range of phenomena involving both non-adhesive and adhesive particles, it has been a research topic for a long period. The purpose of the following section is to give an overview of the different collision mechanisms that govern particle agglomeration.

3.1.1 Particle collision mechanisms

All collisions are directly related to how the particles are being transported by the fluid phase. The fluid phase flow can be anything ranging from uniform with few particle collisions to highly turbulent where collisions are frequent. The following gives an overview of the different collision mechanisms that are expected to dominate for different fluid flows and particles.

For particles in shear flow, see figure 3.2, the particles collide due to differences in velocity and the finite size of the particles involved. Collisions due
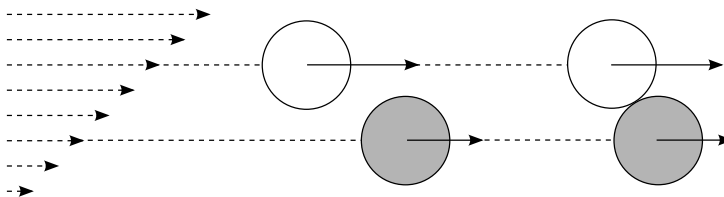
Figure 3.2: Particles colliding in shear flow field due to differences in velocity and the finite size of particles.

to shear in the flow field are expected to dominate the agglomeration process

for particles that follow fluid streamlines closely. By characterising the ability of particles to follow local flow structures with size l_c and velocity u by the local Stokes number $St = \rho_p d_p^2 u / (18\mu l_c)$, Stokes numbers $St \ll 1$ corresponds to cases where the collision mechanism depicted in figure 3.2 dominates. At higher Stokes numbers, the particles begin to drift away from fluid streamlines causing particles to collide as depicted in figure 3.3. The type of collision
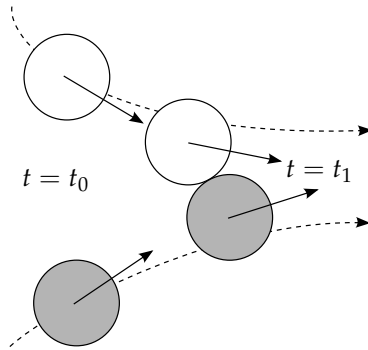
Figure 3.3: Particles mostly follow fluid streamlines but drift slightly due to particles inertia causing collision. At time $t = t_0$ particles follow fluid streamlines while at time $t = t_1$, the particles cannot follow fluid stream-lines due to finite inertia of particles causing collision.

shown in figure 3.3 is expected to occur when small differences between fluid streamlines and particles trajectory exist, that is for Stokes numbers $St \approx 1$. For high Stokes numbers ($St \gg 1$), there is almost no correlation between fluid stream lines and particle trajectories. For such cases, the particles may travel several eddy lengths before colliding with velocities highly different from the local fluid velocity as depicted in figure 3.4. Furthermore, Meyer
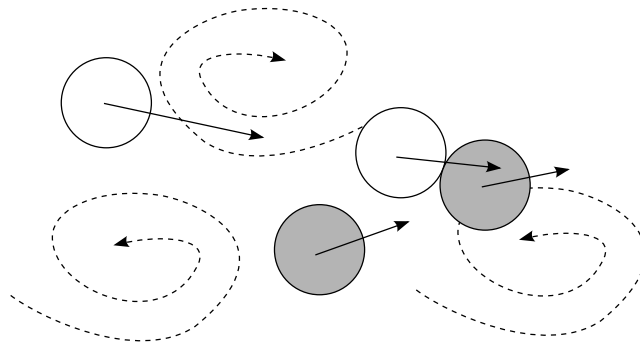
Figure 3.4: Particles are almost unaffected by the local fluid velocity causing particles to collide with a velocity almost uncorrelated with the local fluid velocity.

and Deglon (2011) suggests that Brownian motion and the combination of

gravity and poly-dispersed particles also cause particles to collide due to differing settling velocity. These collision mechanisms are not elaborated further in this study as neither gravity nor Brownian motion are expected to play an important role in the description of how micron-sized particles agglomerate and deposit in a turbulent flow. More details on the relative importance of the different forces are given in Section 3.3.

3.2 Non-dimensional Numbers

To describe the overall particle deposition process, a set of dimensionless numbers will be used. These quantify different aspects of the process such as the amount of turbulence in the flow field, the transport of particles, the collision frequency and the collision process itself. All these sub-processes all affect how and to what extent particles agglomerate and deposit.

The non-dimensional numbers outlined below will be used for various purposes to better understand and quantify the different sub-processes taking place.

3.2.1 Numbers related to the interaction between fluid and individual particles

The size and strength of the turbulence structures found throughout the flow field will inevitably vary in space and time. The intensity of the velocity fluctuations is a function of the Reynolds number alone describing the ratio of inertia to viscous forces. For a flow through a pipe, the Reynolds number Re is commonly based on the stream-wise mean fluid velocity U and the tube diameter D, forming:

$$\Pi_1 = \frac{\rho_f U D}{\mu} = \text{Re} \tag{3.1}$$

To describe the local motion of particles, it is useful to define local Reynolds numbers. In this study, these include a particle Reynolds number and a shear Reynolds number. The particle Reynolds number Re_p is based on the particle diameter d_p and the local slip velocity between particle and fluid phase $|v - u|$ giving: $\text{Re}_p = |v - u| d_p / \nu$. The shear Reynolds number Re_G is based on the local velocity gradient perpendicular to the direction of motion $G = \mathrm{d}u/\mathrm{d}y$ and the particle diameter, forming: $\text{Re}_G = d_p^2 G / \nu$. To describe rotational motion, the rotational Reynolds number $\text{Re}_\Omega = d_p^2 \Omega / \nu$ is used, where Ω denotes the angular velocity of the particle.

Throughout the flow field, turbulence structures with different time and length scales are found. To describe the ability of particles to respond to changes in the turbulent fluid flow, the Stokes number, defining the ratio of

particle response time τ_p to the characteristic time of the fluid flow τ_f, is used. As the length and time scales of the eddies vary throughout the flow field, the local Stokes numbers will vary as well. Therefore, it is convenient to define a global Stokes number based on the stream-wise mean fluid velocity and the pipe diameter, giving:

$$\Pi_2 = \frac{\rho_p d_p^2 U}{18\mu D} = \text{St} \tag{3.2}$$

In the above expression, it is assumed that fluid forces on the particles are dominated by viscous drag ($\text{Re}_p < 1$) so that Stokes drag dominates. In that case, the particle drag coefficient is inversely proportional to the particle Reynolds number. Other parameters describing the interaction between fluid and particulate phase include the density ratio ρ_p/ρ_f, which is important to the relative importance of the different fluid forces:

$$\Pi_3 = \frac{\rho_p}{\rho_f} = \chi \tag{3.3}$$

More details on the relative importance of different fluid force contributions is given in section 3.3. Furthermore, to describe the size of the particles, the dimensionless particle size parameter ϵ, describing the ratio of particle diameter to a characteristic fluid length, is used. For flow through a pipe, it is convenient to base it on the pipe diameter:

$$\Pi_4 = \frac{d_p}{D} = \epsilon \tag{3.4}$$

The Stokes number St can be re-written in terms of the other dimensionless numbers χ and ϵ and Re as: $\Pi_2 = \chi \epsilon^2 \text{Re}/18$. That is, these four dimensionless numbers are not independent of each other, even though they are useful for describing different aspects of how particles agglomerate and deposit in a turbulent pipe flow.

For particles interacting with a fluid, the overall particle concentration plays an important role. At sufficiently low concentrations, the effect of particles on the fluid can typically be neglected. However, for higher particle concentrations, the particles begin to affect the motion of the fluid. Furthermore, the motion of particles is affected by an increase in particle concentration as well. At higher particle concentrations, the collision frequency tends to be higher as well, which ultimately results in more particles agglomerating. For n_p particles each with volume V_p being present in a fluid with volume V_f, the volume concentration of particles is given by:

$$\Pi_5 = \frac{n_p V_p}{V_f + n_p V_p} = \phi \tag{3.5}$$

As particles begin to agglomerate and deposit, as sketched in figure 3.1, the local particle concentration become increasingly anisotropic throughout the flow field. This significantly affects the fluid force acting on individual particles. More information on how the local particle volume fraction is taken into account when describing the fluid force on particles is given in Chapter 5.

3.2.2 Numbers related to particle collisions

Just prior to collision when a particle approaches a surface or another particle, fluid is forced away from the contact region as depicted in figure 3.5. The result is a viscous dissipation force F_{vd} that effectively slows down a
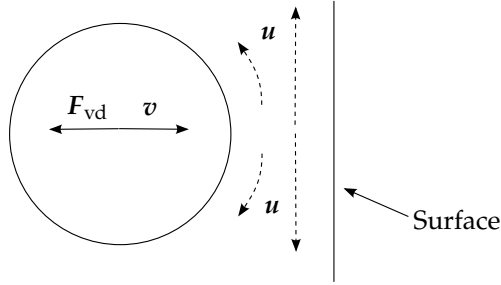
Figure 3.5: Viscous damping just prior to collision as fluid is forced away from the contact region.

approaching particle. For solid particles, Legendre et al. (2005) suggests the viscous dissipation to solely be a function of the collision Stokes number St* as:

$$\Pi_5 = \frac{(m_p + C_M m_f)\, v}{6\pi\mu r_p^2} = \text{St}^*$$

(3.6)

At the instant the particles come in physical contact, the motion of the particles is governed by contact forces in the particle-particle or particle-wall contact region. In the case of non-adhesive particles, the repulsive force upon collision is given by Hertzian theory (Hertz, 1882). In terms of global properties, the elasticity parameter can be written as:

$$\Pi_6 = \frac{E}{\rho_p U^2} = \lambda$$

(3.7)

where E is the effective Young's modulus. For flows containing particles of equal Young's modulus $E_i = E_j = E_p$ and Poisson's ratio $\nu_i = \nu_j = \nu_p$, the effective Young's modulus reduced to $E = (2(1-\nu_p^2)/E_p)^{-1}$. For collision between particle i and particle j or wall j, the effective Young's modulus is generally given by $E = ((1-\nu_i)/E_i + (1-\nu_j)/E_j)^{-1}$.

When adhesive behaviour between two particles, or a particle and a wall, is considered, a dimensionless group describing the strength of adhesive forces in the contact region relative to particle inertia is included as well. For this purpose the surface energy density γ is used forming the dimensionless adhesiveness parameter Ad:

$$\Pi_7 = \frac{\gamma}{\rho_{\mathrm{p}} U^2 d_{\mathrm{p}}} = \mathrm{Ad} \tag{3.8}$$

This formulation is used in the present work to describe particle adhesiveness in a pipe flow.

For local collision between particle i and particle j with radii r_{i} and $r_{\mathrm{j}} = \beta \cdot r_{\mathrm{i}}$ with inter-particle adhesion energy $2\gamma\pi R^2$ and effective particle inertia $(1/2)m|v_{\mathrm{i}} - v_{\mathrm{j}}|^2$, Chen et al. (2015) suggests:

$$\Pi_8 = \frac{2\gamma\pi R^2}{\frac{1}{2}m|v_{\mathrm{i}} - v_{\mathrm{j}}|^2} = \frac{3\gamma}{\rho_{\mathrm{p}}|v_{\mathrm{i}} - v_{\mathrm{j}}|^2 r_{\mathrm{i}}} \cdot \frac{1 + \beta^3}{(1 + \beta^2)\,\beta} = \mathrm{Ad} \tag{3.9}$$

In the case of collision between particle i and a wall j, $r_{\mathrm{j}} = \infty$ so that $\beta = \infty$ and equation (3.9) reduces to $\Pi_8 = 3\gamma/(\rho_{\mathrm{p}}|v_{\mathrm{i}} - v_{\mathrm{j}}|^2 r_{\mathrm{i}})$. In the case of a wall collision with velocity magnitude v_{p} and particle radius r_{p} at an oblique angle ψ, equation (3.9) is modified so that the particle inertia is projected normal to the wall as suggested by Hærvig et al. (2017) so that: $\Pi_8 = 3\gamma/(\rho_{\mathrm{p}}|v|^2\sin(\psi)^2 r_{\mathrm{p}})$.

Even for collisions where inter-molecular adhesive effects are negligible, the particle material still acts to dissipate kinetic energy. The result is particles separating with a relative velocity lower than the relative impact velocity. This is described through the coefficient of restitution, defining the ratio of relative velocity after impact to the relative velocity before impact. In the case of non-adhesive particles, energy is converted into heat and plastic deformation of the particle material upon collision:

$$\Pi_9 = \frac{v_{\mathrm{i,f}} - v_{\mathrm{j,f}}}{v_{\mathrm{j}} - v_{\mathrm{i}}} = e = \mathrm{const} \tag{3.10}$$

This parameter depends solely on particle material and not adhesive forces. However, as inter-molecular forces can cause particles to stick and agglomerate even when $e \neq 0$, it is useful to define an effective coefficient of restitution e_{eff} that takes into account inter-molecular adhesive forces acting in the contact region as well, i.e. van der Waals attraction:

$$\Pi_9 = \frac{v_{\mathrm{i,f}} - v_{\mathrm{j,f}}}{v_{\mathrm{j}} - v_{\mathrm{i}}} = e_{\mathrm{eff}} \tag{3.11}$$

3.3 Importance of the Different Force Contributions

When predicting the motion of particles in a turbulent flow, several mechanisms play important roles in the description of particle transport, particle collisions, particle agglomeration, break-up of agglomerates and deposition on surfaces in turbulent flows.

As the focus in this study is on the point-particle approximation, the description of fluid force relies on correlations describing on the different fluid forces such as drag and lift. The following section discusses the importance of these different fluid force contributions. For particles with $d_p = \mathcal{O}(10\,\mu m)$ not adhered to other particles, Stokes drag tend to be the dominating force. For a particle moving with velocity v in a fluid with local velocity u, Stokes drag is $F_d = 3\pi d_p \mu (v - u)$. However, in dilute flows with high shear where collisions are rare, the critical force required to separate two already adhered particles tend to be the dominating factor for the agglomeration process. For two particles (i and j) with surface energy density γ and effective radius $R = (1/r_i + 1/r_j)^{-1}$, the critical force required to separate them is $F_C = 3\pi R \gamma$ according to JKR theory. More info on JKR theory is given in Section 4.3.2 on page 36. In the following, Stokes drag and the critical separation force predicted by JKR theory are therefore used for normalisation.

3.3.1 Relative importance of forces contributions

This section presents an analysis with the purpose of assessing the importance of the different force contributions. Due to the temporal and spatial velocity fluctuations in the turbulent fluid flow, the purpose of this section is not to present an exact analysis but rather an approximate analysis assessing the importance of the different forces.

Relative importance of adhesive force

Consider two particles adhered to each other due to a surface energy density γ that develop a flattened contact region as predicted by JKR theory so that a critical separation force F_C is required to break contact (see Section 4.3.2 on page 36). The particles are transported in a turbulent pipe flow with diameter D, mean velocity U and shear rate G. The particle and fluid densities are ρ_p and ρ_f respectively and the dynamic viscosity is μ. This scenario is sketched in figure 3.6. The on-going processes of agglomerates being formed and breaking up can be controlled by either fluid forces due to shear in the flow field acting to break up agglomerates or by impacting particles with high kinetic energy that break up agglomerates. For the particles adhered in this work, the separation distance for adhered particles is approximately given
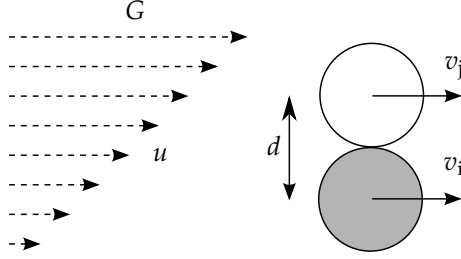
Figure 3.6: At an instant in time, two adhered particles a distance $d \approx r_i + r_j$ apart are being transported with velocities $v_i = v_j$ in a shear flow with local velocity u and shear rate G.

by the sum of the particle radii, so that $d \approx r_i + r_j$. As the particles move together, there is, for a given shear rate G, a velocity difference in the fluid flow across the particles of $u_i - u_j = Gd = G(r_i + r_j)$. This velocity difference acts to separate the particles. Assuming particle i and j to be subject to Stokes drag, the fluid force on each particle is:

$$F_{d,i} = 6\pi r_i \mu (v_i - u_i) \tag{3.12}$$

$$F_{d,j} = 6\pi r_j \mu (v_j - u_j) \tag{3.13}$$

The force acting to separate them F_{sep} is then given by:

$$F_{sep} = F_{d,i} - F_{d,j} = 6\pi\mu(r_i v_i - r_i u_i - r_j v_j + r_j u_j) \tag{3.14}$$

which in the case of equal-sized particles with $r_i = r_j = r_p$ reduces to:

$$F_{sep} = 12\pi\mu r_p^2 G \tag{3.15}$$

For equal sized particles the effective radius becomes $R = r_p/2$, see (4.11) on page 4.11, so that the critical force required to separate adhered particles becomes $F_C = (3/2)\pi r_p \gamma$. By taking the ratio of the critical force required to separate particles to the fluid force acting to separate particles in a shear flow, we obtain a non-dimensional group expression the tendency of adhered particles to break up due to shear in the flow field:

$$\frac{F_C}{F_{sep}} = \frac{(3/2)\pi r_p \gamma}{12\pi\mu r_p^2 G} = \frac{\gamma}{8 r_p \mu G} = \mathcal{O}\left(\frac{\gamma}{r_p \mu G}\right) \tag{3.16}$$

Expressing (3.16) in terms of the other more commonly used non-dimensional groups listed in Section 3.2, we obtain:

$$\frac{F_C}{F_{sep}} = \mathcal{O}\left(\frac{\chi \, \mathrm{Ad} \, \mathrm{Re}^2 \, \epsilon^2}{\mathrm{Re}_G}\right) \tag{3.17}$$

Noting that the Stokes number can be written in terms of the density ratio χ, the dimensionless particle size ϵ and the Reynolds number Re as $\mathrm{St} = \chi \epsilon^2 \mathrm{Re}/18$, the expression in (3.17) can also be written in terms of the Stokes number as: $F_\mathrm{C}/F_\mathrm{sep} = \mathcal{O}(\mathrm{Ad\ Re\ St}/\mathrm{Re_G})$. Using (3.17), values much smaller than 1 define processes where agglomerates tend to break up due to shear in the fluid flow and values much larger than 1 define processes where adhesive forces are strong enough to keep particles subject to a shear flow field adhered.

Similar analyses have already been reported in literature to assess the importance of the different forces affecting small particles in a dilute, dry air flow. These include a shear lift force F_l, a rotational lift force F_m, a Brownian motion force F_b, a buoyancy-corrected gravitational force F_g, an added mass force F_a and a history force F_h. An overview of the results reported by Marshall and Li (2014) is given in table 3.1 for completion. Here particle inertia $F_\mathrm{iner} = m_\mathrm{p} \mathrm{d}v/\mathrm{d}t$, which is in the same order as particle drag, is used for normalisation as well. Besides the non-dimensional groups listed in Section 3.2, the Froude number $\mathrm{Fr} = U/\sqrt{g_\mathrm{r}d_\mathrm{p}}$, describing the importance of gravity force, and the Peclet number $\mathrm{Pe} = DU/D_\mathrm{b}$, describing the importance of Brownian motion through the Brownian diffusion coefficient D_b, are used. The Brownian diffusion coefficient can be estimated through (Einstein, 1905): $D_\mathrm{b} = k_\mathrm{B}T/(3\pi\mu d_\mathrm{p})$, where k_B and T denote the Boltzmann constant and absolute temperature respectively. More details on how the results presented

Table 3.1: Relative importance of different forces governing how particles are transported and agglomerate. The force contributions used are the critical force required to break contact $F_\mathrm{C} = 3\pi\gamma R$, the force acting to separate particles due to shear in the flow field $F_\mathrm{sep} = 12\pi\mu r_\mathrm{p}^2 G$, Stokes drag $F_\mathrm{d} = 3\pi d_\mathrm{p}\mu(v - u)$ and fluid inertia $F_\mathrm{iner} = m\mathrm{d}v/\mathrm{d}t$.

Force contributions	Force ratio	Relative importance
Adhesive force	$F_\mathrm{C}/F_\mathrm{sep}$	$\mathcal{O}(\chi\ \mathrm{Ad\ Re}^2\ \epsilon^2/\mathrm{Re_G})$
Shear lift force	$F_\mathrm{l}/F_\mathrm{d}$	$\mathcal{O}(\mathrm{Re_G^{1/2}})$
Rotational lift force	$F_\mathrm{m}/F_\mathrm{d}$	$\mathcal{O}(\mathrm{Re_G})$
Brownian force	$F_\mathrm{b}/F_\mathrm{d}$	$\mathcal{O}(1/(\epsilon\ \mathrm{St\ Pe_f})^{1/2})$
Gravitational force	$F_\mathrm{g}/F_\mathrm{d}$	$\mathcal{O}(\epsilon\ \mathrm{Fr}^2)^{-1}$
Added mass force	$F_\mathrm{a}/F_\mathrm{iner}$	$\mathcal{O}(1/\chi)$
History force	$F_\mathrm{h}/F_\mathrm{d}$	$\mathcal{O}(\epsilon\ \mathrm{Re\ St})^{1/2}$

in table 3.1 are used to simplify the study of how adhesive particles agglomerate in a turbulent fluid are given in Chapter 6 or in Paper B reprinted on page 133.

Chapter 4

The Discrete Element Modelling Framework

The purpose of this chapter is give a complete overview of the DEM modelling framework used to predict the particle accumulation process. As DEM relies directly on the most simple force-displacement relations, the different sub-processes depicted in figure 3.1 are all implicitly included in the DEM modelling framework when the sub-models for phenomena such as adhesion and rolling resistance are included. Therefore, the purpose of this chapter is to both give a general overview of the contact models in DEM modelling framework as well as introduce the sub-models relevant to adhesive particles affected by van der Waals attractive force and an electrostatic force.

4.1 Governing Equations for Motion of Particles

In general, the motion of every particle at every instant in time is governed by the force balance in (4.1) that describes the instantaneous force. For particle i with mass m_i and position x_i, the force balance can be written as:

$$m_i \frac{d^2 x_i}{dt^2} = F_{i,n} + F_{i,t} + F_{i,ad} + F_{i,f} + F_{i,vd} + F_{i,g} \qquad (4.1)$$

Here the different force contributions include:

- A normal contact force F_n acting to separate particles in contact with other particles or the wall.

- A tangential contact force F_t acting on separate particles in contact with other particles or the wall.

- An adhesive force F_{ad} trying to maintain contact between two adhered particles or the contact between a particle adhered to a surface.

- A fluid force F_f exerted by the fluid on individual particles. For particles in a dilute system, the force contributions are viscous drag, pressure drag, Saffman lift due to shear, Magnus lift due to relative rotation between flow and particle, added mass due to acceleration of the surrounding fluid and Basset history force due to a delay in boundary layer build-up. When particles agglomerate and the local particle volume fraction ϕ_p increases, the force on the i'th particle is changed significantly due to the presence of surrounding particles.

- A viscous dissipation force F_{vd} decelerating the particle prior to collision due to the finite viscosity of the surround fluid.

- A buoyancy corrected gravity force F_g.

Likewise, using the DEM modelling framework, the angular motion of particles is predicted as well. The angular motion, or rather lack of angular motion, is responsible for keeping the particles adhered to a surface when subject to shear flow such as in a boundary layer. Given a spherical particle with mass m_i distributed uniformly, moment of inertia $I_i = md_p^2/10$ and instantaneous angular orientation θ_i, the torque balance can be written as:

$$I_i \frac{d^2\theta_i}{dt^2} = M_{i,con} + M_{i,f} + M_{i,r} \tag{4.2}$$

The different torque contributions can be summarised as:

- A contact torque M_{con} caused by an offset between the contact point and the centre of gravity.

- A fluid induced torque M_f caused by fluid forces.

- A rolling resistance torque M_r opposing rolling on a surface or over other particles causing particles to stay in place in a boundary layer or when subject to a gravity force.

4.2 Contact Force

The purpose of this section is to give an overview of the different contact force contributions in equation (4.1). These are typically several orders of magnitude higher than fluid forces and therefore govern the motion of particles when in contact with other particles or a surface. The contact forces include a normal force F_n acting along the vector from particle centre to particle centre n_{ij}, a tangential force F_t acting perpendicular to the normal force

and an adhesive surface force $\boldsymbol{F}_{\text{ad}}$ trying to maintain contact upon collision. First, general considerations on the DEM framework and its applicability to model particle build-up are given.

Within the DEM framework, two approaches exist for treating particle collisions; the hard-sphere and the soft-sphere approach. Using the hard-sphere approach, particle collisions are described by conservation of momentum laws and are assumed to occur instantaneously. As the collision process occur instantaneously, particles can only be in contact with one other particle at a time using the hard-sphere approach. Therefore the hard-sphere approach is not suited for simulations where particles remain in contact over longer time intervals such as for agglomerated particles. Using the soft-sphere approach, the particle motion is at all times given by the force balance in equation (4.1). Due to the general way particles are treated, the soft-sphere approach poses no restrictions on the agglomeration and deposition process.

4.2.1 Soft-sphere elastic contact

As opposed to the hard-sphere approach, the particles are numerically allowed to overlap slightly in the soft-sphere approach. This is schematically shown in figure 4.1. Considering two particles with radii r_{i} and r_{j} and posi-
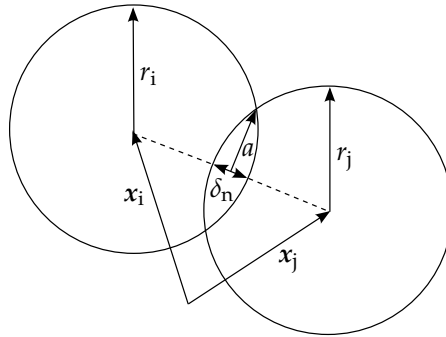
Figure 4.1: Soft-sphere approach where particles temporarily are allowed to overlap with overlap distance δ_{n} and contact radius a. Note that the overlap distance is not to scale with particle size in the drawing.

tions $\boldsymbol{x}_{\text{i}}$ and $\boldsymbol{x}_{\text{j}}$, the numerical overlap distance δ_{n} is found by:

$$\delta_{\text{n}} = r_{\text{i}} + r_{\text{j}} - |\boldsymbol{x}_{\text{i}} - \boldsymbol{x}_{\text{j}}| \tag{4.3}$$

The choice of relation used to relate the normal overlap distance δ_{n} to contact radius a (the radius of the circle formed by the two overlapping spheres) depends on particle properties, which ultimately dictates to what degree adhesive forces flatten out the contact region. More details on this matter is given in section 4.3 on page 35.

Force-displacement relations

To relate particle properties, position and velocity to the instantaneous contact force on particles, different approaches exist. In general, the different models represent the particle-particle interaction as variants of the spring-slider-dashpot system schematically shown in figure 4.2. The simplest mod-
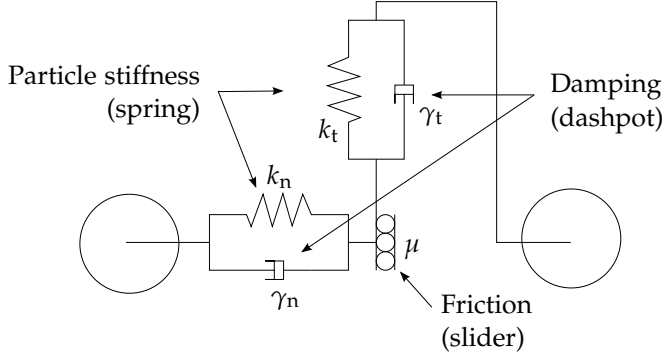
Figure 4.2: Spring-slider-dashpot model for Hertzian contact model.

els assume the normal contact force to be represented by a Hookian spring relation so that normal contact force $F_{n,con}$ depends linearly on the numerical overlap δ_n:

$$F_{n,con} = k_n \delta_n n_{ij} \tag{4.4}$$

where k_n is the spring constant and n is the unit vector between the particle centres:

$$n_{ij} = \frac{x_j - x_i}{|x_j - x_i|} \tag{4.5}$$

Using the Hookian type model, the spring constant k_n cannot be directly related to the properties of the particles. Instead, Hertz (1882) related the spring constant to particle stiffness through the Young's modulus and the contact radius a. As a depends on the normal overlap, the force does not depend linearly on the overlap distance as in the Hookian type model. For two spheres with centres separated by a distance $|x_j - x_i| = d$, the intersecting circle depicted in figure 4.1 has radius: $a = 1/(2d)\sqrt{(d + r_i - r_j) \cdot (d - r_i + r_j) \cdot (-d + r_i + r_j) \cdot (d + r_i + r_j)}$ (Weisstein, 2003). However, for small overlap distances and in the case of negligible adhesive forces, the contact radius is typically estimated as:

$$a = \sqrt{R\delta_n} \tag{4.6}$$

When representing the collision by a spring force only, the relative velocity after impact is equal to the relative velocity before impact. In the case of adhesive surface acting in the contact region, the result is particles that keep oscillating with constant amplitude. When real particles collide, different mechanisms act to dissipate kinetic energy in the particle material. The result is particles separating with a relative velocity lower than the impact velocity or in the case of sufficiently strong adhesive forces, the particles adhering. Kinetic energy being dissipated in the particle material is accounted for through a viscous damping term γ_n so that the normal contact force becomes:

$$\boldsymbol{F}_{n,con} = k_n \delta_n \boldsymbol{n}_{ij} + \gamma_n \boldsymbol{v}_n \tag{4.7}$$

where $\boldsymbol{v}_n$ is the relative normal velocity between the particles. Similarly, spring and viscous damping terms are added in the tangential direction so that the total contact force becomes:

$$\boldsymbol{F}_{con} = \left(k_n \delta_n \boldsymbol{n}_{ij} + \gamma_n \boldsymbol{v}_n\right) + \left(k_t \Delta \boldsymbol{s}_t + \gamma_t \boldsymbol{v}_t\right) \tag{4.8}$$

Using the Hertzian type models, the normal and tangential spring stiffnesses in equation (4.8) are based on properties and overlap of the particles through:

$$k_n = \frac{4}{3} E a = \frac{4}{3} E \sqrt{R \delta_n} \tag{4.9}$$

$$k_t = 8 G a = 8 G \sqrt{R \delta_N} \tag{4.10}$$

so that equation (4.4) becomes $\boldsymbol{F}_{n,con} = \boldsymbol{F}_{hz} = (4/3) E \sqrt{R} \delta_n^{3/2} \boldsymbol{n}_{ij}$, where the effective radius R, effective Young's modulus E and effective shear modulus G are given by:

$$\frac{1}{R} = \frac{1}{r_i} + \frac{1}{r_j} \tag{4.11}$$

$$\frac{1}{E} = \frac{1 - v_i^2}{E_i} + \frac{1 - v_j^2}{E_j} \tag{4.12}$$

$$\frac{1}{G} = \frac{2 - v_i}{G_i} + \frac{2 - v_j}{G_j} \tag{4.13}$$

where $G_i = E_i / (2(1 + v_i))$. Furthermore, the normal and tangential damping coefficients (γ_n and γ_t) are given by:

$$\gamma_n = -2 \sqrt{\frac{5}{6}} \beta \sqrt{S_n m} \tag{4.14}$$

$$\gamma_t = -2 \sqrt{\frac{5}{6}} \beta \sqrt{S_t m} \tag{4.15}$$

where the effective mass is:

$$\frac{1}{m} = \frac{1}{m_i} + \frac{1}{m_j}$$

(4.16)

and the coefficients β, S_n, and S_t are given by:

$$\beta = \frac{\log(e)}{\sqrt{\log^2(e) + \pi^2}}$$

(4.17)

$$S_n = 2E\sqrt{R\delta_n}$$

(4.18)

$$S_t = 8G\sqrt{R\delta_n}$$

(4.19)

The coefficient β ultimately accounts for the kinetic energy dissipated through the coefficient of restitution defining the ratio of final relative velocity after impact to relative velocity before impact:

$$e = \frac{|v_{i,f} - v_{j,f}|}{|v_i - v_j|}$$

(4.20)

The above listed set of equations accurately predicts normal and tangential forces acting on particles when the adhesive force can be neglected. In the following, different ways to include the adhesive force are discussed and compared.

4.3   Adhesive Contact Force

Adhesive forces acting between particles are present independently of the size of the particles. As the motion of larger particles typically is governed by other forces such as fluid, gravity and repulsive Hertzian contact forces, the adhesive forces, which are typically several orders of magnitude lower, can typically be neglected. When the particle size of interest become sufficiently small, adhesive forces become increasingly important and will eventually begin to dominate other forces causing particles to adhere upon collision. The result is particle agglomerates being formed throughout the flow field and a layer of particles building up on surfaces.

This section gives an overview of different modelling strategies to account for particle adhesiveness in the context of the Hertzian contact modelling framework outlined in the previous section.

4.3.1   The surface energy density

Several researchers have observed experimentally that a mechanical force is required to separate small particles close to each other (Adamson, 1997). For
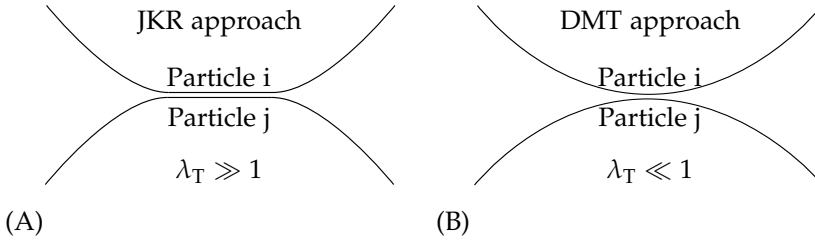
Figure 4.3: Difference in modelling approaches to account for adhesive forces. The figure shows two equilibrium conditions with: (A) JKR approach (Johnson et al., 1971) where the particles develop a flattened contact region; (B) DMT approach (Derjaguin, 1934) where particles are not deformed due to the adhesive force.

micron-sized particles with size $d_\mathrm{p} = \mathcal{O}(10\ \mu\mathrm{m})$ in a dry fluid, this adhesive behaviour is commonly explained by a combination of van der Waals and electrostatic forces (Feng and Hays, 2003). To describe the strength of the combined adhesive force due to van der Waals force and electrostatic effects, the concept of surface energy density γ is commonly used. Having units J/m^2, the surface energy density basically describes the work required to create new surface when separating two adhered particles.

Two distinctly different modelling approaches exist when taking into account adhesiveness through the surface energy density (Tabor, 1977). These are schematically shown in figure 4.3. Depending on the properties of the particles and the strength of adhesive surface forces, the adhesive forces either deform the particle surface slightly (JKR approach by Johnson et al. (1971)) or let the surfaces stay intact (DMT approach by Derjaguin (1934)). To describe to which degree the particles are deformed due to adhesive forces and therefore which approximation is more valid, Tabor (1977) suggested the dimensionless Tabor parameter λ_T, describing the ratio between of deformation in the contact region to the effective range of adhesive forces:

$$\lambda_\mathrm{T} = \left(\frac{4R\gamma^2}{E^2 D_{\min}^3} \right)^{1/3} \tag{4.21}$$

where $D_{\min}$ is the minimum separation distance due to an always present atomic separation (Krupp, 1967). The minimum separation length is typically taken to be $D_{\min} = 1.65$ Å (Parteli et al., 2014; Götzinger, 2003), which compares well to experimental results (Israelachvili, 1992). Based on the value of λ_T, Johnson and Greenwood (1997) suggested a non-dimensional map showing the borders between between the different models. To sum it up, Johnson and Greenwood (1997) suggests the DMT approximation to be valid when $\lambda_\mathrm{T} \ll 1$ (typically $\lambda_\mathrm{T} < 0.1$) and the JKR approach to be valid in the opposite extreme when $\lambda_\mathrm{T} \gg 1$ (typically $\lambda_\mathrm{T} > 10$).

In the following, the different modelling approaches are outlined and

compared.

4.3.2 Modelling approaches

Derjaguin approach

As elastic deformation is assumed to play a negligible role in the DMT model by Derjaguin (1934), the adhesive force upon contact is constant. Using the DMT approach, the normal force on particle i in contact with particle j is given by:

$$F_{\text{DMT}} = \frac{4}{3}E\sqrt{R\delta_n}\delta_n n_{ij} - 4\pi R\gamma n_{ij} \tag{4.22}$$

where the first term is the Hertzian term and the second term is the adhesive DMT term. To take into account an attraction force when the particles are not in physical contact, Parteli et al. (2014) suggests the following piece-wise function for the second term (4.22):

$$F_{\text{vdW}} = \begin{cases} \frac{A_H R}{6D_{\text{min}}^2}n_{ij} & \delta_n > 0 \\ \frac{A_H R}{6(\delta_n - D_{\text{min}})^2}n_{ij} & -D_{\text{max}} \leq \delta_n \leq 0 \\ 0 n_{ij} & \delta_n < -D_{\text{max}} \end{cases} \tag{4.23}$$

where the strength of adhesive forces is described by the Hamaker constant A_H suggested by Hamaker (1937), which relates to the surface energy density through $A_H = 24\pi D_{\text{min}}^2\gamma$. Inserting this expression into equation (4.23), the expression for $\delta_n > 0$ equals the expression in (4.22). Using, the expression in (4.23), a constant force is added upon contact while the adhesive force approaches zero asymptotically when the particles are not in contact. To limit computational efforts, Parteli et al. (2014) suggests the cut-off distance $D_{\text{max}} = 1$ μm after which the attractive force is neglected.

Johnson-Kendall-Roberts approach

To take into account particle deformation on the adhesive force, Johnson et al. (1971) did a series of experiments with soft rubber and gelatine spheres in contact with flat surfaces. They observed a finite contact radius under zero load not, predicted by Hertzian theory, given by:

$$a_0 = \left(\frac{9\pi\gamma R^2}{E}\right)^{1/3} \tag{4.24}$$

To take into account the adhesive forces in the contact region on particle deformation, they proposed a new model relating the normal force to the
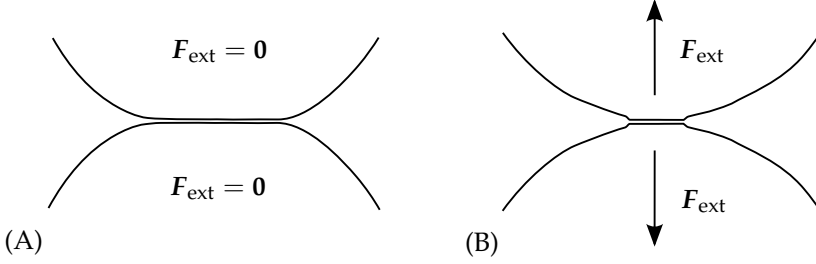
Figure 4.4: Force-displacement relations using the JKR model: (A) Particle are held together by adhesive forces acting to flatten out the contact region; (B) An external force acts to separate the adhered particles but contact is maintained even for $\delta_n < 0$ due to necking of the particle material.

contact radius. Using the JKR model, the normal force containing both the repulsive Hertzian contribution and the adhesive contribution becomes:

$$\boldsymbol{F}_n = \frac{4E}{3R}a^3\boldsymbol{n}_{ij} - 4\sqrt{\pi\gamma Ea^3}\boldsymbol{n}_{ij} \tag{4.25}$$

where the first term denotes the repulsive Hertzian term in a form different from (4.4) with k_n in (4.9) due to the contact area being different when adhesive forces act in the contact region. The second term is JKR adhesive term taking into account adhesiveness through the surface energy density γ. As the adhesive force deforms the contact region in the JKR regime $\lambda_T \gg 1$, there is a finite contact area even when zero load is applied. When an external force acts to separate particles in contact, contact is maintained even for separation distances higher than $r_i + r_j$ due necking of the particle material. This is schematically shown in figure 4.4. As the size of the flattened contact region in figure 4.4 changes with separation distance, so does the adhesive force. The relation between contact radius a and normal overlap δ_n is given by (Parteli et al., 2014; Deng et al., 2013):

$$a^4 - [2R\delta_n]\,a^2 - \left[4\pi\gamma R^2/E\right]a + \left[R^2\delta_n^2\right] = 0 \tag{4.26}$$

To get a better overview of (4.26), it is shown graphically in figure 4.5 for $a > 0$ with the contact radius normalised by the equilibrium contact radius $a_0 = (9\pi\gamma R^2/E)^{1/3}$ and the normal overlap normalised by the critical overlap required to break contact $\delta_C = a_0^2/(2(6^{1/3}R))$. As the figure shows, there is a finite contact radius at $\delta_n/\delta_C = 0$, which is explained by necking in the particle material. As noted by Chokshi et al. (1993), contact is maintained until $\delta_n/\delta_c = -1$ after which the particle material suddenly slips, contact is broken and the particles separate. Figure 4.6 gives an overview of the JKR force-displacement relation from equation (4.25) with the contact radius given by (4.26). As the figure shows, an external force F_C is required to
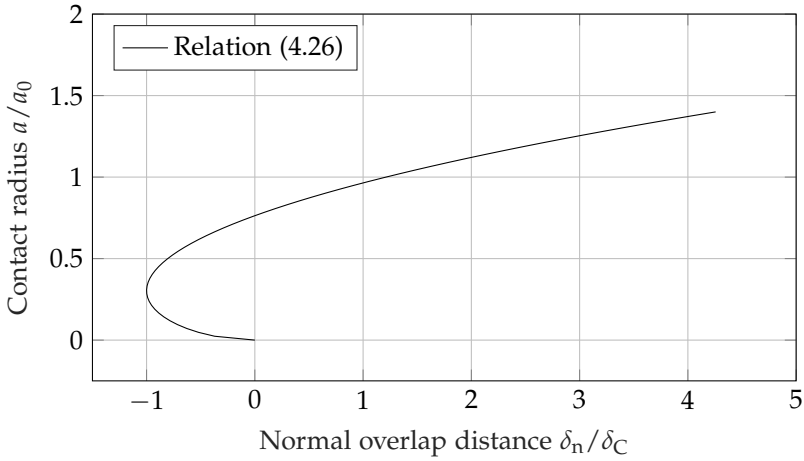
Figure 4.5: Relation between contact radius a and normal overlap distance. The contact radius a and normal overlap distance are made non-dimensional by the equilibrium contact radius $a_0 = (9\pi\gamma R^2/E)^{1/3}$ and critical overlap distance $\delta_C = a_0^2/(2(6^{1/3}R))$ respectively. Contact is broken once the normal overlap reaches $\delta_n/\delta_C = -1$ in the separation process (Chokshi et al., 1993).
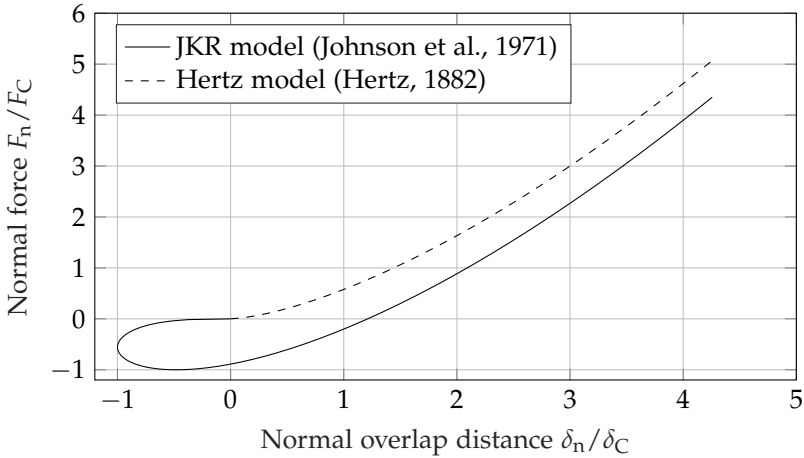
Figure 4.6: Relation normal force and normal overlap distance. The normal force and normal overlap distance are made non-dimensional by the critical force required to break contact $F_C = 3\pi R\gamma$ and the critical overlap distance $\delta_C = a_0^2/(2(6^{1/3}R))$ with a_0 given by (4.24) respectively.

separate particles in contact:

$$F_C = 3\pi R\gamma \tag{4.27}$$

Due to the wide range of particles having Tabor parameters $\lambda_T > 10$ where adhesive contact forces play an important role, the JKR model is applied frequently. Figure 4.7 gives an overview of the popularity of the JKR model visualised by yearly number of citations. As the figure shows,
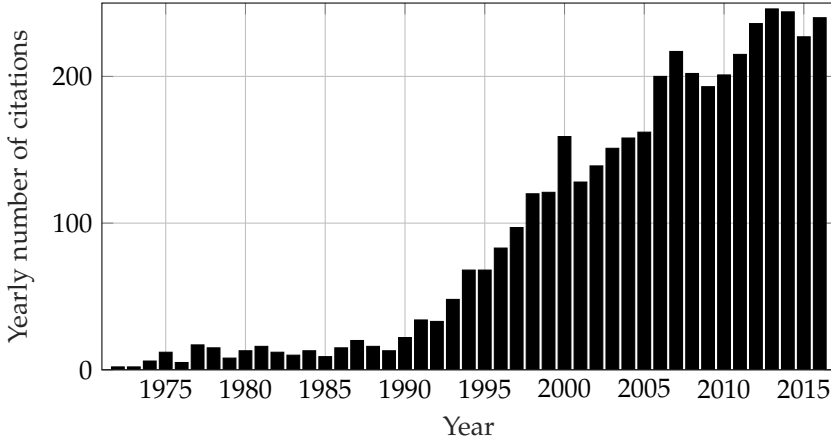
Figure 4.7: Yearly citations to the adhesive JKR model by Johnson et al. (1971). Data extracted from Web of Science at the time of writing.

4.3.3 Comparison of JKR and DMT based adhesiveness models

As already mentioned, the main difference between the JKR and DMT models is whether the contact region is flattened due to adhesive forces or not. This is commonly described through the Tabor parameter in (4.21), where $\lambda_T \gg 1$ denotes flattened contact region and $\lambda_T \ll 1$ denotes particles that stay contact so that the adhesive forces acts between two non-deformed particles. In between these two extremes, the model by Maugis (1992) provides a smooth transition between the two, from $\lambda_T \ll 1$ to $\lambda_T \gg 1$. Figure 4.8 gives an overview of the force-displacement relation of the Hertz model, the JKR model and the DMT model:

Adhesiveness models for the discrete element method simulations

When accounting for the adhesive behaviour of particles in discrete element method simulations, various modifications are commonly used. Such modifications act to speed up the simulations in different ways by various assumptions. One such assumption used in the simplified JKR model (SJKR) is to describe the adhesive force as proportional to the contact area πa^2, so that
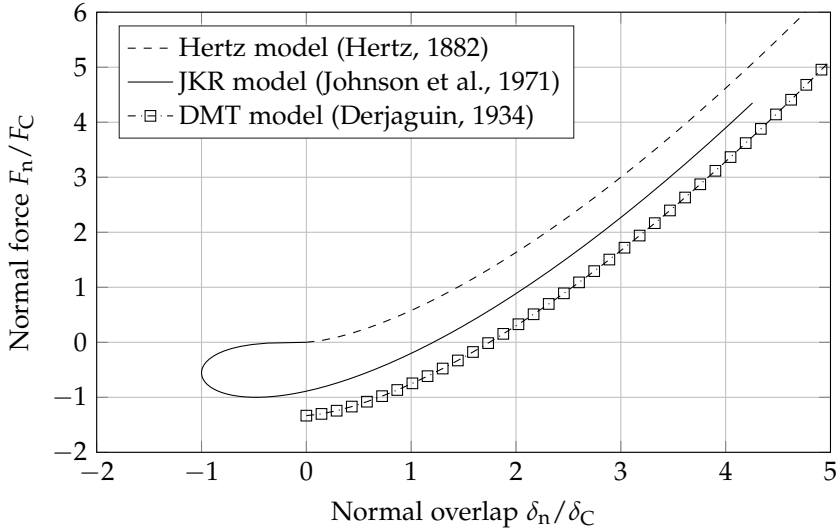
Figure 4.8: Comparison between forces predicted by the Hertz repulsive model, the JKR model by Chokshi et al. (1993), the JKR model by Johnson et al. (1971) and the DMT model by Derjaguin (1934). The critical force and overlap used for normalisation are $F_C = 3\pi R\gamma$ and $\delta_C = a_0^2/(2 \cdot 6^{1/3} R)$ respectively.

the normal force becomes:

$$\boldsymbol{F}_{\mathrm{n}} = \frac{4E}{3R} a^3 \boldsymbol{n}_{\mathrm{ij}} - c_{\mathrm{sjkr}} \pi a^2 \boldsymbol{n}_{\mathrm{ij}} \qquad (4.28)$$

where c_{sjkr} is the cohesion energy density in J/m². Depending on the interest in level of detail, the contact area for particle i is calculated by expressions varying in complexity. These expressions range from $A = 2r_{\mathrm{i}}\delta_{\mathrm{n}}$ to $A = r_{\mathrm{i}}r_{\mathrm{j}}/(r_{\mathrm{i}} + r_{\mathrm{j}})\delta_{\mathrm{n}}$ to the actual area of the intersecting circle (Weisstein, 2003):

$$A = \frac{\pi}{4d^2}(d - r_{\mathrm{i}} - r_{\mathrm{j}})(d + r_{\mathrm{i}} - r_{\mathrm{j}})(d - r_{\mathrm{i}} + r_{\mathrm{j}})(d + r_{\mathrm{i}} + r_{\mathrm{j}}) \qquad (4.29)$$

where d is the distance between particle i and j so that $d = |\boldsymbol{x}_{\mathrm{i}} - \boldsymbol{x}_{\mathrm{j}}|$. By describing the adhesive force through equation (4.28), the adhesive behaviour is significantly different from JKR theory by Johnson et al. (1971). Differences include a zero normal force when the particle come into contact $\delta_{\mathrm{n}} = 0$, a maximum adhesive force for finite contact radii and an equilibrium overlap distance that differs significantly from JKR theory. Therefore, focus is on JKR type models that describe the adhesive model through equation (4.25) with contact radius given by equation (4.26).

JKR based models for discrete element method simulations

When implementing the force-displacement relation shown in 4.6, it is important to note that negative overlap distances $\delta_n/\delta_C < 0$ occur due to necking in the particle material in the separation process. When particles first approach each other and come into contact at $\delta_n = 0$, the normal force suddenly attains a value of $-(8/9)F_C$, which is characteristic for the JKR model. When the particles are separated, contact is maintained for negative overlap distances $\delta_n < 0$ until contact suddenly breaks. This behaviour is shown in figure 4.9. In literature, the behaviour depicted in figure 4.9 is implemented
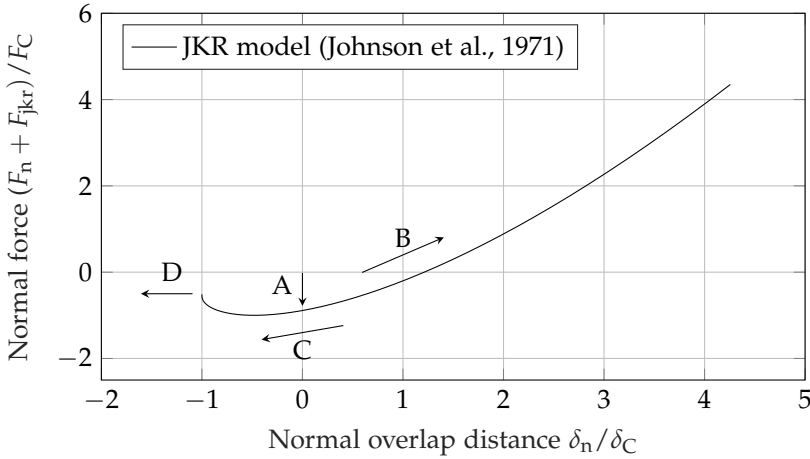
Figure 4.9: History dependent adhesive behaviour taking necking into account using the JKR model: (A) Without external force applied, the particle come in contact at $\delta_n = 0$ and the normal force attains a value $F_n = -(8/9)F_C = -(8/9)3\pi R\gamma$; (B) The particle centres approach each other and a flattened contact region between the particles is obtained. At the equilibrium condition the contact radius is given by (4.24) with normal overlap $\delta_0 = (1/3)a_0^2/R$; (C) An external force is applied to separate the adhered particles. Due to necking of the particle material, contact is maintained for negative overlap distances; (D) The particles separate irreversibly when the particle material cannot sustain contact.

in different ways:

- Implement the full behaviour, including the necking behaviour for $\delta_n < 0$. In this case, an additional boolean variable for each particle-particle and particle-wall pair is required to keep track of whether the particle material necks or the particles are not yet in contact.

- Implement the same behaviour when particles approach each other and separate. In this case, particle necking is accounted for before particles come into physical contact.

- Implement the JKR model and assume particle necking to play a negligible role for the adhesive behaviour. In this case, particles come in contact and separate at $\delta_n = 0$ where the normal force is $F_n = -(8/9)F_C = -(8/9)3\pi R\gamma$ as in common JKR theory.

To the author knowledge, no studies have been carried out comparing the different ways to implement the JKR model listed above. However, the study by Pasha et al. (2013) suggests the latter method to give reasonable agreement with experiments when simulating the interacting behaviour of many particles using the discrete element method. Furthermore, as shown by Hærvig et al. (2017), this method agrees with experimental data for collisions of two particles under well-defined conditions, such as simple head-on collisions, as well.

4.4 Rolling, Sliding and Twisting Friction

As opposed to other methods, the Discrete Element Method solves for particle rotation as well. Besides normal adhesion/repulsive behaviour described in Section 4.3, the particles may roll, slide or twist as schematically shown in figure 4.10. However, as noted in the studies by Dominik and Tielens (1995,
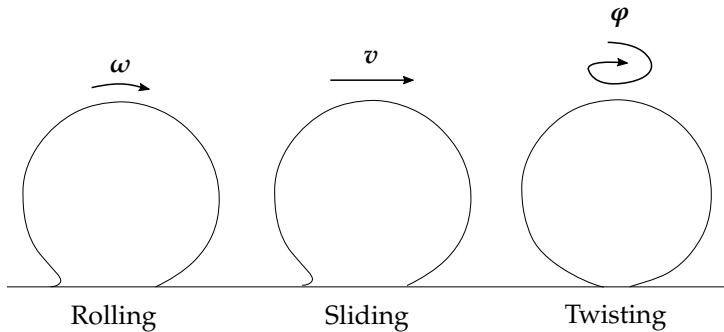
Figure 4.10: Different kinds of adhesive particle motion related to particle/particle or particle/wall contact. Rolling denotes angular motion, where the

1997) investigating the adhesive behaviour of particles, rolling tends to be much more common than sliding and twisting for small particles. As rolling tends to be the dominating mechanism, much research has been focused on deriving a way to accurately describe rolling motion under JKR contact with a wall. For non-adhesive contact with a wall without any external force, the particle will roll with angular velocity ω without the particle material slipping as shown shown in figure 4.11. As the particle material does not slip in the contact region, the rolling velocity v_r is proportional to the angular velocity of the particle as $v_r = r_p\omega \times n_{ij}$. In literature concerned with non-adhesive
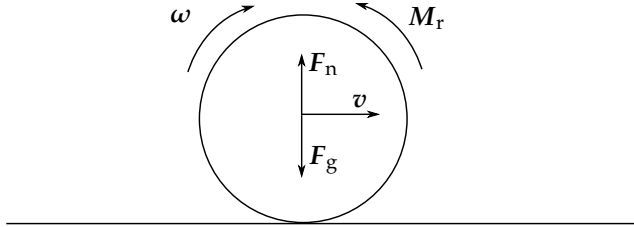
Figure 4.11: Non-adhesive particle in contact with a wall and in normal equilibrium ($F_n = F_g$) moving at a translational velocity v and angular velocity ω while experiencing a rolling resistance torque M_r.

particles, the rolling resistance torque opposing angular motion is often proportional to the angular velocity itself. However, such models are unable to explain the phenomenon of small adhesive particles sticking to vertical surfaces when subjected to an external force parallel to the wall, such as in the case of a fluid force in a boundary layer or gravity force on a vertical surface. These phenomena can only be explained by a torque opposing rotation causing particles to stay in place. This behaviour is suggested by Dominik and Tielens (1995, 1997) to be important when describing how agglomerates are formed and deformed due to impacting particles or fluctuating fluid forces in a turbulent flow.

In the following the modelling framework used to model the adhesive rolling is outlined briefly.

4.5 Adhesive Rolling Resistance

As in the case of JKR contact, a particle in normal equilibrium with a wall develops a flattened contact region. In this case, the centre of gravity of the particle projected onto the surface coincides with the centre of the contact area. This equilibrium condition is schematically shown in figure 4.12(A). However, when an external force F_{ext} is applied parallel to the surface, such as in the case of gravity acting on a particle on a vertical wall, a small shift between the projected centre of gravity and the centre of contact builds up, as depicted in figure 4.12(B). The result is an asymmetric contact region that introduces an adhesive rolling resistance torque that opposes motion and an even more asymmetric contract regions. To describe the adhesive rolling resistance torque, Dominik and Tielens (1995, 1997) introduced a rolling displacement term ξ that defines the rolling distance the centre of contact lags behind the centre of gravity. Based on the rolling velocity v_r, the rolling displacement ξ is calculated directly as by integrating the instantaneous rolling
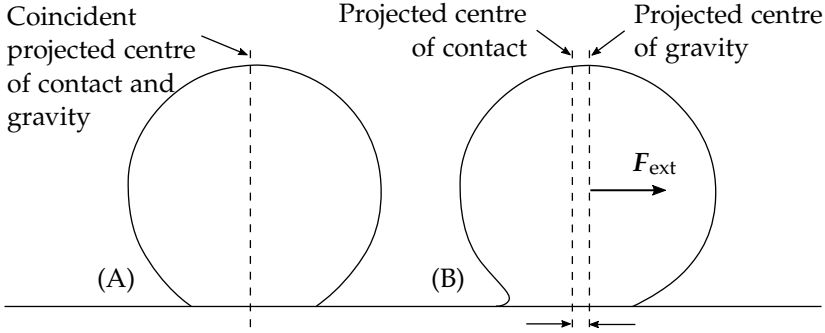
Figure 4.12: JKR contact of a particle in normal equilibrium with a surface ($F_n = F_g$): (A) Normal equilibrium without any external force applied. The centre of gravity projected onto the surface coincides with the centre of the contact region; (B) An external force $F_{ext} \neq 0$ acts on the particle so that a non-coincident projected centre of mass and centre of contact exist. Reprinted from "On the adhesive JKR contact and rolling models for reduced particle stiffness discrete element simulations" by J. Hærvig, U. Kleinhans, C. Wieland, H. Spliethoff, A.L. Jensen, K. Sørensen and T.J. Condra published in Powder Technology, vol. 319, pp. 472–482, 2017, with permission from Elsevier.

velocity as suggested by Marshall (2007):

$$\xi = \left(\int_{t_0}^{t_1} v_r(t) \mathrm{d}t \right) \cdot t_r \tag{4.30}$$

where $t_r = v_r/|v_r|$ is the direction of rolling. When the particle is rolled less than a critical distance $\xi < \xi_{crit}$ when the external force is removed, the particle rolls reversibly back from position B to A. If the rolling displacement exceeds a critical value $\xi > \xi_{crit}$, irreversible rolling occurs, the particle material slips and the centre of contact re-adjusts itself. In that case, a new equilibrium is obtained if the external force is removed. Different studies have proposed values for this critical rolling displacement ξ_{crit}. While Dominik and Tielens (1995, 1997) suggests $\xi_{crit} \approx 2$ Å, the study by Krijt et al. (2014) relates the critical rolling displacement to material properties through:

$$\xi_{crit} = \frac{a_0}{12} \frac{\Delta\gamma}{\gamma} \tag{4.31}$$

where a_0 is the equilibrium contact area defined by (4.24) and $\Delta\gamma/\gamma$ is a dimensionless adhesion hysteresis parameter. Based on the instantaneous rolling displacement ξ, the studies by Dominik and Tielens (1995, 1997) defines the rolling resistance coefficient k_r as:

$$k_r = 4F_C \left(\frac{a}{a_0} \right)^{3/2} \tag{4.32}$$

where F_c, a, and a_0 are the critical force, the instantaneous contact radius, and the equilibrium contact radius respectively. Based on the rolling resistance coefficient k_r and the instantaneous rolling displacement term ξ, the instantaneous rolling resistance torque is obtained as:

$$M_r = \begin{cases} k_r \xi & \text{if } \xi < \xi_{\text{crit}} \\ k_r \xi_{\text{crit}} & \text{if } \xi \geq \xi_{\text{crit}} \end{cases} \tag{4.33}$$

As the rolling displacement term cannot exceed the critical rolling displacement, the rolling displacement is numerically truncated to fulfil $\xi \leq \xi_{\text{crit}}$.

Chapter 5

Interaction Between Particles and Fluid

5.1 Fluid Force Contributions

This chapter outlines the modelling framework used to predict the interaction between fluid and small micron-sized particles. In the following, the force contributions listed below are considered:

- Drag force

- Shear and rotation induced lift forces

- Unsteady forces due to acceleration of finite mass of surrounding fluid

- Gravity and buoyancy forces

- Brownian motion force

- Viscous dissipative force just prior to collision

5.1.1 Drag force in flows with low particle volume fraction

Fluid drag tends to dominate the motion of a wide range of particles. As a result, research has focused on estimating fluid drag on spheres for a long time. Typically, the drag force is formulated as:

$$\boldsymbol{F}_{\mathrm{d}} = C_{\mathrm{d}} \frac{1}{2} \rho_{\mathrm{f}} |\boldsymbol{u} - \boldsymbol{v}| (\boldsymbol{u} - \boldsymbol{v}) A_{\mathrm{p}} \tag{5.1}$$

where C_{D} is a drag coefficient that takes into account different phenomena, $\boldsymbol{u}$ and $\boldsymbol{v}$ are the local fluid and particle velocities respectively and

$A_p = (\pi/4)d_p^2$ is the cross-sectional area of the particle. The following contains a description of how the drag coefficient C_D varies under different conditions.

Generally, the flow around micron-sized spheres tend to stay attached to the surface without separating so that the drag is dominated by viscous drag rather than form drag. That is, the particle Reynolds number tend to be less than 1: $Re_p = \rho_f d_p |u - v|/\mu < 1$. In this particular case, the analytical solution derived by Stokes (1850) suggests the drag coefficient to be inversely proportional to the particle Reynolds number:

$$C_{D,stk} = \frac{24}{Re_p} \tag{5.2}$$

To cover a wider range of Reynolds numbers outside the Stokes regime, the correlation by Schiller and Neumann (1935), which modifies Stokes drag at higher particle Reynolds numbers, is more commonly used:

$$C_D = \frac{24}{Re_p} \left(1 + 0.15 Re_p^{0.687}\right) \tag{5.3}$$

The correlations for drag coefficients are in general given in the following form:

$$C_D = \frac{24}{Re_p} F \tag{5.4}$$

where F is a dimensionless drag force that is used to represent different effects. Using the expression in (5.4), the expressions in (5.2) and (5.3) are recovered by setting $F = 1$ and $F = 1 + 0.15 Re_p^{0.687}$ respectively.

Effect of surface slip

However, as noted by several authors the no-slip condition typically assumed at the particle surface may not be applicable when the particle size considered is sufficiently small or the distance between fluid molecules is high. In these cases, the flow around particles cannot be considered a continuum and instead fluid drag is governed by fluid molecules colliding with the particle surface (Cunningham, 1910). In this case, several authors, including Mallikan (1923), have proposed correction factors that modify Stokes drag as:

$$\frac{C_D}{C_{D,stk}} = \frac{1}{1 + Kn\left(A_1 + A_2 \exp\left(-A_3/Kn\right)\right)} \tag{5.5}$$

The correlation in (5.5) is schematically shown in figure 5.1. For air at normal pressure and temperature, Davies (1945) suggests $A_1 = 2.514$, $A_2 = 0.8$ and $A_3 = 0.55$ so that the slip correction factor as function of the Knudsen number
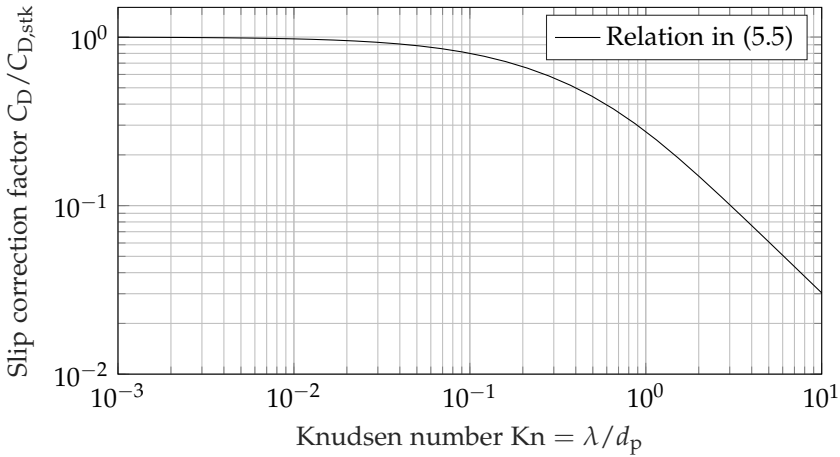
Figure 5.1: Modification of Stokes drag from (5.5) when slip occurs at the particle surface due to either small particle size d_p or high mean free path of fluid molecules λ characterised by the Knudsen number $Kn = \lambda/d_p$. In the figure, the constants are $A_1 = 2.514$, $A_2 = 0.8$ and $A_3 = 0.55$ corresponding to normal conditions (Davies, 1945).

is as shown in figure 5.1. For conditions where $p = 1.0$ bar and $T = 293.15$ K, the mean free path of molecules is $\lambda \approx 60$ nm. For a particle with $d_p = 10$ μm, the Knudsen number is then $Kn = \lambda/d_p \approx 0.06$ so that the slip factor is $C_D/C_{D,stk} \approx 0.985$ according to (5.5). As a result, the effect of surface slip is not further considered in the present work.

Even though extensive experimental validation has been carried out for single spheres in unbounded flows, much work remains to be done for particles affected by the presence of other particles. As particles begin to adhere to one another and agglomerates form, the local particle concentration α_p becomes increasingly anisotropic throughout the flow field. Depending on the particle and fluid properties, the agglomerates have varying morphologies that range from compact to more dentric in shape, see figure 1.1(B) and figure 1.2 respectively. This anisotropic behaviour complicates the description of drag force on individual particles. Therefore, different approaches have been proposed in literature to avoid having to resolve the detailed flow field around every single particle. These different approaches are outlined briefly in the following.

5.1.2 Drag force in flows with high particle volume fraction

The presence of other particles significantly affects the behaviour of the individual particles. Even though analytical solutions exist for simple cases such as laminar flow through concentric arrays of fixed spheres (Happel, 1958),
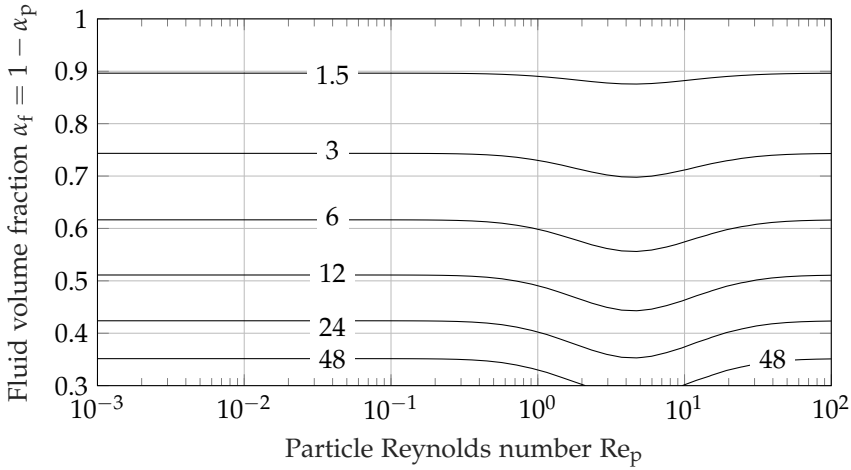
Figure 5.2: Dimensionless drag force F in (5.4) as function of particle Reynolds number $Re_p = \rho_f d_p |\boldsymbol{u} - \boldsymbol{v}|/\mu$ and fluid volume fraction $\alpha_f = 1 - \alpha_p$ according to the model by Felice (1994).

no general solutions exist. Therefore, much effort has been done both experimentally and numerically to propose more or less complex correlations that cover different ranges of particle Reynolds numbers and particle volume fractions. Using the point-particle approach, the particle size is significantly smaller than the computational mesh,

Early attempts to predict pressure loss through randomly packed spheres include Ergun and Orning (1949) and Wen and Yu (1966) who predicted the pressure gradients in fluidized beds as function of fluid volume fraction. The more recent study by Felice (1994) investigated how drag on single particles is modified by the presence of surrounding particles characterised by the fluid volume fraction. By fitting existing data available in literature, Felice (1994) suggests F in (5.4) to be related to the fluid volume fraction $\alpha_f = 1 - \alpha_p$ through:

$$F = \alpha_f^{-\beta} \tag{5.6}$$

where the coefficient β in (5.6) is a function of the particle Reynolds number:

$$\beta = 3.7 - 0.65\exp\left(-\frac{(1.5 - \ln(Re_p))^2}{2}\right) \tag{5.7}$$

More recent studies mainly focus on various numerical approaches to predict how drag is modified due to the presence of surrounding particles. One such model based on numerical simulations is the one proposed by Koch, Hill and Ladd.
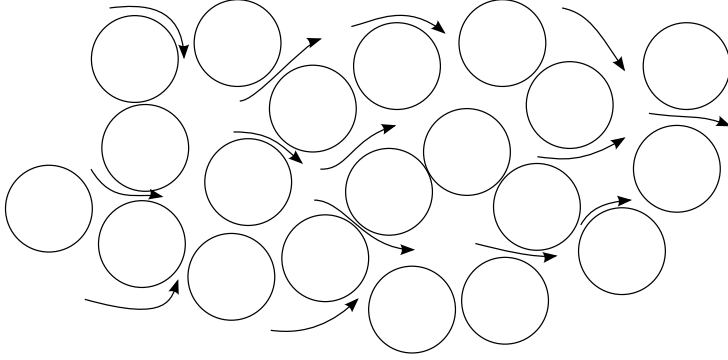
Figure 5.3: Flow through a random array of spheres resolved by Lattice-Boltzmann simulations by Hill et al. (2001a,b).

Koch-Hill-Ladd Model

Hill et al. (2001a,b) did a series of detailed simulations using LBS (Lattice-Boltzmann Simulations) to investigate the detailed flow field through randomly or aligned cubic and face-centred cubic collections of spherical particles, see 5.3. By varying both the particle Reynolds number Re_p and the particle volume fraction α_p, a correlation describing the drag force on individual particles by the fluid flow was proposed. Again, expressing the modified drag coefficient by dimensionless drag force F in (5.4), the modified Koch-Hill-Ladd model formulation by Benyahia et al. (2006), which covers a wider range of particle Reynolds numbers and particle volume fractions, suggests F to be given by (5.8):

$$F = \alpha_f^2 F^* \tag{5.8}$$

with the rather complex expression for F^* listed in (5.9):

$$F^* = \begin{cases} 1 + (3/8)Re_p & \text{if } \alpha_p \leq 0.01 \wedge Re_p \leq \frac{F_2 - 1}{(3/8) - F_3} \\ F_2 + F_3\,Re_p & \text{if } \alpha_p \leq 0.01 \wedge Re_p > \frac{F_2 - 1}{(3/8) - F_3} \\ F_0 + F_1\,Re_p^2 & \text{if } \alpha_p > 0.01 \wedge Re_p \leq \frac{F_3\sqrt{F_3^2 - 4F_1(F_0 - F_2)}}{2F_1} \\ F_2 + F_3\,Re_p & \text{if } \alpha_p > 0.01 \wedge Re_p > \frac{F_3\sqrt{F_3^2 - 4F_1(F_0 - F_2)}}{2F_1} \end{cases} \tag{5.9}$$

where the coefficients F_0 to F_3 are given by:

$$F_0 = \begin{cases} (1 - w)\left(\frac{1 + 3\sqrt{\alpha_p/2} + (135/64)\alpha_p\ln(\alpha_p) + 17.14\alpha_p}{1 + 0.681\alpha_p - 8.48\alpha_p^2 + 8.16\alpha_p^3}\right) + w\left(10\frac{\alpha_p}{(1 - \alpha_p)^3}\right) & \text{if } 0.01 \leq \alpha_p < 0.4 \\ 10\frac{\alpha_p}{(1 - \alpha_p)^3} & \text{if } \alpha_p \geq 0.4 \end{cases} \tag{5.10}$$

$$F_1 = \begin{cases} \sqrt{2/\alpha_p}/40 & \text{if } 0.01 < \alpha_p \leq 0.01 \\ 0.11 + 0.00051\exp(11.6\alpha_p) & \text{if } \alpha_p > 0.01 \end{cases} \tag{5.11}$$
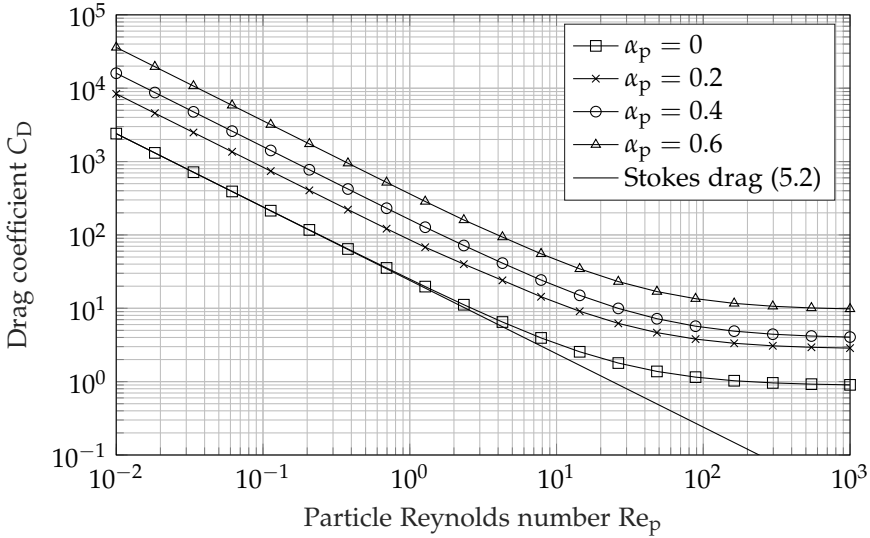
Figure 5.4: Drag coefficient as function of particle Reynolds number for varying particle volume fractions α_p using the modified Koch-Hill-Ladd model proposed by Benyahia et al. (2006). Note that the particle Reynolds number is based on the particle diameter rather than particle radius as commonly done using Koch-Hill-Ladd-based models. The whole range of particle Reynolds numbers are plotted to give an overview of the model and the Stokes drag limit with $C_{D,stk} = 24/Re_p$ is plotted as a reference.

$$F_2 = \begin{cases} (1-w)\left(\dfrac{1+3\sqrt{\alpha_p/2}+(135/64)\alpha_p\ln(\alpha_p)+17.89\alpha_p}{1+0.681\alpha_p-11.03\alpha_p^2+15.41\alpha_p^3}\right) + w\left(10\dfrac{\alpha_p}{(1-\alpha_p)^3}\right) & \text{if } \alpha_p < 0.4 \\ 10\dfrac{\alpha_p}{(1-\alpha_p)^3} & \text{if } \alpha_p \geq 0.4 \end{cases}$$

$$(5.12)$$

$$F_3 = \begin{cases} 0.9351\alpha_p + 0.03667 & \text{if } \alpha_p < 0.0953 \\ 0.0673 + 0.212\alpha_p + 0.0232/(1-\alpha_p)^5 & \text{if } \alpha_p \geq 0.0953 \end{cases}$$

$$(5.13)$$

where the particle Reynolds number is based on the particle radius rather than particle diameter so that $Re_p = d_p|u - v|\alpha_f/(2\nu)$. Figure 5.4 gives an overview of how the dimensionless drag force F varies with Reynolds number and particle volume fraction according to the relation in (5.8). As the figure shows, the drag coefficient is noticeably higher when the particle concentration approaches the closed-pack solution. In the limit of low particle volume fraction, the modified Koch-Hill-Lad model approaches the Stokes solution valid for particle Reynolds numbers $Re_p < 1$. Even though the correlation presented above covers a wide range of particle Reynolds numbers and particle volume fractions, it does not account for a highly anisotropic particle concentrations such as sharp gradients at the edge of agglomerates as shown in figure 5.5.
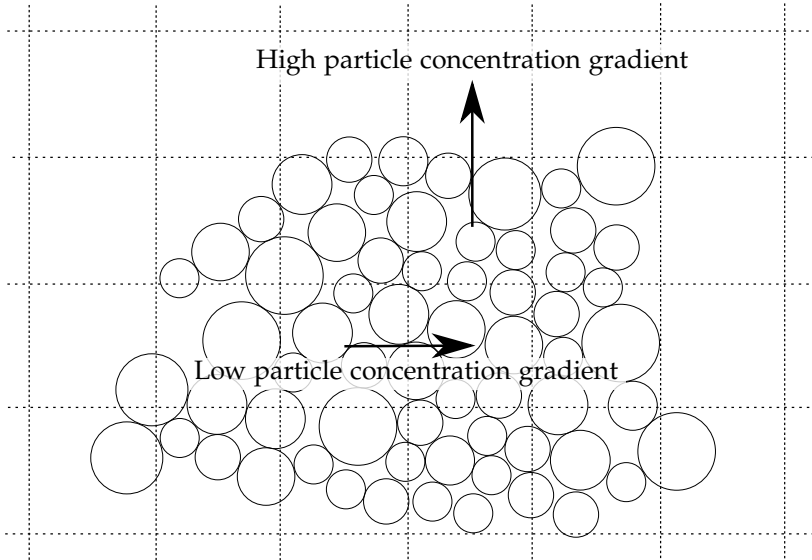
Figure 5.5: Different regions in an agglomerate where the Koch-Hill-Ladd model is expected to give more or less accurate results. In regions where low particle concentration gradients exist, such as in the centre of a compact agglomerate, the model is expected to more accurately predict drag on the individual particles.

To better predict drag, lift and torque on agglomerates such as the one in figure 5.5, the more recent study by Sommerfeld and Stübing (2017) suggests storing the location of all individual particles for each agglomerate. More details on this approach is given in the following.

Correlating drag with various agglomerate properties

Recent efforts to describe the overall fluid force on agglomerated particles include Dietzel and Sommerfeld (2013) who used the Lattice-Boltzmann Method to fully resolve the flow around randomly generated agglomerates that included both compact or dendritic shaped agglomerates. By storing a list containing the locations of all particles relative to one another, the study correlated fluid drag with different agglomerate properties such as volume equivalent sphere, fractal dimension f given by $n_\mathrm{p} = (D_\mathrm{p}/d_\mathrm{p})^f$ and agglomerate porosity of the convex hull, where n_p and D_p denote the number of primary particles and the diameter of bounding sphere respectively. However, when correlating drag with the projected cross section of the convex hull A_agg of the agglomerate perpendicular to the flow direction, see figure 5.6, the study suggests the drag coefficient to be almost independent of agglomerate morphology and orientation. This is indeed a remarkable finding as all the parameters related to the morphology of the agglomerate can be de-
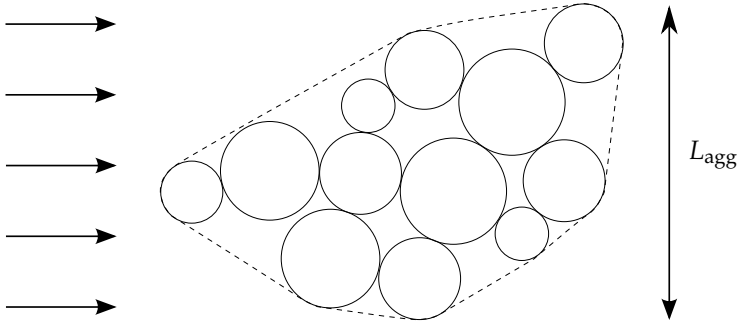
Figure 5.6: Example of the convex hull of an agglomerate, which can be used to correlate drag with the agglomerate structure using the projected agglomerate size perpendicular to the flow direction. Note, the length L_{agg} is naturally an area A_{agg} when considering a three-dimensional agglomerate.

scribed through the projected cross sectional area of the convex hull of the agglomerate. However, when resolving collisions using CFD-DEM simulations, the morphology of the agglomerates changes continuously due to fluid forces and impacting particles. As agglomerate structure changes continuously, the list storing particle locations relative to all other particles has to be updated continuously. Depending on the number of particles and the rate at which agglomerates change morphology, this process is expected to be computational expensive. Furthermore, when using the CFD-DEM to simulate the processes where agglomerates are formed, deform and eventually break up due to fluid forces, information on fluid forces on individual particles is needed. In this case, work remains to be done to relate fluid drag on the whole agglomerate to the fluid force on individual particles or fluid forces on different regions within the agglomerate. Furthermore, quantities such as lift and torque still has to be related to the agglomerate structure. Even though the method presented above is highly effective for calculating properties such as terminal velocities for different agglomerates, it is less useful when simulating how particle interacts and agglomerates are formed and break up in a continuous process.

5.1.3 Lift force contributions

Particles subject to a shear $G = \mathrm{d}u/\mathrm{d}y$ in the velocity field experience a force perpendicular to the flow direction. This force is caused by the non-uniform velocity field resulting in a non-uniform pressure distribution across the particle causing particles to experience a lift force F_L towards the region with higher velocity, see figure 5.7. Saffman (1965, 1968) derived an expression for the lift force in the case with particle Reynolds number $Re_p = d_p|\boldsymbol{u} - \boldsymbol{v}|/\nu \ll 1$, shear Reynolds number $Re_G = d_p^2 G/\nu \ll 1$ and
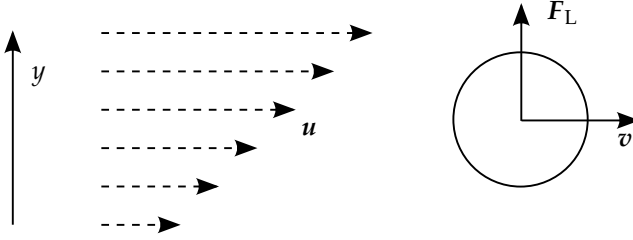
Figure 5.7: Lift force F_L due to shear in the flow field.

particle Reynolds number being much less than the square root of the shear Reynolds number $\mathrm{Re_p} \ll \mathrm{Re_G^{1/2}}$. In this case, Saffman (1965, 1968) suggests the lift force to be given by:

$$F_{L,\text{saffman}} = 1.615 \rho_f \nu^{1/2} d_p^2 |\boldsymbol{u} - \boldsymbol{v}| \left| \frac{\mathrm{d}u}{\mathrm{d}y} \right|^{1/2} \tag{5.14}$$

To overcome some of the limitations listed above, this expression has been modified by several authors. Such modifications include Mei (1992) who, based on the experiments by Dandy and Dwyer (1990), extended the correlation to be valid for $0.1 < \mathrm{Re_p} < 100$:

$$\frac{F_L}{F_{L,\text{saffman}}} = \begin{cases} (1 - 0.3314\alpha^{1/2})\exp\left(-\frac{\mathrm{Re_p}}{10}\right) + 0.3314\alpha^{1/2} & \text{if } \mathrm{Re_p} \leq 40 \\ 0.0524 \left(\alpha \mathrm{Re_p}\right)^{1/2} & \text{if } \mathrm{Re_p} > 40 \end{cases} \tag{5.15}$$

where $\alpha = G(d_p/2)|\boldsymbol{u} - \boldsymbol{v}|^{-1}$. Furthermore, high lift forces can also be induced by particles rotating with a high angular velocity relative to the local fluid. In this case, the particle experiences a lift force caused by an asymmetric pressure distribution around the particle. For particles with small moment of inertia, the particles will reach an equilibrium state where their spin rate is directly related to the shear rate so that the particles does not experience any torque (Loth and Dorgan, 2009). However, when particles collide with other particles or walls, particles may experience high rotational velocities before they finally come to the state of free rotation again. For particles rotating while moving with a small particle Reynolds number, Rubinow and Keller (1961) proposed an analytical solution suggesting the lift force due to rotation to be given by:

$$\boldsymbol{F}_{\text{magnus}} = \pi \rho_f \left(d_p/2\right)^3 \left[\boldsymbol{\Omega} \times (\boldsymbol{u} - \boldsymbol{v})\right] \tag{5.16}$$

where $\boldsymbol{\Omega}$ is the relative rotation between the fluid and the particle.

5.2 Unsteady Fluid Forces

All the above mentioned forces do not take into account particle acceleration or acceleration of the fluid relative to the particle. When particles are accelerated relative to the fluid, particles experience a force acting to slow down the acceleration. This force, commonly denoted added mass force, accounts for the fact that some mass of the fluid surrounding the particles has to be accelerated together with the particle. In the case of small Reynolds numbers, the added mass force F_a is given by:

$$F_a = C_M \frac{\pi \rho_f d_p^3}{6} \left(\frac{d\boldsymbol{u}}{dt} - \frac{d\boldsymbol{v}}{dt} \right) \tag{5.17}$$

For a spherical particle, the added mass force acts in the same direction $\boldsymbol{u} - \boldsymbol{v}$ and has an added mass coefficient $C_M = 0.5$. For non-spherical particles, the added mass effects may induce perpendicular force components and torque contributions. Due to large density ratio between particles and fluid in this study, this effect can typically be neglected, see table (3.1) on page 28. Furthermore, as a particle is accelerated relative to the fluid, the delay in boundary layer build-up adds an additional force, commonly denoted history force or Basset force, given by (Basset, 1888):

$$F_h = \frac{3}{2} d_p^2 \sqrt{\rho_f \mu \pi} \int_{t_0}^{t} \frac{\frac{D\boldsymbol{u}}{Dt'} - \frac{d\boldsymbol{v}}{dt'}}{\sqrt{t - t'}} dt' \tag{5.18}$$

Different authors, including Odar and Hamilton (1964); Michaelides and Roig (2011), have suggested modifications to include cases with higher particle Stokes numbers where $Re_p > 1$.

Chapter 6

Overview of Contributions Related to Adhesive Particles

The purpose of this chapter is to briefly outline the purpose, the methodology and the main results of paper A and B reprinted in Part II. Even though paper C and D are equally important for the overall project, they are not concerned with adhesive particles, which is the main scope of this dissertation. Paper C and D are reprinted on page 163 and 197 respectively.

6.1 Paper A: On the adhesive JKR contact and rolling models for reduced particle stiffness discrete element simulations

Purpose

The purpose of the paper by Hærvig et al. (2017) reprinted on page 105 is to provide an analytically-derived criterion for how to introduce particles with reduced particle stiffness in soft-sphere Discrete Element Method (DEM) simulations of adhesive particles. By introducing a reduced particle stiffness, the particles deform more when colliding causing the collision duration to increase. As a consequence of the increased collision duration, a higher time step size can be used. The criterion is presented in a general manner so that it can be applied to a wide range of problems involving adhesive particles, where the interaction of particles is dominated by collisions rather than external forces acting to separate adhered particles. Particles depositing on surfaces is equally important for a wide range of problems. Therefore, part of the paper is focused on how to ensure the same rolling behaviour when a reduced particle stiffness is introduced.
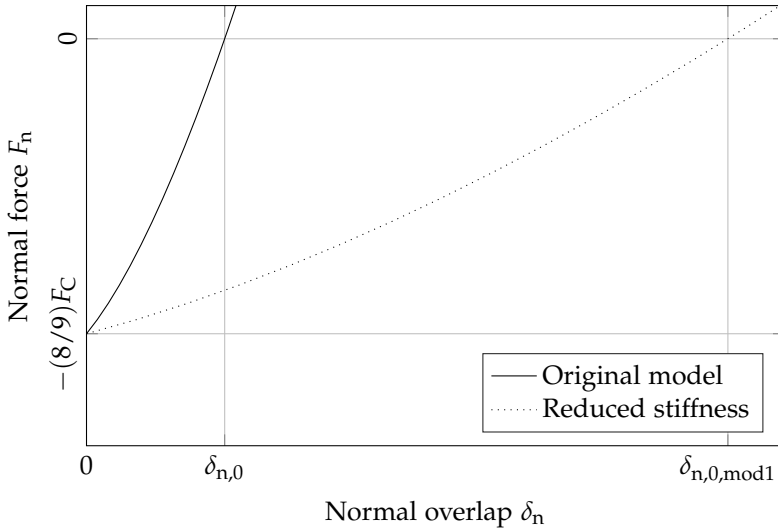
Figure 6.1: Changes in force-displacement relation when introducing a reduced particle stiffness through a reduction in effective Young's modulus from E to E_{mod1} in the JKR model. The equilibrium overlap distances are $\delta_{n,0} = (1/3)a_0^2/R = (3\pi^2\gamma^2 R/E^2)^{1/3}$ and $\delta_{n,0,mod1} = (1/3)a_{0,mod1}^2/R = (3\pi^2\gamma^2 R/E_{mod1}^2)^{1/3}$: —— Original JKR model (Johnson et al., 1971); $\cdots\cdots$ Reduced particle stiffness by a reduction in effective Young's modulus from E to E_{mod1}.

In this study, focus is on particles with $\lambda_T = (4R\gamma^2/(E^2 D_{min}^3))^{1/3} > 3$ so that JKR theory is applicable. This will typically be the case for particles with $d_p = \mathcal{O}(10\ \mu m)$.

Methodology

When a reduced particle stiffness is introduced, the force-displacement relation upon collision is changed significantly. As the particles introduced are softer, the particles overlap more upon collision. The result is the adhesive force acting over a longer distance causing a more adhesive collision. Figure 6.1 gives an overview of how the force-displacement relation is changed the particle stiffness is reduced by a reduction in effective Young's modulus from E to E_{mod}. As shown in Figure A.7 on page 121, a reduced particle stiffness results in a more adhesive collision where the particles either stick or separate with a lower relative velocity. In order to derive a criterion for how the particle adhesiveness should be modified, the following criterion can be set up for the energy required to separate adhered particles to remain the same:

$$\int_0^{\delta_{n,0}} F_n d\delta_n = \int_0^{\delta_{n,0,mod}} F_{n,mod} d\delta_n \tag{6.1}$$

6.1. Paper A: On the adhesive JKR contact and rolling models for reduced particle stiffness discrete element simulations
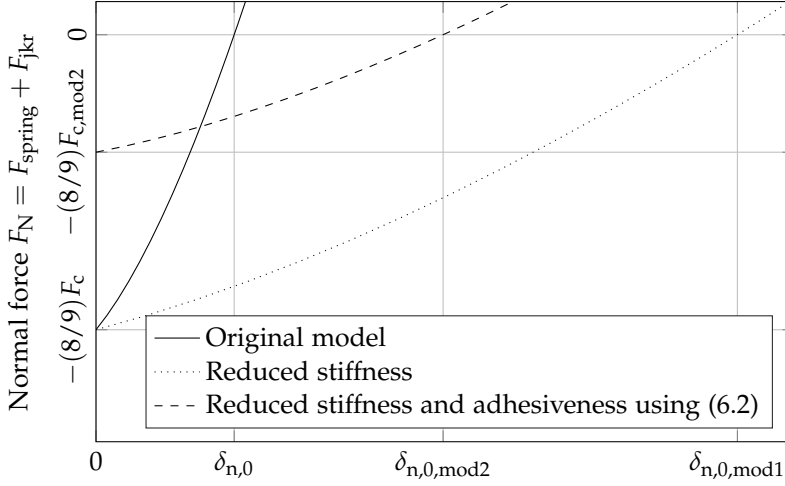
Figure 6.2: Changes in force-displacement relation when modifying the surface energy density from γ to γ_{mod} by (6.2) when reducing the effective Young's modulus from E to E_{mod}. The equilibrium overlap distance when using (6.2) is $\delta_{n,0,mod2} = (1/3)a_{0,mod2}^2/R = (3\pi^2\gamma_{mod2}^2 R/E_{mod2}^2)^{1/3}$ and the normal force at $\delta_n = 0$ is $F_N = -(8/9)F_{C,mod2} = -(8/9)3\pi R\gamma_{mod2}$: —— Original JKR model (Johnson et al., 1971); $\cdots\cdots$ Reduced particle stiffness by a reduction in effective Young's modulus from E to E_{mod}; - - - - Reduced Young's modulus and modified surface energy density given by the criterion in (6.2).

where $\delta_{n,0}$ denote the equilibrium overlap distance. Carrying out the integrals in (6.1) as shown in Appendix A on page 126, we finally obtain the following criterion suggesting how the surface energy density γ should be modified:

$$\gamma_{mod} = \gamma \left(\frac{E_{mod}}{E} \right)^{2/5} \tag{6.2}$$

If the criterion in (6.2) is used when reducing the particle stiffness from E to E_{mod}, the force-displacement shown with a dashed line in figure 6.2 is obtained.

Results

To validate the criterion in (6.2), head-on collisions with varying impact velocities of two particles are performed and compared to experimental data by Dahneke (1975) in terms of effective coefficient of restitution. As figure A.5 on page 119 shows, the collisions with reduced particle stiffness using (6.2) yield the exact same effective coefficient of restitution. Furthermore, simulation data agrees well with the experimental data suggesting DEM simulations to be able to predict the collision outcome.

Next, results are presented in terms of three non-dimensional groups that together dictate the outcome of collisions; namely the elasticity parameter $\lambda = E/(\rho_{\mathrm{p}} v^2)$, the adhesiveness parameter $\mathrm{Ad} = \gamma/(\rho_{\mathrm{p}} v^2 R)$ and the coefficient of restitution measured when adhesive forces are negligible e. By introducing a constant c that depends solely on the coefficient of restitution e, the study outlines the border between collisions where particles rebound and collisions where particles stay attached.

Finally, simulations with varying reduced stiffness are carried out and the collision duration is found to be linked to a reduction in effective Young's modulus as:

$$\Delta t_{\mathrm{col,mod}} = \Delta t_{\mathrm{col}} \left(\frac{E}{E_{\mathrm{mod}}} \right)^{2/5} \tag{6.3}$$

The criterion in (6.3) can be used to estimate the possible speed-up of DEM simulations when introducing particles with reduced stiffness.

6.2   Paper B: Early stages of agglomeration and deposition of adhesive micron-sized particles in fully-developed turbulent pipe flows

Purpose

The purpose of paper B reprinted on page 133 is to provide a better understanding of how changes in parameters governing particle transport and adhesiveness affect the early stages of agglomeration and deposition in turbulent pipe flows. Furthermore, a part of the study is focused on investigating the applicability of the criterion for reduced particle stiffness in (6.2) presented in paper A.

Methodology

The agglomeration process is a result of particles colliding with one another. Therefore, this study uses the soft-sphere Discrete Element Method (DEM), relying directly on the properties of the particles, to resolve collisions over numerous time steps. As particles agglomerate and the particle concentration increases locally, the interaction between the fluid and particles become increasingly important. Therefore, the two phases are fully-coupled through a momentum-exchange term. As collisions generally take place over time step sizes significantly smaller than the larger scales of fluid turbulence, two different time step sized are used. The collisions are resolved using a time step size a factor 500 smaller than the time step size used for the fluid phase.

The larger scales of the turbulent flow are resolved using Large Eddy Simulations (LES). To ensure that the motion of particles is unaffected by the unresolved smaller turbulence scales, the grid resolution is together with the response time of particles, described through the Stokes number.

To save computational time, the particle stiffness is reduced using the criterion proposed in paper A. When applying this criterion, the critical force required to break contact is reduced. In order not to change the mechanism causing agglomerates to break up, it is therefore important that critical force required to break contact F_C stays several orders of magnitude higher than fluid forces acting to break up agglomerates F_{sep}. To estimate the order of the ratio between the critical force required to break contact and the separating fluid force due to shear in the flow, the criterion in (3.16) on page 27 can be used.

The domain considered is periodic in the stream-wise direction. To ensure the results are independent of the length of the periodic domain, the domain is made periodic over a length $L/D = 4$ corresponding to $L_x^+ \approx 2500$ in terms of viscous units.

The particles considered have size $d_p = 10$ µm, density $\rho_p = 2500$ kg/m^3 and are transported in a pipe flow of dry air with $D = 40$ mm and mean velocity $U = 5$ m/s. Using the approximate expressions in table 3.1 on page 28, it is found that fluid drag is the dominating force. Added mass force and Brownian force are several orders of magnitude lower than fluid drag. Both lift due to shear in the flow field and lift due to rotation are much lower than Stokes drag. However, these are included due to the high velocity gradients near the wall and due to collisions with other particles or walls which could result in high angular velocities. Furthermore, both gravity and unsteady forces are neglected in the present study.

Results

First, an analysis is carried out to make sure the motion of most responsive particles is independent of the turbulent eddies not being resolved by the large eddy simulations. The results show the grid resolution required varies with response time of the particles of interest. As expected the more responsive particles require a finer grid resolution as these particles are affected by the smaller turbulent eddies resolved using finer grids. Other results show that the agglomeration rate is almost independent of changes in particle stiffness when applying the criterion for reduced particle stiffness proposed in paper A.

Next, simulations are done for particles with varying response times and adhesiveness. The results clearly shows how particles with intermediate response times, described through the Stokes number, have higher agglomeration rates. This is explained through changes in collision mechanisms when the particle response time is either decreased or increased. Changes in Stokes number are furthermore linked to the radial particle distribution in the pipe. More responsive particles are found to be more uniformly distributed in the pipe while less response particles tend to move toward the centre of the pipe. In all cases, particles are observed to stick to the surface.

By varying the particle adhesiveness resulting in particles that range from almost non-adhesive to highly adhesive, the effects on the agglomeration rate are documented. Changes in adhesiveness for almost non-adhesive particles are found to have a limited effect on the agglomeration rate. For particles with higher adhesiveness, changes in adhesiveness are found to have a more pronounced effect on the agglomeration rate. Furthermore, the adhesiveness is observed to have almost no effect on the radial particle distribution in the pipe.

Chapter 7

Closure

This chapter sums up the main results of this dissertation. Furthermore, suggestions for how to continue the work in various directions are given.

7.1 Final Remarks

Particles sticking to other particles or to surfaces is a problem in a wide range of applications. In this dissertation, focus has been to get a better fundamental understanding of how properties governing particle transport and adhesiveness affect particle agglomeration. The micron-sized particles investigated in this dissertation were subject to van der Waals attraction in a dry environment. For this purpose, the adhesiveness of the particles have been accounted for through JKR theory. In order to predict interactions between thousands of particles, various sub-models related to adhesiveness have been implemented in the open-source discrete element method software LIGGGHTS. Such effects include an additional force upon contact acting to maintain contact and a rolling resistance torque acting to oppose rolling motion of particles.

   Even though discrete element method simulations scale well with number of processors, computational power still remains a limiting factor when applying the discrete element method to investigate more complex problems. Therefore, an analytically-based approach was first used to derive a criterion for how to introduce softer particles while maintaining the adhesive behaviour. To validate this criterion, simple, well-controlled DEM simulations of head-on collisions between two particles have been carried out and compared to experimental data available in literature. As particle rolling plays a central role when particles stick to one another or to surfaces, the criterion was extended to include rolling behaviour of particles. Based on a set of non-dimensional groups governing adhesiveness of particles, a non-dimensional

collision map was proposed to predict if particles would rebound, stick or roll upon collision with a surface.

Next, the applicability of large eddy simulations to predict transport and agglomeration of particles in fully-developed turbulent pipe flows was investigated. For this purpose, the discrete element method was two-way coupled to large eddy simulations of turbulent pipe flows using the open-source software OpenFOAM. First, without particles added to the flow, various measures were taken to ensure the characteristics of the turbulent flow was well-represented by the large eddy simulations. With particles added to the turbulent flow, a set of simulations were carried out with varying Stokes numbers using different grid resolutions to investigate how the smaller eddies resolved using finer grids affect particle agglomeration. When more responsive particles were used, differences in agglomeration rates were observed when using different grid resolutions. Furthermore, the applicability of the analytically-based criterion was analysed by simulating particles that varied by a factor 10 in Young's modulus and only minor differences in agglomeration rates were observed.

Next, the effects of particle response time and adhesiveness on the agglomeration rate were investigated. The agglomeration rate was found to be highest for intermediate Stokes numbers, which can be explained by an increase in collision rate. At this Stokes number, particles were observed to form larger agglomerates in the centre of the pipe. At lower Stokes numbers, the particles were more uniformly distributed throughout the pipe with smaller agglomerates being formed. The size of the agglomerates was observed to be directly related to the particle adhesiveness with larger agglomerates being formed for more adhesive particles.

To sum it up, this dissertation has contributed to the DEM modelling framework of adhesive particles following JKR theory. The criterion proposed, $\gamma_{\mathrm{mod}}/\gamma = (E_{\mathrm{mod}}/E)^{2/5}$ can be used to speed up numerical simulations of a wide range of problems to ultimately allow more complex problems to be solved in future studies. Furthermore, the coupled DEM-LES simulations provide details on how small micron-sized particles agglomerate under various conditions in well-defined turbulent pipe flows.

7.2 Suggestions for Future Work

In this dissertation focus has been on point-particle approach where the fluid force on every particle is described through a set of correlations. Even though these correlations are well-validated for dilute flow conditions, work still remains to be done when particles agglomerate and the particle concentration increases locally. Even though correlations have been proposed in literature to account for increased particle concentrations, work still remains to be done

when high particle concentration gradients exist. Examples include the surface of the agglomerate of a compact agglomerate where the local particle concentration varies from $\alpha_p = 0$ outside the agglomerate to $\alpha_p \approx 0.6$ inside the agglomerate. For this purpose, fully-resolved simulations of different agglomerate morphologies could provide new information that could relate the fluid force on particles to the relative positions of nearby particles.

For the criterion for reduced stiffness presented in paper A, $\gamma_{mod}/\gamma = (E_{mod}/E)^{2/5}$, to be applicable, it is assumed that the agglomeration process is controlled by collisions with other particles rather than external forces acting to break up agglomeration. Using the criterion above, the surface energy density is reduced when introducing particles with reduced stiffness. As the critical force required to break contact is proportional to the surface energy density ($F_C \propto \gamma$) according to JKR theory, it is important that F_C stays some orders of magnitude higher than external forces, e.g. fluid forces, that act to break up up agglomerates. While studies in literature have suggested agglomeration processes to be controlled by collisions rather than fluid forces, more studies with different particles and fluid flows have to be investigated. In the present dissertation, an expression for the ratio between the critical force required to separate two adhered particles F_C and the fluid force acting to separate the particles due to shear in the flow field F_{sep} is proposed: $F_C/F_{sep} = \gamma/(8r_p\mu G)$. Future work could be focused on documenting the relation between this ratio and the validity of the criterion proposed in paper A by simulating simple shear flows.

Due to computational requirements, the present study was limited to a small periodic domain. While a fully-developed turbulent flow is well-represented by such a periodic domain of sufficient length, e.g. $L_x^+ = 2500$ in terms of viscous units for Re $= 10,000$, the agglomeration process takes place over much longer distances. In this study, this was handled by a periodic domain for the particles as well. The main limitation of this approach is the fact that the number of particles and therefore overall particle concentration in the domain remains constant. To model the whole agglomeration including later stages where a layer of particles build up, particles would have to be added continuously throughout the simulation. Or better yet, a domain sufficiently long for the number of particles deposited per length pipe to stay constant so that $d\phi/dx = 0$.

All the sub-models used to describe the behaviour of particles in this dissertation have been experimentally validated in literature. However, test cases documenting the interactions between thousands of particles experimentally, remain few in literature. Even though DEM simulations by Parteli et al. (2014) have documented how adhesiveness affects the packing density of glass spheres, no studies have experimentally documented how various properties affect particle agglomeration and deposition in turbulent flows. Future work should be focused on doing measurements on simple, well-

defined test cases, such as turbulent flow through a pipe, to document some of the numerical findings being reported in literature more recently.

References

Arthur W. Adamson. *Physical Chemistry of Surfaces*. John Wiley & Sons, 6. edition, 1997. ISBN: 0-471-14873-3.

D.T. Alexander. Brown carbon spheres in east asian outflow and their optical properties. *Science*, 321:833–836, 2008. URL `http://dx.doi.org/10.1126/science.1155296`.

A.B. Basset. *A treatise on hydrodynamics, with numerous examples*. Cambridge: Deighton, Bell and Co., 1888.

Sofiane Benyahia, Madhava Syamlal, and Thomas J. O'Brien. Extension of hill-koch-ladd drag correlation over all ranges of reynolds number and solids volume fraction. *Powder Technology*, 162:166–174, 2006. URL `http://dx.doi.org/10.1016/j.powtec.2005.12.014`.

T.C. Bond, S.J. Doherty, D.W. Fahey, P.M. Forster, T. Berntsen, B.J. DeAngelo, M.G. Flanner, S. Ghan, B. Kärcher, D. Koch, S. Kinne, Y. Kondo, P.K. Quinn, M.C. Sarofim, M.G. Schultz, M. Schulz, C. Venkataraman, H. Zhang, S. Zhang, N. Bellouin, S.K. Guttikunda, P.K. Hopke, M.Z. Jacobson, J.W. Kaiser, Z. Klimont, U. Lohmann, J.P. Schwarz, D. Shindell, T. Storelvmo, S.G. Warren, and C.S. Zender. Bounding the role of black carbon in the climate system: A scientific assessment. *J. Geophys. Res. Atmos.*, 118:5380–5552, 2013. URL `http://dx.doi.org/10.1002/jgrd.50171`.

Sheng Chen, Shuiqing Li, and Mengmeng Yang. Sticking/rebound criterion for collisions of small adhesive particles: Effects of impact parameter and particle size. *Powder Technology*, 274:431–440, 2015. URL `http://dx.doi.org/10.1016/j.powtec.2015.01.051`.

Arati Chokshi, A. G. G. M. Tielens, and D. Hollenbach. Dust coagulation. *The Astrophysical Journal*, 407:806–819, 1993. URL `http://dx.doi.org/10.1086/172562`.

Clayton T. Crowe, John D. Schwarzkopf, Martin Sommerfeld, and Yutaka Tsuji. *Multiphase Flows with Droplets and Particles*. CRC Press, 2. edition, 2011. ISBN: 9781439840504.

References

C.T. Crowe, M.P. Sharme, and D.E. Stock. The particle-source-in-cell method for gas droplet flow. *Journal of Fluids Engineering*, 99:325–332, 1977. URL `http://dx.doi.org/10.1115/1.3448756`.

P.A. Cundall and O.D.L. Strack. A discrete numerical model for granular assemblies. *Géotechnique*, 29:47–65, 1979. URL `http://dx.doi.org/10.1680/geot.1979.29.1.47`.

E. Cunningham. On the velocity of steady fall of spherical particles through fluid medium. *Proceedings of the Royal Society A*, 83:357–365, 1910. URL `http://dx.doi.org/10.1098/rspa.1910.0024`.

Barton Dahneke. Further measurements of the bouncing of small latex spheres. *Journal of Colloid and Interface Science*, 51:58–65, 1975. URL `http://doi.org/10.1016/0021-9797(75)90083-1`.

David S. Dandy and Harry A. Dwyer. A sphere in shear flow at finite reynolds number: effect of shear on particle lift, drag, and heat transfer. *Journal of Fluid Mechanics*, 216:381–410, 1990. URL `http://dx.doi.org/10.1017/S0022112090000477`.

C. N. Davies. Definitive equations for the fluid resistance of spheres. *The Proceedings of the Physical Society*, 57:259–270, 1945. URL `http://stacks.iop.org/0959-5309/57/i=4/a=301`.

Xiaoliang Deng, James V. Scicolone, and Rajesh N. Davé. Discrete element method simulation of cohesive particles mixing under magnetically assisted impaction. *Powder Technology*, 243:96–109, 2013. URL `http://dx.doi.org/10.1016/j.powtec.2013.03.043`.

B. Derjaguin. Untersuchungen über die reibung und adhäsion, iv. *Kolloid-Zeitschrift*, 69:155–164, 1934. URL `http://dx.doi.org/10.1007/BF01433225`.

Mathias Dietzel and Martin Sommerfeld. Numerical calculation of flow resistance for agglomerates with different morphology by the lattice-boltzmann method. *Powder Technology*, 250:122–137, 2013. URL `http://dx.doi.org/10.1016/j.powtec.2013.09.023`.

C. Dominik and A.G.G.M Tielens. Resistance to rolling in the adhesive contact of two elastic spheres. *Philosophical Magazine A*, 72:783–803, 1995. URL `http://dx.doi.org/10.1080/01418619508243800`.

C. Dominik and A.G.G.M Tielens. The physics of dust coagulation and the structure of dust aggregates in space. *The Astrophysical Journal*, 480:647–673, 1997. URL `http://dx.doi.org/10.1086/303996`.

References

M.L. Eggersdorfer and S.E. Pratsinis. The structure of agglomerates consisting of polydisperse particles. *Aerosol Science and Technology*, 46:347–353, 2012. URL http://dx.doi.org/10.1080/02786826.2011.631956.

A. Einstein. Über die von der molekularkinetischen theorie der wärme geforderte bewegung von in ruhenden flüssigkeiten suspendierten teilchen. *Annalen der Physik*, 322:549–560, 1905. URL http://dx.doi.org/10.1002/andp.19053220806.

Sabri Ergun and A. A. Orning. Fluid flow through randomly packed columns and fluidized beds. *Industrial & Engineering Chemistry*, 41:1179–1184, 1949. URL http://dx.doi.org/10.1021/ie50474a011.

R. Di Felice. The voidage function for fluid-particle interaction systems. *International Journal of Multiphase Flow*, 20:153–159, 1994. URL http://dx.doi.org/10.1016/0301-9322(94)90011-6.

James Q. Feng and Dan A. Hays. Relative importance of electrostatic forces on powder particles. *Powder Technology*, 135–136:65–75, 2003. URL http://doi.org/10.1016/j.powtec.2003.08.005.

Martin Götzinger. Dispersive forces of particle–surface interactions: direct afm measurements and modelling. *Powder Technology*, 130:102–109, 2003. URL http://doi.org/10.1016/S0032-5910(02)00234-6.

T.J. Grahame and R.B. Schlesinger. Cardiovascular health and particulate vehicular emissions: a critical evaluation of the evidence. *Air Qual Atmos Health*, 3:3–27, 2010. URL http://dx.doi.org/10.1007/s11869-009-0047-x.

J. Hærvig, U. Kleinhans, C. Wieland, H. Spliethoff, A. L. Jensen, K. Sørensen, and T. J. Condra. On the adhesive jkr contact and rolling models for reduced particle stiffness discrete element simulations. *Powder Technology*, 319:472–482, 2017. URL http://dx.doi.org/10.1016/j.powtec.2017.07.006.

H.C. Hamaker. The london — van der waals attraction between spherical particles. *Physica*, 4:1058–1072, 1937. URL http://dx.doi.org/10.1016/S0031-8914(37)80203-7.

John Happel. Viscous flow in multiparticle systems: Slow motion of fluids relative to beds of spherical particles. *AIChE Journal*, 4:197–201, 1958. URL http://dx.doi.org/10.1002/aic.690040214.

Christophe Henry, Jean-Pierre Minier, and Grégory Lefévre. Towards a description of particulate fouling: From single particle deposition to clogging. *Advances in Colloid and Interface Science*, 185–186:34–76, 2012. URL http://dx.doi.org/10.1016/j.cis.2012.10.001.

References

Heinrich Hertz. Über die berührung fester elastischer körper. *Journal für die reine und angewandte Mathematik (Crelles Journal)*, 92:156–171, 1882. URL http://dx.doi.org/10.1515/crll.1882.92.156.

Reghan J. Hill, Donald L. Koch, and Anthony J. C. Ladd. The first effects of fluid inertia on flows in ordered and random arrays of spheres. *J. Fluid Mech.*, 448:213–241, 2001a. URL http://dx.doi.org/10.1017/S0022112001005936.

Reghan J. Hill, Donald L. Koch, and Anthony J. C. Ladd. Moderate-reynolds-number flows in ordered and random arrays of spheres. *J. Fluid Mech.*, 448:243–278, 2001b. URL http://dx.doi.org/10.1017/S0022112001005948.

J.N. Israelachvili. *Intermolecular and Surface Forces*. Academic Press, 2. edition, 1992. ISBN: 978-0-12-375182-9.

K.L. Johnson and J.A. Greenwood. An adhesion map for the contact of elastic spheres. *Journal of Colloid and Interface Science*, 192:326–333, 1997. URL http://doi.org/10.1006/jcis.1997.4984.

K.L. Johnson, K. Kendall, and A.D. Roberts. Surface energy and the contact of elastic solids. *Proc. R. Soc. Lond.*, 324:301–313, 1971. URL http://dx.doi.org/10.1098/rspa.1971.0141.

S. Krijt, C. Dominik, A.G.G.MC. Dominik, and A.G.G.M Tielens. Rolling friction of adhesive microspheres. *Journal of Physics D: Applied Physics*, 47:175302 (9pp), 2014. URL http://dx.doi.org/10.1088/0022-3727/47/17/175302.

H. Krupp. *Particle Adhesion: Theory and Experiment*. Advances in Colloid Interface Science, 1. edition, 1967.

Dominique Legendre, Claude Daniel, and Pascal Guiraud. Experimental study of a drop bouncing on a wall in a liquid. *Physics of Fluids*, 17:097105, 2005. URL http://dx.doi.org/10.1063/1.2010527.

E. Loth and A.J. Dorgan. An equation of motion for particles of finite reynolds number and size. *Environmental Fluid Mechanics*, 9:187–206, 2009. URL http://dx.doi.org/10.1007/s10652-009-9123-x.

R. A. Mallikan. The general law of fall of a small spherical body through a gas, and its brearing upon the nature of molecular reflection from surfaces. *Physical Review*, 22:1–23, 1923. URL http://dx.doi.org/10.1103/PhysRev.22.1.

Jeffrey S. Marshall and Shuiqing Li. *Adhesive Particle Flow*. Cambridge University Press, 1. edition, 2014. URL http://dx.doi.org/10.1017/CBO9781139424547. ISBN: 978-1-107-03207-1.

References

J.S. Marshall. Particle aggregation and capture by walls in a particulate aerosol channel flow. *Aerosol Science*, 38:333–351, 2007. URL `http://dx.doi.org/j.jaerosci.2007.01.004`.

John S. Mathis, William Rumpl, and Kenneth H. Nordsieck. The size distribution of interstellar grains. *The Astrophysical Journal*, 217:425–433, 1977. URL `http://dx.doi.org/10.1086/155591`.

Daniel Maugis. Adhesion of spheres: The jkr-dmt transition using a dugdale model. *Journal of Colloid and Interface Science*, 150:243–269, 1992. URL `http://doi.org/10.1016/0021-9797(92)90285-T`.

R. Mei. An approximate expression for the shear lift force on a spherical particle at finite reynolds number. *International Journal of Multiphase Flow*, 18:145–147, 1992. URL `http://dx.doi.org/10.1016/0301-9322(92)90012-6`.

C. J. Meyer and D. A. Deglon. Particle collision modeling - a review. *Minerals Engineering*, 24:719–730, 2011. URL `http://dx.doi.org/10.1016/j.mineng.2011.03.015`.

Efstathios E. Michaelides and Adam Roig. A reinterpretation of the odar and hamilton data on the unsteady equation of motion of particles. *AIChE Journal*, 57:2997–3002, 2011. URL `http://dx.doi.org/10.1002/aic.12498`.

Fuat Odar and Wallis S. Hamilton. Forces on a sphere accelerating in a viscous fluid. *Journal of Fluid Mechanics*, 18:302–314, 1964. URL `http://dx.doi.org/10.1017/S0022112064000210`.

Eric J. R. Parteli, Jochen Schmidt, Christina Brümel, Karl-Ernst Wirth, Wolfgang Peukert, and Thorsten Pöschel. Attractive particle interaction forces and packing density of fine glass powders. *Nature Scientific Reports*, 4:1–7, 2014. URL `http://dx.doi.org/10.1038/srep06227`.

M. Pasha, C. Hare, A. Hassanpour, and M. Ghadiri. Analysis of ball indentation on cohesive powder beds using distinct element modelling. *Powder Technology*, 233:80–90, 2013. URL `http://dx.doi.org/10.1016/j.powtec.2012.08.017`.

S. I. Rubinow and Joseph B. Keller. The transverse force on a spinning sphere moving in a viscous fluid. *Journal of Fluid Mechanics*, 11:447–459, 1961. URL `http://doi.org/10.1017/S0022112061000640`.

P.G. Saffman. The lift on a small sphere in a slow shear flow. *Journal of Fluid Mechanics*, 22:261–274, 1965. URL `http://dx.doi.org/10.1017/S0022112065000824`.

References

P.G. Saffman. Corrigendum to the lift on a small sphere in a slow shear flow. *Journal of Fluid Mechanics*, 31:624–625, 1968. URL `http://dx.doi.org/10.1017/S0022112068999990`.

L. Schiller and A. Neumann. *Ver. Deutsch. Ing.*, 77:318, 1935.

Drew Shindell, Johan C. I. Kuylenstierna, Elisabetta Vignati, Rita van Dingenen, Markus Amann, Zbigniew Klimont, Susan C. Anenberg, Nicholas Muller, Greet Janssens-Maenhout, Frank Raes, Joel Schwartz, Greg Faluvegi, Luca Pozzoli, Kaarle Kupiainen, Lena Höglund-Isaksson, Lisa Emberson, David Streets, V. Ramanathan, Kevin Hicks, N. T. Kim Oanh, George Milly, Martin Williams, Volodymyr Demkine, and David Fowler. Simultaneously mitigating near-term climate change and improving human health and food security. *Science 13*, 335:183–189, 2012. URL `http://dx.doi.org/10.1126/science.1210026`.

M. Sommerfeld and S. Stübing. A novel lagrangian agglomerate structure model. *Powder Technology*, 319:34–52, 2017. URL `http://dx.doi.org/10.1016/j.powtec.2017.06.016`.

Martin Sommerfeld. Validation of a stochastic lagrangian modelling approach for inter-particle collisions in homogeneous isotropic turbulence. *International Journal of Multiphase Flow*, 27:1829–1858, 2001. URL `http://doi.org/10.1016/S0301-9322(01)00035-0`.

George Gabriel Stokes. On the effect of the internal friction of fluids on the motion of pendulums. *Transactions of the Cambridge Philosophical Society*, IX: 8, 1850. URL `http://adsabs.harvard.edu/abs/1851TCaPS...9....8S`.

D. Tabor. Surface forces and surface interactions. *Journal of Colloid and Interface Science*, 58:2–13, 1977. URL `http://dx.doi.org/10.1016/0021-9797(77)90366-6`.

Dale R. Tree and Kenth I. Svensson. Soot processes in compression ignition engines. *Progress in Energy and Combustion Science*, 33:272–309, 2007. URL `http://doi.org/10.1016/j.pecs.2006.03.002`.

Stuart J. Weidenschilling. Formation of planetesimals and accretion of terrestrial planets. *Space Science Reviews*, 92:295–310, 2000. URL `http://dx.doi.org/10.1023/A:1005259615299`.

Eric W. Weisstein. *CRC concise encyclopedia of mathematics*. Chapman & Hall / ORC, 2. edition, 2003. ISBN: 9780849396403.

C.Y. Wen and Y.H. Yu. Mechanics of fluidization. *Chem. Eng. Prog. Symp. Ser.*, 62:100–111, 1966.

References

Q. Zhou and S.C. Yao. Group modeling of impacting spray dynamics. *International Journal of Heat and Mass Transfer*, 35:121–129, 1992. URL http://doi.org/10.1016/0017-9310(92)90013-I.

References

Terminology

Abbreviations	Description
CFD	Computational Fluid Dynamics
DEM	Discrete Element Method
DMT	Derjaguin-Muller-Toporov (model)
DPM	Discrete Phase Method
GA	Genetic Algorithm
IBM	Immersed Boundary Method
JKR	Johnson-Kendall-Roberts (model)
LAMMPS	Large-scale Atomic/Molecular Massively Parallel Simulator
LBM	Lattice-Boltzmann Method
LES	Large Eddy Simulation
LIGGGHTS	LAMMPS Improved for General Granular and Granular Heat Transfer Simulations
OpenFOAM	Open source Field Operation And Manipulation
ORC	Organice Rankine Cycle

Subscripts	Description
a	Added mass
ad	Adhesivenss
b	Brownian
con	Contact
C	Critical
d	Drag
ext	External
f	Fluid
f	Final velocity

Terminology

g	Buoyancy-corrected gravity
h	History or Basset
hz	Hertzian
iner	Inertia
l	Lift
m	Magnus
mod	Modified values
n	Normal direction
p	Plate
r	Rolling resistance
r	Rolling
sep	Separation
sjkr	Simplified Johnson-Kendall-Roberts (model)
stk	Stokes
t	Tangential direction
vd	Viscous dissipation
vdW	Van der Waals
x	x-direction
y	y-direction
z	z-direction
i, j	Indices

Non-dimensional groups	Description	Definition
Ad	Adhesiveness parameter	$\gamma/(\rho_\mathrm{p} U^2 d_\mathrm{p})$
e	Coefficient of restitution	$(v_\mathrm{i,f} - v_\mathrm{j,f})/(v_\mathrm{j} - v_\mathrm{i})$
e_eff	Effective coefficient of restitution	$(v_\mathrm{i,f} - v_\mathrm{j,f})/(v_\mathrm{j} - v_\mathrm{i})$
Fr	Froude number	$U/\sqrt{g_\mathrm{r} d_\mathrm{p}}$
Kn	Knudsen number	λ/d_p
Pe	Peclet number	$D\,U/D_\mathrm{b}$
Re	Flow Reynolds number	$U\,D/\nu$
Re$_\mathrm{p}$	Particle Reynolds number	$|\boldsymbol{v} - \boldsymbol{u}|d_\mathrm{p}/\nu$
Re$_\mathrm{G}$	Shear Reynolds number	$G d_\mathrm{p}^2/\nu$
Re$_\Omega$	Rotational Reynolds number	$\Omega d_\mathrm{p}^2/\nu$
St	Global Stokes number	$\rho_\mathrm{p} d_\mathrm{p}^2 U/(18\mu D)$
St	Local Stokes number	$\rho_\mathrm{p} d_\mathrm{p}^2 u/(18\mu l_\mathrm{c})$
St*	Collision Stokes number	$(m_\mathrm{p} + C_\mathrm{M} m_\mathrm{f})v/(6\pi\mu r_\mathrm{p}^2)$
ϵ	Particle to pipe size ratio	d_p/D

λ	Elasticity parameter	$E/(\rho_p U^2)$
λ_T	Tabor parameter	$(4R\gamma^2/(E^2 D_{min}^3))^{1/3}$
ϕ	Particle concentration	$n_p V_p/(V_f + n_p V_p)$
χ	Density ratio	ρ_p/ρ_f

Greek symbol	Description	Dimensions	Units
α	Local concentration	—	—
β	Particle diameter ratio	—	—
β	Energy dissipation parameter	—	—
β	Parameter used for Di Felice drag formulation	—	—
δ_C	Critical normal overlap	L	m
δ_n	Normal overlap	L	m
Δs_t	Tangential displacement	L	m
Δt_{col}	Collision duration	T	s
$\Delta\gamma/\gamma$	Adhesion hysteresis parameter	—	—
γ	Surface energy density	MT^{-2}	J/m^2
γ_n	Normal damping coefficient	MT^{-1}	kg/s
γ_t	Tangential damping coefficient	MT^{-1}	kg/s
θ	Angular orientation	—	rad
λ	Mean free path of molecules	—	m
μ	Dynamic viscosity	$ML^{-1}T^{-1}$	kg/(m s)
ν	Kinematic viscosity	$L^2 T^{-1}$	m^2/s
ν	Poisson's ratio	—	—
ξ	Rolling displacement	L	m
ρ	Density	ML^{-3}	kg/m^3
τ	Response time	T	s
ψ	Collision angle	—	rad
Ω	Rotational velocity	T^{-1}	rad/s

Symbol	Description	Dimensions	Units
a	Contact radius	L	m
a_0	Equilibrium contact radius	L	m
A_{agg}	projected cross section of convex hull	L^2	m^2
A_H	Hamaker constant	$ML^2 T^{-2}$	J

A_p	Particle cross-sectional area	L^2	m^2
c_{sjkr}	SJKR constant	$ML^{-1}T^{-2}$	J/m^3
C_D	Drag coefficient	$-$	$-$
d	Separation distance	L	m
d_p	Particle diameter	L	m
D	Pipe diameter	L	m
D_b	Brownian diffusion coefficient	L^2T^{-1}	m^2/s
D_{max}	Cut-off distance	L	m
D_{min}	Minimum separation distance	L	m
D_p	Diameter of bounding sphere	L	m
E	Effective Young's modulus	$ML^{-1}T^{-2}$	Pa
E_i, E_j	Young's modulus for particle i,j	$ML^{-1}T^{-2}$	Pa
$\boldsymbol{F}$	Force	MLT^{-2}	N
F	Dimensionless drag force	$-$	$-$
F^*	Parameter used in Koch-Hill-Ladd drag formulation	$-$	$-$
F_1	Parameter used in Koch-Hill-Ladd drag formulation	$-$	$-$
F_2	Parameter used in Koch-Hill-Ladd drag formulation	$-$	$-$
F_3	Parameter used in Koch-Hill-Ladd drag formulation	$-$	$-$
f	Fractal dimension	$-$	$-$
g_r	Buoyancy corrected gravity	LT^{-2}	m/s^2
G	Shear rate	T^{-1}	1/s
G	Shear modulus	$ML^{-1}T^{-2}$	Pa
I	Moment of inertia	ML^2	$kg\ m^2$
k	Spring constant	MT^{-2}	kg/s^2
k_B	Boltzmann constant	$ML^2T^{-2}\Theta^{-1}$	J/K
k_r	Rolling resistance coefficient	MLT^{-2}	N
l_c	Characteristic length	L	m
L_{agg}	Length of the projected convex hull	L	m
m	Effective mass	M	kg
$\boldsymbol{M}$	Torque	ML^2T^{-2}	N m
$\boldsymbol{n}$	Unit vector	$-$	$-$
n_p	Number of particles	$-$	$-$
p	Pressure	$ML^{-1}T^{-2}$	Pa
R	Effective particle radius	L	m
r_i, r_j	particle radii for particle i,j	L	m
t	Time	T	s
$\boldsymbol{t}_r$	Direction of rolling	$-$	$-$

Terminology

T	Temperature	Θ	K
$\boldsymbol{u}$	Local fluid velocity	LT^{-1}	m/s
U	Mean flow velocity	LT^{-1}	m/s
$\boldsymbol{v}$	Particle velocity	LT^{-1}	m/s
V	Volume	L^3	m^3
$\boldsymbol{x}$	Particle position	L	m
x, y, z	Cartesian coordinates	L	m

Terminology

Appendix A

Agglomerate Tracking Algorithm

To quantify the agglomeration taking place, the total number of agglomerates and the number of particles per agglomerate are tracked over time. Approaches range from simply brute force checking contact between all particles to more sophisticated purpose-developed algorithm.

A.1 Brute force

The most simple method is to check for contact between particles in the domain. The following steps summarise such an approach:

1. Check contact between all particles n. Then bonds are formed between particles are in contact. Computational time scales with $n(n+1)/2$.

2. Check for particles contained in multiple agglomerates and merge those agglomerates. Repeat process until list of agglomerates do not change any longer. This is an iterative approach as new bonds discovered suddenly can link already detected agglomerates. Computational time is highly depended on number of agglomerates.

Even the first step takes approximately $5 \cdot 10^{11}$ calculations with 10^6 particles. The other step depend on the number and structure of agglomerates. Even though this method is well-suited for parallel computations, the high number possible contact pairs, makes the method inefficient and computational expensive.

A.2 Limited search distance algorithm

Instead of checking for contact between all particle pairs, a search distance is introduced. For particle i with $r_{p,i}$, the search distance is $r_{p,i} + r_{p,max}$ as shown in figure A.1. In this work, an algorithm consisting of the following
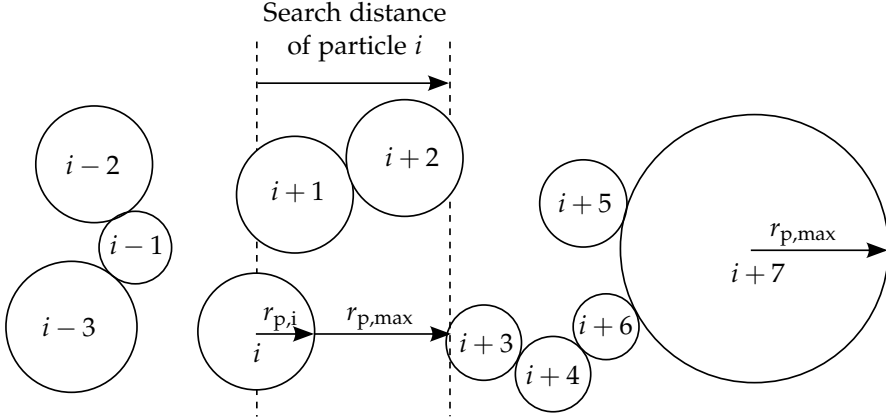
Figure A.1: Sketch showing search distance of particle i used in the particle agglomeration algorithm depicted in figure A.2.

steps is used to effectively speed up agglomerate detection:

1. Sort particle according to their position

2. Determine maximum particle size $r_{p,max}$ and the number of particles n_p

3. Start with particle $i = 1$

4. Calculate search distance for particle i as $r_{p,i} + r_{p,max}$

5. Start with $j = i + 1$

6. Is particle j within the search distance of particle i? If not, $i = i + 1$ and go to step 3

7. Is particle j in contact with particle i? If not, $j = j + 1$ and go to step 5

8. Store particle $i - j$ as an agglomerate and calculate spatial extent (convex hull) of agglomerate

9. Is either particle i or j contained in another agglomerate. If not, add as new agglomerate

10. Merge with existing agglomerate and update spatial extent

11. Advance to step 6

12. Continue until $i = n_p$

Figure A.2 gives a graphical overview of the algorithm.

$$\boxed{\text{List of particle positions } (x, y, z) \text{ and radii } r_p}$$

$$\boxed{\begin{array}{c}\text{Sort particles according to streamwise position } x \\ \text{and determine maximum particle radius } r_{p,max} \\ \text{and total number of particles } n_p\end{array}}$$

Start with particle 1 ($i = 1$)

$i = i + 1$

Searched all particles ($i = n_p$)? — Yes → Return list of agglomerates

No

$$\boxed{\begin{array}{c}\text{Calculate search distance for particle } i \text{ as:} \\ x_i + r_{p,i} + r_{p,max}\end{array}}$$

Start with next particle ($j = i + 1$)

is particle j within search distance of particle i? — No ; $j = j + 1$

Yes

Is particle j in contact with particle i? — No

Yes

$$\boxed{\text{Calculate spatial extent of agglomerate } i, j \text{ in } x, y, z}$$

Is particle i or j already in another nearby agglomerate?

No → Add i, j as new agglomerate and calculate spatial extent

Yes → Merge with existing agglomerate(s) and update spatial extent

Figure A.2: Structure of the algorithm developed to efficiently detect agglomerates.

Appendix A. Agglomerate Tracking Algorithm

Appendix B

Implementation in LIGGGHTS

B.1 Code: Implementation of adhesive JKR model for normal contact

Listing B.1: Modified "normal_model_hertz.h" file to include JKR adhesiveness model in the LIGGGHTS modelling framework. The complete file is reprinted to help the implementation process for readers interested in doing similar simulations.

```
1  #ifdef NORMAL_MODEL
2  NORMAL_MODEL(HERTZ,hertz,3)
3  #else
4  #ifndef NORMAL_MODEL_HERTZ_H_
5  #define NORMAL_MODEL_HERTZ_H_
6  #include "global_properties.h"
7  #include <math.h>
8
9  namespace LIGGGHTS {
10
11 namespace ContactModels
12 {
13   template<>
14   class NormalModel<HERTZ> : protected Pointers
15   {
16   public:
17     static const int MASK = CM_REGISTER_SETTINGS | CM_CONNECT_TO_PROPERTIES |
             CM_SURFACES_INTERSECT;
18
19     NormalModel(LAMMPS * lmp, IContactHistorySetup* hsetup, class
             ContactModelBase *c) : Pointers(lmp),
20       modifiedSurfaceEnergyDensity(NULL),
21       poissonsRatio(NULL),
22       youngsModulus(NULL),
```

```
23        Yeff(NULL),
24        Geff(NULL),
25        betaeff(NULL),
26        limitForce(false),
27        displayedSettings(false),
28        heating(false),
29        heating_track(false),
30        elastic_potential_offset_(-1),
31        elasticpotflag_(false),
32        disable_when_bonded_(false),
33        bond_history_offset_(-1),
34        cmb(c)
35      {
36
37      }
38
39      void registerSettings(Settings & settings)
40      {
41
42        settings.registerOnOff("tangential_damping", tangential_damping, true);
43        settings.registerOnOff("limitForce", limitForce);
44        settings.registerOnOff("heating_normal_hertz",heating,false);
45        settings.registerOnOff("heating_tracking",heating_track,false);
46        settings.registerOnOff("computeElasticPotential", elasticpotflag_, false);
47        settings.registerOnOff("disableNormalWhenBonded", disable_when_bonded_,
                 false);
48        //TODO error->one(FLERR,"TODO here also check if right surface model used
                 ");
49      }
50
51      inline void postSettings(IContactHistorySetup * hsetup, ContactModelBase *
              cmb)
52      {
53        if (elasticpotflag_)
54        {
55          elastic_potential_offset_ = cmb->get_history_offset("elastic_potential");
56          if (elastic_potential_offset_ == -1)
57          {
58            elastic_potential_offset_ = hsetup->add_history_value("
                   elastic_potential", "0");
59            cmb->add_history_offset("elastic_potential", elastic_potential_offset_)
                   ;
60          }
61        }
62        if (disable_when_bonded_)
63        {
64          bond_history_offset_ = cmb->get_history_offset("bond_contactflag");
65          if (bond_history_offset_ < 0)
66            error->one(FLERR, "Could not find bond history offset");
67        }
68      }
69
70      void connectToProperties(PropertyRegistry & registry)
71      {
```

B.1. Code: Implementation of adhesive JKR model for normal contact

```
72    registry.registerProperty("modifiedSurfaceEnergyDensity", &MODEL_PARAMS::
          createModifiedSurfaceEnergyDensity,"model␣hertz");
73    registry.connect("modifiedSurfaceEnergyDensity",
          modifiedSurfaceEnergyDensity,"model␣hertz");
74    registry.registerProperty("poissonsRatio", &MODEL_PARAMS::
          createPoissonsRatio,"model␣hertz");
75    registry.connect("poissonsRatio", poissonsRatio,"model␣hertz");
76    registry.registerProperty("youngsModulus", &MODEL_PARAMS::
          createYoungsModulus,"model␣hertz");
77    registry.connect("youngsModulus", youngsModulus,"model␣hertz");
78
79    registry.registerProperty("Yeff", &MODEL_PARAMS::createYeff,"model␣hertz")
          ;
80    registry.registerProperty("Geff", &MODEL_PARAMS::createGeff,"model␣hertz")
          ;
81    registry.registerProperty("betaeff", &MODEL_PARAMS::createBetaEff,"model␣
          hertz");
82
83    registry.connect("Yeff", Yeff,"model␣hertz");
84    registry.connect("Geff", Geff,"model␣hertz");
85    registry.connect("betaeff", betaeff,"model␣hertz");
86  }
87
88  // effective exponent for stress-strain relationship
89
90  inline double stressStrainExponent()
91  {
92    return 1.5;
93  }
94
95  inline void surfacesIntersect(SurfacesIntersectData & sidata, ForceData &
          i_forces, ForceData & j_forces)
96  {
97
98    //if(!sidata.is_wall) // bond_history_offset_ >= 0)
99    //{
100        //double * const bond_contact_flag = &sidata.contact_history[
              bond_history_offset_];
101        //if(!MathExtraLiggghts::compDouble(bond_contact_flag[0],0.))
102  //        return;
103    //}
104
105    const int itype = sidata.itype;
106    const int jtype = sidata.jtype;
107    const double radi = sidata.radi;
108    const double radj = sidata.radj;
109    double reff = sidata.is_wall ? radi : (radi*radj/(radi+radj));
110
111    #ifdef SUPERQUADRIC_ACTIVE_FLAG
112      if(sidata.is_non_spherical) {
113        if(sidata.is_wall)
114          reff = MathExtraLiggghtsNonspherical::get_effective_radius_wall(
                sidata, atom->roundness[sidata.i], error);
115        else
```

```
116              reff = MathExtraLiggghtsNonspherical::get_effective_radius(sidata,
                     atom->roundness[sidata.i], atom->roundness[sidata.j], error);
117          }
118      #endif
119      const double meff=sidata.meff;
120
121      const double sqrtval = sqrt(reff*sidata.deltan);
122
123      const double Sn=2.*Yeff[itype][jtype]*sqrtval;
124      const double St=8.*Geff[itype][jtype]*sqrtval;
125
126      double kn=4./3.*Yeff[itype][jtype]*sqrtval;
127      double kt=St;
128      const double sqrtFiveOverSix =
                  0.91287092917527685576161630466800355658790782499663875;
129      const double gamman=-2.*sqrtFiveOverSix*betaeff[itype][jtype]*sqrt(Sn*meff
                  );
130      const double gammat= tangential_damping ? -2.*sqrtFiveOverSix*betaeff[
                  itype][jtype]*sqrt(St*meff) : 0.0;
131
132      if(!displayedSettings)
133      {
134          displayedSettings = true;
135
136          /*
137          if(limitForce)
138              if(0 == comm->me) fprintf(screen," NormalModel<HERTZ_STIFFNESS>: will
                      limit normal force.\n");
139          */
140      }
141      // convert Kn and Kt from pressure units to force/distance^2
142      kn /= force->nktv2p;
143      kt /= force->nktv2p;
144
145      //ADD JKR MODEL
146      const double c0 = reff*reff*sidata.deltan*sidata.deltan;
147      const double c1 = -8.0*(1.0-poissonsRatio[itype]*poissonsRatio[itype])*
                  M_PI*modifiedSurfaceEnergyDensity*reff*reff/youngsModulus[itype];
148      const double c2 = -2.0*reff*sidata.deltan;
149      //const double c3 = 0.0;
150      //const double c4 = 1.0;
151      const double P = -c2*c2/12.0-c0;
152      const double Q = -c2*c2*c2/108.0+(c0*c2)/3.0-c1*c1/8.0;
153      const double U = pow((-Q/2.0+sqrt(Q*Q/4.0+P*P*P/27)),1.0/3.0);
154      const double s = -5.0*c2/6.0+U-P/(3.0*U);
155      //const double s1 = -5.0*c2/6.0-Q;
156      const double w = sqrt(c2+2.0*s);
157      const double lambda = c1/(2.0*w);
158      double a_jkr = 0.5*(w+sqrt(w*w-4.0*(c2+s+lambda)));
159      double F_jkr = 4.0*sqrt((M_PI*a_jkr*a_jkr*a_jkr*
                  modifiedSurfaceEnergyDensity*youngsModulus[itype])/(2.0*(1.0-
                  poissonsRatio[itype]*poissonsRatio[itype])));
160      double Fn_jkr = 4.0/3.0*Yeff[itype][jtype]*a_jkr*a_jkr*a_jkr/reff;
161      double Fn_contact = Fn_jkr-F_jkr;
```

B.1. Code: Implementation of adhesive JKR model for normal contact

```
162
163        const double Fn_damping = -gamman*sidata.vn;
164        double Fn = Fn_damping + Fn_contact;
165
166        //limit force to avoid the artefact of negative repulsion force
167        if(limitForce && (Fn<0.0) )
168        {
169            Fn = 0.0;
170        }
171
172        sidata.Fn = Fn;
173        sidata.kn = kn;
174        sidata.kt = kt;
175        sidata.gamman = gamman;
176        sidata.gammat = gammat;
177
178        #ifdef NONSPHERICAL_ACTIVE_FLAG
179            double torque_i[3] = {0., 0., 0.};
180            double Fn_i[3] = { Fn * sidata.en[0], Fn * sidata.en[1], Fn * sidata.en
                  [2]};
181            if(sidata.is_non_spherical) {
182              double xci[3];
183              vectorSubtract3D(sidata.contact_point, atom->x[sidata.i], xci);
184              vectorCross3D(xci, Fn_i, torque_i);
185            }
186
187        #endif
188
189        if(heating)
190        {
191          sidata.P_diss += fabs(Fn_damping*sidata.vn); //fprintf(screen," contrib %
                  f\n",fabs(Fn_damping*sidata.vn));}
192          if(heating_track && sidata.is_wall) cmb->tally_pw(fabs(Fn_damping*sidata.
                  vn),sidata.i,jtype,0);
193          if(heating_track && !sidata.is_wall) cmb->tally_pp(fabs(Fn_damping*sidata
                  .vn),sidata.i,sidata.j,0);
194        }
195
196        // apply normal force
197        if (!disable_when_bonded_ || MathExtraLiggghts::compDouble(sidata.
                  contact_history[bond_history_offset_], 0.0, 1e-5))
198        {
199          // compute increment in elastic potential
200          if (elasticpotflag_ && sidata.computeflag && sidata.shearupdate)
201            sidata.contact_history[elastic_potential_offset_] += -update->dt*sidata
                  .vn*Fn_contact;
202
203          if(sidata.is_wall) {
204            const double Fn_ = Fn * sidata.area_ratio;
205            i_forces.delta_F[0] += Fn_ * sidata.en[0];
206            i_forces.delta_F[1] += Fn_ * sidata.en[1];
207            i_forces.delta_F[2] += Fn_ * sidata.en[2];
208            #ifdef NONSPHERICAL_ACTIVE_FLAG
209                  if(sidata.is_non_spherical) {
```

```
210                    //for non-spherical particles normal force can produce torque!
211                    i_forces.delta_torque[0] += torque_i[0];
212                    i_forces.delta_torque[1] += torque_i[1];
213                    i_forces.delta_torque[2] += torque_i[2];
214                }
215        #endif
216      } else {
217        i_forces.delta_F[0] += sidata.Fn * sidata.en[0];
218        i_forces.delta_F[1] += sidata.Fn * sidata.en[1];
219        i_forces.delta_F[2] += sidata.Fn * sidata.en[2];
220
221        j_forces.delta_F[0] += -i_forces.delta_F[0];
222        j_forces.delta_F[1] += -i_forces.delta_F[1];
223        j_forces.delta_F[2] += -i_forces.delta_F[2];
224        #ifdef NONSPHERICAL_ACTIVE_FLAG
225                if(sidata.is_non_spherical) {
226                    //for non-spherical particles normal force can produce torque!
227                    double xcj[3], torque_j[3];
228                    double Fn_j[3] = { -Fn_i[0], -Fn_i[1], -Fn_i[2]};
229                    vectorSubtract3D(sidata.contact_point, atom->x[sidata.j], xcj)
                            ;
230                    vectorCross3D(xcj, Fn_j, torque_j);
231
232                    i_forces.delta_torque[0] += torque_i[0];
233                    i_forces.delta_torque[1] += torque_i[1];
234                    i_forces.delta_torque[2] += torque_i[2];
235
236                    j_forces.delta_torque[0] += torque_j[0];
237                    j_forces.delta_torque[1] += torque_j[1];
238                    j_forces.delta_torque[2] += torque_j[2];
239                }
240        #endif
241      }
242    }
243  }
244
245  void surfacesClose(SurfacesCloseData&, ForceData&, ForceData&){}
246  void beginPass(SurfacesIntersectData&, ForceData&, ForceData&){}
247  void endPass(SurfacesIntersectData&, ForceData&, ForceData&){}
248
249 protected:
250    double ** Yeff;
251    double ** Geff;
252    double ** betaeff;
253    double modifiedSurfaceEnergyDensity;
254    double * poissonsRatio;
255    double * youngsModulus;
256
257    bool tangential_damping;
258    bool limitForce;
259    bool displayedSettings;
260    bool heating;
261    bool heating_track;
262    int elastic_potential_offset_;
```

```
263      bool elasticpotflag_;
264      bool disable_when_bonded_;
265      int bond_history_offset_;
266      class ContactModelBase *cmb;
267
268    };
269
270  }
271
272  }
273  #endif
274  #endif
```

B.2 Code: Implementation of adhesive JKR model for tangential contact

Listing B.2: Modified "tangential_model_history.h" file to include JKR adhesiveness on tangential motion in the LIGGGHTS modelling framework. The complete file is reprinted to help the implementation process for readers interested in doing similar simulations.

```
1  #ifdef TANGENTIAL_MODEL
2  TANGENTIAL_MODEL(TANGENTIAL_HISTORY,history,2)
3  #else
4  #ifndef TANGENTIAL_MODEL_HISTORY_H_
5  #define TANGENTIAL_MODEL_HISTORY_H_
6  #include "contact_models.h"
7  #include <math.h>
8  #include "update.h"
9  #include "global_properties.h"
10 #include "atom.h"
11
12 namespace LIGGGHTS {
13 namespace ContactModels
14 {
15   template<>
16   class TangentialModel<TANGENTIAL_HISTORY> : protected Pointers
17   {
18     double modifiedSurfaceEnergyDensity;
19     double ** coeffFrict;
20     int history_offset;
21
22   public:
23     static const int MASK = CM_CONNECT_TO_PROPERTIES | CM_SURFACES_INTERSECT |
           CM_SURFACES_CLOSE;
24
25     TangentialModel(LAMMPS * lmp, IContactHistorySetup * hsetup,class
           ContactModelBase *c) : Pointers(lmp),
26       modifiedSurfaceEnergyDensity(NULL),
27       coeffFrict(NULL),
28       heating(false),
29       heating_track(false),
30       cmb(c)
31     {
32       history_offset = hsetup->add_history_value("shearx", "1");
33       hsetup->add_history_value("sheary", "1");
34       hsetup->add_history_value("shearz", "1");
35
36     }
37
38     inline void postSettings(IContactHistorySetup * hsetup, ContactModelBase *
           cmb)
39     {}
40
41     inline void registerSettings(Settings& settings)
42     {
```

```
43        settings.registerOnOff("heating_tangential_history",heating,false);
44        settings.registerOnOff("heating_tracking",heating_track,false);
45        //TODO error->one(FLERR,"TODO here also check if right surface model used
              ");
46      }
47
48      inline void connectToProperties(PropertyRegistry & registry)
49      {
50        registry.registerProperty("modifiedSurfaceEnergyDensity", &MODEL_PARAMS::
              createModifiedSurfaceEnergyDensity);
51        registry.connect("modifiedSurfaceEnergyDensity",
              modifiedSurfaceEnergyDensity,"tangential_model history");
52
53        registry.registerProperty("coeffFrict", &MODEL_PARAMS::createCoeffFrict);
54        registry.connect("coeffFrict", coeffFrict,"tangential_model history");
55      }
56
57      inline void surfacesIntersect(const SurfacesIntersectData & sidata,
            ForceData & i_forces, ForceData & j_forces)
58      {
59        // normal forces = Hookian contact + normal velocity damping
60        const double enx = sidata.en[0];
61        const double eny = sidata.en[1];
62        const double enz = sidata.en[2];
63
64        // shear history effects
65        if(sidata.contact_flags) *sidata.contact_flags |= CONTACT_TANGENTIAL_MODEL
              ;
66        double * const shear = &sidata.contact_history[history_offset];
67
68        const bool update_history = sidata.computeflag && sidata.shearupdate;
69        if (update_history) {
70          const double dt = update->dt;
71          shear[0] += sidata.vtr1 * dt;
72          shear[1] += sidata.vtr2 * dt;
73          shear[2] += sidata.vtr3 * dt;
74
75          // rotate shear displacements
76
77          double rsht = shear[0]*enx + shear[1]*eny + shear[2]*enz;
78          shear[0] -= rsht * enx;
79          shear[1] -= rsht * eny;
80          shear[2] -= rsht * enz;
81        }
82
83        const double shrmag = sqrt(shear[0]*shear[0] + shear[1]*shear[1] + shear
              [2]*shear[2]);
84        const double kt = sidata.kt;
85        const double xmu = coeffFrict[sidata.itype][sidata.jtype];
86
87        // tangential forces = shear + tangential velocity damping
88        double Ft1 = -(kt * shear[0]);
89        double Ft2 = -(kt * shear[1]);
90        double Ft3 = -(kt * shear[2]);
```

```
91
92      // rescale frictional displacements and forces if needed
93      const double Ft_shear = kt * shrmag; // sqrt(Ft1 * Ft1 + Ft2 * Ft2 + Ft3 *
            Ft3);
94
95      double ri = sidata.radi;
96      double rj = sidata.radj;
97      double reff = sidata.is_wall ? sidata.radi : (ri*rj/(ri+rj));
98      const double Fc = 3*M_PI*reff*modifiedSurfaceEnergyDensity;
99      //const double Ft_friction = xmu * fabs(sidata.Fn); //without adhesion
100     const double Ft_friction = xmu * fabs(sidata.Fn + 2.0*Fc); //with adhesion
101     // energy loss from sliding or damping
102     if (Ft_shear > Ft_friction) {
103       if (shrmag != 0.0) {
104         const double ratio = Ft_friction / Ft_shear;
105
106         if(heating)
107         {
108           sidata.P_diss += (vectorMag3DSquared(shear)*kt - ratio*ratio*
                vectorMag3DSquared(shear)*kt) / (update->dt);
109           if(heating_track && sidata.is_wall) cmb->tally_pw((vectorMag3DSquared
                (shear)*kt - ratio*ratio*vectorMag3DSquared(shear)*kt) / (update
                ->dt),sidata.i,sidata.jtype,2);
110           if(heating_track && !sidata.is_wall) cmb->tally_pp((
                vectorMag3DSquared(shear)*kt - ratio*ratio*vectorMag3DSquared(
                shear)*kt) / (update->dt),sidata.i,sidata.j,2);
111         }
112         Ft1 *= ratio;
113         Ft2 *= ratio;
114         Ft3 *= ratio;
115
116         if (update_history)
117         {
118             shear[0] = -Ft1/kt;
119             shear[1] = -Ft2/kt;
120             shear[2] = -Ft3/kt;
121         }
122       }
123       else Ft1 = Ft2 = Ft3 = 0.0;
124     }
125     else
126     {
127       const double gammat = sidata.gammat;
128       Ft1 -= (gammat*sidata.vtr1);
129       Ft2 -= (gammat*sidata.vtr2);
130       Ft3 -= (gammat*sidata.vtr3);
131       if(heating)
132       {
133           sidata.P_diss += gammat*(sidata.vtr1*sidata.vtr1+sidata.vtr2*sidata.
                vtr2+sidata.vtr3*sidata.vtr3);
134           if(heating_track && sidata.is_wall) cmb->tally_pw(gammat*(sidata.vtr1
                *sidata.vtr1+sidata.vtr2*sidata.vtr2+sidata.vtr3*sidata.vtr3),
                sidata.i,sidata.jtype,1);
135           if(heating_track && !sidata.is_wall) cmb->tally_pp(gammat*(sidata.
```

```
                      vtr1*sidata.vtr1+sidata.vtr2*sidata.vtr2+sidata.vtr3*sidata.vtr3
                      ),sidata.i,sidata.j,1);
136         }
137       }
138
139       // forces & torques
140       const double tor1 = eny * Ft3 - enz * Ft2;
141       const double tor2 = enz * Ft1 - enx * Ft3;
142       const double tor3 = enx * Ft2 - eny * Ft1;
143
144       #ifdef NONSPHERICAL_ACTIVE_FLAG
145           double torque_i[3];
146           if(sidata.is_non_spherical) {
147             double xci[3];
148             double Ft_i[3] = { Ft1, Ft2, Ft3 };
149             vectorSubtract3D(sidata.contact_point, atom->x[sidata.i], xci);
150             vectorCross3D(xci, Ft_i, torque_i);
151           } else {
152             torque_i[0] = -sidata.cri * tor1;
153             torque_i[1] = -sidata.cri * tor2;
154             torque_i[2] = -sidata.cri * tor3;
155           }
156       #endif
157       // return resulting forces
158       if(sidata.is_wall) {
159         const double area_ratio = sidata.area_ratio;
160         i_forces.delta_F[0] += Ft1 * area_ratio;
161         i_forces.delta_F[1] += Ft2 * area_ratio;
162         i_forces.delta_F[2] += Ft3 * area_ratio;
163         #ifdef NONSPHERICAL_ACTIVE_FLAG
164               i_forces.delta_torque[0] += torque_i[0] * area_ratio;
165               i_forces.delta_torque[1] += torque_i[1] * area_ratio;
166               i_forces.delta_torque[2] += torque_i[2] * area_ratio;
167         #else
168               i_forces.delta_torque[0] += -sidata.cri * tor1 * area_ratio;
169               i_forces.delta_torque[1] += -sidata.cri * tor2 * area_ratio;
170               i_forces.delta_torque[2] += -sidata.cri * tor3 * area_ratio;
171         #endif
172       } else {
173         i_forces.delta_F[0] += Ft1;
174         i_forces.delta_F[1] += Ft2;
175         i_forces.delta_F[2] += Ft3;
176         j_forces.delta_F[0] += -Ft1;
177         j_forces.delta_F[1] += -Ft2;
178         j_forces.delta_F[2] += -Ft3;
179         #ifdef NONSPHERICAL_ACTIVE_FLAG
180               double torque_j[3];
181               if(sidata.is_non_spherical) {
182                 double xcj[3];
183                 vectorSubtract3D(sidata.contact_point, atom->x[sidata.j], xcj);
184                 double Ft_j[3] = { -Ft1, -Ft2, -Ft3 };
185                 vectorCross3D(xcj, Ft_j, torque_j);
186               } else {
187                 torque_j[0] = -sidata.crj * tor1;
```

```
188                    torque_j[1] = -sidata.crj * tor2;
189                    torque_j[2] = -sidata.crj * tor3;
190                }
191                i_forces.delta_torque[0] += torque_i[0];
192                i_forces.delta_torque[1] += torque_i[1];
193                i_forces.delta_torque[2] += torque_i[2];
194
195                j_forces.delta_torque[0] += torque_j[0];
196                j_forces.delta_torque[1] += torque_j[1];
197                j_forces.delta_torque[2] += torque_j[2];
198        #else
199                i_forces.delta_torque[0] += -sidata.cri * tor1;
200                i_forces.delta_torque[1] += -sidata.cri * tor2;
201                i_forces.delta_torque[2] += -sidata.cri * tor3;
202
203                j_forces.delta_torque[0] += -sidata.crj * tor1;
204                j_forces.delta_torque[1] += -sidata.crj * tor2;
205                j_forces.delta_torque[2] += -sidata.crj * tor3;
206        #endif
207        }
208    }
209
210    inline void surfacesClose(SurfacesCloseData & scdata, ForceData&, ForceData
              &)
211    {
212      // unset non-touching neighbors
213      // TODO even if shearupdate == false?
214      if(scdata.contact_flags) *scdata.contact_flags &= ~
              CONTACT_TANGENTIAL_MODEL;
215      if(!scdata.contact_history)
216        return; //DO NOT access contact_history if not available
217      double * const shear = &scdata.contact_history[history_offset];
218      shear[0] = 0.0;
219      shear[1] = 0.0;
220      shear[2] = 0.0;
221    }
222
223    inline void beginPass(SurfacesIntersectData&, ForceData&, ForceData&){}
224    inline void endPass(SurfacesIntersectData&, ForceData&, ForceData&){}
225
226  protected:
227    bool heating;
228    bool heating_track;
229    class ContactModelBase *cmb;
230  };
231 }
232 }
233 #endif // TANGENTIAL_MODEL_HISTORY_H_
234 #endif
```

B.3   Code: Implementation of adhesive JKR rolling resistance torque model

Listing B.3: New "rolling_model_jkr.h" file to include the effect of adhesivenss on the rolling motion through a modified rolling resistance torque in the LIGGGHTS modelling framework. The complete file is reprinted to help the implementation process for readers interested in doing similar simulations.

```
1   #ifdef ROLLING_MODEL
2   ROLLING_MODEL(ROLLING_JKR,jkr,5)
3   #else
4   #ifndef ROLLING_MODEL_JKR_H_
5   #define ROLLING_MODEL_JKR_H_
6   #include "contact_models.h"
7   #include <algorithm>
8   #include "math.h"
9   #include "domain.h"
10  #include "math_extra_liggghts.h"
11
12  namespace LIGGGHTS {
13  namespace ContactModels
14  {
15    using namespace LAMMPS_NS;
16
17    template<>
18    class RollingModel<ROLLING_JKR> : protected Pointers
19    {
20    public:
21      static const int MASK = CM_CONNECT_TO_PROPERTIES | CM_SURFACES_INTERSECT |
            CM_SURFACES_CLOSE;
22
23      RollingModel(class LAMMPS * lmp, IContactHistorySetup * hsetup,class
            ContactModelBase *) :
24          Pointers(lmp)
25      {
26        history_offset = hsetup->add_history_value("xi_x_old", "1");
27        hsetup->add_history_value("xi_y_old", "1");
28        hsetup->add_history_value("xi_z_old", "1");
29      }
30
31      void registerSettings(Settings&) {}
32
33      inline void postSettings(IContactHistorySetup * hsetup, ContactModelBase *
            cmb)
34      {}
35
36      void connectToProperties(PropertyRegistry & registry) {
37        registry.registerProperty("adhesionHysteresis", &MODEL_PARAMS::
            createAdhesionHysteresisParameter);
38        registry.connect("adhesionHysteresis", adhesionHysteresis,"rolling_model␣
            jkr");
39        registry.registerProperty("surfaceEnergyDensity", &MODEL_PARAMS::
```

```
             createSurfaceEnergyDensity);
40      registry.connect("surfaceEnergyDensity", surfaceEnergyDensity,"
             rolling_model␣jkr");
41      registry.registerProperty("modifiedSurfaceEnergyDensity", &MODEL_PARAMS::
             createModifiedSurfaceEnergyDensity);
42      registry.connect("modifiedSurfaceEnergyDensity",
             modifiedSurfaceEnergyDensity,"rolling_model␣jkr");
43      registry.registerProperty("poissonsRatio", &MODEL_PARAMS::
             createPoissonsRatio);
44      registry.connect("poissonsRatio", poissonsRatio,"rolling_model␣jkr");
45      registry.registerProperty("youngsModulus", &MODEL_PARAMS::
             createYoungsModulus);
46      registry.connect("youngsModulus", youngsModulus,"rolling_model␣jkr");
47
48      registry.registerProperty("Yeff", &MODEL_PARAMS::createYeff);
49      registry.connect("Yeff", Yeff,"rolling_model␣jkr");
50
51      // error checks on coarsegraining
52      if(force->cg_active())
53        error->cg(FLERR,"rolling␣model␣jkr");
54    }
55
56    void surfacesIntersect(SurfacesIntersectData & sidata, ForceData & i_forces,
             ForceData & j_forces)
57    {
58      double r_torque[3];
59      vectorZeroize3D(r_torque);
60
61      if(sidata.contact_flags) *sidata.contact_flags |= CONTACT_ROLLING_MODEL;
62
63      if(sidata.is_wall) {
64        const double wr1 = sidata.wr1;
65        const double wr2 = sidata.wr2;
66        const double wr3 = sidata.wr3;
67        const double radius = sidata.radi;
68
69        double r_inertia;
70        if (domain->dimension == 2) r_inertia = 1.5*sidata.mi*radius*radius;
71        else  r_inertia = 1.4*sidata.mi*radius*radius;
72
73        calcRollTorque(r_torque,sidata,radius,wr1,wr2,wr3,r_inertia);
74
75      } else {
76        double wr_roll[3];
77
78        const int i = sidata.i;
79        const int j = sidata.j;
80
81        const double radi = sidata.radi;
82        const double radj = sidata.radj;
83        const double reff = sidata.is_wall ? radi : (radi*radj/(radi+radj));
84        const double * const * const omega = atom->omega;
85
86        const double r_inertia_red_i = sidata.mi*radi*radi;
```

```
87        const double r_inertia_red_j = sidata.mj*radj*radj;
88        double r_inertia;
89        if (domain->dimension == 2) r_inertia = 1.5 * r_inertia_red_i *
              r_inertia_red_j/(r_inertia_red_i + r_inertia_red_j);
90        else r_inertia = 1.4 * r_inertia_red_i * r_inertia_red_j/(
              r_inertia_red_i + r_inertia_red_j);
91
92        // relative rotational velocity
93        vectorSubtract3D(omega[i],omega[j],wr_roll);
94
95        calcRollTorque(r_torque,sidata,reff,wr_roll[0],wr_roll[1],wr_roll[2],
              r_inertia);
96      }
97
98      i_forces.delta_torque[0] -= r_torque[0];
99      i_forces.delta_torque[1] -= r_torque[1];
100     i_forces.delta_torque[2] -= r_torque[2];
101     j_forces.delta_torque[0] += r_torque[0];
102     j_forces.delta_torque[1] += r_torque[1];
103     j_forces.delta_torque[2] += r_torque[2];
104   }
105
106   void surfacesClose(SurfacesCloseData & scdata, ForceData&, ForceData&)
107   {
108     if(scdata.contact_flags) *scdata.contact_flags &= ~CONTACT_ROLLING_MODEL;
109     double * const xi_history = &scdata.contact_history[history_offset];
110     xi_history[0] = 0.0;
111     xi_history[1] = 0.0;
112     xi_history[2] = 0.0;
113   }
114
115   void beginPass(SurfacesIntersectData&, ForceData&, ForceData&){}
116   void endPass(SurfacesIntersectData&, ForceData&, ForceData&){}
117
118 private:
119   double ** Yeff;
120   double adhesionHysteresis;
121   double surfaceEnergyDensity;
122   double modifiedSurfaceEnergyDensity;
123   double * poissonsRatio;
124   double * youngsModulus;
125   int history_offset;
126
127   inline void calcRollTorque(double (&r_torque)[3],const SurfacesIntersectData
          & sidata,double reff,double wr1,double wr2,double wr3,double r_inertia)
          {
128
129     double wr_n[3],wr_t[3],d_xi[3],xi[3];
130
131     const int itype = sidata.itype;
132     const int jtype = sidata.jtype;
133
134     const double enx = sidata.en[0];
135     const double eny = sidata.en[1];
```

99

```
136        const double enz = sidata.en[2];
137
138        const double dt = update->dt;
139
140        double * const xi_history = &sidata.contact_history[history_offset]; //
               requires Style::TANGENTIAL == TANGENTIAL_HISTORY
141
142        const double wr_dot_delta = wr1*enx+ wr2*eny + wr3*enz;
143        wr_n[0] = enx * wr_dot_delta;
144        wr_n[1] = eny * wr_dot_delta;
145        wr_n[2] = enz * wr_dot_delta;
146        wr_t[0] = wr1 - wr_n[0];
147        wr_t[1] = wr2 - wr_n[1];
148        wr_t[2] = wr3 - wr_n[2];
149
150        // spring
151        const double c0 = reff*reff*sidata.deltan*sidata.deltan;
152        const double c1 = -8.0*(1.0-poissonsRatio[itype]*poissonsRatio[itype])*
               M_PI*modifiedSurfaceEnergyDensity*reff*reff/youngsModulus[itype];
153        const double c2 = -2.0*reff*sidata.deltan;
154        //const double c3 = 0.0;
155        //const double c4 = 1.0;
156        const double P = -c2*c2/12.0-c0;
157        const double Q = -c2*c2*c2/108.0+(c0*c2)/3.0-c1*c1/8.0;
158        const double U = pow((-Q/2.0+sqrt(Q*Q/4.0+P*P*P/27)),1.0/3.0);
159        const double s = -5.0*c2/6.0+U-P/(3.0*U);
160        //const double s1 = -5.0*c2/6.0-Q;
161        const double w = sqrt(c2+2.0*s);
162        const double lambda = c1/(2.0*w);
163        double a_mod = 0.5*(w+sqrt(w*w-4.0*(c2+s+lambda)));
164
165        const double a0_mod = pow(9.0*M_PI*modifiedSurfaceEnergyDensity*reff*reff
               /(Yeff[itype][jtype]),1.0/3.0);
166        const double a0 = pow(9.0*M_PI*surfaceEnergyDensity*reff*reff/(Yeff[itype
               ][jtype]*pow(surfaceEnergyDensity/modifiedSurfaceEnergyDensity
               ,5.0/2.0)),1.0/3.0);
167        const double Fc = 3.0*M_PI*surfaceEnergyDensity*reff;
168        const double kr = 4.0*Fc*pow(a_mod/a0_mod,3.0/2.0);
169
170        // change in rolling displacement (d_xi)
171        vectorScalarMult3D(wr_t,dt*reff,d_xi);
172        xi[0] = xi_history[0] + d_xi[0];
173        xi[1] = xi_history[1] + d_xi[1];
174        xi[2] = xi_history[2] + d_xi[2];
175        const double xi_mag = vectorMag3D(xi);
176
177        const double xi_crit = a0/12.0*adhesionHysteresis;
178
179        if(xi_mag > xi_crit)
180        {
181          const double factor = xi_crit / xi_mag;
182          xi[0] *= factor;
183          xi[1] *= factor;
184          xi[2] *= factor;
```

B.3. Code: Implementation of adhesive JKR rolling resistance torque model

```
185
186        r_torque[0] = kr*xi[0];
187        r_torque[1] = kr*xi[1];
188        r_torque[2] = kr*xi[2];
189
190        xi_history[0] = xi[0];
191        xi_history[1] = xi[1];
192        xi_history[2] = xi[2];
193      } else {
194        r_torque[0] = kr*xi[0];
195        r_torque[1] = kr*xi[1];
196        r_torque[2] = kr*xi[2];
197
198        xi_history[0] = xi[0];
199        xi_history[1] = xi[1];
200        xi_history[2] = xi[2];
201      }
202    }
203  };
204 }
205 }
206 #endif // ROLLING_MODEL_JKR_H_
207 #endif
```

Appendix B. Implementation in LIGGGHTS

Part II

Papers

Appendix A

On the adhesive JKR contact and rolling models for reduced particle stiffness discrete element simulations

J. Hærvig, U. Kleinhans, C. Wieland, H. Spliethoff, K. Sørensen, T.J. Condra

On the adhesive JKR contact and rolling models for reduced particle stiffness discrete element simulations

J. Hærvig[a], U. Kleinhans[b], C. Wieland[b], H. Spliethoff[b], A.L. Jensen[a], K. Sørensen[a], T.J. Condra[a]

[a] *Aalborg University, Department of Energy Technology, Pontoppidanstræde 111, DK-9220 Aalborg, Denmark*
[b] *Technical University of Munich, Institute of Energy Systems, Boltzmannstraße 15, DE-85748 Garching, Germany*

Abstract

Discrete Element Method (DEM) simulations are a promising approach to accurately predict agglomeration and deposition of micron-sized adhesive particles. However, the mechanistic models in DEM combined with high particle stiffness for most common materials require time step sizes in the order of nano seconds, which makes DEM simulations impractical for more complex applications.

In this study, analytically derived guidelines on how to reduce computational time by using a reduced particle stiffness are given. The guidelines are validated by comparing simulations of particles with and without reduced particle stiffness to experimental data. Then two well-defined test cases are investigated to show the applicability of the guidelines.

When introducing a reduced particle stiffness in DEM simulations by reducing the effective Young's modulus from E to E_{mod}, the surface energy density γ in the adhesive Johnson-Kendall-Roberts (JKR) model by Johnson et al. (1971) should be modified as $\gamma_{mod} = \gamma \left(E_{mod} / E \right)^{2/5}$. Using this relation, the stick/rebound threshold remains the same but the collision process takes place over a longer time period, which allows for a higher time step size. When rolling motion is important, the commonly used adhesive rolling resistance torque model proposed by Dominik and Tielens (1995, 1997); Krijt et al. (2014) can be used by modifying the contact radius ratio $(a / a_0)^{3/2}$ to $(a_{mod} / a_{0,mod})^{3/2}$, whilst keeping the other terms unaltered in the description of the rolling resistance torque $M_{r,mod} = -4 F_C \left(a / a_0 \right)^{3/2} \xi$. Furthermore, as the particle stiffness is reduced from E to E_{mod}, the time period for collisions (or oscillations when particles stick upon impact) Δt_{col} is found to vary as $\Delta t_{col,mod} = \Delta t_{col} (E / E_{mod})^{2/5}$. As the collision duration and the collision time step size are directly related, this criterion can be used to estimate how much the time step size can be changed as a reduced particle stiffness is introduced.

Introducing particles with a reduced particle stiffness has some limitations when strong external forces are acting to break-up formed agglomerates or re-entrain particles deposited on a surface out into the free stream. Therefore, care should be taken in flows with high local shear to make sure that an external force, such as a fluid drag force, acting to separate agglomerated particles, is several orders of magnitude lower than the critical force required to separate particles.

A.1 Introduction

Discrete Element Method (DEM) simulations are typically used to accurately predict the motion of particles in systems with high local particle volume fraction where particle-particle collisions are important. Recently, the motion of adhesive particles has received increased attention (Barthel, 2008) due to the wide range of applications which include, but are not limited to, particulate fouling layers in heat exchangers, food processing, sediment transport, aerosol modelling, fluidized beds and dust coagulating to form early stages of planets in space. As opposed to other methods, DEM simulations resolve particle-particle collisions directly using a mechanistic approach. As each particle-particle collision is resolved over numerous time steps, the required computational time is high compared to other methods (Henry et al., 2012). A widely used approach to decrease computational costs is to decrease the particle stiffness, namely Young's modulus, and thereby make collisions take place over longer time periods allowing for an increased time step size. For collisions involving non-adhesive particles, numerous studies suggest that the particle stiffness can be reduced by several orders of magnitude without altering the collisions in terms of separating velocity after collision (Tsuji et al., 1993; Gu et al., 2016). However, when introducing adhesive particles, recent studies have pointed out that a reduced particle stiffness has to be balanced by a reduced adhesive force. Therefore, Kobayashi et al. (2013) introduced a dynamic van der Waals adhesion model upon collision that scales the adhesive force F_{ad} according to the square root of the ratio of particle spring constants k as: $F_{\text{ad,mod}}/F_{\text{ad}} = \sqrt{k_{\text{mod}}/k}$, where subscript *mod* denotes modified values. Gu et al. (2016) extended the work and included the fact that the van der Waals force is effective over a finite distance before the particles come into physical contact. Common for these studies is the fact that they assume particle deformation to play a negligible role on the adhesive force upon collision. This assumption is valid for sufficiently small particles, where particle deformation is negligible (Johnson and Greenwood, 1997).

When the particle diameter is large (typically $d_{\text{p}} > 10$ μm), particle deformation cannot be neglected when describing the adhesive force. The importance of particle deformation on the adhesive behaviour is described by Tabor (1977) through the dimensionless Tabor parameter λ_{T} where R, γ, E

and $D_{\min}$ define effective particle radius, surface energy density, effective Young's modulus and minimum atomic separation distance between particles (typically taken to be 1.65 Å (Israelachvili, 1992; Parteli et al., 2014)):

$$\lambda_{\mathrm{T}} = \left(\frac{4R\gamma^2}{E^2 D_{\min}^3} \right)^{1/3} \tag{A.1}$$

$$\frac{1}{R} = \frac{1}{r_{\mathrm{i}}} + \frac{1}{r_{\mathrm{j}}}, \qquad \frac{1}{E} = \frac{1 - \nu_{\mathrm{i}}^2}{E_{\mathrm{i}}} + \frac{1 - \nu_{\mathrm{j}}^2}{E_{\mathrm{j}}} \tag{A.2}$$

where r and ν refer to particle radius and Poisson's ratio respectively and subscripts i and j refer to particle i, j. The study by Johnson and Greenwood (1997) shows that the adhesive Johnson-Kendall-Roberts (JKR) model by Johnson et al. (1971) is valid for $\lambda_{\mathrm{T}} > 3$, the Derjaguin-Muller-Toporov (DMT) model by Derjaguin et al. (1975) is valid for $\lambda_{\mathrm{T}} < 0.1$ and the model by Maugis (1992) is valid in between the two when $0.1 \leq \lambda_{\mathrm{T}} \leq 3$.

With an increasing number of studies on collisions of adhesive particles being carried out, the aim of this paper is to emphasise the importance of reducing the particle adhesiveness when a reduced particle stiffness is introduced. For this purpose an analytically derived criterion on how to adjust the surface energy density to account for a reduced particle stiffness for collisions in the JKR limit ($\lambda_{\mathrm{T}} > 3$) is presented. This paper is structured as follows: Firstly, the adhesive DEM modelling framework is briefly outlined. Secondly, the criterion on how to reduce particle stiffness is presented for both collisions and rolling behaviour. Thirdly, numerical simulations of adhesive particles are compared to experimental data found in literature. Lastly, two simple test cases are investigated in more details to show the applicability of the proposed criterion. These test cases represent types of collisions commonly encountered in the particle agglomeration and deposition processes:

1. Binary head-on adhesive particle/particle or particle/wall collisions forming agglomerates or deposition.

2. Collisions of single adhesive particles with a wall. Here the particles are affected by a constant external force parallel to the wall (e.g. a gravity force, time-independent fluid force or a constant magnetic force). Here focus is on the rolling resistance torque, which causes particles to stick to a surface, despite being affected by a constant force.

A.2 Modelling Framework

The translational and rotational motion of particles is obtained using the DEM, where Newton's equation of motion is solved to obtain the instan-
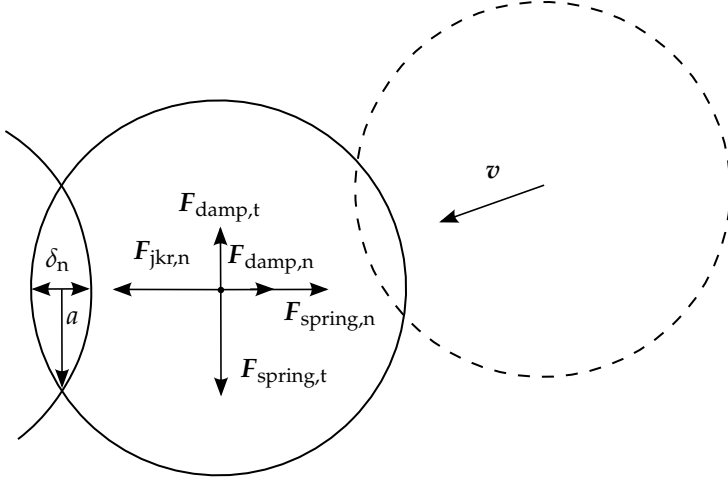
Figure A.1: Illustration of contact forces upon collision of two adhesive particles shown with solid black lines. The particles are still approaching each other so that the normal damping force points in the direction opposite of motion.

taneous translational and rotational position for each particle:

$$m\frac{\mathrm{d}^2 x}{\mathrm{d}t^2} = F_{\text{con}} + F_{\text{ext}} \tag{A.3}$$

$$I\frac{\mathrm{d}\omega}{\mathrm{d}t} = M_{\text{con}} + M_{\text{r}} \tag{A.4}$$

where the forces contributing are the contact force upon impact F_{con} and an external force F_{ext} which could represent a gravity force, a time-independent fluid force or a constant magnetic force. Likewise, the total torque is the sum of a contact torque M_{con} and a rolling resistance torque M_{r}. The contact force is split into normal and tangential contributions ($F_{\text{con,n}}$ and $F_{\text{con,t}}$), where the normal contact force is the sum of a spring force, an adhesive force and a damping force contribution:

$$F_{\text{con,n}} = F_{\text{spring,n}} + F_{\text{jkr,n}} + F_{\text{damp,n}} \tag{A.5}$$

In the tangential direction, spring and damping force contributions are taken into account through:

$$F_{\text{con,t}} = F_{\text{spring,t}} + F_{\text{damp,t}} \tag{A.6}$$

Figure A.1 gives an overview of the force contributions acting on a particle upon collision with another particle (partly shown on the left).

A.2.1 Adhesive contact between particles and a surface

Numerous approaches have been suggested to account for an adhesive force. Common for the approaches is that they rely on a surface energy density γ to describe the adhesive force. For small λ_T, the contact independent van der Waals formulation by Hamaker (1937) is used in studies such as (Kobayashi et al., 2013; Abbasfard et al., 2016; Gu et al., 2016; Chaumeil and Crapper, 2014) to account for the adhesive force. For higher λ_T (softer particles), the contact dependent adhesive JKR force proposed by Johnson et al. (1971) is used in studies such as (Marshall, 2007, 2009). In the present study, focus is on the simplified JKR model suited for DEM simulations and used in studies such as (Pasha et al., 2013; Deng et al., 2013; Parteli et al., 2014). The simplified JKR model has the same force-displacement relation as the original model, requires the same 8/9 of the critical force $F = (8/9)F_C = (8/9)3\pi R\gamma$ to break contact but assumes contact is broken as soon as the normal overlap becomes negative in the particle separation process. At equilibrium condition when the adhesive force balances the spring force, the contact radius is given by (Chokshi et al., 1993):

$$a_0 = \left(\frac{9\pi\gamma R^2}{E} \right)^{1/3} \tag{A.7}$$

as in the original JKR model. The normal spring force described by the Hertzian contact model is modified as follows due to an adhesive force:

$$\boldsymbol{F}_{jkr,n} = 4\sqrt{\pi\gamma Ea^3}\boldsymbol{n} \tag{A.8}$$

$$\boldsymbol{F}_{spring,n} = -\frac{4E}{3R}a^3\boldsymbol{n} \tag{A.9}$$

where the relation between contact radius a and normal overlap δ_n (see figure A.1) for adhesive JKR contact is given by (Deng et al., 2013; Parteli et al., 2014):

$$a^4 - 2R\delta_n a^2 - \frac{4\pi\gamma}{E}R^2 a + R^2\delta_n^2 = 0 \tag{A.10}$$

which can be solved using an iterative approach or the analytical expression derived by Parteli et al. (2014). Furthermore, a normal damping force contributes to the contact normal force by dissipating kinetic energy in the particle material:

$$\boldsymbol{F}_{damp,n} = -2\frac{5}{6}\beta\sqrt{S_n m}\boldsymbol{v}_n \tag{A.11}$$

where β accounts for the energy lost upon collision through the coefficient of restitution e while S_n takes the particle properties into account:

$$\beta = \frac{\ln(e)}{\sqrt{\ln^2(e) + \pi^2}} \tag{A.12}$$

$$S_n = 2E\sqrt{R\delta_n} \tag{A.13}$$

where m is particle mass, v_n is the relative normal velocity, and $\boldsymbol{n}$ is the normal unit vector. In the tangential direction, the spring force contribution is:

$$\boldsymbol{F}_{\text{spring,t}} = -S_t \Delta s_t \tag{A.14}$$

where Δs_t is tangential displacement between the particles and $S_t = 8G\sqrt{R\delta_n}$ with the effective shear modulus G:

$$\frac{1}{G} = \frac{2 - v_i}{G_i} + \frac{2 - v_j}{G_j} \tag{A.15}$$

Where the shear moduli for particle i,j are related to the Young's modulus through $G_i = E_i/(2(1 + v_i))$ and $G_j = E_j/(2(1 + v_j))$. Likewise, energy is dissipated in the tangential direction by a damping force:

$$\boldsymbol{F}_{\text{damp,t}} = -2\sqrt{\frac{5}{6}}\beta\sqrt{S_t m}\boldsymbol{v}_t \tag{A.16}$$

where v_t is the relative tangential velocity of the particles. In the case of adhesive contact, the tangential force is truncated to fulfil (Thornton, 1991; Thornton and Yin, 1991):

$$|\boldsymbol{F}_{\text{con,t}}| \leq \mu_s |F_N + 2F_C| \tag{A.17}$$

where μ_s is the sliding friction coefficient.

A.2.2 Adhesive rolling, sliding and twisting resistance

To predict the formation of agglomerates or particles sticking to a wall, a description of adhesive rolling plays a major role (Dominik and Tielens, 1995, 1997; Krijt et al., 2014). Due to the small particle inertia of micron-sized particles, twisting (rotation along the axis connecting two particles) and sliding (relative tangential motion without rotation) are less important than rolling, to accurately predict formation/break-up of agglomerates (Oda et al., 1982; Marshall, 2007). Therefore, focus is on the adhesive rolling behaviour and how to modify the adhesive rolling resistance model to account for the reduced particle stiffness.
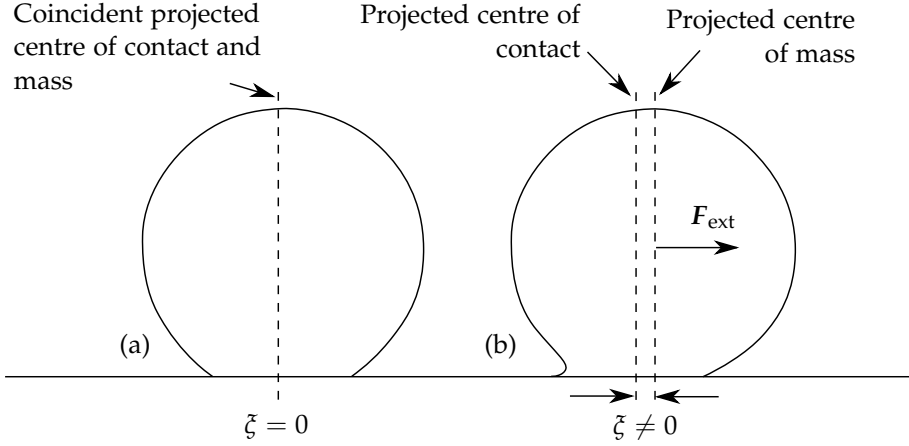
Figure A.2: Adhesive particle in contact with a wall and in normal equilibrium ($F_{jkr,n} = F_{spring,n}$): (a) Zero force applied results in particle centre of mass and centre of contact being coincident; (b) An external force applied $F_{ext} \neq 0$ results in a non-coincident projected centre of mass and centre of contact.

When a particle is in normal equilibrium with a wall, the centre of contact and projected centre of gravity are coincident, see figure A.2(a). However, when an external force F_{ext} is applied, a small shift between the centre of contact and projected centre of gravity will build up, as illustrated in figure A.2(b). The result of this asymmetric contact region is a torque M_r opposing rotation and trying to obtain the symmetric contact region as in figure A.2(a). If the particle is rolled less than a critical rolling distance ($\xi < \xi_{crit}$), the particle rolls back to obtain the same contact point when the external force is removed. However, when the particle is rolled a distance longer than the critical rolling displacement ($\xi > \xi_{crit}$), the particle is moved irreversibly. While Dominik and Tielens (1995, 1997) suggest a critical rolling displacement in the order of an atom diameter, the more recent study by Krijt et al. (2014) relates the critical rolling displacement to the equilibrium contact radius a_0 and a material dependent adhesion hysteresis parameter $\Delta\gamma/\gamma$ to obtain improved experimental agreement through:

$$\xi_{crit} = \frac{a_0}{12}\frac{\Delta\gamma}{\gamma} \tag{A.18}$$

In general as a particle rolls, the rolling displacement ξ is obtained by integrating the rolling velocity:

$$\xi = \left(\int_{t_0}^{t_1} v_L(t)dt\right) \cdot t_r \tag{A.19}$$

where the rolling velocity v_L is defined as:

$$v_L = R\left(\omega_i - \omega_j\right) \times n + \frac{1}{2}\frac{r_i - r_j}{r_i + r_j}v_S \tag{A.20}$$

which can conveniently be implemented into the DEM method by incremental changes between two successive time steps. The rolling resistance torque is then given by (Dominik and Tielens, 1995, 1997):

$$M_r = \begin{cases} k_r\xi & \text{if } \xi < \xi_{crit} \\ k_r\xi_{crit} & \text{if } \xi \geq \xi_{crit} \end{cases} \tag{A.21}$$

with rolling stiffness $k_r = 4F_C\left(a/a_0\right)^{3/2}$. As the rolling displacement ξ cannot exceed the critical rolling displacement ξ_{crit}, the rolling displacement is numerically truncated to fulfil:

$$|\xi| \leq |\xi_{crit}| \tag{A.22}$$

A.3 Reduced Particle Stiffness

A.3.1 Modified adhesive JKR model for reduced particle stiffness

When a reduced particle stiffness is introduced in DEM simulations, the particles will inevitably overlap more during collision. If the surface energy density γ is left unchanged, the result is a more adhesive collision as the kinetic energy lost upon collision is increased significantly. Therefore, a reduced particle stiffness has to be balanced by a reduced surface energy density for the outcome of the collision to remain the same. For the separation energy required to separate two particles in contact to remain constant, the following criterion has to be fulfilled:

$$\int_0^{\delta_{n,0}} \left(F_{jkr} + F_{spring} \right) d\delta_n =$$
$$\int_0^{\delta_{n,0,mod}} \left(F_{jkr,mod} + F_{spring,mod} \right) d\delta_n \tag{A.23}$$

where $\delta_{n,0} = (1/3)a_0^2/R$ is the normal overlap at equilibrium. Inserting expressions for F_{jkr} and F_{spring} from equation (B.9) and (B.8) with the contact radius given by equation (B.11) into equation (A.23) gives an expression for the modified surface energy density as a result of modified effective Young's modulus:

$$\gamma_{mod} = \gamma \left(\frac{E_{mod}}{E} \right)^{2/5} \tag{A.24}$$

Details on how this derived from (A.23) are given in appendix A. The result in (A.24) is actually the same criterion Gu et al. (2016) found for the contact independent van der Waals formulation (Hamaker, 1937) $F_{vdW} = A_H R/(6D_{min}^2)$ with the effective Hamaker constant $A_H = 24\pi D_{min}^2 \gamma$. Figure A.3 shows a comparison of the original JKR model, the JKR model with reduced particle stiffness and the JKR model with reduced particle stiffness and reduced surface energy density using equation (A.24). As the figure shows, by only reducing the particle stiffness (by the Young's modulus E) the same force ($F_N = -(8/9)F_C$) is required to break contact. However, the equilibrium overlap is increased significantly as $\delta_{n,0,mod} = (1/3)a_{0,mod}^2/R = (3\pi^2\gamma^2 R/E_{mod}^2)^{1/3}$. By reducing both the stiffness and adhesiveness (by the surface energy density γ) using equation (A.24), the force-displacement relation is changed so that the separation energy remains the same as in the original model. The result is a higher overlap distances during collision and consequently larger time step sizes. However, the normal force required to break contact is reduced to
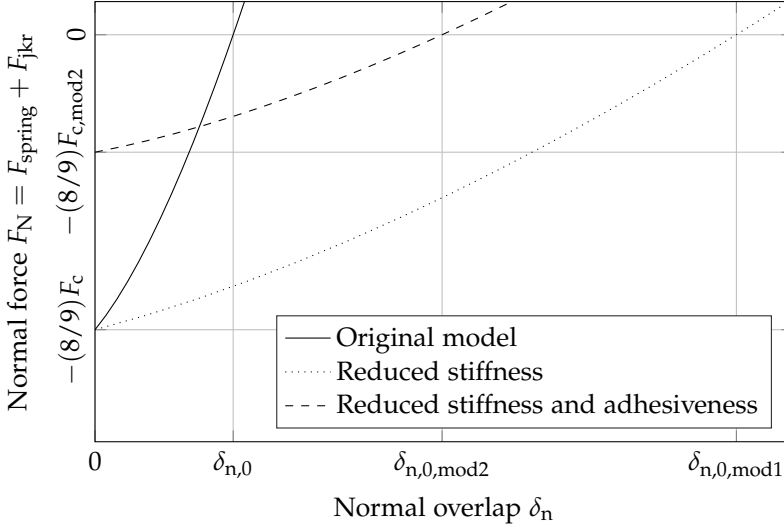
Figure A.3: Comparison of force-displacement relations using the original JKR model and different modified versions: —— Original Hertz and JKR model (Johnson et al., 1971); · · · · · · Reduced Young's modulus but unaltered surface energy density; - - - - Reduced Young's modulus and modified surface energy density given by the criterion in equation (A.24).

$F_N = -(8/9)F_{C,mod} = -(8/9)3\pi R\gamma_{mod}$. This can pose some impracticalities for systems with large external forces acting to separate the particles. This is discussed further in section A.6.

A.3.2 Modified adhesive rolling torque model for reduced particle stiffness

In the prediction of particle deposition, the adhesive rolling resistance model acts to stop particles from rolling on a surface even when a constant external force is applied parallel to the surface. When introducing a reduced particle stiffness model, it is important that the particles will deposit predicted by the original model.

When a reduced particle stiffness is introduced in the rolling torque model, the equilibrium contact radius a_0 in (A.7) is increased. As a consequence, the critical rolling displacement distance in (A.18) is increased as well causing particles to roll a longer distance before beginning to roll irreversibly with constant rolling resistance torque opposing rolling. This is shown in figure A.4, which shows the rolling torque on particles in normal equilibrium with a surface ($a = a_0$) affected by constant external force. Likewise, if both the particle stiffness and adhesiveness are reduced using (A.24), both the critical rolling distance and the critical rolling torque are changed as
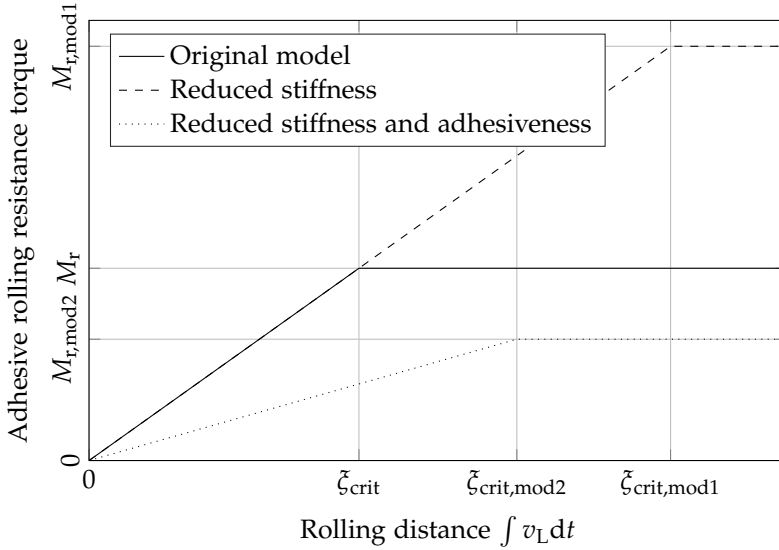
Figure A.4: Comparison of torque-rolling distance relations using the original JKR model and different modified versions: —— Original adhesive rolling resistance torque model by (Dominik and Tielens, 1995, 1997; Krijt et al., 2014); · · · · · · Reduced Young's modulus but unaltered surface energy density; - - - - Reduced Young's modulus and modified surface energy density given by the criterion in equation (A.24).

shown in figure A.4 as well.

Therefore, the only way to retain the behaviour of the original model is to keep all terms but the $(a/a_0)^{3/2}$ term unaltered. The $(a/a_0)^{3/2}$ term is modified to include modified values for the instantaneous and equilibrium contact radii, so that $(a/a_0)^{3/2}$ is replaced by $(a_{\text{mod}}/a_{0,\text{mod}})^{3/2}$.

In that way, particles have the same behaviour when in normal equilibrium with a surface as in the original model but uses modified values before equilibrium is established. It should be noted that as a natural consequence of introducing a reduced particle stiffness, the particles will travel longer distances upon collision due to the changed force-displacement relation, see figure A.3. When collisions with a plane wall at an oblique angle are considered, the result is particles travelling a slightly longer distance before coming to rest. However, this is typically not of importance in DEM simulations involving many particles.

A.4 Validation by Experimental Data

Collisions of small spheres have been studied thoroughly. At sufficiently low impact velocities, the collisions are dominated by adhesive forces in the

contact region resulting in sticking behaviour, where the effective coefficient of restitution e_{eff} is zero. At higher impact velocities when the particles are unable to stick, the effective coefficient of restitution increases rapidly with increasing impact velocity. At sufficiently high velocities where the collisions become increasingly unaffected by adhesive forces, the effective coefficient of restitution approaches the coefficient of restitution e.

In the following, simulation results obtained by integrating (A.3) for both non-modified and modified stiffness using (A.24) are compared to experimental data presented by Dahneke (1975). As noted by Krijt et al. (2013), expected collision outcomes typically differ slightly from experiments as even small imperfections in particle or wall material result in a non-perfect collision. Therefore, the fitted values suggested by Krijt et al. (2013) are used when comparing to experiments. Figure A.5 shows how the simulation results with both non-modified and modified stiffnesses compare to experimental data.

Figure A.5 shows that the DEM methodology described above is capable of predicting the effective coefficient of restitution. Furthermore, by reducing the particle stiffness from E to E_{mod} and modifying the surface energy density by analytical solution in (A.24), the exact same results are indeed obtained. More details on how introducing softer particles allows for a higher time step size are given in section A.6.

A.5 Test Cases

A.5.1 Dimensionless quantities

To generalise the analysis, particle properties are reported based on a set of dimensionless quantities that control different aspects of the adhesion and rolling processes, which ultimately govern the agglomeration and deposition processes. Based on the effective Young's modulus E, effective radius R, relative particle velocity before impact v, particle density ρ_{p}, collision angle ψ, and coefficient of restitution e, the adhesion process is fully described. The above mentioned parameters form three governing parameters: an elasticity parameter describing the ratio between particle stiffness and particle inertia $\lambda = E/(\rho_{\text{p}}v^2)$, an adhesiveness parameter describing the ratio between particle adhesiveness and particle inertia $\text{Ad} = 3\gamma/(\rho_{\text{p}}v^2 r_{\text{i}}) \cdot (1+\beta^3)/((1+\beta^2)\beta)$ (Chen et al., 2015), and the effective coefficient of restitution describing the ratio between relative velocity after collision (subscript f) and before collision $e_{\text{eff}} = (v_{\text{i,f}} - v_{\text{j,f}})/(v_{\text{j}} - v_{\text{i}})$. To describe the effect of adhesiveness on the collision, the coefficient of restitution is reported as a scaled value between 0 and 1, giving the ratio between the effective and the non-adhesive coefficient of restitution $\hat{e} = e_{\text{eff}}/e$. In the case of collision with a wall
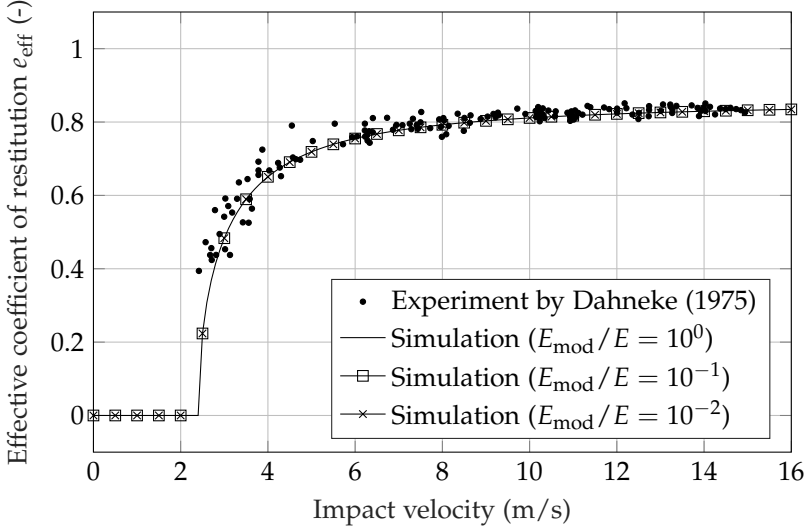
Figure A.5: Comparison to experiment by Dahneke (1975) with PSL spheres colliding with a plane wall of polished quartz. Collision properties are $d_p = 1.27$ μm, $E = 271$ MPa, $\gamma = 0.11$ J/m^2, $\rho_p = 1026$ kg/m^3 and $e = 0.86$ (fitted to experimental data at high velocities), see Krijt et al. (2013) and supplementary online material for collision properties. When a reduced particle stiffness is introduced in the simulations, the surface energy density is modified using the criterion proposed in (A.24).

at an oblique angle ψ, the collision angle is accounted for in the elasticity parameter and adhesiveness parameter, so that $\lambda = E / \left(\rho_p v^2 \sin^2 \psi \right)$ and $\text{Ad} = 3\gamma / (\rho_p v^2 \sin^2(\psi) r_i) \cdot (1 + \beta^3) / ((1 + \beta^2)\beta)$. In the case of particle-wall collisions, the adhesiveness parameter reduces to $\text{Ad} = 3\gamma / (\rho_p v^2 \sin^2(\psi) r_p)$, where r_p is the particle radius.

To describe adhesive rolling, the adhesion hysteresis parameter $\Delta\gamma/\gamma$ is used as well. To describe adhesion followed by rolling on a plane wall, the external force is made non-dimensional by the yield force required to overcome the critical rolling resistance torque, forming $\hat{F} = F_{\text{ext}}/F_{\text{yield}}$, where $F_{\text{yield}} = M_r/R$. In the case of normal equilibrium $a = a_0$, the yield force reduces to $F_{\text{yield}} = 4F_C a_0(\Delta\gamma/\gamma)/12$. That is, $\hat{F} < 1$ describes processes where particles eventually come to a halt due to adhesive forces in the contact region. Likewise, $\hat{F} \geq 1$ describes rolling processes where particles will keep rolling regardless of the adhesive rolling resistance torque. The effective coefficient of restitution e_{eff} of an adhesive collision processes is generally lower than that of a non-adhesive collision e.
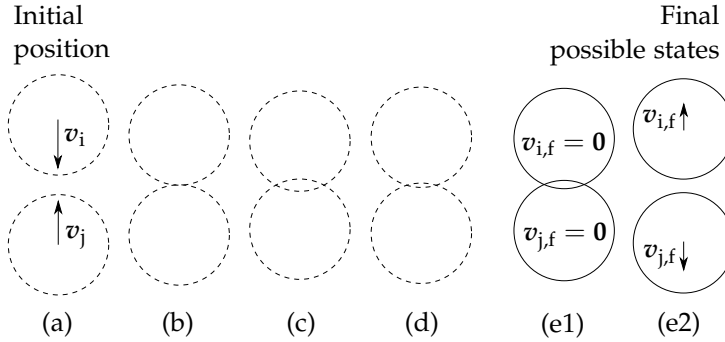
Figure A.6: Overview of the different stages of a particle-particle collision: (a) Particles approaching each other; (b) Just prior to contact the particles are still unaffected and move with velocity v; (c) particles reach maximum normal overlap δ_n; (d) Particles begin to separate; (e1-e2) Depending on the strength of the adhesive force the particles will either remain in contact (e1) or separate completely (e2).

A.5.2 Binary adhesive collision

Binary particle collisions are encountered in most problems being solved using the DEM method. Therefore it is important that the model proposed for reduced particle stiffness simulations yields similar results for particle collisions. This is investigated in the following with figure A.6 giving an overview of the head-on particle-particle collision being simulated to validate the proposed model. By varying the elasticity parameter λ and the adhesiveness parameter Ad, the particles either stay attached, as in figure A.6(e1), or separate with velocity v_f as in figure A.6(e2). Figure A.7 shows how variations in elasticity parameter at different adhesiveness parameter affect the effective coefficient of restitution. The figure shows how the particles stay attached below a certain critical elasticity parameter. This critical elasticity parameter depends on the adhesiveness parameter and increases with increasing adhesiveness parameter. As the results show, decreasing the particle stiffness does, in most cases, result in a different effective coefficient of restitution. The exception is at sufficiently low elasticity parameters, where the particle stay attached upon collision. Furthermore, the figure shows that as long as $e_{\mathrm{eff}}/e \approx 1$, corresponding to high elasticity parameters, the elasticity parameter can be reduced with only small changes in effective coefficient of restitution as the collision behaves as non-adhesive.

Figure A.8 shows how using the criterion in (A.24) makes the effective coefficient of restitution independent of changes in elasticity parameter from a base value $\lambda = 10^6$. As figure A.8 shows, the effective coefficient of restitution e_{eff}/e retains the values from $\lambda = 10^6$ in figure A.7 when the elasticity parameter is changed at various adhesiveness values. Even though the stiffness of particles undergoing binary particle-particle collisions can be greatly
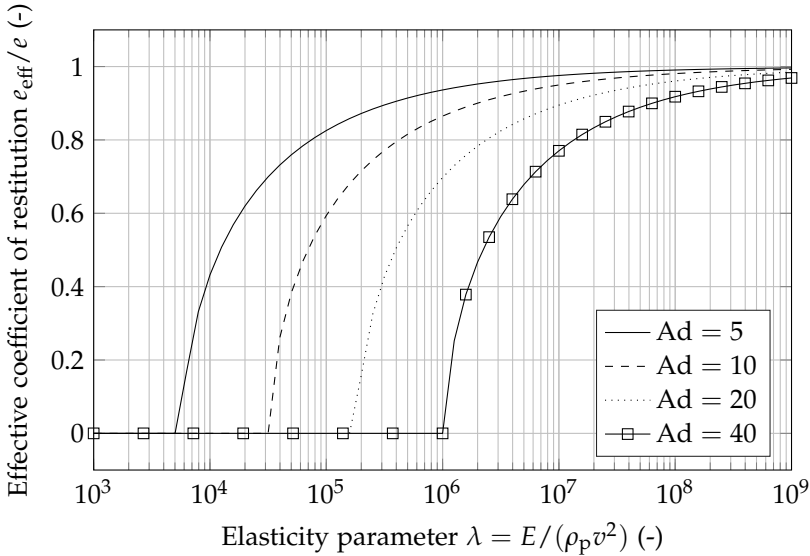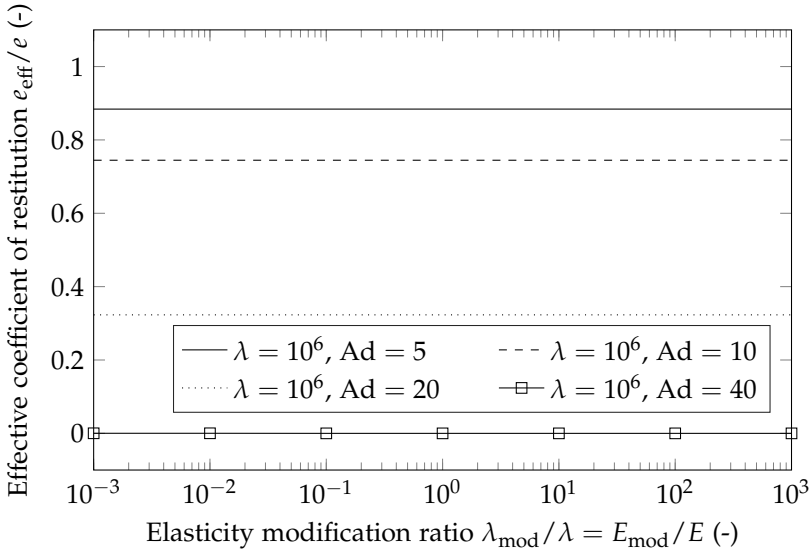
Figure A.7: Numerical simulations showing head-on particle-particle adhesive collisions by the non-modified model showing the effective coefficient of restitution as function of the elasticity parameter at various adhesive parameters $\text{Ad} = \gamma/(\rho_p v^2 R)$ for a coefficient of restitution $e = 0.3$.

reduced, studies by Kobayashi et al. (2013) and Gu et al. (2016) show that collisions involving larger agglomerates behave differently when the particle stiffness is reduced beyond a certain point. In this study, this phenomenon is addressed in the following section where particle deposition on both a clean surface and a surface with an initial layer of particles is investigated.

A.5.3 Deposition on a plane surface

Most problems being solved using DEM involve particles colliding with a plane surface. This case is different from the previous head-on particle collisions as particles may roll on the surface or other particles and eventually come to rest due to adhesive rolling resistance torque described by equation (B.19). Therefore, this section is focused on the validity of the proposed model for particles with reduced stiffness colliding with a plane surface. Figure A.9 gives an overview of the oblique angle particle-wall collision process investigated. As the figure shows, three possible outcomes are expected as collision parameters are varied: rebound behaviour, particle deposition followed by rolling motion and particle deposition where the particle rolls a certain distance before coming to a halt. For most DEM simulations of particulate deposition, it is important that the outcome (rebound, rolling or sticking) remains the same when the particle stiffness is reduced. Simu-

Figure A.8: Numerical simulation showing head-on particle-particle adhesive collisions showing how the effective coefficient of restitution remains constant when the particle stiffness is reduced (or increased) when the surface energy density is changed using the criterion proposed in (A.24). Again, results are shown for coefficient of restitution $e = 0.3$.
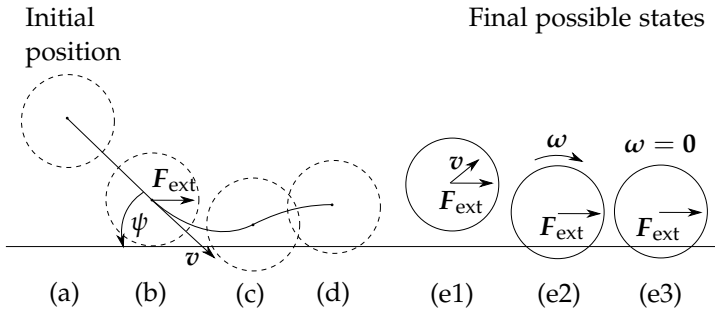
Figure A.9: Overview of the different stages of the particle-wall collision: (a) The particle moving towards the wall; (b) Just prior to contact the particle is still unaffected by the wall and moves with velocity v at an angle ψ to the wall while affected by an external fluid/gravity force F_{ext}; (c)-(d) Particle in contact with the wall. If the particle stay in contact with the wall, the normal equilibrium is established here; (e1-e3) The particle will either rebound and move away from the surface (e1), stay at the surface but keep rolling with a constant angular velocity $\omega \neq 0$ (e2) or stay in place as a result of adhesiveness with shifted centre of contact and centre of mass $\omega = 0$ (e3), see figure A.2(b).

lations of particles colliding with a wall at oblique angles $\psi \in \,]0; \pi/2]$ were done. The three possible outcomes are located as shown in the dimensionless map in figure A.10, where elasticity and adhesiveness parameter are modified to account for the collision angle ψ so that: $\lambda = E/(\rho_{\text{p}} v^2 \sin^2 \psi)$ and
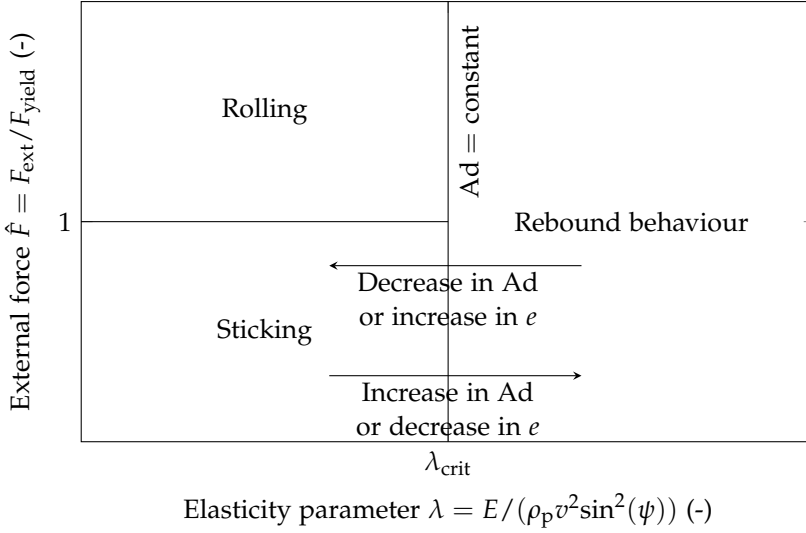
Figure A.10: The three possible outcomes of an adhesive collision with a plane wall and the effect of increasing/decreasing adhesiveness parameter $\text{Ad} = 3\gamma/(\rho_p v^2 \sin^2(\psi) r_p)$ and coefficient of restitution e. The particle is affected by a constant external force F_{ext} parallel to the wall (see figure A.9) and the yield force is given by $F_{\text{yield}} = 4F_C a_0 (\Delta\gamma/\gamma)/12$.

$\text{Ad} = 3\gamma/(\rho_p v^2 \sin^2(\psi) r_p)$. A high elasticity parameter, high coefficient of restitution or low adhesiveness parameter will all inherently cause the particles to rebound. When the particles stay attached to the wall, the external force $\hat{F}$ dictates if the particles stay in place due to adhesiveness ($\hat{F} < 1$) or keep rolling ($\hat{F} \geq 1$).

To find the critical elasticity parameter causing particles to rebound from figure A.10, the bisection algorithm is used with convergence criterion $|\delta_n/r_p| = 10^{-7}$. Figure A.11 shows the critical elasticity parameter as function of adhesiveness parameter at various coefficients of restitution. All the lines of constant coefficient of restitution in figure A.11 follow the equation:

$$\lambda_{\text{crit}} = c \cdot \text{Ad}^{5/2} \tag{A.25}$$

where the value of c is solely a function of the coefficient of restitution e as shown in figure A.12. That is, the above equation can be used to find the critical elasticity parameter giving the border between rebound and sticking behaviour.
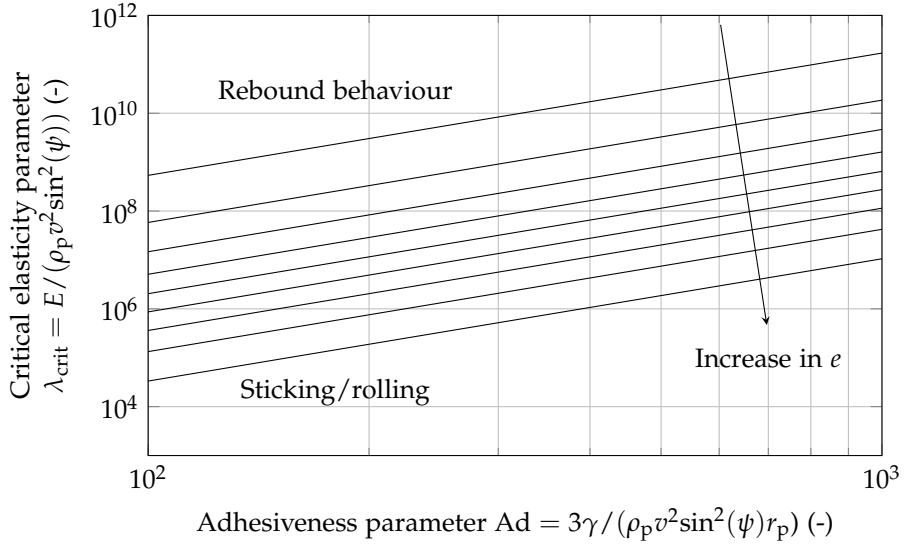
Figure A.11: The critical elasticity parameter describing the border between sticking/rolling and rebound behaviour from figure A.10. Lines indicate increasing coefficient of restitution e from 0.1 to 0.9 at intervals of 0.1 as indicated by the arrow.
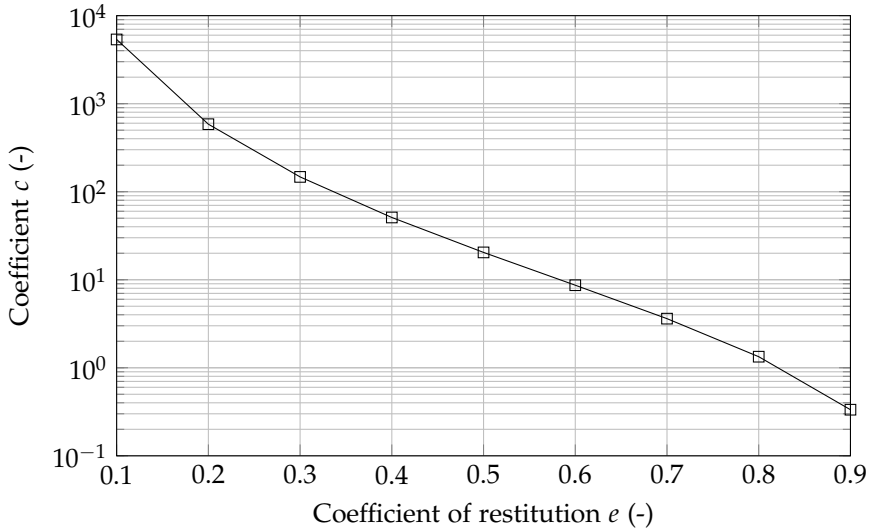
Figure A.12: Coefficient c in equation (A.25) as function of coefficient of restitution e.

A.6 Summary and Discussion

A.6.1 Summary

A method has been presented for reducing the particle stiffness for DEM simulations using a Hertzian approach to predict collisions of adhesive micronsized particles for which the adhesive model by Johnson-Kendall-Roberts (JKR) model is applicable. The following conclusions can be drawn:

- When using the simplified JKR model (equation (B.9)), the particle Young's modulus can be reduced from E to E_{mod} as long as the surface energy density is reduced as well using $\gamma_{mod} = \gamma(E_{mod}/E)^{2/5}$. That way, the border between sticking and rebounding behaviour remains the same when the particle stiffness is reduced.

- To use the rolling resistance model by Dominik and Tielens (1995, 1997); Krijt et al. (2014) (equation (A.18) to (A.22)) for reduced particle stiffness simulations, only the term $(a/a_0)^{3/2}$ should be changed to use modified values. That way, the border between rolling and sticking remains the same. As a natural result of the reduced particle stiffness, the particles will travel a longer distance before the equilibrium condition is reached.

A.6.2 Discussion on computational time and limitations

As the particle stiffness is reduced, the time step size can be greatly increased. Figure A.13 shows the velocity during a collision of a small PSL sphere impacting a polished quartz surface, corresponding to the experiment by Dahneke (1975).

As the figure shows, the separation velocity is unaffected by a change in particle stiffness when the surface energy density is modified using (A.24). However, the particle collision process now takes place over significantly longer time periods. When resolving a collision over fixed number of time steps (Silbert et al. (2001) suggests $\Delta t_{col}/\delta t \approx 50$), the time step size can now be greatly increased. By looking at how the collision time Δt_{col} scales with a reductions in particles stiffness, it is found that $\Delta t_{col,mod} = \Delta t_{col}(E/E_{mod})^{2/5}$, see figure A.13. This criterion can be used to estimate the possible speed-up for adhesive DEM simulations when introducing a reduced particle stiffness.

As a consequence of a reduced particle stiffness, the critical force required to separate two agglomerated particles is reduced as well. This fact is important when simulating particles in flow or magnetic fields where local external forces on particles can be strong. A such example could be a strong shear flow field. Therefore, care should be taken when introducing reduced particle stiffness to make sure that the critical force $F_C = 3\pi R\gamma_{mod}$ still remains
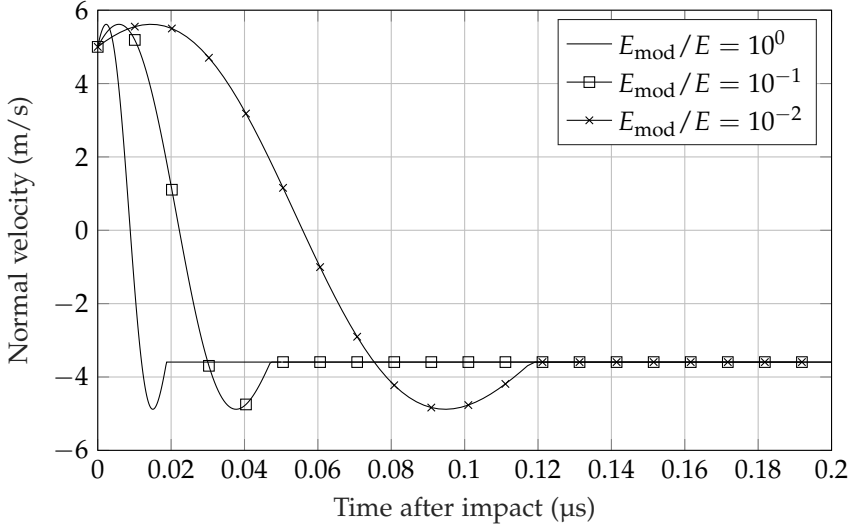
Figure A.13: Velocity as function of time during a collision for a PSL sphere colliding with a polished quartz wall with an impact velocity of 5 m/s. When the particle stiffness is reduced from $E_{mod}/E = 10^0$ to $E_{mod}/E = 10^{-1}$ and $E_{mod}/E = 10^{-2}$, the surface energy density is modified using the criterion proposed in (A.24).

significantly higher than typical external forces trying to separate the particles.

Additionally, it should be noted that for collisions involving many particles with a local volume fraction approaching the closed-pack solution, the adhesive behaviour might be changed slightly if the particle stiffness is reduced too much, $E_{mod}/E < 10^{-3}$ (Kobayashi et al., 2013; Gu et al., 2016).

Acknowledgement

Appendix A. Details on Derivation of the Criterion in (A.24)

Instead of deriving (A.24) from (A.23) directly, we use integration by substitution to rewrite (A.23) in terms of contact radius a instead of normal

126

overlap δ_n:

$$\int_{a(\delta_n=0)}^{a(\delta_n=\delta_{n,0})} \left(F_{jkr} + F_{spring} \right) da =$$
$$\int_{a(\delta_n=0)}^{a(\delta_n=\delta_{n,0,mod})} \left(F_{jkr,mod} + F_{spring,mod} \right) da \tag{A.26}$$

Next, expressions for the contact radius at $\delta_n = 0$, $\delta_n = \delta_{n,0}$ and $\delta_n = \delta_{n,0,mod}$ are found. The contact radius at zero-overlap is found by isolating a in (B.11) with $\delta_n = 0$:

$$a^4 - 2R\delta_n a^2 - \frac{4\pi\gamma}{E} R^2 a + R^2 \delta_n^2 = 0 \tag{A.27}$$

The two real roots are:

$$a_1 = 0 \tag{A.28}$$

$$a_2 = \left(\frac{4\pi\gamma R^2}{E} \right)^{1/3} \tag{A.29}$$

Here we are interested in the non-zero root a_2, which is the lower limit of the integrals in (A.26):

$$a(\delta_n = 0) = \left(\frac{4\pi\gamma R^2}{E} \right)^{1/3} \tag{A.30}$$

The upper limits for a at $\delta_n = \delta_{n,0}$ and a at $\delta_n = \delta_{n,0,mod}$ are the equilibrium contact radius given directly by (A.7):

$$a(\delta_n = \delta_{n,0}) = \left(\frac{9\pi\gamma R^2}{E} \right)^{1/3} \tag{A.31}$$

$$a(\delta_n = \delta_{n,0,mod}) = \left(\frac{9\pi\gamma_{mod} R^2}{E_{mod}} \right)^{1/3} \tag{A.32}$$

Next, we look for an expression for $d\delta_n$. First, we derive an expression for $\delta_n(a)$ using (B.11). We obtain two solutions:

$$\delta_{n,1} = \frac{Ea^2 + 2R\sqrt{E\gamma a\pi}}{ER} \tag{A.33}$$

$$\delta_{n,2} = \frac{Ea^2 - 2R\sqrt{E\gamma a\pi}}{ER} \tag{A.34}$$

Here only the solution in (A.34) fulfills the criteria in (A.30) and (A.31). Next, we find the derivative $d\delta_n/da$ using (A.34) and isolate for $d\delta_n$:

$$d\delta_n = \left(\frac{2a}{R} - \frac{2\sqrt{\gamma\pi}}{\sqrt{Ea}} \right) da \tag{A.35}$$

Carrying out the integral in (A.26) with the limits given by (A.30), (A.31) and (A.32) and inserting the expression for $\mathrm{d}\delta_\mathrm{n}$ from (A.35), we obtain:

$$\frac{\gamma^{5/3}}{E^{2/3}} = \frac{\gamma_\mathrm{mod}^{5/3}}{E_\mathrm{mod}^{2/3}} \tag{A.36}$$

which reduces to the expression in (A.24).

Bibliography

Hamad Abbasfard, Geofferey Evans, and Roberto Moreno-Atanasio. Effect of van der waals force cut-off distance on adhesive collision parameters in dem simulation. *Powder Technology*, 299:9–18, 2016. URL `http://dx.doi.org/10.1016/j.powtec.2016.05.020`.

E. Barthel. Adhesive elastic contacts: Jkr and more. *Journal of Physics D: Applied Physics*, 41:163001 (20pp), 2008. URL `http://dx.doi.org/10.1088/0022-3727/41/16/1630`.

Florian Chaumeil and Martin Crapper. Using the dem-cfd method to predict brownian particle deposition in a constrained tube. *Particuology*, 15:94–106, 2014. URL `http://dx.doi.org/10.1016/j.partic.2013.05.005`.

Sheng Chen, Shuiqing Li, and Mengmeng Yang. Sticking/rebound criterion for collisions of small adhesive particles: Effects of impact parameter and particle size. *Powder Technology*, 274:431–440, 2015. URL `http://dx.doi.org/10.1016/j.powtec.2015.01.051`.

Arati Chokshi, A. G. G. M. Tielens, and D. Hollenbach. Dust coagulation. *The Astrophysical Journal*, 407:806–819, 1993. URL `http://dx.doi.org/10.1086/172562`.

Barton Dahneke. Further measurements of the bouncing of small latex spheres. *Journal of Colloid and Interface Science*, 51:58–65, 1975. URL `http://doi.org/10.1016/0021-9797(75)90083-1`.

Xiaoliang Deng, James V. Scicolone, and Rajesh N. Davé. Discrete element method simulation of cohesive particles mixing under magnetically assisted impaction. *Powder Technology*, 243:96–109, 2013. URL `http://dx.doi.org/10.1016/j.powtec.2013.03.043`.

B. V. Derjaguin, V. M. Muller, and YU. P. Toporov. Effect of contact deformations on the adhesion of particles. *Journal of Colloid and Interface Science*, 53:314–356, 1975. URL `http://dx.doi.org/10.1016/0079-6816(94)90044-2`.

C. Dominik and A.G.G.M Tielens. Resistance to rolling in the adhesive contact of two elastic spheres. *Philosophical Magazine A*, 72:783–803, 1995. URL `http://dx.doi.org/10.1080/01418619508243800`.

C. Dominik and A.G.G.M Tielens. The physics of dust coagulation and the structure of dust aggregates in space. *The Astrophysical Journal*, 480:647–673, 1997. URL `http://dx.doi.org/10.1086/303996`.

Yile Gu, Ali Ozel, and Sankaran Sundaresan. A modified cohesion model for cfd-dem simulations of fluidization. *Powder Technology*, 296:17–28, 2016. URL `http://dx.doi.org/10.1016/j.powtec.2015.09.037`.

H.C. Hamaker. The london — van der waals attraction between spherical particles. *Physica*, 4:1058–1072, 1937. URL `http://dx.doi.org/10.1016/S0031-8914(37)80203-7`.

Christophe Henry, Jean-Pierre Minier, and Grégory Lefévre. Towards a description of particulate fouling: From single particle deposition to clogging. *Advances in Colloid and Interface Science*, 185–186:34–76, 2012. URL `http://dx.doi.org/10.1016/j.cis.2012.10.001`.

J.N. Israelachvili. *Intermolecular and Surface Forces*. Academic Press, 2. edition, 1992. ISBN: 978-0-12-375182-9.

K.L. Johnson and J.A. Greenwood. An adhesion map for the contact of elastic spheres. *Journal of Colloid and Interface Science*, 192:326–333, 1997. URL `http://doi.org/10.1006/jcis.1997.4984`.

K.L. Johnson, K. Kendall, and A.D. Roberts. Surface energy and the contact of elastic solids. *Proc. R. Soc. Lond.*, 324:301–313, 1971. URL `http://dx.doi.org/10.1098/rspa.1971.0141`.

Tomonari Kobayashi, Toshitsugu Tanaka, Naoki Shimada, and Toshihiro Kawaguchi. Dem-cfd analysis of fluidization behavior of geldart group a particles using a dynamic adhesion force model. *Powder Technology*, 248:143–152, 2013. URL `http://dx.doi.org/10.1016/j.powtec.2013.02.028`.

S. Krijt, G. Güttler, D. Heißelmann, C. Dominik, and A. G. G. M. Tielens. Energy dissipation in head-on collisions of spheres. *Journal of Physics D: Applied Physics*, 46:435303, 2013. URL `http://doi.org/10.1088/0022-3727/46/43/435303`.

S. Krijt, C. Dominik, A.G.G.MC. Dominik, and A.G.G.M Tielens. Rolling friction of adhesive microspheres. *Journal of Physics D: Applied Physics*, 47:175302 (9pp), 2014. URL `http://dx.doi.org/10.1088/0022-3727/47/17/175302`.

J.S. Marshall. Particle aggregation and capture by walls in a particulate aerosol channel flow. *Aerosol Science*, 38:333–351, 2007. URL `http://dx.doi.org/j.jaerosci.2007.01.004`.

J.S. Marshall. Discrete-element modelling of particulate aerosol flows. *Journal of Computational Physics*, 228:1541–1561, 2009. URL `http://dx.doi.org/j.jcp.2008.10.035`.

Daniel Maugis. Adhesion of spheres: The jkr-dmt transition using a dugdale model. *Journal of Colloid and Interface Science*, 150:243–269, 1992. URL `http://doi.org/10.1016/0021-9797(92)90285-T`.

Masanobu Oda, Junichi Konishi, and SiavoucheNemat-Nasser. Experimental micromechanical evaluation of strength of granular materials: Effects of particle rolling. *Mechanics of Materials*, 1:269–283, 1982. URL `http://doi.org/10.1016/0167-6636(82)90027-8`.

Eric J. R. Parteli, Jochen Schmidt, Christina Brümel, Karl-Ernst Wirth, Wolfgang Peukert, and Thorsten Pöschel. Attractive particle interaction forces and packing density of fine glass powders. *Nature Scientific Reports*, 4:1–7, 2014. URL `http://dx.doi.org/10.1038/srep06227`.

M. Pasha, C. Hare, A. Hassanpour, and M. Ghadiri. Analysis of ball indentation on cohesive powder beds using distinct element modelling. *Powder Technology*, 233:80–90, 2013. URL `http://dx.doi.org/10.1016/j.powtec.2012.08.017`.

Leonardo E. Silbert, Deniz Ertas, Gary S. Grest, Thomas C. Halsey, Dov Levine, and Steven J. Plimpton. Granular flow down an inclined plane: Bagnold scaling and rheology. *Physical Review*, page 051302, 2001. URL `http://dx.doi.org/10.1103/PhysRevE.64.051302`.

D. Tabor. Surface forces and surface interactions. *Journal of Colloid and Interface Science*, 58:2–13, 1977. URL `http://dx.doi.org/10.1016/0021-9797(77)90366-6`.

C. Thornton. Interparticle sliding in the presence of adhesion. *Journal of Physics D: Applied Physics*, 24:1942–1946, 1991. URL `http://doi.org/10.1088/0022-3727/24/11/007`.

C. Thornton and K.K. Yin. Impact of elastic spheres with and without adhesion. *Powder Technology*, 65:153–166, 1991. URL `http://dx.doi.org/10.1016/0032-5910(91)80178-L`.

Y. Tsuji, T. Kawaguchi, and T. Tanaka. Discrete element simulation of two-dimensional fluidized bed. *Powder Technology*, 77:79–87, 1993. URL `http://dx.doi.org/10.1016/0032-5910(93)85010-7`.

Nomenclature

Ad	adhesiveness parameter (-)
A_H	effective Hamaker constant (J)
a	contact radius (m)
d_p	particle diameter (m)
D_{min}	minimum separation distance (m)
E (no subscripts)	effective Young's modulus (Pa)
E_i, E_j	Young's modulus for particle i, j (Pa)
e	coefficient of restitution (-)
$\boldsymbol{F}$	force (N)
F_C	critical force (N)
I	particle moment of inertia (kg m^2)
k	spring constant (N m^{-1})
k_r	rolling stiffness (N)
M	particle torque (Nm)
m (no subscripts)	effective particle mass (kg)
m_i, m_j	particle mass for particle i, j (kg)
$\boldsymbol{n}$	normal unit vector (-)
R	effective particle radius (m)
r_p	particle radius (m)
r_i, r_j	particle radius for particle i,j (m)
S	damping force coefficient (kg s^{-2})
t	time (s)
$\boldsymbol{v}$	relative velocity (m s^{-1})
$\boldsymbol{v}_L$	relative rolling velocity (m s^{-1})
$\boldsymbol{v}_S$	slip velocity (m s^{-1})
$\boldsymbol{x}$	particle position (m)

Greek letters

β	coefficient used for damping force (-)
$\Delta\gamma/\gamma$	adhesion hysteresis value (-)
Δt_{col}	time period for oscillations or collision (s)

δt	collision time step size (s)
δs_{t}	tangential displacement (m)
δ_{n}	normal overlap (m)
γ	surface energy density (J m^{-2})
λ	elasticity parameter (-)
λ_{T}	Tabor parameter (-)
μ_{s}	sliding friction coefficient (-)
ν	Poisson's ratio (-)
ϕ	adhesiveness parameter (-)
ρ_{P}	particle density (kg m^{-3})
ψ	collision angle (-)
ω	particle angular velocity (s^{-1})
ξ	rolling displacement (m)

Subscripts

0	equilibrium condition
ad	adhesive
crit	critical
con	contact
damp	damping
eff	effective
ext	external
f	final
mod	modified values
i	particle i
j	particle j
n	normal direction
r	rolling resistance
t	tangential direction
vdW	van der Waals

Acronyms

DEM	Discrete Element Modelling
DMT	Derjaguin-Muller-Toporov model
JKR	Johnson-Kendall-Roberts model

Appendix B

Early stages of agglomeration and deposition of adhesive micron-sized particles in fully-developed turbulent pipe flows

J. Hærvig, K. Sørensen, T.J. Condra

The layout has been revised.

Early stages of agglomeration and deposition of adhesive micron-sized particles in fully-developed turbulent pipe flows

J. Hærvig, K. Sørensen, T.J. Condra

Aalborg University, Department of Energy Technology, Pontoppidanstræde 111, DK-9220 Aalborg, Denmark

Abstract

This study presents numerical results on how micron-sized adhesive particles agglomerate and deposit in fully-developed turbulent pipe flows. Particle-particle and particle-wall interactions are modelled using the mechanistically-based soft-sphere Discrete Element Method (DEM) and fluid turbulence is resolved using Large Eddy Simulations (LES). In this study, the adhesive behaviour of particles, ultimately resulting in agglomeration and deposition of particles, is predicted using JKR theory.

In this study, the agglomerating behaviour of mono-sized particles with constant volume fraction $\phi = 0.001$ in turbulent flows with $Re = U \cdot D / \nu = 10,000$ is investigated. By varying the Stokes number $St = \rho_p d_p^2 U / (18 \mu D)$ in the range 0.4 to 25.6, the study presents results on how changes in dominant collision mechanism affect the agglomeration rate. The results show highest agglomeration rate for intermediate Stokes numbers where the accelerative-correlated collision mechanism is dominant. At either extreme of lower or higher Stokes number, the agglomeration rate is decreased. Furthermore, at low Stokes numbers, the radial particle concentration is almost uniform throughout the flow field. At higher Stokes numbers, particles tend to accumulate either accumulate in the centre of the pipe or deposit on the wall.

Furthermore, to investigate the transition from weakly adhesive particles to highly adhesive particles, the non-dimensional adhesiveness parameter $Ad = \gamma / (\rho_p U^2 d_p)$ is varied at constant elasticity parameter $\lambda = E / (\rho_p U^2)$ and coefficient of restitution e. The results show a sharp increase in agglomeration rate and fraction of particles captured by the wall.

B.1 Introduction

The transport, agglomeration and subsequently deposition of small adhesive particles play important roles in many industrial and fundamental processes. These processes range from particles accumulating at heat transfer surfaces,

particles blocking pores in membrane filtration systems, particles being inhaled and deposited in our lungs to interstellar medium agglomerating causing early stages of new planets to form in space.

All agglomeration and deposition processes are a result of particles colliding with one another or a wall. The mechanisms governing particle collisions of non-adhesive particles in turbulent flows have been devoted much attention in literature. These studies date back to Saffman and Turner (1956) who investigated the collision frequency in isotropic turbulent flows in the limiting case of finite size tracer particles with response times much lower than the fluid response time $\tau_\mathrm{p} \ll \tau_\mathrm{f}$ and Abrahamson (1975) who investigated the collision frequency in the other limiting case of heavy particles with $\tau_\mathrm{p} \gg \tau_\mathrm{f}$. For particles having $\tau_\mathrm{p} \approx \tau_\mathrm{f}$, various correlations have been proposed in literate (Meyer and Deglon, 2011). However, as particles begin to adhere and the turbulent flow of interest is anisotropic, e.g. a pipe flow, a common approach is to resolve only the turbulence scales that affect motion of the particles considered using LES.

Different approaches exist to model the agglomeration process. One approach is to represent agglomerates by equivalent spheres that grow in size as the number of particles contained in the agglomerate increase (Brunk et al., 1998a,b). However, as shown by Brasil et al. (2001), the morphology of agglomerates differs significantly depending on how the agglomerates are formed, the properties of the primary particles and properties of the fluid flow surrounding the particles. Based on the Euler-Lagrangian approach, Sommerfeld and Stübing (2017) proposed a computational efficient agglomerate structure model. Using this model, agglomerates are treated as point particles that carry additional information such as locations of the primary particles and binding forces holding the agglomerates together. Based on these properties, parameters such as the convex hull and fractal dimension can be calculated and used to relate agglomerate structure to flow resistance coefficients.

Another approach is to track each particle but assume the particles to stay adhered when agglomerated or deposited on a wall. However, the DEM study of laminar channel flow by Marshall (2007) shows that phenomena such as bending and break-off of agglomerates occur frequently and play important roles to accurately predict the state where the rate of particles being re-entrained back into the fluid asymptotically approaches the rate of particles being deposited. Furthermore, the study suggests the mechanism of agglomerates continuously breaking up as agglomerates are formed to be controlled by impacting particles or agglomerates rather that fluid forces.

As noted in most studies coupling DEM to a fluid phase, there is typically a large difference between the time step sizes required to resolve particle collisions δt_DEM and fluid flows δt_f, so that $\delta t_\mathrm{col} \ll \delta t_\mathrm{f}$. As $\delta t_\mathrm{col} = \mathcal{O}(10^{-9}\ \mathrm{s})$, this is also valid for a wide range of turbulent flows. This fact is commonly

used to speed up coupled simulations by introducing softer particles by lowering the particle stiffness and thereby making particle collisions take place over longer time periods. However, as noted in studies by Kobayashi et al. (2013); Gu et al. (2016); Hærvig et al. (2017), depending on the adhesiveness model, introducing softer particles should be accompanied by a lower adhesive forces in order for the collision outcome (stick/rebound) to stay the same.

When the agglomerates increase in size, the study by Dizaji and Marshall (2017) shows that the local fluid velocity in an agglomerate becomes increasingly correlated with the agglomerate velocity. In this case, a two-way coupling between particles and fluid is needed to accurately represent the presence of particles on the fluid. Furthermore, due to differences in agglomerate morphology, it is not trivial to model the particle-fluid interaction without resolving the flow fluid around each particle. Attempts to correlate particle drag with particle volume fraction and Reynolds number include Ergun and Orning (1949) who experimentally correlated pressure gradients in fluidized beds to the particle void fraction. Later studies by Hill et al. (2001a,b) rely on the Lattice-Boltzmann Method (LBM) to resolve the flow around particles and correlate the drag force exerted on particles with particle volume fraction and the Reynolds number. While this method is highly accurate for homogeneous packing, the spatial variations in agglomerates that range from compact to dendritic in structure complicate the formulation of a general drag model. Dietzel and Sommerfeld (2013) resolved the flow in agglomerates by local grid-refined Lattice-Boltzmann Method (LBM) simulations and correlated the overall drag force on different agglomerate morphologies to the projected cross section of the convex hull perpendicular to the mean flow direction. However, as the agglomerating and break-up mechanisms are governed by the particles being affected by different fluid forces, this approach is not suitable for this study.

While numerous studies on two-way coupled particle-fluid interactions have been reported, only a few account for the adhesive behaviour by fully resolving collision using the soft-sphere DEM approach. Afkhami et al. (2015) studied the effect of particle adhesiveness using three different particle surface energy densities and showed a direct link between surface energy density and agglomeration rate.

The purpose of this study is look into how particle response time and particle adhesiveness affect the agglomeration rate. To obtain a fully-developed flow, the computational domain is made periodic in the stream-wise direction. To avoid imposing any limitations on the agglomeration process, the soft-sphere DEM approach is used to resolve how particles collide, agglomerate, deposit and are re-entrained into the fluid due to collisions with other particles or by fluid forces. Figure B.1 gives an overview of these different processes.
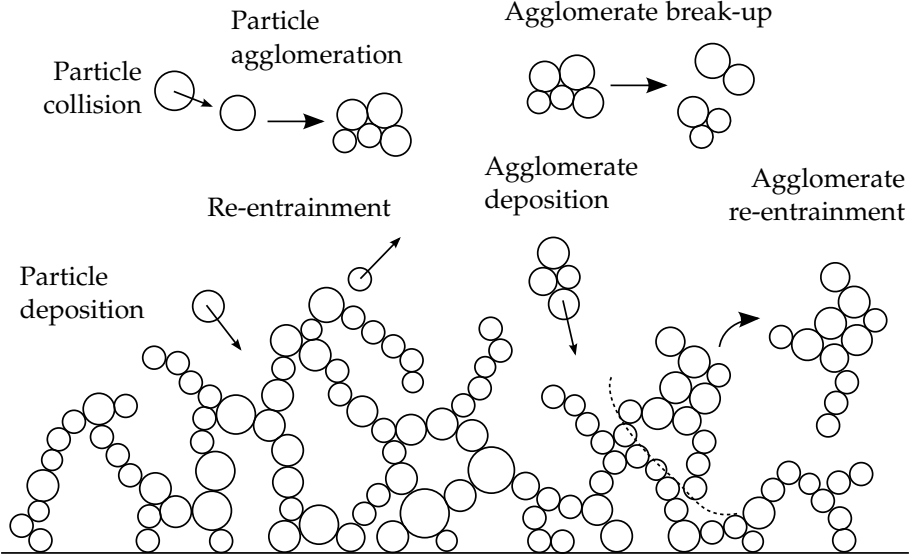
Figure B.1: Overview of the different processes in the vicinity of a surface and away from a surface that are resolved directly by the soft-sphere DEM approach. The early stages of interest in this study are typically limited to particles colliding, particles agglomerating, agglomerates breaking up and a single particles depositing at surfaces.

B.1.1 Governing equations for fluid flow

The filtered LES equations governing unsteady, in-compressible, three-dimensional viscous fluid flow in a periodic domain with two-way coupling between particle and fluid phases are the continuity and momentum equations given by (C.11) and (C.12) respectively:

$$\frac{\partial \left(\alpha_{\mathrm{f}} \bar{u}_{\mathrm{i}} \right)}{\partial x_{\mathrm{i}}} = 0 \tag{B.1}$$

$$\frac{\partial \left(\alpha_{\mathrm{f}} \bar{u}_{\mathrm{i}} \right)}{\partial t} + \frac{\partial \left(\alpha_{\mathrm{f}} \bar{u}_{\mathrm{i}} \bar{u}_{\mathrm{j}} \right)}{\partial x_{\mathrm{j}}} = -\frac{\alpha_{\mathrm{f}}}{\rho_{\mathrm{f}}} \frac{\partial \bar{p}}{\partial x_{\mathrm{i}}} + \alpha_{\mathrm{f}} \frac{\partial}{\partial x_{\mathrm{j}}} \left(\left(\nu + \nu_{\mathrm{sgs}} \right) \frac{\partial \bar{u}_{\mathrm{i}}}{\partial x_{\mathrm{j}}} \right)$$
$$+ \beta \delta_{1,\mathrm{i}} + f \tag{B.2}$$

where α_{f} denoting the local fluid volume fraction and $\beta \delta_{1,\mathrm{i}}$ defines a momentum source term dynamically being changed to balance out the pressure gradient across the periodic domain. The sub-grid scale viscosity ν_{sgs} accounts for sub-grid scale turbulence and naturally approaches zero in the case of DNS. In this study, focus is on LES where the sub-grid scale viscosity is modelled through the the wall-adapting local eddy-viscosity (WALE)

model by Nicoud and Ducros (1999):

$$\nu_{\text{sgs}} = \left(C_{\text{w}} V^{1/3}\right)^2 \frac{\left(\bar{s}_{ij}^{\text{d}} \bar{s}_{ij}^{\text{d}}\right)^{3/2}}{\left(\bar{s}_{ij}^{\text{d}} \bar{s}_{ij}^{\text{d}}\right)^{5/2} + \left(\bar{s}_{ij}^{\text{d}} \bar{s}_{ij}^{\text{d}}\right)^{5/4}} \tag{B.3}$$

where:

$$s_{ij}^{\text{d}} = \frac{1}{2}\left(\bar{g}_{ij}^2 + \bar{g}_{ji}^2\right) - \frac{1}{3}\delta_{ij}\bar{g}_{kk}^2, \quad \bar{s}_{ij} = \frac{1}{2}\left(\frac{\partial \bar{u}_i}{\partial x_j} + \frac{\partial \bar{u}_j}{\partial x_i}\right) \tag{B.4}$$

$$g_{ij} = \frac{\partial \bar{u}_i}{\partial x_j}, \quad g_{ij}^2 = g_{ik}g_{kj} \tag{B.5}$$

with constant $C_{\text{w}} = 0.325$ and where V is the local cell volume. Compared to the Smagorinsky-type models, the WALE model is more suited for wall-bounded flows, as the local sub-grid scale eddy-viscosity automatically goes to zero at the wall. Therefore, no dynamic constant adjusting or damping functions are needed to correct for walls.

B.1.2 Governing equations for particles

To model collisions of particles, the soft-sphere discrete element method (DEM) first proposed by Cundall and Strack (1979) is used to track the translational and angular velocity throughout the simulations. For the i'th particle with mass m_i, radius r_i and mass moment of inertia $I_i = (2/5)m_i r_i^2$, the position x_i and angular velocity ω_i are governed by:

$$m_i \frac{\text{d}^2 x_i}{\text{d}t^2} = F_{i,\text{con}} + F_{i,\text{fluid}} \tag{B.6}$$

$$I_i \frac{\text{d}\omega_i}{\text{d}t} = M_{i,\text{con}} + M_{i,\text{roll}} + M_{i,\text{fluid}} \tag{B.7}$$

where the F_{con} is a contact force upon collision and F_{fluid} is the combined fluid force acting on the particle. In the angular momentum equation, M_{con} is the contact torque by a tangential off-set between colliding particles, M_{roll} is the adhesive rolling resistance torque and M_{fluid} is the torque caused by interaction with the fluid phase.

Contact forces

Due to the small size of the particles of interest, the van der Waals force plays a dominant role in the collision process, which ultimately results in particles agglomerating and sticking to walls. Based on properties and size of the particles, particle deformation in contact region upon collision may be important

in the description of the adhesive force. In this study, the van der Waals attractive force is modelled using the Johnson-Kendall-Roberts (JKR) adhesive model by Johnson et al. (1971), which assumes particle deformation in the contact region to be important when describing the adhesive force. As noted by Tabor (1977), the JKR model is valid when $\lambda_T = \left(4R\gamma^2/(E^2 D_{min}^3)\right)^{1/3} > 3$, where γ is the surface energy density, defining half the energy required to separate two particles in contact and D_{min} is the minimum separation distance between two particles, which is commonly assumed to be 1.65 Å (Israelachvili, 1992; Parteli et al., 2014).

Using the JKR model, the normal contact force upon collision is balanced by a spring force $F_{spring,n}$ and an adhesive force $F_{jkr,n}$:

$$F_{spring,n} = -\frac{4E}{3R}a^3 \boldsymbol{n} \tag{B.8}$$

$$F_{jkr,n} = 4\sqrt{\pi\gamma E a^3}\boldsymbol{n} \tag{B.9}$$

where the effective Young's modulus E and effective radius R are given by:

$$\frac{1}{E} = \frac{1 - \nu_i^2}{E_i} + \frac{1 - \nu_j^2}{E_j}, \qquad \frac{1}{R} = \frac{1}{r_i} + \frac{1}{r_j} \tag{B.10}$$

and the contact radius a is the radius of contact area. In equilibrium state where $F_{spring,} + F_{jkr,n} = 0$, the contact radius is $a = (9\pi\gamma R^2/E)^{1/3} = a_0$. When using DEM, the overlap distance δ_n between particle i and j with positions x_i and x_j is calculated as $\delta_n = r_i + r_j - |x_i - x_j|$. For collisions following JKR theory, the relation between normal overlap δ_n and contact radius a is given by (Deng et al., 2013; Parteli et al., 2014):

$$a^4 - 2R\delta_n a^2 - \frac{4\pi\gamma}{E}R^2 a + R^2\delta_n^2 = 0 \tag{B.11}$$

which in this study is solved using the analytical solution derived by Parteli et al. (2014). Furthermore, the collision is damped by a normal damping force $F_{damp,n}$ causing kinetic energy to be dissipated upon impact:

$$F_{damp,n} = -2\frac{5}{6}\beta\sqrt{S_n m}v_n \tag{B.12}$$

with effective mass $m^{-1} = m_i^{-1} + m_j^{-1}$, v_n denoting the relative normal velocity, β accounting for the kinetic energy lost upon impact through the coefficient of restitution e and S_n taking the properties of the particles into account:

$$\beta = \frac{\ln(e)}{\sqrt{\ln^2(e) + \pi^2}} \tag{B.13}$$

$$S_n = 2E\sqrt{R\delta_n} \tag{B.14}$$

where e is material property. Due relatively low collision velocities, plastic deformation of particle material is not expected to be important. In the tangential direction, the spring force is given by:

$$F_{\text{spring,t}} = -S_t \Delta s_t \tag{B.15}$$

where Δs_t is the tangential overlap and S_t takes particle properties into account through $S_t = 8G\sqrt{R\delta_n}$ with effective shear modulus G:

$$\frac{1}{G} = \frac{2 - \nu_i}{G_i} + \frac{2 - \nu_j}{G_j} \tag{B.16}$$

Like in the normal direction, energy is dissipated in the tangential direction, described by a tangential damping force:

$$F_{\text{damp,t}} = -2\sqrt{\frac{5}{6}}\beta\sqrt{S_t m}v_t \tag{B.17}$$

where v_t is the tangential relative velocity. As suggested by Thornton (1991); Thornton and Yin (1991), the total tangential force is in the case of JKR adhesion truncated to fulfil $|F_{\text{con,t}}| \leq \mu_s|F_N + 2F_C|$ with μ_s and F_C being the sliding friction coefficient and the critical force required to separated agglomerated particles respectively.

Contact torques

In the case of adhesive particles, the formation of agglomerates and motion of particles on a surface tend to be dominated by particles rolling while particles sliding and twisting play negligible roles due to the small particle inertia (Oda et al., 1982; Iwashita and Oda, 1998). As a consequence of the deformed contact region described through JKR theory, the rolling motion differs from that of non-adhesive particles.

In the case of adhesive forces in the contact region between two particles or a particle and a wall, the point of contact stays behind the centre of mass projected onto the surface, which results in a torque opposing motion. This rolling resistance torque acts to obtain the equilibrium condition where the projected centre of mass and centre of contact are coincident. The rolling resistance torque is commonly described as proportional to the rolling displacement ξ, which is found by integrating the rolling velocity v_r:

$$\xi = \left(\int_{t_0}^{t_1} v_r(t)\mathrm{d}t\right) \cdot t_r \tag{B.18}$$

where $t_r = v_r/|v_r|$ is the direction of rolling. Based on the instantaneous rolling displacement ξ, the rolling resistance torque opposing motion is given

by (Dominik and Tielens, 1995, 1997):

$$M_r = \begin{cases} k_r \xi & \text{if } \xi < \xi_{\text{crit}} \\ k_r \xi_{\text{crit}} & \text{if } \xi \geq \xi_{\text{crit}} \end{cases} \tag{B.19}$$

where the rolling stiffness is given by $k_r = 4F_C \left(a/a_0\right)^{3/2}$. When the particle is rolled a distance longer than a critical rolling displacement ξ_{crit}, the particle material slips and a new equilibrium contact region is found. The studies by Dominik and Tielens (1995, 1997) suggests that after rolling displacement reaches a critical value ξ_{crit}, the rolling resistance torque is constant. Based on experiments, Krijt et al. (2014) suggests this critical rolling displacement to be linked to the equilibrium contact radius a_0 and a material dependent adhesion hysteresis parameter $\Delta\gamma/\gamma$ through:

$$\xi_{\text{crit}} = \frac{a_0}{12} \frac{\Delta\gamma}{\gamma} \tag{B.20}$$

A value $\Delta\gamma/\gamma = 0.5$ representing a typical value (Krijt et al., 2014) is used throughout this study.

B.1.3 Non-dimensional groups

The results are reported based on a set of non-dimensional groups that govern different aspects of particle transport, particle collision and subsequently the agglomeration and deposition processes.

The numbers governing the transport of particles are the Reynolds number $\text{Re} = U \cdot D/\nu$, the dimensionless particle size $\epsilon = d_p/D$, the particle to fluid density ratio $\chi = \rho_p/\rho_f$, the Stokes number $\text{St} = \rho_p d_p^2 U/(18\mu D) = \chi\epsilon^2\text{Re}/18$ and the particle volume fraction defining the volume occupied by particles in the fluid domain $\phi = \sum_{n=1}^{N} V_p / (\sum_{n=1}^{N} V_p + V_f)$. The importance of gravity is described through the Froude number $\text{Fr} = U/\sqrt{g_r d_p}$, where $g_r = (1 - 1/\chi)g$ is the buoyancy corrected gravity acceleration.

Likewise, the collision and agglomeration processes are governed by a set of non-dimensional groups. The stiffness of a common collision is described by making the effective Young's modulus dimensionless using the particle density, bulk velocity and particle density forming $\lambda = E/(\rho_p U^2)$. Likewise, to describe the sticking behaviour upon impact, the surface energy density, describing the strength of the adhesive force, is made non-dimensional by the particle density, bulk velocity and particle diameter, forming $\text{Ad} = \gamma/(\rho_p U^2 d_p)$.

Due to stiffness of most common materials, the time step size required to resolve particle collisions is typically in the order of nano seconds. A common approach to deal with the low time step sizes is to reduce the particle

stiffness several orders of magnitude making collisions take place over longer time periods. For non-adhesive particles colliding without any plastic deformation, the rebound velocity is solely a function of velocity before collision and the coefficient of restitution. However, for collisions involving adhesive particles, the reduced particle stiffness has to be balanced by a reduction in adhesive inter-molecular force so that the collision outcome remains the same. In this study, the high particle stiffness is reduced by decreasing the effective Young's modulus while modifying the surface energy density as:

$$\gamma_{\text{mod}} = \gamma \left(\frac{E_{\text{mod}}}{E} \right)^{2/5} \tag{B.21}$$

or in terms of the dimensionless elasticity parameter λ and adhesiveness parameter Ad:

$$\text{Ad}_{\text{mod}} = \text{Ad} \left(\frac{\lambda_{\text{mod}}}{\lambda} \right)^{2/5} \tag{B.22}$$

which is shown by Hærvig et al. (2017) to make the collision outcome independent of a reduction in Young's modulus. For particles colliding in a viscous fluid, the fluid being forced away in the contact prior to collision may have a non-negligible effect on the rebound velocity (Gondret et al., 1999, 2002). This importance of this effect is described through the collision Stokes number $\text{St}^* = \left(m_{\text{p}} + C_{\text{M}} m_{\text{f}} \right) v / (6\pi \mu r_{\text{p}})$, where $C_{\text{M}} = 0.5$ is the added mass coefficient for spheres and v denotes the velocity before being affected by the surface. For solid particles colliding with $\text{St}^* < 10$, Legendre et al. (2005) suggests all energy to be dissipated while for higher values of St^*, this effect quickly becomes negligible.

B.1.4 Particle-fluid interaction

The fluid force governing the transport of particles F_{fluid} in equation (B.6) is obtained by point-force approximations due to the large number of particles involved. The fluid force is split up into different contributions that include: a fluid drag force, Saffman lift force due to local shear in the flow field, Magnus lift force due to local relative angular velocity between particle and fluid, a buoyancy-corrected gravity force, a added mass force due to acceleration of nearby fluid, a Basset history force due to delay in boundary layer build-up and a Brownian motion force due to random collisions with fluid molecules.

Due to the large density ratio between particles and air, typically $\chi = \rho_{\text{p}}/\rho_{\text{f}} > 1000$, the added mass and history forces are neglected in the present study as suggested by Dritselis (2017); Armenio and Fiorotto (2001).

Also, gravity plays a minor role compared to drag for the small particles considered. As shown by Marshall and Li (2014), the ratio of gravity to Stokes

drag can be approximated by combining the dimensionless particle diameter and the Froude number as: $F_g/F_d = \mathcal{O}\left(\epsilon\,\mathrm{Fr}^2\right)^{-1}$. For particles investigated in this study, this ratio is $F_g/F_d = \mathcal{O}\left(10^{-2}\right)$ and thus gravity is expected to play a negligible role. Furthermore, molecular effects due to Brownian motion are neglected as the particles considered are several orders of magnitude larger than fluid molecules. Moreover, it is assumed that the mean free path of fluid molecules is much smaller than the particle size (Kn $\ll$ 1), so that the standard continuum assumption is valid and the effect of surface slip is negligible.

Fluid force contributions

As inter-particle van der Waals forces cause agglomerates to form and particles to deposit, the particle volume fraction α_p increases locally. When particles agglomerate, the individual particles in the agglomerate are affected by fluid forces that are significantly different from the fluid force on single particles in dilute flows. Therefore, a drag formulation taking the presence of surrounding particles into account is used. In this study, the Lattice-Boltzmann-based drag formulation suggested by Hill et al. (2001b,a) and later modified by Benyahia et al. (2006) to cover particle Reynolds numbers up to 100 and particle volume fractions approaching the closed-pack solution is used.

For particles in the viscous sub-layer, where strong velocity gradients exist, Saffman lift force is expected to be important as suggested by McLaughlin (1989). Furthermore, Magnus lift due to relative angular velocity between particle and fluid is included as off-centre collisions may result in particles rebounding with non-negligible angular velocities. To model these fluid force contributions, the expressions derived by Kurose and Komori (1999) and McLaughlin (1965) are used.

B.2   Results and Validation

B.2.1   Fluid domain and discretisation

To make the results independent of stream-wise boundaries, the fluid domain is made periodic with a length longer than the elongated coherent turbulence structures in the boundary layer extending around $L_x^+ \approx 1000$ (Robinson, 1991). In this study, a domain length of $L/D = 4$, corresponding to $L_x^+ \approx 2500$ in viscous units, is chosen to make sure no coherent structures extend throughout the domain. Thus, the turbulence statistics are not affected by the size of the computational domain. A quarter of the cross-sectional mesh topology is shown in figure B.2. As the agglomeration formation process takes place over stream-wise distances significantly longer than
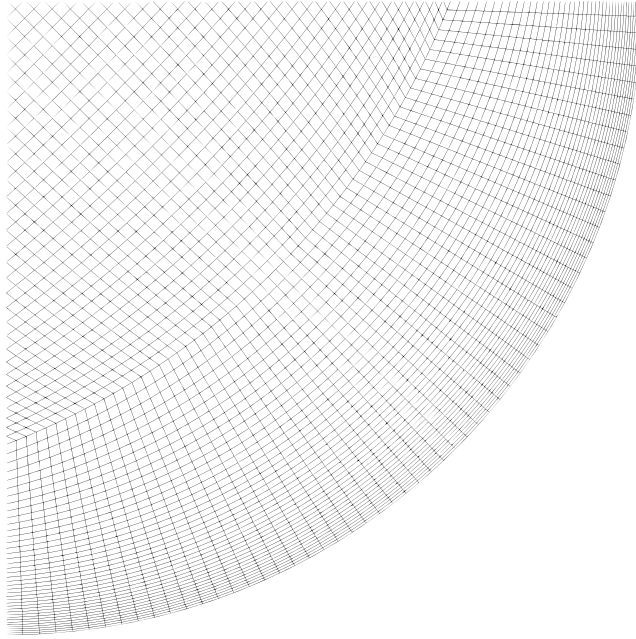
Figure B.2: Mesh topology visualised by a quarter of the cross-sectional plane.

$L/D = 4$, the DEM domain is made periodic as well. In that way, the overall particle volume fraction ϕ stays constant throughout the simulation. This approach gives detailed information on the mechanisms governing agglomeration and deposition and how changes in fluid/particle properties affect early stages of agglomeration and deposition. Later stages of the deposition process where bridges and layers of multiple particles form, see figure B.1, would require particles to be added throughout the simulation or a significantly higher initial particle concentration, which would alter the early stages of agglomeration and deposition processes.

B.2.2 Validation of flow field

To validate the statistics of the flow field without particles added, the boundary layer velocity profile is compared for the different meshes listed in table B.1. The various grid resolutions are compared to experiments by den Toonder and Nieuwstadt (1997) and boundary layer theory. Parameters for the different meshes are listed in table B.1. In this section, the time-averaged turbulent flow obtained by LES simulations without particles is compared to theory to ensure reasonable accuracy compared to experimental data and theory. The time-averaged flow field is found by averaging over a time period of $t^+ = t \cdot U/D = 400$ after which the mean flow field statistics are found to

Table B.1: Details of the three different meshes with θ, r and x denoting circumferential, radial and axial directions respectively. The mesh topology is shown in figure B.2.

Resolution	(N_θ, N_r, N_x)	$\Delta\theta^+_{max}$	Δx^+_{max}
Coarse	(160,90,160)	12	15
Medium	(200,110,200)	10	12.5
Fine	(240,140,240)	8	10
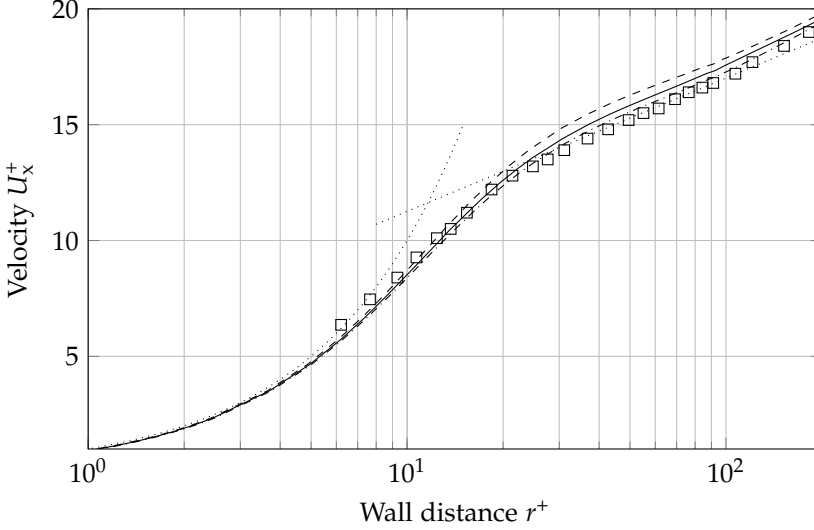
Figure B.3: Time-averaged turbulent boundary layer velocity profile for Re $= UD/\nu = 10,000$ for different mesh resolutions, see table B.1: (- - -) Coarse resolution LES; (——) Medium resolution LES; (-·-·-) Fine resolution LES; (·······) Viscous sub-layer with $U^+_x = r^+$ and log-law layer with $U^+_x = 2.5\ln(r^+) + 5.5$; $\square$ Experiment for Re $= 10,000$ by den Toonder and Nieuwstadt (1997).

be independent of time. Figure B.3 shows how the numerical simulations compare to boundary layer theory and experiments at Re $= 10,000$. As seen in figure B.3, the more resolving LES simulations approach the experiment by den Toonder and Nieuwstadt (1997).

B.2.3 Particle properties

Particles with $d_p = 10$ μm and $\rho_p = 2500$ kg/m³ are transported in pipe flow with $D = 40$ mm and mean velocity $U = 5$ m/s so that Re $= U \cdot D/\nu \approx 10,000$, St $= \rho_p d_p^2 U/(18\mu D) \approx 0.1$ and $\epsilon = d_p/D = 0.25 \cdot 10^{-3}$.

The particles are affected by an inter-particle adhesive force characterised by a surface energy density and develop a flattened contact region as predicted by JKR theory. The particles have stiffness and adhesiveness such

that $\lambda = E/(\rho_p U^2) \approx 500 \cdot 10^3$, Ad $= \gamma/(\rho_p U^2 d_p) \approx 0.08$ and coefficient of restitution $e \approx 0.3$. The particles are initially placed randomly throughout the turbulent flow without any particles being in contact. Instead of using a more or less sophisticated correlation to prescribe the initial velocity of particles, the particles are inserted with zero velocity in the present study. A constant volume fraction $\phi = 10^{-3}$ is used in all simulations.

However, due to the significant difference in particle to pipe size ratio $\epsilon = d_p/D = 0.25 \cdot 10^{-6}$, it takes $\approx 0.4 \cdot 10^9$ particles to get a volume fraction $\phi = 0.001$, making the simulations practically computationally impossible for the DEM method. Instead, the particle size is increased from $\epsilon = 0.25 \cdot 10^{-3}$ to $\epsilon = 5 \cdot 10^{-3}$, while scaling the other non-dimensional groups to get the parameters listed above. For example, to ensure the artificially larger particles have the same particle to fluid response time, the density ratio χ is scaled according to St $= \chi \epsilon^2 \mathrm{Re}/18$. Furthermore, as the adhesiveness parameter is a function of particle diameter, the surface energy density γ is scaled as well so that the adhesive behaviour remains the same despite an increase in particle size.

B.2.4   Overview of simulations

The following gives an overview of the different simulations carried out in the present study. The simulation parameters are summarised in terms of non-dimensional numbers in table B.2.

Simulation no. 1–21   Depending on the Stokes number, the particles will be affected by different turbulence scales. As the Stokes number approaches zero, the particles will be affected by increasingly smaller eddies. In this study where LES is used, it is important that particles are unaffected by the eddies not being resolved. Therefore, simulations with varying Stokes number St $= 0.4 \cdot 2^x$, $x = 0..6$ and carried out using the three meshes listed in table B.1.

Simulation no. 22–28   As already mentioned, the agglomeration processes considered in this study have elasticity parameter $\lambda \approx 500 \cdot 10^3$. Using this value, particle-particle and particle-wall collisions happen over time intervals in the order of nano seconds. To reduce computational time, a modified elasticity parameter is introduced: $\lambda_{\mathrm{mod}} = \lambda \cdot 0.001 = 500$. By reducing the elasticity parameter, the particles behave more adhesive. Therefore, to ensure the collision outcome stays independent of reduction in elasticity parameter, the criterion in (B.22) is used to reduce the adhesiveness parameter so that $\mathrm{Ad}_{\mathrm{mod}} = 0.08 \cdot 0.001^{2/5} = 0.005$. However, as noted in the study, introducing a lower adhesiveness parameter also reduces the critical force $F_C = 3\pi R\gamma$ required to separate two agglomerated particles. Therefore, simulations 22–28

Table B.2: Details on the simulations in terms of non-dimensional groups: Flow Reynolds number Re $= U \cdot D/\nu$, particle size $\epsilon = d_\text{p}/D$, Stokes number St $= \chi \epsilon^2 \text{Re}/18$, elasticity parameter $\lambda = E/(\rho_\text{p} U^2)$, adhesiveness parameter Ad $= \gamma/(\rho_\text{p} U^2 d_\text{p})$, coefficient of restitution e, particle volume fraction ϕ and LES resolution (see table B.1). The integer x is used to describe a range of simulation parameters.

No.	x	Re	ϵ	St	λ	Ad	e	ϕ	LES res.
1–7	$0..6$	10^4	0.005	$0.4 \cdot 2^x$	500	0.05	0.3	10^{-3}	Coarse
8–14	$0..6$	10^4	0.005	$0.4 \cdot 2^x$	500	0.05	0.3	10^{-3}	Medium
15–21	$0..6$	10^4	0.005	$0.4 \cdot 2^x$	500	0.05	0.3	10^{-3}	Fine
22–28	$0..6$	10^4	0.005	$0.4 \cdot 2^x$	5000	$0.05 \cdot 10^{2/5}$	0.3	10^{-3}	Medium
29–35	$0..6$	10^4	0.005	1	500	$0.001 \cdot 2^x$	0.3	10^{-3}	Medium
36–42	$0..6$	10^4	0.005	10	500	$0.001 \cdot 2^x$	0.3	10^{-3}	Medium

are carried out with $\lambda_\text{mod} = \lambda/100$ instead of $\lambda_\text{mod} = \lambda/1000$ to ensure the agglomeration rate is in fact independent of a reduction in elasticity and adhesiveness parameter.

Simulation no. 29-42 The purpose of simulation 29–42 is to investigate the transition from particles acting almost non-adhesive to particles being highly adhesive at constant Stokes numbers. For this purpose, the adhesive parameter is varied in the range 0.001 to 0.064 at a constant Stokes number St $= 1$ (simulations 29–35). Similar simulations are carried out for St $= 10$ (simulations 36–42).

B.2.5 Effect of sub-grid scale turbulence eddies on particle agglomeration

As the smallest eddy scales are modelled by a sgs-model, it is important that these unresolved scales do not affect particle motion and subsequently agglomeration and deposition. Ultimately, as particles with sufficiently low response time, e.g. tracer particles, would respond to all turbulence scales, a DNS solution would be required in this case. However, as pointed out by Armenio (1999), particles with finite mass do not respond to smaller turbulence scales, suggesting LES to be an appreciate method to investigate particles interactions in a turbulent flow. Figure B.4 shows how the agglomeration rate by the average number of particles in each agglomerate as function of time for different particle Stokes numbers. As the figure shows, particles with St $= \mathcal{O}(10)$ are almost unaffected by changes in mesh resolution. This suggests that these particles are unaffected by eddies smaller than the grid size of the coarse mesh. For particles with St $= \mathcal{O}(1)$, there is pronounced difference between the coarse and medium mesh resolutions, suggesting particles with St $= \mathcal{O}(1)$ to respond to eddies not being resolved by the coarsest mesh. The difference is insignificant when comparing the medium and fine mesh resolutions, suggesting that the particles are almost unaffected by the
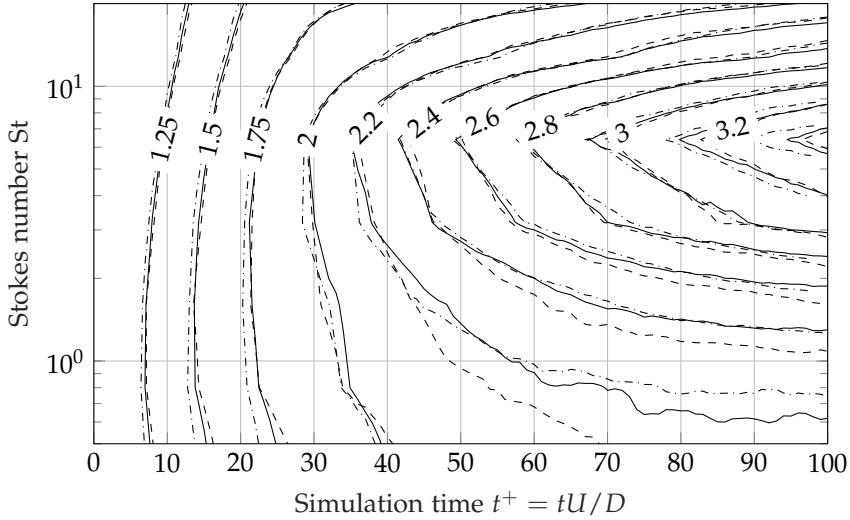
Figure B.4: Effect of mesh resolution, see table B.1, and Stokes number on particle agglomeration behaviour visualised by the average number of particles per agglomerate. As no particles are in contact at $t^+ = 0$, the average number of particles is 1. See simulation no. 1–21 in table B.2 for simulation parameters: (– – –) Coarse resolution LES; (——) Medium resolution LES; (– · –)
Fine resolution LES.

smaller eddies not being resolved by the medium resolution mesh. As a consequence, the medium resolution mesh from table B.1 is used to investigate how changes particle response time and adhesiveness affect the agglomeration rate.

B.2.6 Effect of introducing softer particles

In the present study, the particle stiffness is reduced by a factor 1000 from $\lambda = 500 \cdot 10^3$ to $\lambda_{\text{mod}} = 500$ in order to increase collision duration and consequently allow for an increased DEM time step size. The result is smaller difference between fluid time step size δt_{f} and particle time step size δt_{col} that decrease the computational time. In order for the collision outcome (sticking/rebounding) to remain the same despite a reduced particle stiffness, the particle adhesiveness is modified using the criterion given in (B.22), giving a modified collision duration $\Delta t_{\text{col,mod}} = \Delta t_{\text{col}} \left(\lambda/\lambda_{\text{mod}}\right)^{2/5}$ (Hærvig et al., 2017). To ensure that the agglomeration process is in fact independent of this change, an additional set of simulations with $\lambda = 5000$ is carried out. Figure B.5 shows results for $\lambda_1 = 500$ and $\lambda_2 = 5000$ with adhesiveness parameters $\text{Ad}_1 = 0.05$ and $\text{Ad}_2 = \text{Ad}_1(\lambda_2/\lambda_1)^{2/5}$. As figure B.5 shows, the agglomeration process is almost independent of a change in elasticity parameter from $\lambda = 500$ to $\lambda = 5000$ when reducing the adhesiveness parameter by
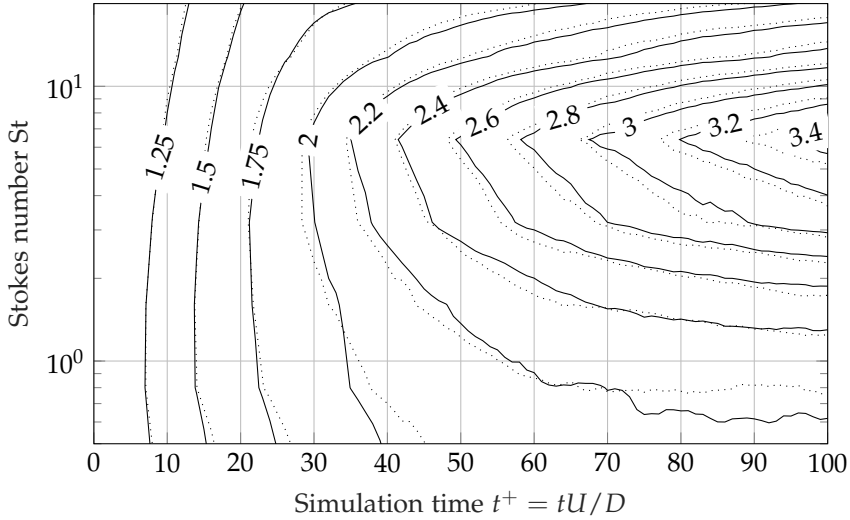
Figure B.5: Effect of introducing softer particles using the criterion in (B.22). Contours show particle agglomeration rate visualised by the average number of particles contained in each agglomerate for particle elasticity parameters $\lambda = 500$ and $\lambda = 5000$. See simulation no. 8–14 and 22–28 in table B.2 for simulation parameters: (——) $\lambda_1 = 500$, $Ad_1 = 0.05$; (······) $\lambda_2 = 5000$, $Ad_2 = Ad_1 \cdot (\lambda_2/\lambda_1)^{2/5}$.

(B.22) for particles with Stokes numbers in the range $St = 0.4$ to $St = 25.6$.

B.2.7 Effect of particle Stokes number on agglomeration and deposition

Depending on the Stokes number, the agglomeration process is governed by different distinct mechanisms. At sufficiently low Stokes numbers $St \ll 1$, the particles behave as tracer particles and respond to all turbulence scales. That is, collisions happen due to the finite size of particles that all follow different fluid streamlines. At sufficiently high Stokes numbers $St \gg 1$, the particle velocity is only weakly correlated with the local fluid velocity. Figure B.6 gives an overview of the agglomerates formed at time $t^+ = 100$ for Stokes numbers of 0.8, 6.4 and 25.6. As shown in figure B.6, the agglomeration rate is highest at intermediate Stokes numbers where larger agglomerates are being formed in the centre of the pipe, see B.6(b). This can be explained by the increased collision frequency when the accelerative-correlated collision mechanism is dominant. Figure B.7 gives an overview of the agglomeration process in terms of particle location. Figure B.7 shows the radial concentration of particles in terms of local volume fraction ϕ_r normalised by the overall particle volume fraction ϕ in different radial intervals r normalised by the pipe radius R at different times for simulation no. 9 in table B.2. As
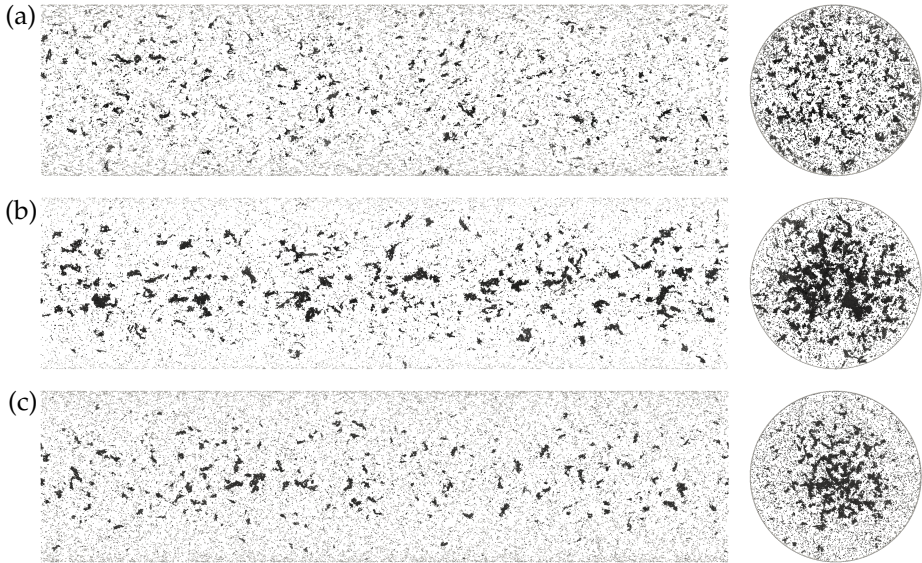
Figure B.6: Agglomerating and depositing behaviour at time $t^+ = tU/D = 100$: (a) St = 0.8, see simulation no. 9 in table B.2; (b) St = 6.4, see simulation no. 12 in table B.2; (c) St = 25.6, see simulation no. 14 in table B.2. To distinguish between moving particles and deposited particles, the particles are coloured according to their velocity magnitude. White corresponds to low velocity and black corresponds to high velocity.

shown in figure B.7, there is an increasing amount of particles sticking to the wall, while the concentration profile throughout the pipe remains relatively constant. This can be explained by the low Stokes number where $\tau_p < \tau_f$ causing particles to respond to most of the eddies resolved in turbulent flow. Figure B.8 shows how the particle concentration profile is affected by an increase in Stokes number. At a slightly higher Stokes number St = 6.4, particle accumulate in the centre of the pipe and near the wall. This phenomenon is explained by an increased collision frequency, causing agglomerates to form quickly. As agglomerates are formed, the effective response time for agglomerates is greatly increased, causing agglomerates to drift towards the centre of the pipe due to the shear velocity profile. Figure B.9 shows the radial particle concentration profile for higher Stokes number of St = 25.6. At a higher Stokes number, the primary particles are expected to almost unaffected by turbulent fluctuations so that the average flow field cause particles to drift towards the centre of the pipe. However, compared to the lower Stokes number in figure B.7, more particles adhere to the surface of the pipe. This can be explained by the particles not responding as quickly to the high velocity gradient close to the wall, causing particles to move through the boundary layer and adhere to the wall.
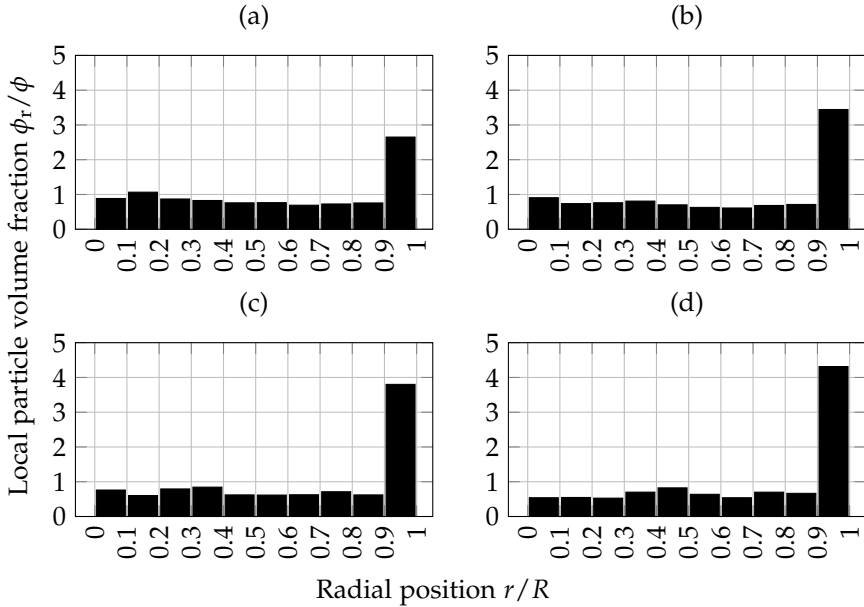
Figure B.7: Local particle volume fraction ϕ_r in radial intervals of $r/R = 0.1$ normalised by the overall particle volume fraction ϕ at different times. Stokes number St = 0.8, see simulation no. 9 in table B.2 for simulation parameters: (a) $t^+ = tU/D = 25$; (b) $t^+ = tU/D = 50$; (c) $t^+ = tU/D = 75$; (d) $t^+ = tU/D = 100$.

## B.2.8   Effect of particle adhesiveness on agglomeration

In the following, the effect of increased particle adhesiveness is investigated. The surface energy density γ is varied, resulting in adhesiveness parameters in the range Ad = 0.001 to Ad = 0.064, covering particles that range from weakly to highly adhesive. Figure B.10 gives an overview of how the adhesiveness parameter changes the agglomerating behaviour for particles with St = 1. As figure B.10(a) shows, the weakly adhesive particles only form smaller agglomerates in the centre of the tube and are significantly more uniformly distributed than the more adhesive particles in figure B.10(b) and B.10(c). Figure B.11 shows the average number of particles per agglomerate as function of simulation time at different adhesiveness parameters. As figure B.11 shows, the weakly adhesive particles with Ad = 0.001 are in average contained in agglomerates consisting of less than 1.025 particles. Even for non-adhesive particles with Ad = 0, a non-zero average agglomeration size is expected due to the finite collision duration, causing particles to be in contact for short durations before they separate again due to repulsive contact forces. At slightly higher adhesiveness parameters, significant agglomeration is observed with agglomerates being present throughout the flow field. Figure B.12 shows how an increase in adhesiveness parameter from
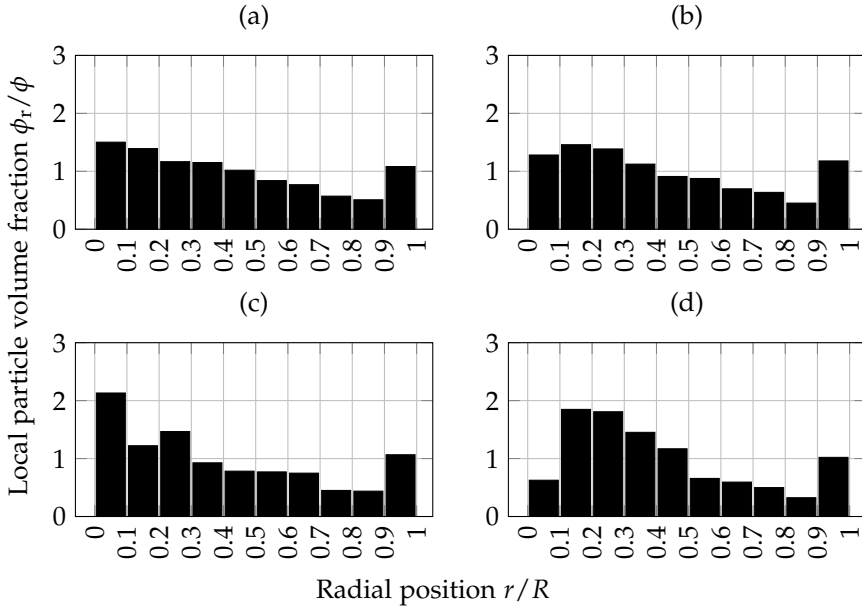
Figure B.8: Local particle volume fraction ϕ_r in radial intervals of $r/R = 0.1$ normalised by the overall particle volume fraction ϕ at different times. Stokes number St $= 6.4$, see simulation no. 12 in table B.2 for simulation parameters: (a) $t^+ = tU/D = 25$; (b) $t^+ = tU/D = 50$; (c) $t^+ = tU/D = 75$; (d) $t^+ = tU/D = 100$.

Ad $= 0.002$ to Ad $= 0.064$ affects the local particle concentration. As depicted in figure B.12, an increasing amount of particles adhere to the wall when the adhesiveness parameter is increased.

B.3 Conclusions and Discussion

Numerical results of how micron-sized agglomerate and deposit in a periodic, fully-developed turbulent pipe flow with Re $= 10000$ flow are presented. In this study, focus is on the first stages of agglomeration and deposition up to $t^+ = tU/D = 100$.

Firstly, Large Eddy Simulations (LES) are compared to experiments from literate in terms of boundary layer profile. With particles added, the effect of sub-grid scale fluctuations are linked to the Stokes number to ensure particle motion is independent of the unresolved velocity fluctuations. Fluid-particle interactions are based on the point-particle approach while particle-particle and particle-wall interactions are resolved directly using the soft-sphere DEM approach relying on the physical properties of the particles, where the adhesive behaviour is described through JKR theory.

Secondly, the effects of changes in particle response time on the agglom-
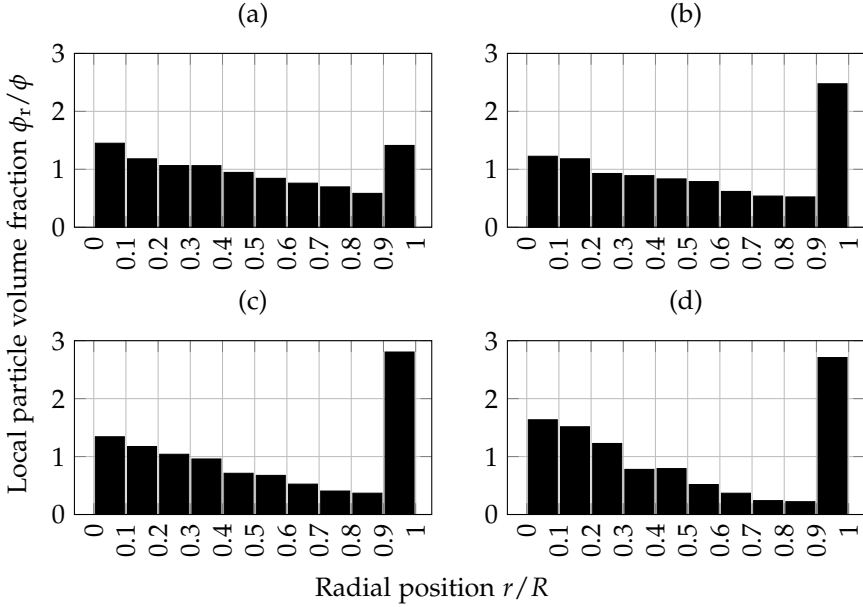
Figure B.9: Local particle volume fraction ϕ_r in radial intervals of $r/R = 0.1$ normalised by the overall particle volume fraction ϕ at different times. Stokes number St = 25.6, see simulation no. 14 in table B.2 for simulation parameters: (a) $t^+ = tU/D = 25$; (b) $t^+ = tU/D = 50$; (c) $t^+ = tU/D = 75$; (d) $t^+ = tU/D = 100$.

eration and deposition rates are investigated. By varying the Stokes number from 0.4 to 25.6, the results show a peak in agglomeration rate at St = 6.4, which can be explained by a high collision frequency. For a low Stokes number of St = 0.8, agglomerates are found throughout the flow field. Due to low particle response time, the particle concentration is close to uniform throughout the tube with a increase in particle concentration near the wall due to particle being captured by the wall. At a higher Stokes number St = 6.4, the particles tend to accumulate in the centre of the tube. This is expected to be caused by the high collision rate that quickly form agglomerates that increase the effective particle size so that the Saffman lift force dominates their radial motion causing them to move towards the centre of the pipe. At an even higher Stokes number St = 25.6, the particles are observed to accumulate in the centre of the pipe as well.

Thirdly, The adhesiveness parameter Ad = $\gamma/(\rho_p U^2 d_p)$ is varied from 0.001 to 0.064 resulting in particles that behave only weakly adhesive to highly adhesive. Regardless of adhesiveness parameter, the particle concentration throughout the flow field is observed to be more or less uniform with a peak at the wall that increases with adhesiveness parameter due to particles adhering to the wall.
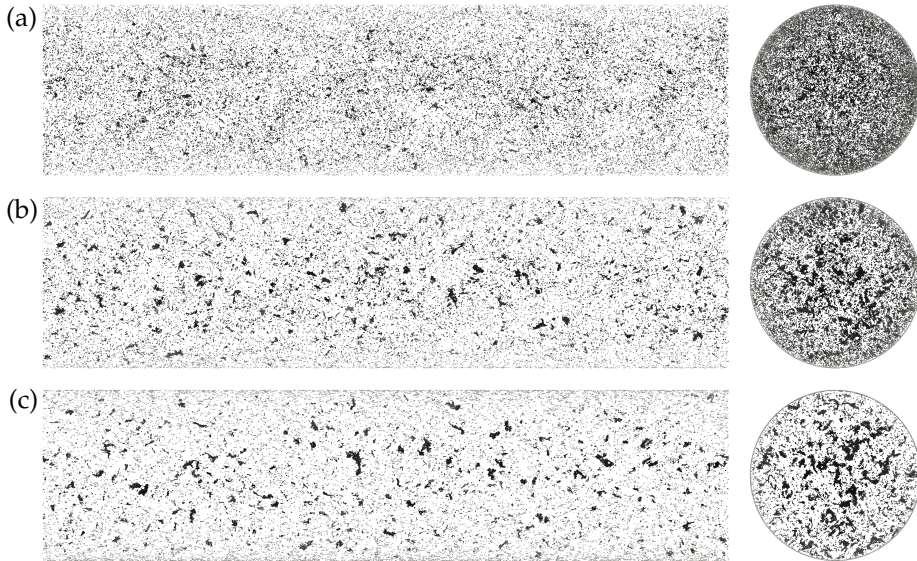
Figure B.10: Overview of agglomerating behaviour of mono-dispersed particles with different adhesiveness parameters at time $t^+ = tU/D = 100$: (a) Ad = 0.016; (b) Ad = 0.032; (c) Ad = 0.064. To distinguish between moving particles and deposited particles, the particles are coloured according to their velocity. White corresponds to low velocity and black corresponds to high velocity.

Acknowledgement

Bibliography

J. Abrahamson. Collision rates of small particles in a vigorously turbulent fluid. *Chemical Engineering Science*, 30:1371–1379, 1975. URL `http://doi.org/10.1016/0009-2<509(75)85067-6`.

M. Afkhami, A. Hassanpour, M. Fairweather, and D.O. Njobuenwu. Fully coupled les-dem of particle interaction and agglomeration in a turbulent channel flow. *Computers and Chemical Engineering*, 78:24–38, 2015. URL `http://dx.doi.org/10.1016/j.compchemeng.2015.04.003`.

Vincenzo Armenio. Effect of the subgrid scales on particle motion. *Physics of Fluids*, 11:3030, 1999. URL `http://dx.doi.org/10.1063/1.870162`.
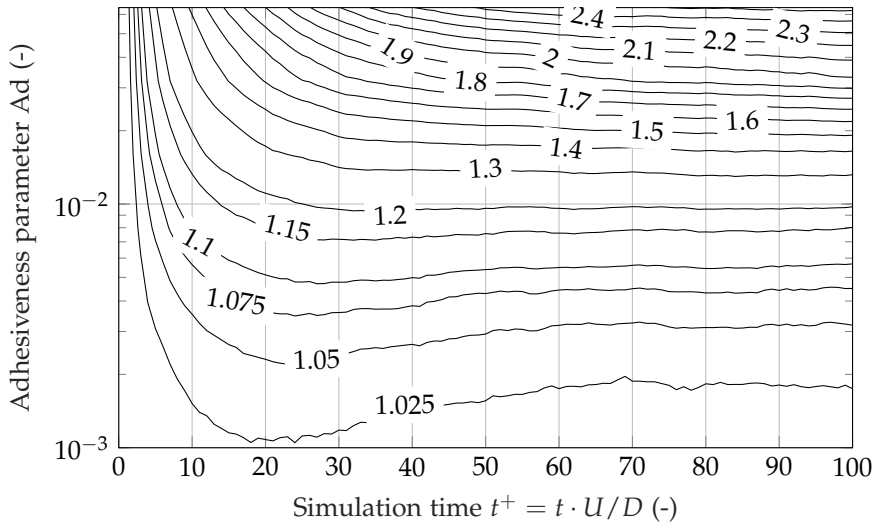
Figure B.11: Effect of particle adhesiveness parameter Ad $= \gamma/(\rho_p U^2 d_p)$ on particle agglomeration behaviour visualised by the average number of particles in each agglomerate, see simulation no. 29–35 in table B.2 for simulation parameters.

Vincenzo Armenio and Virgilio Fiorotto. The importance of the forces acting on particles in turbulent flows. *Physics of Fluids*, 13:2437, 2001. URL `http://dx.doi.org/10.1063/1.1385390`.

Sofiane Benyahia, Madhava Syamlal, and Thomas J. O'Brien. Extension of hill-koch-ladd drag correlation over all ranges of reynolds number and solids volume fraction. *Powder Technology*, 162:166–174, 2006. URL `http://dx.doi.org/10.1016/j.powtec.2005.12.014`.

A.M. Brasil, T.L. Farias, M.G.Carvalho, and U.O. Koylu. Numerical characterization of the morphology of aggregated particles. *Aerosol Science*, 32: 489–508, 2001. URL `http://doi.org/10.1016/S0021-8502(00)00097-5`.

Brett K. Brunk, Donald L. Kock, and Leonard W. Lion. Turbulent coagulation of colloidal particles. *Journal of Fluid Mechanics*, 364:81–113, 1998a. URL `http://doi.org/10.1017/S0022112098001037`.

Brett K. Brunk, Donald L. Kock, and Leonard W. Lion. Observations of coagulation in isotropic turbulence. *Journal of Fluid Mechanics*, 371:81–107, 1998b. URL `http://doi.org/10.1017/S0022112098001037`.

P.A. Cundall and O.D.L. Strack. A discrete numerical model for granular assemblies. *Géotechnique*, 29:47–65, 1979. URL `http://dx.doi.org/10.1680/geot.1979.29.1.47`.
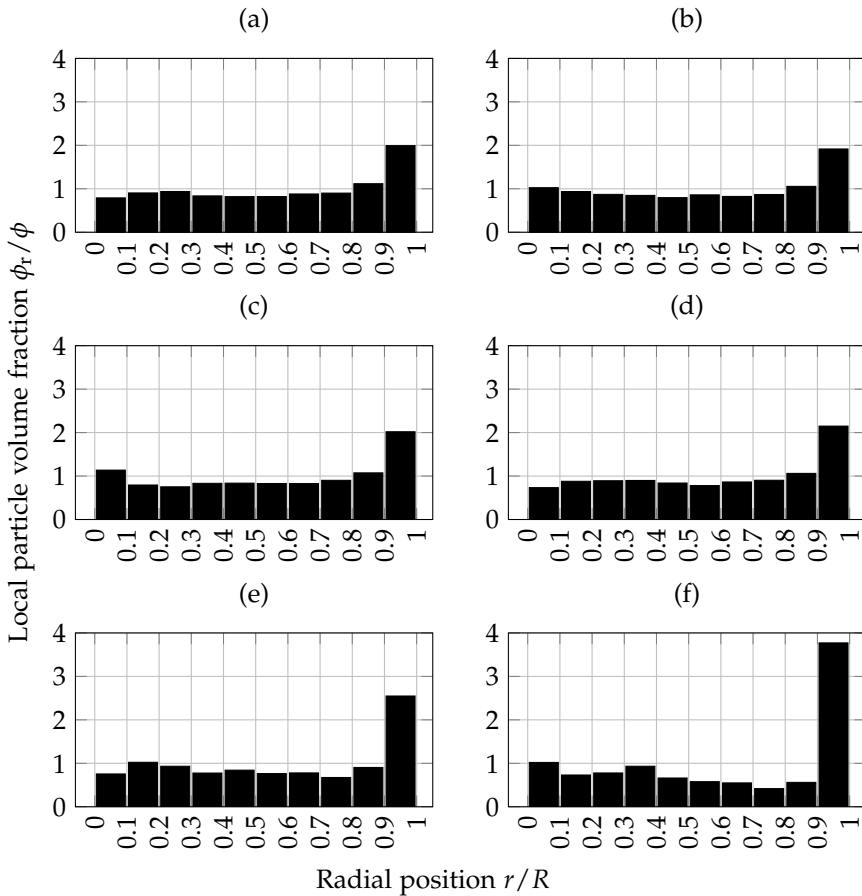
Figure B.12: Local particle volume fraction ϕ_r in radial intervals of $r/R = 0.1$ normalised by the overall particle volume fraction ϕ at $t^+ = 100$. Varying adhesiveness parameter, see simulation no. 30–35 in table B.2 for simulation parameters: (a) Ad = 0.002; (b) Ad = 0.004; (c) Ad = 0.008; (d) Ad = 0.016; (e) Ad = 0.032; (f) Ad = 0.064.

J.M.J. den Toonder and F.T.M Nieuwstadt. Reynolds number effects in a turbulent pipe flow for low to moderate re. *Physics of Fluids*, 9:3398–3409, 1997. URL `http://dx.doi.org/10.1063/1.869451`.

Xiaoliang Deng, James V. Scicolone, and Rajesh N. Davé. Discrete element method simulation of cohesive particles mixing under magnetically assisted impaction. *Powder Technology*, 243:96–109, 2013. URL `http://dx.doi.org/10.1016/j.powtec.2013.03.043`.

Mathias Dietzel and Martin Sommerfeld. Numerical calculation of flow resistance for agglomerates with different morphology by the lattice-boltzmann

method. *Powder Technology*, 250:122–137, 2013. URL `http://dx.doi.org/10.1016/j.powtec.2013.09.023`.

Farzad D. Dizaji and Jeffrey S. Marshall. On the significance of two-way coupling in simulation of turbulent particle agglomeration. *Powder Technology*, 318:83–94, 2017. URL `http://doi.org/10.1016/j.powtec.2017.05.027`.

C. Dominik and A.G.G.M Tielens. Resistance to rolling in the adhesive contact of two elastic spheres. *Philosophical Magazine A*, 72:783–803, 1995. URL `http://dx.doi.org/10.1080/01418619508243800`.

C. Dominik and A.G.G.M Tielens. The physics of dust coagulation and the structure of dust aggregates in space. *The Astrophysical Journal*, 480:647–673, 1997. URL `http://dx.doi.org/10.1086/303996`.

C.D. Dritselis. Numerical study of particle deposition in a turbulent channel flow with transverse roughness elements on one wall. *International Journal of Multiphase Flow*, 91:1–18, 2017. URL `http://dx.doi.org/10.1016/j.ijmultiphaseflow.2017.01.004`.

Sabri Ergun and A. A. Orning. Fluid flow through randomly packed columns and fluidized beds. *Industrial & Engineering Chemistry*, 41:1179–1184, 1949. URL `http://dx.doi.org/10.1021/ie50474a011`.

P. Gondret, E. Hallouin, M. Lance, and L. Petit. Experiments on the motion of a solid sphere toward a wall: From viscous dissipation to elastohydrodynamic bouncing. *Physics of Fluids*, 11:2803–2805, 1999. URL `http://dx.doi.org/10.1063/1.870109`.

P. Gondret, M. Lance, and L. Petit. Bouncing motion of spherical particles in fluids. *Physics of Fluids*, 14:643–652, 2002. URL `http://dx.doi.org/10.1063/1.1427920`.

Yile Gu, Ali Ozel, and Sankaran Sundaresan. A modified cohesion model for cfd-dem simulations of fluidization. *Powder Technology*, 296:17–28, 2016. URL `http://dx.doi.org/10.1016/j.powtec.2015.09.037`.

J. Hærvig, U. Kleinhans, C. Wieland, H. Spliethoff, A. L. Jensen, K. Sørensen, and T. J. Condra. On the adhesive jkr contact and rolling models for reduced particle stiffness discrete element simulations. *Powder Technology*, 319:472–482, 2017. URL `http://dx.doi.org/10.1016/j.powtec.2017.07.006`.

Reghan J. Hill, Donald L. Koch, and Anthony J. C. Ladd. The first effects of fluid inertia on flows in ordered and random arrays of spheres. *J. Fluid Mech.*, 448:213–241, 2001a. URL `http://dx.doi.org/10.1017/S0022112001005936`.

Bibliography

Reghan J. Hill, Donald L. Koch, and Anthony J.C. Ladd. Moderate-reynolds-number flows in ordered and random arrays of spheres. *Journal of Fluid Mechanics*, 448:243–278, 2001b. URL https://doi.org/10.1017/S0022112001005936.

J.N. Israelachvili. *Intermolecular and Surface Forces*. Academic Press, 2. edition, 1992. ISBN: 978-0-12-375182-9.

K. Iwashita and M. Oda. Rolling resistance at contacts in simulation of shear band development by dem. *Journal of Engineering Mechanics*, 124:285–292, 1998. URL http://dx.doi.org/10.1061/(ASCE)0733-9399(1998)124:3(285).

K.L. Johnson, K. Kendall, and A.D. Roberts. Surface energy and the contact of elastic solids. *Proc. R. Soc. Lond.*, 324:301–313, 1971. URL http://dx.doi.org/10.1098/rspa.1971.0141.

Tomonari Kobayashi, Toshitsugu Tanaka, Naoki Shimada, and Toshihiro Kawaguchi. Dem-cfd analysis of fluidization behavior of geldart group a particles using a dynamic adhesion force model. *Powder Technology*, 248:143–152, 2013. URL http://dx.doi.org/10.1016/j.powtec.2013.02.028.

S. Krijt, C. Dominik, A.G.G.MC. Dominik, and A.G.G.M Tielens. Rolling friction of adhesive microspheres. *Journal of Physics D: Applied Physics*, 47:175302 (9pp), 2014. URL http://dx.doi.org/10.1088/0022-3727/47/17/175302.

Ryoichi Kurose and Satoru Komori. Drag and lift forces on a rotating sphere in a linear shear flow. *Journal of Fluid Mechanics*, 384:183–206, 1999. URL http://doi.org/10.1017/S0022112099004164.

Dominique Legendre, Claude Daniel, and Pascal Guiraud. Experimental study of a drop bouncing on a wall in a liquid. *Physics of Fluids*, 17:097105, 2005. URL http://dx.doi.org/10.1063/1.2010527.

Jeffrey S. Marshall and Shuiqing Li. *Adhesive Particle Flow*. Cambridge University Press, 1. edition, 2014. URL http://dx.doi.org/10.1017/CBO9781139424547. ISBN: 978-1-107-03207-1.

J.S. Marshall. Particle aggregation and capture by walls in a particulate aerosol channel flow. *Aerosol Science*, 38:333–351, 2007. URL http://dx.doi.org/j.jaerosci.2007.01.004.

J.B. McLaughlin. Inertial migration of a small sphere in linear shear flows. *Journal of Fluid Mechanics*, 224:385–400, 1965. URL http://dx.doi.org/10.1017/S0022112091001751.

John B. McLaughlin. Aerosol particle deposition in numerically simulated channel flow. *Physics of Fluids A*, 1:1211, 1989. URL `http://dx.doi.org/10.1063/1.857344`.

C. J. Meyer and D. A. Deglon. Particle collision modeling - a review. *Minerals Engineering*, 24:719–730, 2011. URL `http://dx.doi.org/10.1016/j.mineng.2011.03.015`.

F. Nicoud and F. Ducros. Subgrid-scale stress modelling based on the square of the velocity gradient tensor. *Flow, Turbulence and Combustion*, 62:183–200, 1999. URL `http://dx.doi.org/10.1023/A:1009995426001`.

Masanobu Oda, Junichi Konishi, and SiavoucheNemat-Nasser. Experimental micromechanical evaluation of strength of granular materials: Effects of particle rolling. *Mechanics of Materials*, 1:269–283, 1982. URL `http://doi.org/10.1016/0167-6636(82)90027-8`.

Eric J. R. Parteli, Jochen Schmidt, Christina Brümel, Karl-Ernst Wirth, Wolfgang Peukert, and Thorsten Pöschel. Attractive particle interaction forces and packing density of fine glass powders. *Nature Scientific Reports*, 4:1–7, 2014. URL `http://dx.doi.org/10.1038/srep06227`.

Stephen K. Robinson. Coherent motions in the turbulent boundary layer. *Annual Review of Fluid Mechanics*, 23:601–639, 1991. URL `http://dx.doi.org/10.1146/annurev.fl.23.010191.003125`.

P.G. Saffman and J.S. Turner. On the collision of drops in turbulent clouds. *Journal of Fluid Mechanics*, 1:16–30, 1956. URL `http://doi.org/10.1017/S0022112056000020`.

M. Sommerfeld and S. Stübing. A novel lagrangian agglomerate structure model. *Powder Technology*, 319:34–52, 2017. URL `http://dx.doi.org/10.1016/j.powtec.2017.06.016`.

D. Tabor. Surface forces and surface interactions. *Journal of Colloid and Interface Science*, 58:2–13, 1977. URL `http://dx.doi.org/10.1016/0021-9797(77)90366-6`.

C. Thornton. Interparticle sliding in the presence of adhesion. *Journal of Physics D: Applied Physics*, 24:1942–1946, 1991. URL `http://doi.org/10.1088/0022-3727/24/11/007`.

C. Thornton and K.K. Yin. Impact of elastic spheres with and without adhesion. *Powder Technology*, 65:153–166, 1991. URL `http://dx.doi.org/10.1016/0032-5910(91)80178-L`.

Nomenclature

$\text{Ad} = \gamma/(\rho_\text{p} U^2 d_\text{p})$	Adhesiveness parameter	-
$\text{Fr} = U/\sqrt{g_\text{r} d_\text{p}}$	Froude number	-
D	Pipe diameter	m
d_p	Particle diameter	m
$g_\text{r} = (1 - 1/\chi)g$	Buoyancy corrected gravity	m/s^2
$\text{Kn} = \lambda/d_\text{p}$	Knudsen number	-
L	Length of pipe section	m
p	Pressure	Pa
R	Effective particle radius	m
R	Pipe radius	m
r	Particle radius	m
r	Radial position	m
t	Time	s
$t^+ = tU/D$	Dimensionless time	-
U	Fluid bulk velocity	m/s
V	Cell volume	m^3
$\text{Re} = U\rho_\text{f} D/\mu$	Reynolds number	-
$\text{St} = \rho_\text{p} d_\text{p}^2 U/(18\mu D)$	Stokes number	-

Greek letters

δ	Kroneckers delta	-
δt	Time step size	s
Δ	Cell length	m
$\Delta\gamma/\gamma$	Adhesion hysteresis parameter	-
$\epsilon = d_\text{p}/D$	Dimensionless particle diameter	-
$\lambda = E/(\rho_\text{p} U^2)$	Elasticity parameter	-
λ	Mean free molecular path	m
μ	Dynamic viscosity	kg/(m·s)
ρ	Density	kg/m^3
τ	Response time	s
$\chi = \rho_\text{p}/\rho_\text{f}$	Density ratio	-

Subscripts

f	Fluid
i,j	particle indices
mod	Stiffness-modified values
p	Particle
x, y, z	Spatial coordinates

Superscripts

—	Filtered values
+	Viscous units

Acronyms

sgs	Sub-grid scale
CFD	Computational Fluid Dynamics
DEM	Discrete Element Method
DNS	Direct Numerical Simulation
LES	Large Eddy Simulation
WALE	Wall-Adapting Local Eddy-viscosity

Appendix C

On the fully-developed heat transfer enhancing flow field in sinusoidally, spirally corrugated tubes using computational fluid dynamics

J. Hærvig, K. Sørensen, T.J. Condra

On the fully-developed heat transfer enhancing flow field in sinusoidally, spirally corrugated tubes using computational fluid dynamics

J. Hærvig, K. Sørensen, T.J. Condra

Aalborg University, Department of Energy Technology, Pontoppidanstræde 111, DK-9220 Aalborg, Denmark

Abstract

A numerical study has been carried out to investigate heat transfer enhancing flow field in 28 geometrically different sinusoidally, spirally corrugated tubes. To vary the corrugation, the height of corrugation e/D and the length between two successive corrugated sections p/D are varied in the ranges 0 to 0.16 and 0 to 2.0 respectively. The 3D Unsteady Reynolds-averaged Navier-Stokes (URANS) equations combined with the transition SST turbulence model are solved using the finite volume method to obtain the fully-developed flow field in a repeatable section of the heat exchangers at a constant wall temperature and at $Re = 10,000$. By studying the wide range of geometrically different tubes, the flow conditions vary significantly.

At low corrugation heights, only a weak secondary flow centred in the corrugated section is present. At higher corrugations heights, the tangential velocity component increases and eventually exceeds the axial velocity component causing the highest pressure to be located at the centre of the corrugated section. At these high corrugation heights, a further increase in corrugation height will at best only result in a small increase in Nusselt number but at a significantly higher pressure loss. To assess the performance as a heat exchanger, the ratio of enhanced Nusselt number to enhanced friction factor $\eta = (Nu/Nu_s)/(f/f_s)^{1/3}$ compared to the non-corrugated tube is used. Using this parameter, the simulations show a decrease in performance at higher corrugation heights. To link the detailed flow fields to the performance as a heat exchanger, non-dimensional correlations for heat transfer, pressure loss, and performance parameter are given.

C.1   Introduction

Transferring heat through a straight tube is used in numerous applications. These applications include, but are not limited to, power generation, air-conditioning, petrochemical, and diary applications. Two distinct different

techniques for enhancing heat transfer are commonly used; namely a passive or active, where the active requires additional power input whereas the passive does not. Therefore, the passive technique is commonly used where the geometry is altered in a more of less sophisticated manner deforming the thermal boundary layer, creating recirculating local flow structures, or larger secondary flow structures flowing tangentially to the main flow. All these phenomena affect both heat transfer and friction characteristics.

To enhance the forced convection inside a passive heat exchanger tube, two different methods are typically used. One method is to alter the flow by changing the inner geometry of the tube. Another method is to insert loose or fastened geometrical inserts filling the cross-section of the tube, thereby promoting mixing resulting in enhanced heat transfer. These techniques do in general increase the pressure loss as well, which results in the best geometry having an optimal combination of increased heat transfer at slightly higher pressure loss. As a result, numerous studies have already been carried out to investigate the effect of both spirally and transversely tube corrugation. Ganeshan and Rao (1982) investigated the effect of Prandtl number in seven different spirally corrugated tubes having different width and height of corrugation while suggesting the ratio between heat exchanger capacity to pumping power to be 100 to 150 % more efficient for $Pr = 4.3$ than for $Pr = 109$. As a result, this study suggests the spirally corrugated tubes to be attractive especially for fairly viscous fluids with high Prandtl numbers.

Zimparov et al. (1991) conducted experiments on 25 spirally corrugated tubes having pitch heights e/D in the range 0.017 to 0.046 and pitch length in the range 0.25 to 0.65. The study found heat transfer enhancement factors ranging from 1.77 to 2.73 while the friction factor was increased from 100 to 400 %.

While most studies focus on the region unaffected by entrance effects, Rainieri and Pagliarini (2002) investigated entrance for highly viscous fluids with Reynolds number ($90 < Re < 800$) using experiments and found that even a high swirl component does not always result in enhanced heat transfer for $200 < Re < 800$.

The number of studies on corrugated tubes of different shapes are increasing in literature. They range from twisted square ducts (Bhadouriya et al. (2015)), twisted oval tubes (Tan et al. (2013)), sinusoidal transversely corrugated tubes (Zheng et al. (1990)), to more commonly reported corrugated tubes of different shapes. Ağra et al. (2011) does a numerical study on two corrugated and two helically finned tubes and while concluding that the helically finned tubes generally have better heat transfer and higher pressure loss, more studies should be carried out on a wider range of geometrical parameters to investigate the detailed flow. Han et al. (2012) investigated convex corrugated tubes using 2D axisymmetric CFD simulations. The study concluded that asymmetric corrugated tubes exhibit an increased heat transfer

performance of 8-18% compared to symmetric corrugated tubes. Mohammed et al. (2013) reported integral values of heat transfer and pressure loss for tubes categorised by pitch height, rib height and rib width. The study concluded that of the geometries investigated, the highest Nusselt number was obtained for the highest height and width and lowest pitch. Han et al. (2016) investigated opposite flow directions in the same corrugated tubes and found that the larger corrugation radius should be located in the upstream direction for corrugations described by two corrugation radii.

The more recent study by Vicente et al. (2004) presents a systematic investigation where both the Reynolds and Prandtl numbers are varied from 2000 to 90,000 and 2.9 to 92 respectively for ten different corrugated tubes. Furthermore, the study gives an overview of different correlations presented in literature and concludes that for the same corrugation type, the published results deviate by a factor of 1.3 to 3 in friction factor augmentation and between 1.2 to 2 for Nusselt number augmentation. Likewise, the literature overview by Kareem et al. (2015) gives a great overview of all the studies published in the period 1977 to 2015. The study clearly shows that the number of publications on passive heat transfer enhancement has increased in recent years, which is attributed an increased awareness of energy savings. Furthermore, the study concludes that even though quite a number of studies already have been published, more parameters should be investigated to cover larger design spaces.

While a large number of experimental studies on different spirally corrugated tubes have been carried out, more detailed studies on the flow field in various corrugations are limited. This study presents a systematic approach where geometrical changes are made to the sinusoidally, corrugated tube by varying the corrugation height and length. Furthermore, the effects of changing the geometry are quantified by comparing to non-dimensional maps for heat transfer and pressure loss.

C.2 Geometry and Parameters of Interest

C.2.1 Terminology and representation of the geometry

The geometry in this study is fully described by two parameters; a corrugation height and a corrugation length. Depending on the type of corrugated tube, different sets of dimensionless numbers are typically used to describe the geometry. For sinusoidally corrugated tube investigated in this study, the geometry is fully described by two numbers; a corrugation height and length defined as:

1. Corrugation length p: the corrugation length being the stream-wise distance between two successive points where the geometry repeats itself.

2. Corrugation height e: the corrugation height being the constant distance between the surface of corrugated tube and the non-corrugated tube with same diameter.

While including a lot of parameters defining the corrugations, numerous studies have shown that two main parameters are required to describe the performance; namely corrugation height and length. The purpose of this study is therefore to vary these parameters widely. To make the results applicable to any size of corrugated tube, the rest of the study reports corrugation heights and lengths made non-dimensional with the tube diameter, forming Π_1 and Π_2:

$$\Pi_1 = p/D \tag{C.1}$$
$$\Pi_2 = e/D \tag{C.2}$$

The tubes in this study differ from other studies by having a perfect circular cross-section. Corrugation is therefore introduced by having a centre line that twists in the stream-wise direction. The centre line section for one repeatable part of heat exchanger geometry is described by the sinusoidal function in (C.3) for $t \in [0; 1]$:

$$
\begin{aligned}
x(t) &= e \cdot \sin(2\pi t) \\
y(t) &= e \cdot \cos(2\pi t) \\
z(t) &= p \cdot t
\end{aligned}
\tag{C.3}
$$

Based on the parametric representation in (C.3), the geometries will take the form shown in figure C.1.

C.2.2 Normalisation and performance parameters

The quantities reported in this study are all made non-dimensional. All velocities are normalised by the stream-wise bulk velocity u_b and all temperatures by the bulk temperature T_b. The bulk velocity is based on the stream-wise velocity component z of the velocity field. The bulk velocity and temperature at position z along the tube length are defined as:

$$u_b(z) = \frac{1}{A} \int \int u_z(z, r, \theta) \, dr d\theta \tag{C.4}$$

$$T_b(z) = \frac{1}{A} \int \int \frac{T(z, r, \theta) \, u(z, r, \theta)}{u_b(z)} dr d\theta \tag{C.5}$$

Where A denotes the cross-sectional area of the tube. To report flow velocities, the Reynolds number based on the bulk velocity is used. To evaluate and compare the performance of the different corrugated tubes, two dimensionless quantities describing the heat transfer and pressure loss are used. In
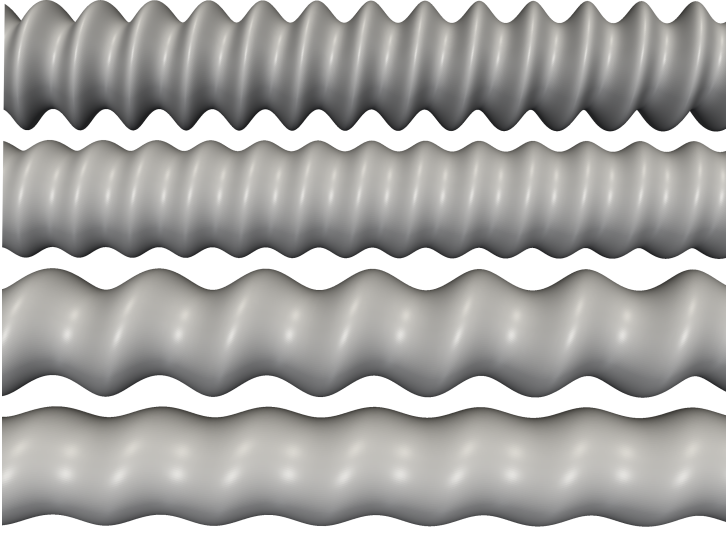
Figure C.1: Examples of spirally corrugated tubes having different corrugations. From top to bottom: Tube 1: $p/D = 0.5$, $e/D = 0.10$; Tube 2: $p/D = 0.5$, $e/D = 0.05$; Tube 3: $p/D = 1.0$, $e/D = 0.10$; Tube 4: $p/D = 1.0$, $e/D = 0.05$.

the case of corrugated tubes, two distinct different phenomena contributed to the pressure loss; wall shear stresses related to the local velocity gradients normal to the tube surface, and pressure drag related to the local pressure distribution along the surface. By integrating the two over the surface and averaging yields a single friction factor parameter that takes both into account and is a direct measure of the pressure loss in the tube. The Darcy-Weisbach friction factor describing pressure loss and Nusselt number describing heat transfer are defined as:

$$f = \Delta p \frac{2}{\rho u_b^2} \frac{D}{p} \tag{C.6}$$

$$\mathrm{Nu} = \frac{hD}{k} \tag{C.7}$$

where δp is the pressure loss over the periodic section with stream-wise length p. To evaluate the performance of the corrugated tubes, numerous criteria have been proposed in studies by Bergles et al. (1974) and Webb (1981). In this study, the purpose is to increase heat transfer performance while maintaining the same pumping power power. In the case of constant inlet temperature and no additional thermal resistances due to for example fouling, Webb (1981) suggests the criterion given by eq. (C.8) for constant Re and Pr. This criterion has been used in numerous studies to evaluate changes

in heat exchanger geometries (Han et al., 2016), (Pethkool et al., 2011):

$$\eta = \frac{\mathrm{Nu}/\mathrm{Nu_s}}{(f/f_s)^{1/3}} \tag{C.8}$$

where subscript s denotes non-corrugated tubes ($e/D = 0$). As reference for the non-corrugated tubes, the widely accepted correlations for the straight tube suggested by Gnielinski (1976) and Filonenko (1960) are used:

$$\mathrm{Nu_s} = \frac{(f_s/8)\,(\mathrm{Re} - 1000)\,\mathrm{Pr}}{1 + 12.7\sqrt{(f_s/8)}\left(\mathrm{Pr}^{\frac{2}{3}} - 1\right)}\left[1 + \left(\frac{D}{L}\right)^{\frac{2}{3}}\right]K \tag{C.9}$$

$$f_s = \left(1.8\,\log_{10}\mathrm{Re} - 1.5\right)^{-2} \tag{C.10}$$

where tube diameter to total pipe length ratio D/L takes entrance effects into account. In this study where the fully-developed flow is investigated by using stream-wise periodicity, this term equals zero. The correction factor K used for this study is $(T_b/T_w)^n$ with n being 0.45 as discussed by Hufschmidt and Burck (1968) and Jakovlev (1960).

C.3 Numerical Setup

C.3.1 Governing equations

The governing equations being solved are the URANS (Unsteady Reynolds-averaged Navier-Stokes) equations. That is, the continuity (C.11) and momentum (C.12) equations are solved respectively:

$$\frac{\partial \bar{u}_i}{\partial x_i} = 0 \tag{C.11}$$

$$\frac{\partial \bar{u}_i}{\partial t} + \frac{\partial \left(\bar{u}_i \bar{u}_j\right)}{\partial x_j} = -\frac{1}{\rho}\frac{\partial \bar{p}}{\partial x_i} + \frac{\partial}{\partial x_j}\left((\nu + \nu_t)\frac{\partial \bar{u}_i}{\partial x_j}\right) + \beta \delta_{3,i} \tag{C.12}$$

where the last term in equation (C.12) is added to account for the pressure loss in the periodic domain using the in-built function in ANSYS Fluent. The β term is found by iteration in Fluent to account for the pressure loss over the small periodic section being modelled. To make the temperature field periodic, the periodic heat transfer model in Fluent is used where equation (C.13) is being solved:

$$\frac{\partial \theta}{\partial t} + \frac{\partial \bar{u}_j \theta}{\partial x_j} = \frac{\partial}{\partial x_j}\left(\frac{\partial \theta}{\partial x_j}\left(\frac{\nu}{\mathrm{Pr}} + \frac{\nu_t}{\mathrm{Pr_t}}\right)\right) \tag{C.13}$$

where the eddy-viscosity ν_t is the additional viscosity due to the turbulent scales being modelled using the URANS approach. In this study, the transition SST turbulence model is used to model turbulence. The transition SST turbulence model combines transition modelling by Menter et al. (2006) and the standard SST model by Menter (1992). Using the transition SST turbulence model, the boundary layer separation downstream a corrugation is more accurately predicted. The following explains the momentum source term $\beta\delta_{3,i}$ and the scaled temperature field θ.

Stream-wise periodicity

As the flow in the majority of the heat exchanger tubes is both hydrodynamically and thermally fully developed, focus will be on this part of the heat exchanger. Instead of simulating the whole heat exchanger starting with a non-developed flow and dealing with how the flow develops hydrodynamically and thermally, periodic boundaries are utilised to couple the inlet and outlet. Using this approach, the inlet and outlet are two-way coupled and therefore a driving force is required to balance out the pressure loss to keep the fluid flowing. Likewise, modifications are required to keep the temperature from asymptotically approaching the wall temperature. All turbulent properties used for SST transition turbulence modelling are made periodic as well, so that the values at the inlet and outlet boundaries are obtained as the simulation converges. Therefore all boundary values at the periodic inlet and outlet are obtained during convergence. The approach suggested by Patankar et al. (1977) is used to make both the temperature and pressure field repeat itself in a periodic manner. Therefore the $\beta\delta_{3,i}$ term is added to eq. (C.12) to make the pressure and velocity field periodic. When using this approach, only the computational domain shown in figure C.2 is used. Assuming a constant wall temperature, the fully-developed temperature field is obtained by solving for the scaled temperature field θ as suggested by Patankar et al. (1977):

$$\theta(x,y,z) = \frac{T(x,y,z) - T_w}{T_z{}^* - T_w} \tag{C.14}$$

where $T(x,y,z)$ is the temperature field, T_w is the constant wall temperature, and $T_z{}^*$ is a local reference temperature profile at the inlet. The reference temperature $T_z{}^*$ at stream-wise position z is given by the following integral over the cross-sectional surface A:

$$T_z{}^* = \frac{\int_A T |\rho\vec{u} \cdot \mathrm{d}\vec{A}|}{\int_A |\rho\vec{u} \cdot \mathrm{d}\vec{A}|} \tag{C.15}$$

That is, solving eq. (C.14) yields the stream-wise periodic temperature profile, which is used directly to evaluate the local heat transfer coefficient and consequently Nusselt numbers.
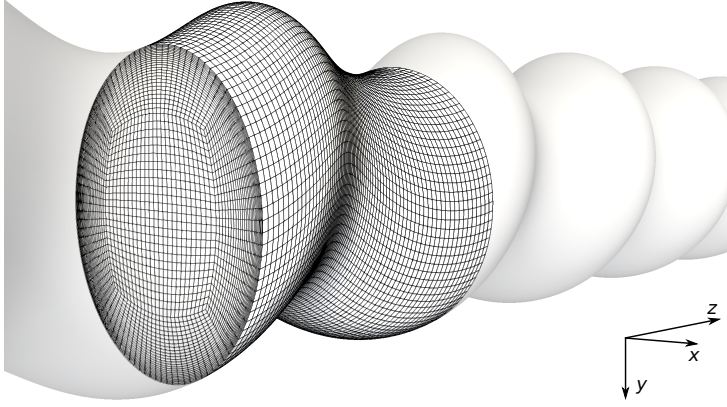
Figure C.2: Overview of the computational mesh and the stream-wise periodic boundaries used.

C.3.2   Numerical procedures

Simulations are carried out using the commercial ANSYS Fluent 16.2 software. The governing equations are discretised using the finite volume method. The pressure and temperature equations are discretised using a 2nd order schemes, while the momentum equation is discretised using a 2nd order upwind scheme. Turbulent kinetic energy, specific dissipation rate, intermittency, and momentum thickness Reynolds number are all solved using 1st order upwind scheme. The transient term is discretised using a 1st order implicit formulation. To couple the velocity and pressure fields, the SIMPLE algorithm is used.

C.3.3   Mesh topology

Structured meshes consisting of hexahedral elements are formed using the meshing tool blockMesh. A quarter of the cross-sectional mesh is shown in figure C.3 while the overall mesh is visualised in figure C.2. The cross-sectional mesh is extruded along the path described by (C.3) resulting in a structured mesh having the same cross-sectional mesh along the length of the tube. The first cell normal to the wall is placed at $y^+ \approx 1$ to resolve the viscous sub-layer part of the boundary layer. Figure C.4 and C.5 shows the quality of the mesh in terms of cell angles defined by orthogonal quality and equiangular skew quality defined as:

$$\text{Orthogonal quality} = \max \left[\frac{\theta_{\max} - \theta_{\mathrm{e}}}{180° - \theta_{\mathrm{e}}}, \frac{\theta_{\mathrm{e}} - \theta_{\min}}{\theta_{\mathrm{e}}} \right] \tag{C.16}$$

$$\text{Equiangular skew} = \min \left[\frac{\boldsymbol{A} \cdot \boldsymbol{f}}{|\boldsymbol{A}||\boldsymbol{f}|}, \frac{\boldsymbol{A} \cdot \boldsymbol{c}}{|\boldsymbol{A}||\boldsymbol{c}|} \right] \tag{C.17}$$
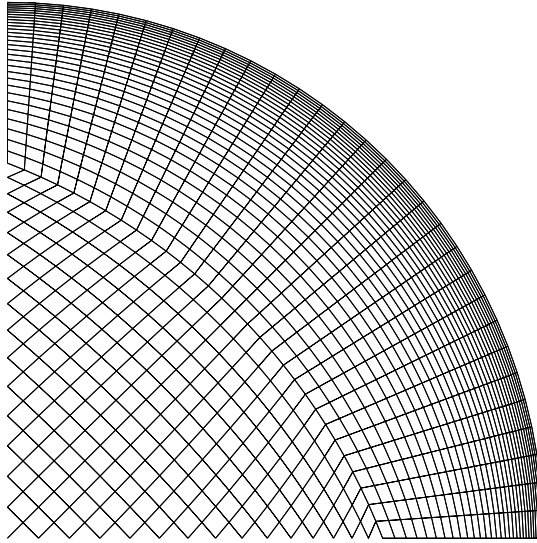
Figure C.3: Overview of the computational mesh visualised by a quarter of the cross-sectional mesh.
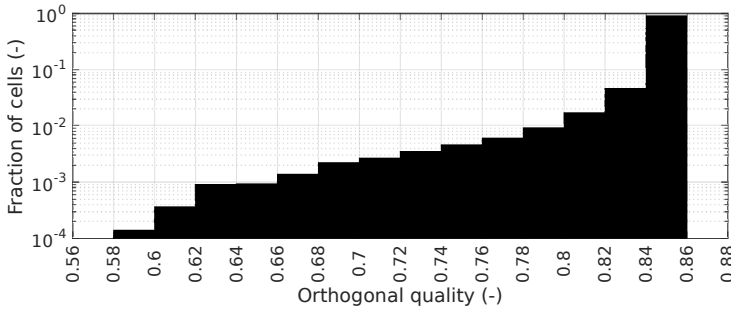
Figure C.4: Overview of orthogonal quality for the mesh.

where $\theta_e = 90°$ for the hexahedral elements in this study. In (C.17), A is a face cell normal vector, f is vector from the cell centroid to the face centroid and c is a vector between two adjacent cell centroids. As shown in figure C.4 and C.5, 90.4 % of the cells have a high orthogonal quality above 0.84 and 98.2 % have an equiangular skew quality below 0.36. The first boundary layer cells have a maximum aspect ratio of 24.

C.3.4 Validation of results

To ensure the results reported in this study are reliable, two measures are taken. First, the number of cells is approximately doubled until the results are
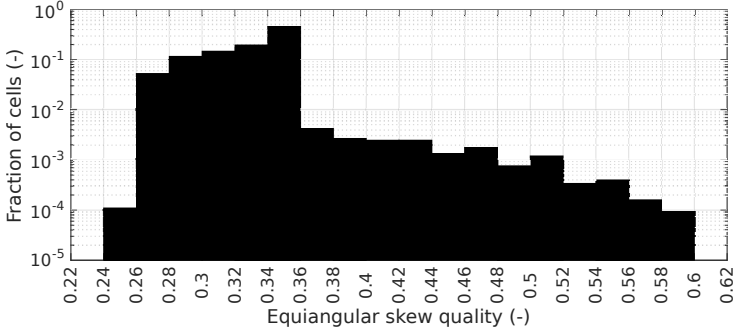
Figure C.5: Overview of equiangular skew quality for the mesh.
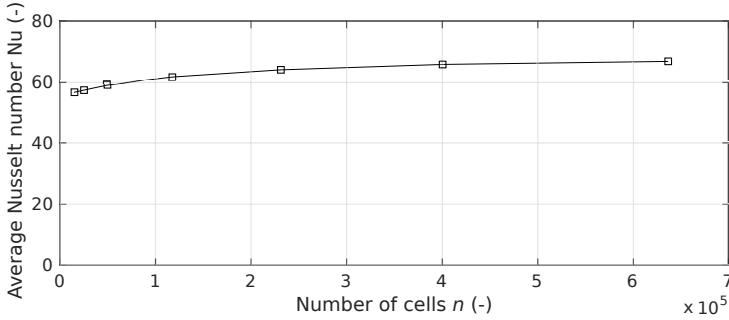
Figure C.6: Grid independence study to investigate the importance of cell count for a corrugated pipe ($\Pi_1 = 1$ and $\Pi_2 = 0.1$).

well within the asymptotic range and close to the estimated true numerical value. For all meshes, the first cell height is placed within the viscous sub-layer at $y^+ \approx 1$ so that the transition SST turbulence model is applicable. Figure C.6 shows the grid convergence study in terms of average Nusselt number. To estimate the numerical error, Richardson extrapolation is used as suggested by Roache (1994). To check whether the different meshes are within the asymptotic range of the true numerical value for zero grid spacing, the order of convergence p is estimated as:

$$p = \frac{\ln\left[\frac{f_3 - f_2}{f_2 - f_1}\right]}{\ln(r)} \tag{C.18}$$

where f_1, f_2 and f_3 refer to values obtained by the finest, second finest and third finest grids respectively while r refers to grid refinement ratio between two successive grid refinements. Using Richardson extrapolation, the true
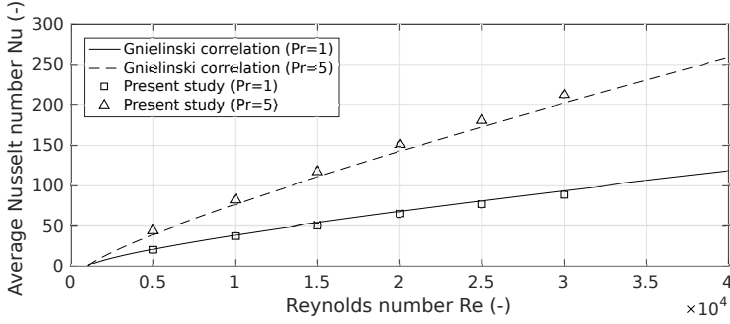
Figure C.7: Comparison to the Gnielinski correlation ($\Pi_1 = 1$ and $\Pi_2 = 0$).
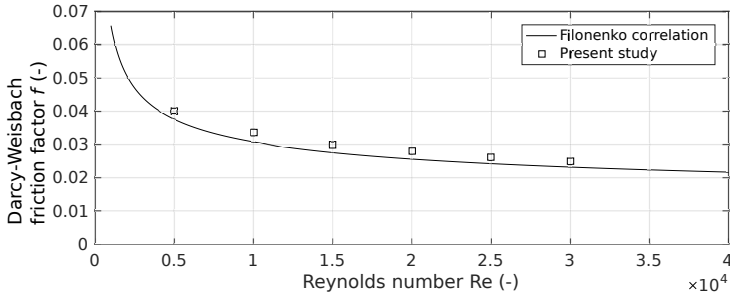
Figure C.8: Comparison to the Filonenko correlation ($\Pi_1 = 1$ and $\Pi_2 = 0$).

value at zero grid spacing f_0 is estimated as (Roache, 1994):

$$f_0 \approx f_1 + \frac{f_1 - f_2}{p^r - 1} \tag{C.19}$$

To estimated the required grid resolution, the grid convergence index (GCI) proposed by Roache (1994) is used:

$$\text{GCI}_n = \frac{F_s |\epsilon|}{r^p - 1} \tag{C.20}$$

where F_s is a safety factor, ϵ is the relative error between two grids $\epsilon = (f_n - f_{n+1})/f_n$. Using a safety factor of 3.0, grid refinement factors $\text{GCI}_{12} = 0.037$ and $\text{GCI}_{23} = 0.067$ are obtained. In this study, the Nusselt number obtained by the mesh having 400,500 cells is within the error band $\text{Nu}_0 \pm \text{Nu}_0 \cdot \text{GCI}_{12}$ and therefore the mesh having 400,500 cells is used for the rest of the simulations.

The results obtained for a straight tube ($\Pi_1 = 1$, $\Pi_2 = 0$) are in figure C.7 and C.8 compared to eq. (C.9) and (C.10) by Gnielinski (1976) and Filonenko (1960) for various Reynolds and Prandtl numbers. The comparison suggests the CFD simulations to be able to predict smooth pipe performance. For
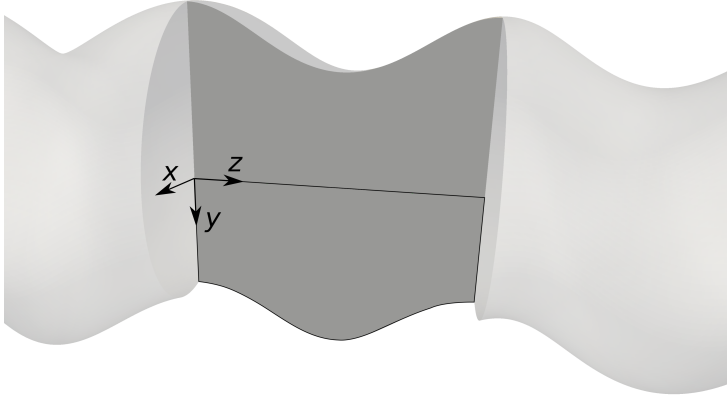
Figure C.9: Region outlined with black is used for visualisation of the flow field. Note the upper half shows the exact same flow field but is shifted half a period.

the results in figure C.7 and C.8, the Nusselt numbers and friction factors numbers are within a maximum deviation of 5.4 % and 8.6 % respectively.

C.4 Detailed Flow Field

To understand the mechanisms governing heat transfer and pressure loss, the flow is visualised in a wide range of geometrically different corrugated tubes. The flow fields are plotted in the representative periodic region shown with black in Fig. C.9. The region outlined in Fig. C.9 gives a complete overview of the three-dimensional fully-developed flow field. That is, all quantities of interest such as velocity, pressure and temperature at $z = 0$ for positive y-values are the same at $z = D \cdot \Pi_1 / 2$ (middle of periodic section) for negative y-values.

To generalise the observations, all quantities of interest are reported in dimensionless quantities. The position in the tube is made non-dimensional by the tube diameter D. The static pressure in the tube is reported using the pressure coefficient C_p, which is the ratio between static pressure and the dynamic pressure based on the bulk velocity in:

$$C_\mathrm{p}(x,y,z) = \frac{p(x,y,z) - p_\infty}{\frac{1}{2}\rho u_\mathrm{b}^2} \tag{C.21}$$

Where the free stream pressure p_∞ is taken at the centre of the tube at $(x,y,z) = (0,0,0)$. The swirling flow is quantified by the ratio of absolute tangential velocity $|u_\mathrm{tan}|$ to bulk velocity u_b:

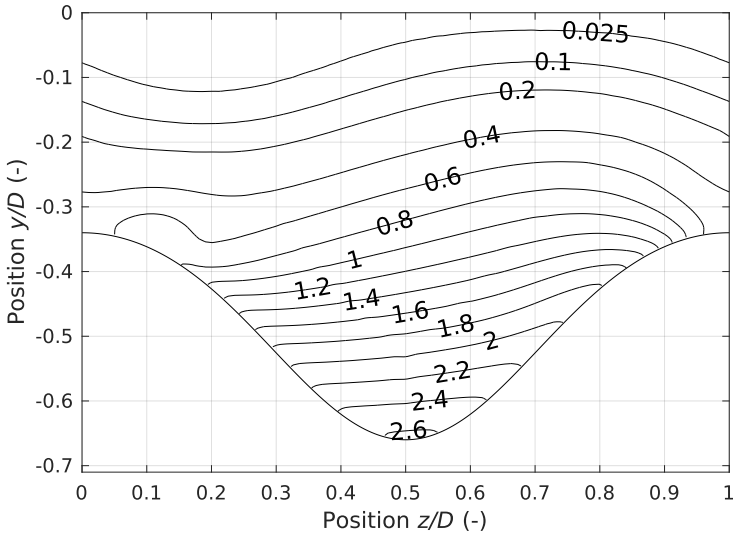$$\psi(x,y,z) = \frac{|u_\mathrm{tan}(x,y,z)|}{u_\mathrm{b}(z)} \tag{C.22}$$
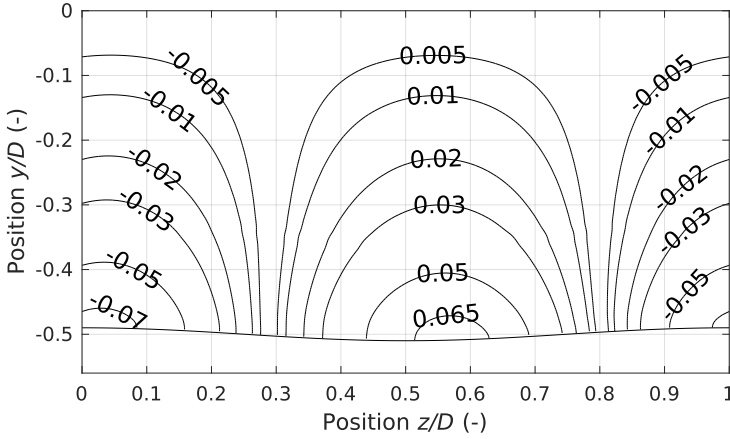
Figure C.10: Pressure field visualised by the pressure coefficient $C_p = (p - p_\infty) / (1/2\rho u_b^2)$ in a corrugated tube with corrugation height and length of $e/D = 0.01$ and $p/D = 1.0$ respectively at Re $= 10,000$.

Using this ratio, $\psi = 0$ corresponds to a purely axial flow, while values $\phi \geq 1$ shows regions where the tangential velocity locally exceeds the local axial flow. To quantify the re-circulation zones, a re-circulation factor is defined as the ratio of stream-wise velocity u_z to bulk velocity:

$$\phi(x, y, z) = \frac{u_z(x, y, z)}{u_b(z)} \tag{C.23}$$

Using this dimensionless number, re-circulation zones are visualised as having $\phi < 0$. In the following section, the corrugation height and length are varied and the corresponding changes in flow fields are reported using the above mentioned dimensionless numbers.

C.4.1 Effect of corrugation height on the flow field

In the following, changes in flow field caused by varying corrugation height from $e/D = 0.01$ to $e/D = 0.16$ are reported.

Pressure field

Fig. C.10 to C.13 show how changes in corrugation height affects the pressure field visualised by pressure coefficient given by (C.21). At a low corrugation $e/D = 0.01$, the point of maximum pressure is located close to the centre of corrugation $z/D \approx 0.55$ but with low pressure coefficients $C_p < 0.1$. At a slightly higher corrugation height of $e/D = 0.05$, the point of highest pressure coefficient is moved further downstream to $z/D \approx 0.7$, while the pressure coefficient is increased to 0.25. At both $e/D = 0.01$ and $e/D = 0.05$,
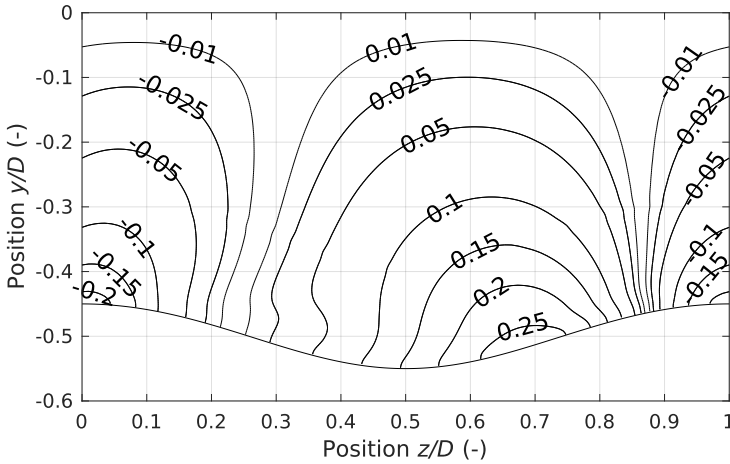
Figure C.11: Pressure field visualised by the pressure coefficient $C_\mathrm{p} = (p - p_\infty) / \left(1/2\rho u_\mathrm{b}^2\right)$ in a corrugated tube with corrugation height and length of $e/D = 0.05$ and $p/D = 1.0$ respectively at $\mathrm{Re} = 10,000$.
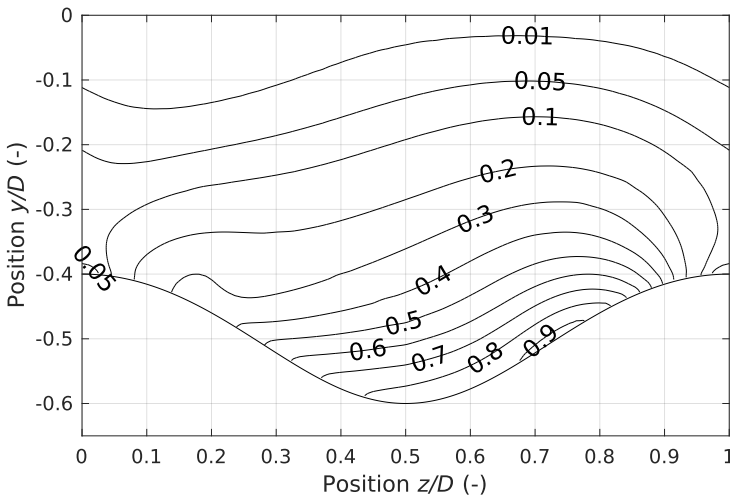
Figure C.12: Pressure field visualised by the pressure coefficient $C_\mathrm{p} = (p - p_\infty) / \left(1/2\rho u_\mathrm{b}^2\right)$ in a corrugated tube with corrugation height and length of $e/D = 0.10$ and $p/D = 1.0$ respectively at $\mathrm{Re} = 10,000$.

the pressure contours are orientated normal to the stream-wise direction. Increasing the corrugation height to $e/D = 0.10$ results in the point of highest pressure coefficient to move further downstream to $z/D \approx 0.75$, while pressure contours changes direction to be mostly stream-wise oriented revealing a significant swirl component, which is described below. At a extreme corrugation height of $e/D = 0.16$, the point of highest pressure coefficient is

Figure C.13: Pressure field visualised by the pressure coefficient $C_p = (p - p_\infty) / (1/2\rho u_b^2)$ in a corrugated tube with corrugation height and length of $e/D = 0.16$ and $p/D = 1.0$ respectively at Re $= 10,000$.

moved upstream again to the centre of corrugation $e/D = 0.5$ where the pressure coefficient obtains values $C_p \geq 2.6$. To explain the sudden change in orientation of pressure coefficient contours from $e/D = 0.05$ to $e/D = 0.10$, the swirling flow fields are presented in the following.

Swirling flow field

Fig. C.14 to C.17 show how changes in corrugation height from $e/D = 0.01$ to $e/D = 0.16$ affect the flow field in terms of swirl defined by (C.22).

At a low corrugation height $e/D = 0.01$, there is an insignificant swirl which is maximum at the centre of corrugation at $z/D \approx 0.5$. Increasing the corrugation height from $e/D = 0.01$ to $e/D = 0.05$ causes the swirl to increase by a factor 10, while still being located close to the corrugation centre at $z/D \approx 0.5$. Introducing more severe corrugation heights of $e/D = 0.10$ and $e/D = 0.16$, increases the swirl while moving the point of maximum swirl upstream. At an extreme corrugation height of $e/D = 0.16$, the point of maximum swirl is located in the first part of the corrugated section at $z/D \approx 0.25$. Furthermore, at this corrugation height, swirl numbers above 1 suggests that the tangential velocity exceeds the bulk velocity in most of the corrugated section of the tube. The result is a flow field that differs significantly from the flow field in tubes having lower corrugation heights with insignificant swirl.
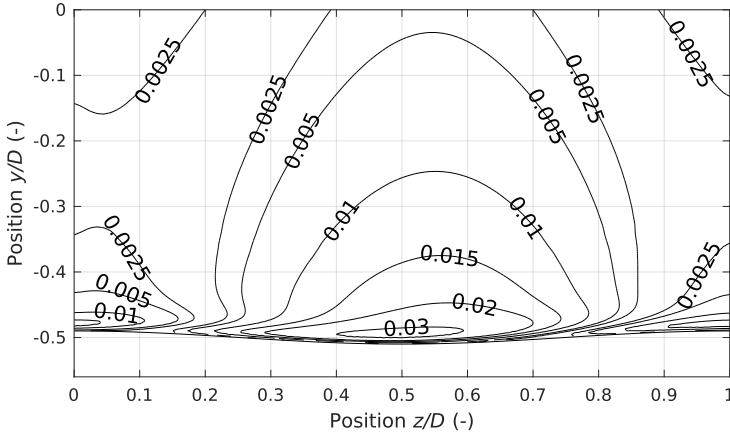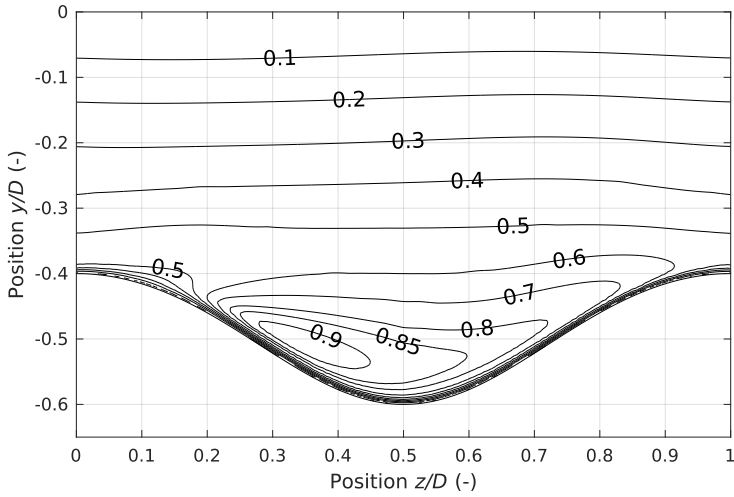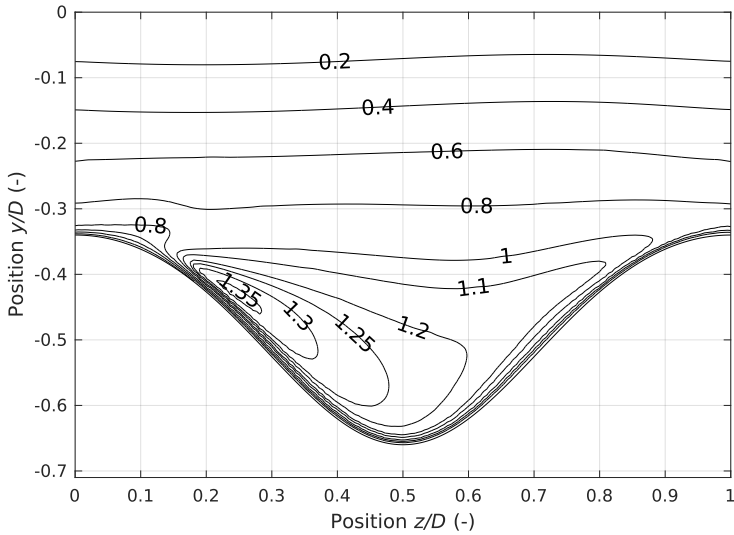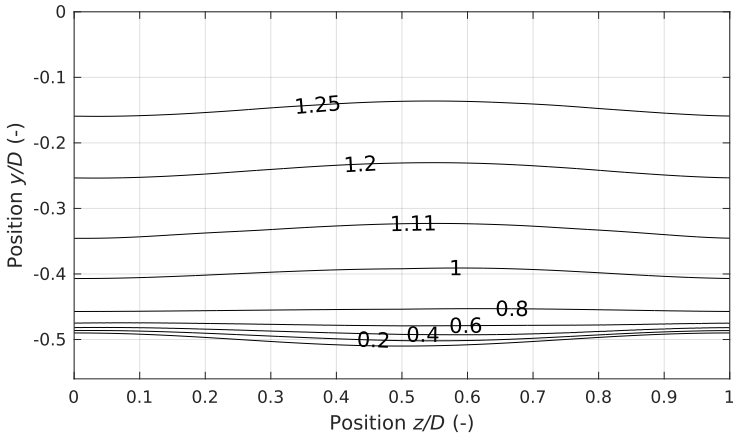
Figure C.14: Swirling flow field visualised by contours of $\psi = |u_{\text{tan}}|/u_{\text{b}}$ in a corrugated tube with corrugation height and length of $e/D = 0.01$ and $p/D = 1.0$ respectively at Re $= 10,000$.
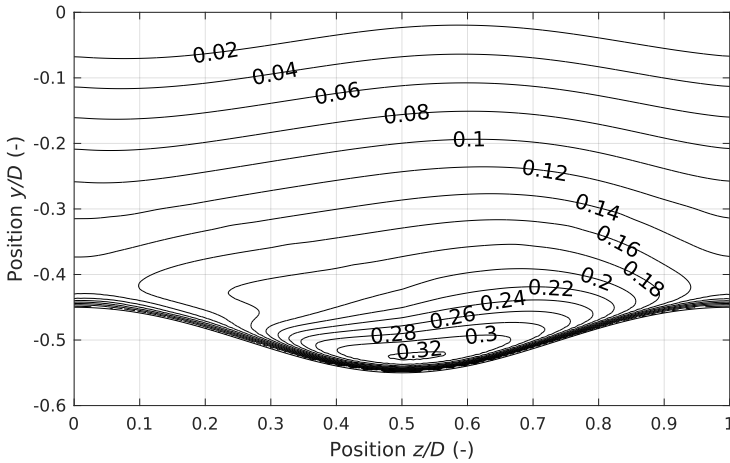
Figure C.15: Swirling flow field visualised by contours of $\psi = |u_{\text{tan}}|/u_{\text{b}}$ in a corrugated tube with corrugation height and length of $e/D = 0.05$ and $p/D = 1.0$ respectively at Re $= 10,000$.

Re-circulating flow field

Fig. C.18 to C.21 show how changes in corrugation height from $e/D = 0.01$ to $e/D = 0.16$ affect the flow field in terms of re-circulating flow field defined by (C.23). At a low corrugations height of $e/D = 0.01$, the flow stay attached to the surface and no re-circulation zone is formed. At a slightly higher corrugation height of $e/D = 0.05$, the strong adverse pressure gradient causes the flow to separate and form a re-circulation zone in the first part of the corrugation section. At a higher corrugation height of $e/D = 0.10$ with a significantly higher swirl, the re-circulation zone is almost eliminated
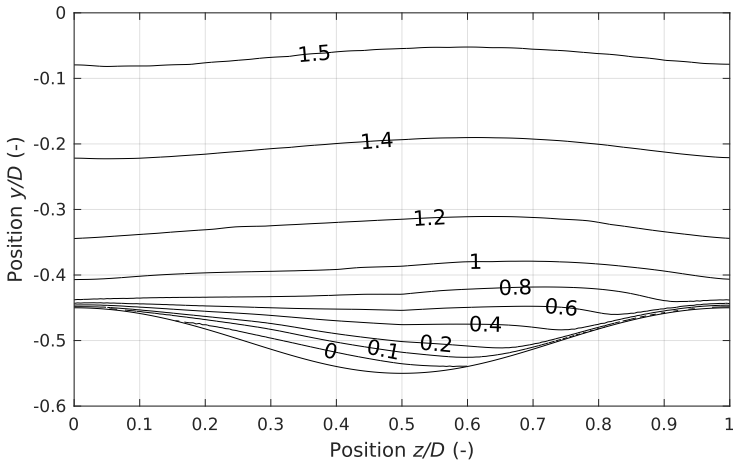
Figure C.16: Swirling flow field visualised by contours of $\psi = |u_{\text{tan}}|/u_b$ in a corrugated tube with corrugation height and length of $e/D = 0.10$ and $p/D = 1.0$ respectively at Re $= 10,000$.
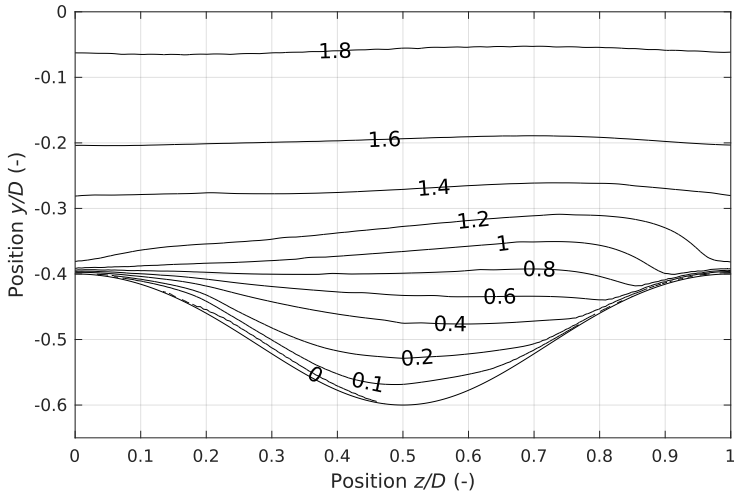

Figure C.17: Swirling flow field visualised by contours of $\psi = |u_{\text{tan}}|/u_b$ in a corrugated tube with corrugation height and length of $e/D = 0.16$ and $p/D = 1.0$ respectively at Re $= 10,000$.

compared to the lower corrugation height of $e/D = 0.05$. That suggests the high swirl to suppress the re-circulation zone. At a even higher corrugation height of $e/D = 0.16$, the re-circulation zone is completely eliminated as a result of highest pressure being located at the centre of the corrugation as already shown in Fig. C.13.

Figure C.18: Re-circulation zones visualised by axial flow component normalised bulk velocity $u_{\mathrm{axial}}/u_{\mathrm{b}}$ in a corrugated tube with corrugation height and length of $e/D = 0.01$ and $p/D = 1.0$ respectively at Re $= 10,000$.

Figure C.19: Re-circulation zones visualised by axial flow component normalised bulk velocity $u_{\mathrm{axial}}/u_{\mathrm{b}}$ in a corrugated tube with corrugation height and length of $e/D = 0.05$ and $p/D = 1.0$ respectively at Re $= 10,000$.

C.4.2 Effect of corrugation length on the flow field

In the following, changes in flow field as a result of varying the corrugation length from $p/D = 0.5$ to $p/D = 2.0$ are reported.

Figure C.20: Re-circulation zones visualised by axial flow component normalised bulk velocity $u_{\text{axial}}/u_{\text{b}}$ in a corrugated tube with corrugation height and length of $e/D = 0.10$ and $p/D = 1.0$ respectively at Re $= 10,000$.
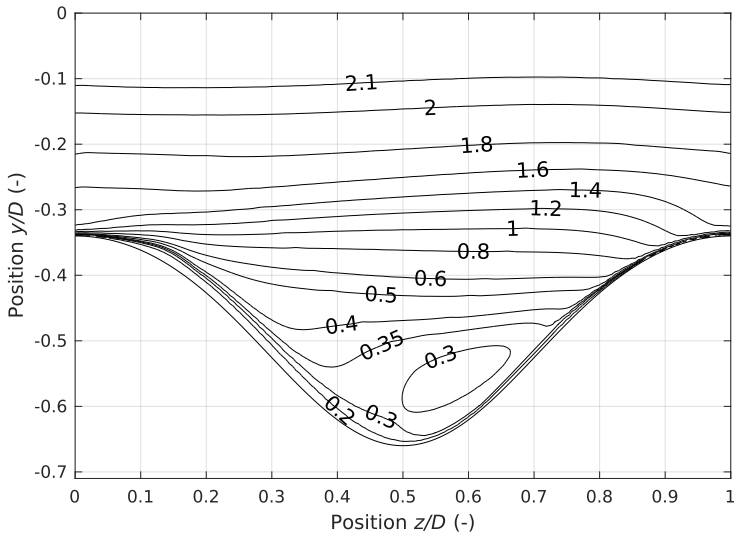

Figure C.21: Re-circulation zones visualised by axial flow component normalised bulk velocity $u_{\text{axial}}/u_{\text{b}}$ in a corrugated tube with corrugation height and length of $e/D = 0.16$ and $p/D = 1.0$ respectively at Re $= 10,000$.

Pressure field

Fig. C.22 to C.24 shows how lowering and increasing the corrugation length from $p/D = 0.10$ affects the pressure field in the corrugated tubes. The
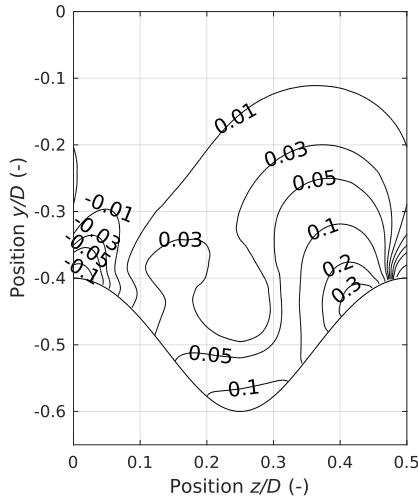
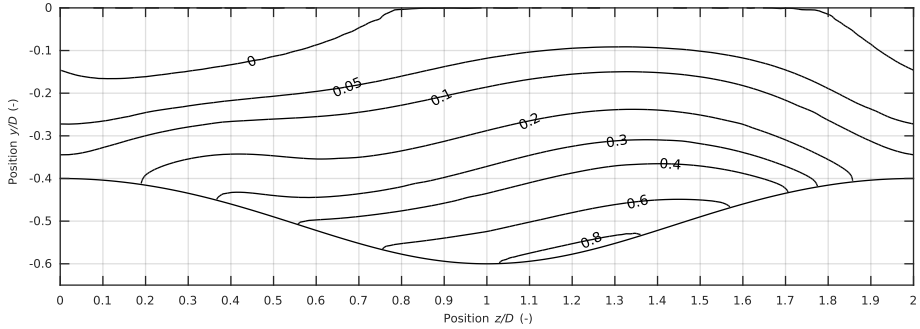**Figure C.22:** Pressure field visualised by the pressure coefficient $C_{\mathrm{p}} = (p - p_\infty) / \left(1/2\rho u_{\mathrm{b}}^2\right)$ in a corrugated tube with corrugation height and length of $e/D = 0.10$ and $p/D = 0.5$ respectively at Re $= 10,000$.
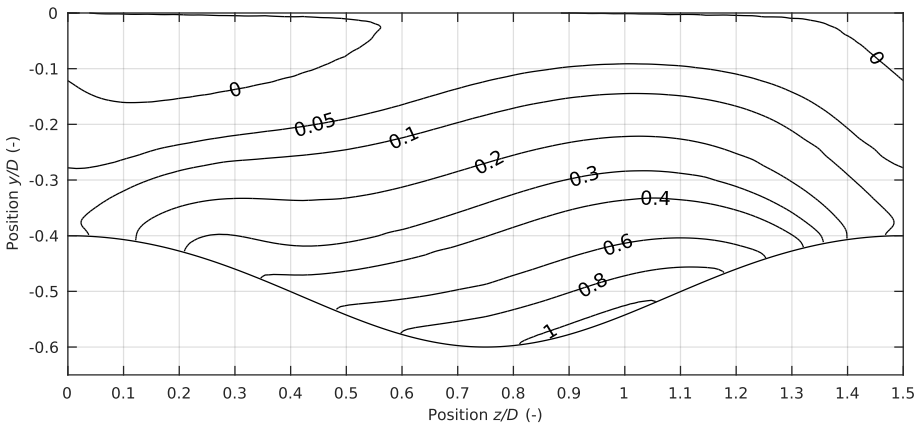

Figure C.23: Pressure field visualised by the pressure coefficient $C_{\mathrm{p}} = (p - p_\infty) / \left(1/2\rho u_{\mathrm{b}}^2\right)$ in a corrugated tube with corrugation height and length of $e/D = 0.10$ and $p/D = 1.5$ respectively at Re $= 10,000$.

case with $p/D = 0.10$ is already presented in Fig. C.12. Increasing the corrugation length from $p/D = 0.5$ to $p/D = 1.5$ causes the the maximum pressure coefficient to increase (Fig. C.22, C.12 and C.23). Furthermore, the location moves towards the centre of the corrugated section. Increasing the corrugation length further to $p/D = 2.0$, causes a slight decrease in maximum pressure coefficient. This can be explained by the tube approaching a non-corrugated tube as $p/D \to \infty$.

Figure C.24: Pressure field visualised by the pressure coefficient $C_p = (p - p_\infty) / \left(1/2\rho u_b^2\right)$ in a corrugated tube with corrugation height and length of $e/D = 0.10$ and $p/D = 2.0$ respectively at Re $= 10,000$.
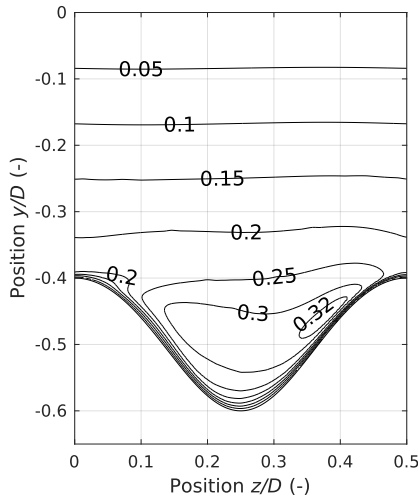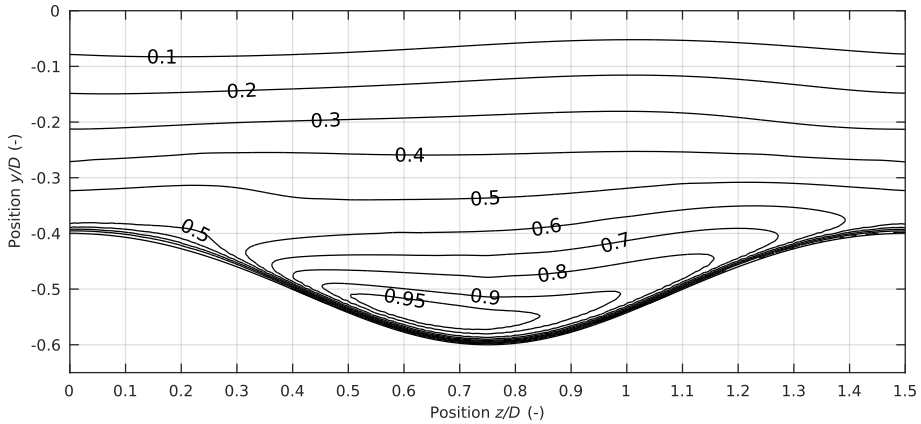

Figure C.25: Swirling flow field visualised by contours of $\psi = |u_{\text{tan}}|/u_b$ in a corrugated tube with corrugation height and length of $e/D = 0.10$ and $p/D = 0.5$ respectively at Re $= 10,000$.
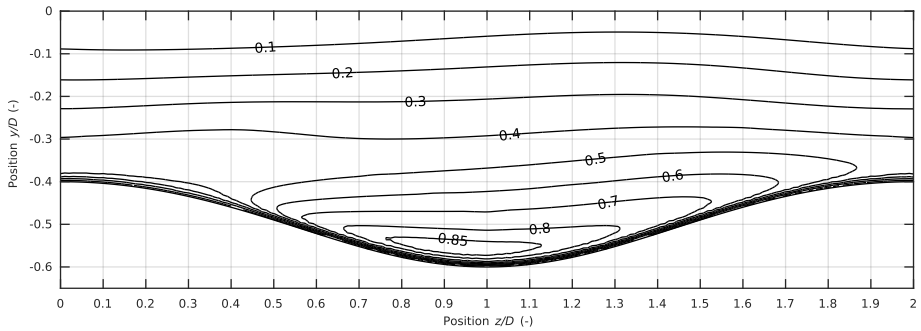
Swirling flow

Fig. C.25 to C.27 show how the swirling flow field is altered as the corruga-tion length is changed from a corrugation length of $p/D = 1.0$ to $p/D = 0.5$, $p/D = 1.5$ and $p/D = 2.0$. At a low corrugation length of $p/D = 0.5$, an almost swirl with almost constant magnitude is present in the corruga-tion section. When the corrugation length is increased from $p/D = 0.5$ to $p/D = 1.0$, the maximum swirl is increased from $\psi \approx 0.3$ to $\psi \approx 0.9$. With a further increase in corrugation length to $p/D = 1.5$, there is a minimal in-crease in swirl from $\psi \approx 0.9$ to $\psi \approx 0.95$, while the point of maximum swirl moves towards the centre of the corrugated section. Increasing the corruga-

185

Figure C.26: Swirling flow field visualised by contours of $\psi = |u_{\text{tan}}|/u_{\text{b}}$ in a corrugated tube with corrugation height and length of $e/D = 0.10$ and $p/D = 1.5$ respectively at Re $= 10,000$.
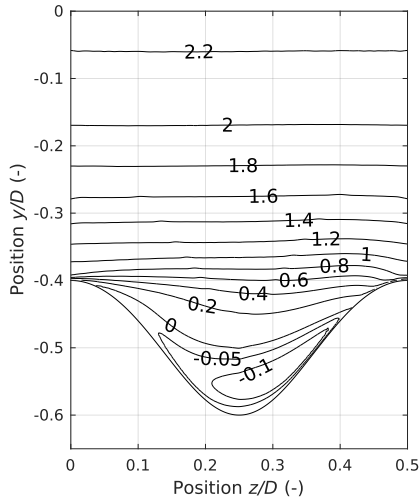

Figure C.27: Swirling flow field visualised by contours of $\psi = |u_{\text{tan}}|/u_{\text{b}}$ in a corrugated tube with corrugation height and length of $e/D = 0.10$ and $p/D = 2.0$ respectively at Re $= 10,000$.

tion length further to $p/D = 2.0$ results in decrease in swirl. This can be explained by the fact that the corrugated tube approaching a non-corrugated tube as $p/D \to \infty$, where no swirl is present.

Re-circulating flow field

Fig. C.28 to C.30 show how the stream-wise flow field is altered as the corrugation length is changed from a corrugation length of $p/D = 1.0$ to $p/D = 0.5$, $p/D = 1.5$ and $p/D = 2.0$. Decreasing the corrugation length from $p/D = 1.0$ to $p/D = 0.5$ causes the flow to separate and form a large re-circulation zone filling up most of the corrugation section. This can be explained by significantly lower swirl velocity at the low corrugation length of $p/D = 0.5$ compared to $p/D = 1.0$. Increasing the corrugation length to $p/D = 1.5$ and $p/D = 2.0$ eliminates the re-circulation zone present at lower

Figure C.28: Re-circulation zones visualised by axial flow component normalised bulk velocity u_{axial}/u_b in a corrugated tube with corrugation height and length of $e/D = 0.10$ and $p/D = 0.5$ respectively at Re $= 10,000$.
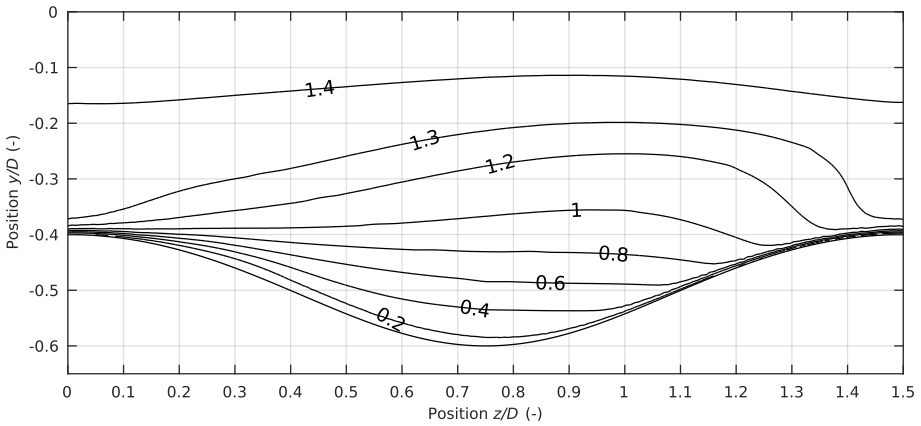
Figure C.29: Re-circulation zones visualised by axial flow component normalised bulk velocity u_{axial}/u_b in a corrugated tube with corrugation height and length of $e/D = 0.10$ and $p/D = 1.5$ respectively at Re $= 10,000$.

corrugations lengths of $p/D = 0.5$ and $p/D = 1.0$.

In the following section, the flow field presented in this section are linked to heat transfer and pressure loss characteristics.
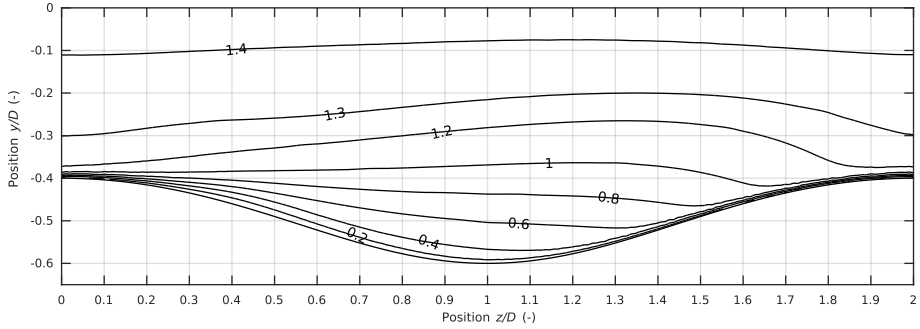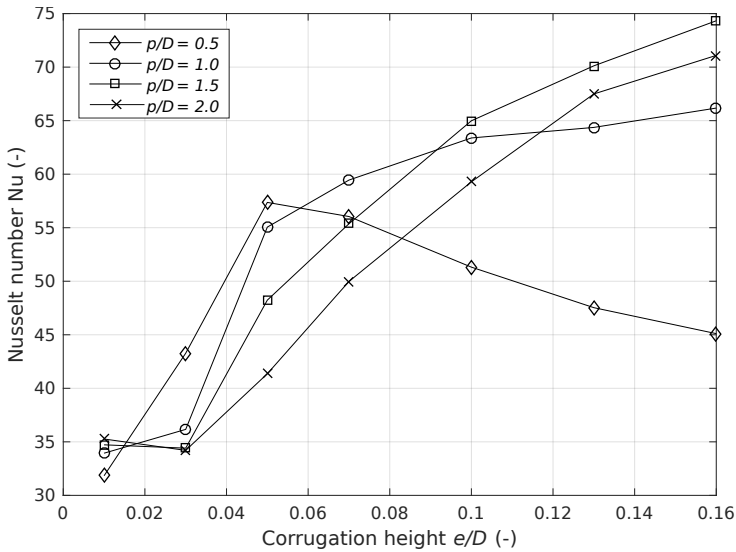
Figure C.30: Re-circulation zones visualised by axial flow component normalised bulk velocity u_{axial}/u_b in a corrugated tube with corrugation height and length of $e/D = 0.10$ and $p/D = 2.0$ respectively at Re = 10,000.

Figure C.31: Nusselt number as function of dimensionless corrugation length p/D and height e/D at Re = 10,000 and Pr = 1.0.

C.5   Link Between Flow Field and Heat Exchanger Performance

Heat transfer and pressure loss are reported by the dimensionless Nusselt number defined by (C.7) and friction factor defined by (C.6). Fig. C.31 and C.32 show how changes in corrugation height and length affect the Nusselt number and Darcy-Weisbach friction factor. At sufficiently low corrugation heights $e/D = 0.01$, the performance in terms of Nusselt number approaches
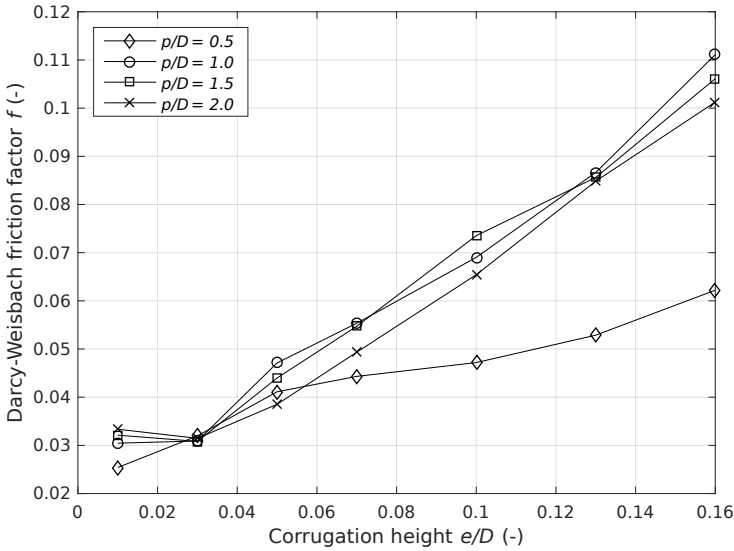
Figure C.32: Darcy-Weisbach friction factor as function of dimensionless corrugation length p/D and height e/D at Re $= 10,000$.

the non-corrugated tube as the flow fields are only affected to a minor degree. That is, the flow stay attached to the surface and only a small insignificant swirl is induced by the corrugation. At a slightly higher corrugation height $e/D = 0.05$, the Nusselt number is increased significantly. At this corrugation height, the flow separates and a higher swirl is induced. The result is an increased heat transfer at an increased pressure loss. At an even higher corrugation height, the swirl is increased even further and the swirling velocity eventually exceeds the stream-wise velocity. The result is steeper velocity gradients at the surface resulting in both higher heat transfer and pressure loss. When the corrugation height is increased beyond a certain point, the Nusselt number is expected to decrease as the heat transfer area increases without any additional increment in heat transfer. This point depends on the corrugation length. At a lower corrugation length $p/D = 0.5$, the decrease in Nusselt number happens between $e/D = 0.03$ and $e/D = 0.07$. At higher corrugation lengths $p/D = 1.0$, $p/D = 1.5$ and $p/D = 2.0$, the decrease in Nusselt number takes place at $e/D > 0.16$. At this point, a large re-circulation zone with low swirl velocities is present in the corrugation section. Here the flow is dominated by core flow with a high stream-wise velocity. Fig. C.32 shows that the friction factor in general increases with corrugation height. However, the friction factor increases slower above the point where the Nusselt number begins to decrease.

To compare the various corrugated tubes at a constant pumping power
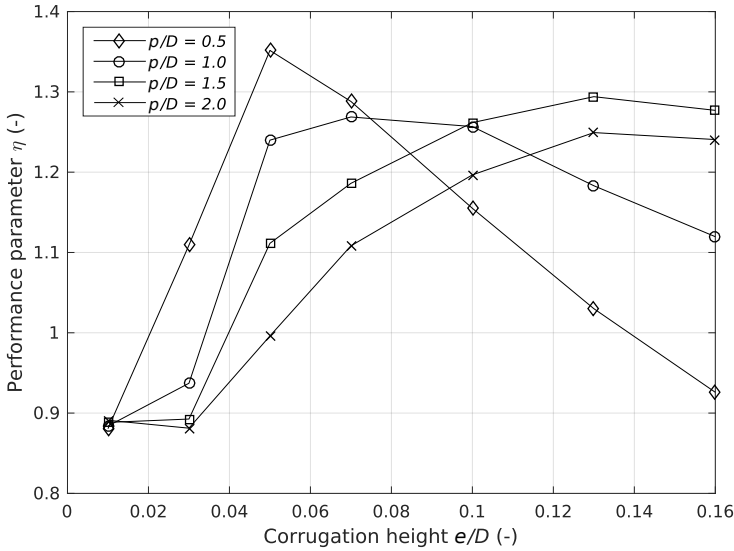
Figure C.33: Performance parameter $\eta = (\mathrm{Nu}/\mathrm{Nu_s})/(f/f_s)^{1/3}$ as function of dimensionless corrugation length p/D and height e/D at $\mathrm{Re} = 10{,}000$ and $\mathrm{Pr} = 1.0$.

and taking both Nusselt number and friction factor into account, the performance evaluation criterion given by (C.8) is used. This criterion is shown in Fig. C.33 for the different corrugated tubes. Fig. C.33 shows that there is a corrugation height for every corrugation length that results in the highest performance parameter. For lower corrugation lengths, this point is found at lower corrugation heights. This optimum condition is explained by the fact that the friction factor continues to increase as the Nusselt number only increases slightly for $p/D = 1.0$, $p/D = 1.5$, and $p/D = 2.0$ or even decreases for $p/D = 0.5$.

C.6 Conclusion

In this study the fully-developed flow field in different sinusoidally, spirally corrugated tubes is investigated by computational fluid dynamics for a Reynolds number of 10,000 and Prandtl number of 1.0. The tubes have a constant cross-sectional area and corrugation is introduced by the tubes having a centre-line described by a sinusoidal function. The investigated corrugations have corrugations heights in the range 0 to 0.16 and corrugation lengths in the range 0.5 to 2.0. The results suggests that sinusoidally, corrugated tubes of the sinusoidally, spirally type exhibit significant heat-transfer enhancing flow characteristics. To sum up, the major findings on how changes in corrugation height affects the flow field are:

- At low corrugations heights $e/D = 0.01$, the flow stay attached to the surface and only a small swirl is present with maximum at the centre of the corrugation.

- At slightly higher corrugations heights $e/D = 0.05$, the increased adverse pressure gradient causes the flow to separate resulting in a significant re-circulation zone. The swirling magnitude is increased again but is still centred at the corrugation centre.

- At a corrugation height $e/D = 0.10$, the swirling flow begins to dominate with tangential velocities in the order of the bulk velocity.

- At a high corrugation height $e/D = 0.16$, a strong swirl with a tangential velocity component exceeding the stream-wise velocity component is present in almost all the corrugation section. The high swirl eliminates re-circulation zones by a high pressure centred in the corrugation section.

Likewise, major findings on how changes in corrugation length affect the flow field are:

- At sufficiently low corrugation lengths (this corrugation length depends on the corrugation height), a re-circulation zone filling up most of the corrugated section is present.

- At a slightly higher corrugation length, the swirl velocity is increased while the re-circulation zone is decreased. The result is increased Nusselt number and friction factor.

- When increasing the corrugation length further, the re-circulation zone is completly eliminated while the swirl is increased to its maximum. This is the point resulting in the highest Nusselt number.

- As the corrugation length is further increased, the swirl starts to decrease as the tube approaches the non-corrugated tube.

By comparing the flow field to the Nusselt number and Darcy-Weisbach friction factor, the results show that the radically different flow field at high corrugations only increases the heat transfer slightly at a significant increase in pressure loss. In general, the tubes without stream-wise re-circulating flow seems to be optimal for transferring heat at constant pumping power when comparing to a non-corrugated tube.

Furthermore, tubes having a high swirling velocity combined with eliminated re-circulation zones are expected to be less prone to particulate deposition. Therefore, further numerical or experimental studies could be focused on investigating the optimal tube by a combination of Nusselt number, friction factor and tendency to deposit particulate matter.

Acknowledgement

Bibliography

Özden Ağra, Hakan Demir, Ş. Özgür Atayılmaz, Fatih Kantaş, and Ahmet Selim Dalkılıç. Numerical investigation of heat transfer and pressure drop in enhanced tubes. *International Communications in Heat and Mass Transfer*, 38:1384–1391, 2011. URL `http://dx.doi.org/10.1016/j.icheatmasstransfer.2011.07.013`.

A. E. Bergles, A. R. Blumenkrantz, and J. Taborek. Performance evaluation criterion for enhanced heat transfer surfaces. In *Proceedings of the 5th International Heat Transfer Conference*, volume 2, pages 234–238. The Japan Society of Mechanical Engineers, 1974.

Rambir Bhadouriya, Amit Agrawal, and S.V. Prabhu. Experimental and numerical study of fluid flow and heat transfer in a twisted square duct. *International Journal of Heat and Mass Transfer*, 82:143–158, 2015. URL `http://dx.doi.org/10.1016/j.ijheatmasstransfer.2014.11.054`.

G.K. Filonenko. Hydraulischer widerstand von rohrleitungen. *Teploenergetika*, 1:1098–1099, 1960.

S. Ganeshan and M. Rajo Rao. Studies on thermohydraulics of single- and multi-start spirally corrugated tubes for water and time-independent power law fluids. *International Journal of Heat and Mass Transfer*, 25:1013–1022, 1982. URL `http://dx.doi.org/10.1016/0017-9310(82)90076-X`.

V. Gnielinski. New equations for heat and mass transfer in turbulent pipe and channel flow. *Int. Chem. Eng*, 16:359–368, 1976. URL `http://dx.doi.org/10.1007/BF02559682`.

Huai-Zhi Han, Bing-Xi Li, Bi-Yong Yu, Yu-Rong He, and Feng-Chen Li. Numerical study of flow and heat transfer characteristics in outward convex corrugated tubes. *International Journal of Heat and Mass Transfer*, 55:7782–7802, 2012. URL `http://dx.doi.org/10.1016/j.ijheatmasstransfer.2012.08.007`.

Huaizhi Han, Bingli Li, and Wei Shao. Effect of flow direction for flow and heat transfer characteristics in outward convex asymmetrical corrugated

tubes. *International Journal of Heat and Mass Transfer*, 92:1236–1251, 2016. URL `http://dx.doi.org/10.1016/j.ijheatmasstransfer.2014.11.076`.

W. Hufschmidt and E. Burck. Der einfluss temperaturabhängiger stoffwerte auf den wärmeübergang bei turbulenter strömung von flüssigkeiten in rohren bei hohen wärmestromdichten und prandtlzahlen. *Int. J. Heat Mass Transfer*, 11:1041–1104, 1968. URL `http://dx.doi.org/10.1016/0017-9310(68)90009-4`.

V.V. Jakovlev. Örtliche und mittlere wärmeübetragung bei turbulenter rohrströmung nichtsiedenden wassers und hohen wärmebelastungen. *Kernenergie*, 3:1098–1099, 1960.

Zaid S. Kareem, M. N. Mohd Jaafar, Tholudin M. Lazim, Shahrir Abdullah, and Ammar F. Abdulwahid. Passive heat transfer enhancement review in corrugation. *Experimental Thermal and Fluid Science*, 68:22–38, 2015. URL `http://dx.doi.org/10.1016/j.expthermflusci.2015.04.012`.

F. R. Menter, R. Langtry, and S. Vølker. Transition modelling for general purpose cfd codes. *Flow Turbulence Combust*, 77:277–303, 2006. URL `http://dx.doi.org/10.1007/s10494-006-9047-1`.

Florian R. Menter. Improved two-equation k-omega turbulence models for aerodynamic flows. Technical report, National Aeronautics and Space Administration, 1992.

H. A. Mohammed, Abdalrazzaq K. Abbas, and J. M. Sheriff. Influence of geometrical parameters and forced convective heat transfer in transversely corrugated circular tubes. *International Communications in Heat and Mass Transfer*, 44:116–126, 2013. URL `http://dx.doi.org/10.1016/j.icheatmasstransfer.2013.02.005`.

S.V. Patankar, C.H. Liu, and E.M. Sparrow. Fully developed flow and heat transfer in ducts having streamwise-periodic variations of cross-sectional area. *Journal of Heat Transfer*, 99:180–186, 1977. URL `http://dx.doi.org/10.1115/1.3450666`.

S. Pethkool, S. Eiamsa-ard, S. Kwankaomeng, and P. Promvonge. Turbulent heat transfer enhancement in a heat exchanger using helically corrugated tube. *International Communications in Heat and Mass Transfer*, 38:340–347, 2011. URL `http://dx.doi.org/10.1016/j.icheatmasstransfer.2010.11.014`.

S. Rainieri and G. Pagliarini. Convective heat transfer to temperature dependent property fluids in the entry region of corrugated tubes. *International Journal of Heat and Mass Transfer*, 45:4525–4536, 2002. URL `http://dx.doi.org/10.1016/S0017-9310(02)00156-4`.

P. J. Roache. Perspective: A method for uniform reporting of grid refinement studies. *Journal of Fluids Engineering*, 116:405–413, 1994. URL `http://dx.doi.org/10.1115/1.2910291`.

X. S. Tan, D. S. Zhu, G. Y. Zhou, and L. Yang. 3d numerical simulation on the shell side heat transfer and pressure drop performances of twisted oval tube heat exchanger. *International Journal of Heat and Mass Transfer*, 65:244–253, 2013. URL `http://dx.doi.org/10.1016/j.ijheatmasstransfer.2013.06.011`.

P. G. Vicente, A. García, and A. Viedma. Experimental investigation on heat transfer and frictional characteristics of spirally corrugated tubes in turbulent flow at different prandtl numbers. *International Journal of Heat and Mass Transfer*, 47:671–681, 2004. URL `http://dx.doi.org/10.1016/j.ijheatmasstransfer.2003.08.005`.

R. L. Webb. Performance evaluation criteria for use of enhanced heat transfer surfaces in heat exchanger design. *International Journal of Heat and Mass Transfer*, 24:715–726, 1981. URL `http://dx.doi.org/10.1016/0017-9310(81)90015-6`.

R. Zheng, N. Phan-Thien, R. Tanner, and M. Bush. Numerical analysis of viscoelastic flow through a sinusoidally corrugated tube using a boundary element method. *Journal of Rheology*, 34:79, 1990. URL `http://dx.doi.org/10.1122/1.550115`.

V. D. Zimparov, N. L. Vulchanov, and L. B. Delov. Heat transfer and friction characteristics of spirally corrugated tubes for power plant condensers — 1. experimental investigation and performance evaluation. *International Journal of Heat and Mass Transfer*, 34:2187–2197, 1991. URL `http://dx.doi.org/10.1016/0017-9310(91)90045-G`.

Nomenclature

A	Cross-sectional area
C_p	Pressure coefficient
D	Pipe diameter
e	Corrugation height

f	Darcy–Weisbach friction factor
h	Convective heat transfer coefficient
k	Thermal conductivity
L	Length of pipe section
p	Pressure
p	Corrugation length
Pr	Prandtl number
Re	Reynolds number
T	Temperature
u	Fluid velocity
y^+	Dimensionless wall distance

Greek letters

η	Thermal performance parameter
μ	Dynamic viscosity
ν	Kinematic viscosity
ρ	Density
τ	Wall shear stress
ϕ	Axial flow parameter
ψ	Swirling flow parameter

Subscripts

b	Bulk values
s	non-corrugated reference pipe
w	Wall values
z	Local coordinate along pipe length

Acronyms

CFD	Computational Fluid Dynamics
GCI	Grid Convergence Index
SST	Shear-Stress Transport
URANS	Unsteady Reynolds-averaged Navier-Stokes

Bibliography

Appendix D

Guidelines for optimal selection of working fluid for an organic Rankine cycle in relation to waste heat recovery

J. Hærvig, K. Sørensen, T.J. Condra

Guidelines for optimal selection of working fluid for an organic Rankine cycle in relation to waste heat recovery

J. Hærvig, K. Sørensen, T.J. Condra

Aalborg University, Department of Energy Technology, Pontoppidanstræde 111, DK-9220 Aalborg, Denmark

Abstract

General guidelines on how to choose the optimal working fluid based on the hot source temperature available are reported. Based on a systematic approach, 26 commonly used working fluids are investigated by optimisations at hot source temperatures in the range 50-280 °C at intervals of 5 K. The genetic optimisation algorithm is used to optimise net power output by an optimal combination of turbine inlet pressure and temperature, condenser pressure, hot fluid outlet temperature, and mixture composition for mixtures.

The results suggest that the optimum working fluid in terms of maximum net power output has a critical temperature approximately 30-50 K below the hot source temperature. When two or more fluids with the same critical temperature are available, the ones with a positive slope of vapour saturation line are generally favoured. When mixtures are considered, the optimal mixture composition should be chosen so that the critical temperature of mixture is approximately 30-50 K below the hot source temperature and the temperature glide during condensing should approximate the temperature rise of the cold source.

D.1 Introduction

To help reduce the consumption of fossil fuels, some currently non-utilised low-grade heat sources can be used. Heat sources with temperatures in the range 50-280°C are found in numerous places ranging from geothermal sources to waste heat from process industries to marine vessels. For these purposes, the Rankine cycle can be implemented to convert thermal energy into mechanical or electrical power. Traditionally, water has been used as working fluid due to the fact that it is both chemically stable, non-toxic, non-flammable, environmental friendly, cheap, and widely available (Tchanche et al., 2011). Organic fluid alternatives do however exhibit thermodynamic

properties that make them highly suited for extracting energy at low temperatures. As pointed out by Tchanche et al. (2011) these include a lower heat of vapourisation, lower temperature and pressure for the evaporation process, an expansion process that ends up in the vapour region, and a lower pressure ratio between evaporation and condensation resulting in a smaller turbine requirements. Other important thermodynamic properties include significantly lower critical temperatures and pressures, lower specific volume and different transport properties resulting generally in worse heat transfer characteristics and therefore different heat exchanger requirements. Furthermore, characteristics such as toxicity, flammability, fluid cost, ozone depletion potential, and global warming potential should be considered as well.

Due to the above mentioned differences, much research has already been carried out on ORC (organic Rankine cycles) for utilising low-grade energy with temperatures in the range 50-280°C. Some studies mainly focus on cycle design or working parameters while others focus mainly on working fluid selection. Some limit their research to a particular application with a single hot source temperature while other study different cases having different hot source temperatures. The literature overview by Bao and Zhao (2013) gives a great overview of the amount of literature dealing with working fluid selection. Furthermore, the study sums up the recommendations for working fluid selection for different hot source temperature ranges presented in the literature.

While some studies investigate and optimise the molecular composition of the working fluid by CAMD (computer aided molecular design) (Papadopoulos et al., 2010), other studies focus on more or less sophisticated equations of state to predict the properties of pure fluids and mixtures to model the cycles and compare the fluids in terms of first or second law efficiency, net power output, or total irreversibility. Saleh et al. (2007) used the BACKONE equation of state to screen the thermodynamic properties of 31 pure component working fluids resulting in a set of general guidelines on cycle design depending on the type of fluid. These guidelines suggest that the highest amount of energy can be transferred to super-critical fluid whereas the high temperature sub-critical fluid provides the worst heat transfer. In terms of thermodynamic efficiency, the highest values are obtained for high boiling substances with overhanging saturation domes operated at sub-critical conditions. Newer studies do however typically rely on the state-of-the-art commercially available REFPROP library by Lemmon et al. (2013) to estimate thermodynamic and transport properties of both pure fluids and mixtures. This thermodynamic database relies on experimentally obtained equations of state.

Studies on zeotropic mixtures include Heberle et al. (2012); Radulovic and Castaneda (2014) who reports second law increments of up to 15 % by utilising mixtures instead of the pure fluids involved. Studies such as Li et al.

(2014); Andreasen et al. (2014) point out how the temperature glide results in a better thermal match between the hot source and working fluid but results in larger heat exchanger areas as well. The study by Prasad et al. (2015) does however suggest the required expander size to decrease when zeotropic mixtures are utilised.

The study by Maraver et al. (2014) presents a systematic approach where cycles with R134a, R245fa, Solkatherm, m-Pentane, Octamethyltrisiloxane, and Toluene are optimised. Based on these optimisations, guidelines on how to maximise the exergy efficiency are given. One conclusion is that the heat capacity flow of the hot source should be similar to the heat capacity flow of the working fluid. Furthermore, the working fluids whose critical temperature is much lower than the hot source temperature result in lower thermodynamic performance. The results presented by Braimakis et al. (2015) for hot source temperatures in the range between 150°C and 300°C suggest the optimal fluids in terms of exergy efficiency to be mixtures when the hot sources temperature exceeds 170°C. Furthermore, the study concludes that at below 170°C, pure fluids in trans-critical cycles perform better.

Common for most fluid selection studies in relation to organic Rankine cycles is that they typically consider a single or set of cases with a specific hot source temperatures. As pointed put by the literature review by Lecompte et al. (2015), the difference in boundary conditions, makes a direct comparison between the studies a challenge. Therefore, a recent trend in ORC studies is to propose more general guidelines whenever possible. Xu and Yu (2014) screened 57 fluid candidates to be used with a flue gas hot source. The study suggests that the optimal fluids candidates in terms of thermal efficiency have critical temperature in the range of 20-30 K below to 100 K above the hot source temperature. Other recent studies report optimal and constant values of $T_{\mathrm{crit}}/T_{\mathrm{hf,in}} \approx 0.5$ (Andreasen et al., 2014), $T_{\mathrm{crit}}/T_{\mathrm{hf,in}} \approx 0.8$ (Vetter et al., 2013), which focus on two or three hot source temperatures respectively. The recent fluid selection study by Vivian et al. (2015) investigated three different hot source temperatures of 120°C, 150°C, and 180°C. Based on the results given in this study, the optimal fluids have $T_{\mathrm{crit}} - T_{\mathrm{hf,in}} \approx 35°C$, which is quite different from the previous studies.

By varying the hot source temperature and investigating a high number of commonly used working fluids, the purpose of this study is to establish a set of guidelines which can be used as preliminary design tool when a Rankine cycle is to be designed for a specific purpose. These guidelines extend the ones by Vivian et al. (2015) and gives a secondary selection criterion that can be used, when more fluids have approximately the same critical temperature. First the applicability of the working fluid selection guideline presented by Vivian et al. (2015) is extended to the temperature range 50°C to 280°C as this interval covers most low temperatures ranging from geothermal sources at 50°C to exhaust gas from marine engines at 280°C. Secondly, it is shown
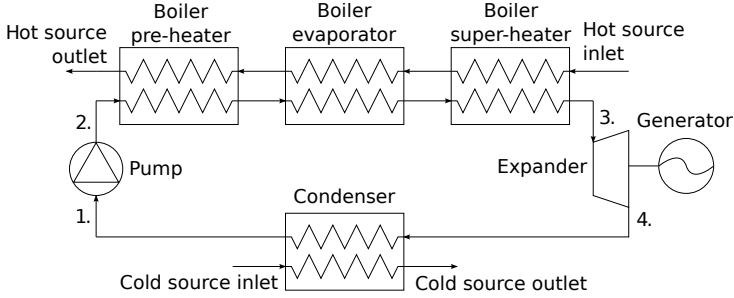
Figure D.1: Schematic of the Rankine cycle considered along with annotations used in this study.

that the slope of vapour saturation line can be used to choose between two fluids having the approximately same critical temperature, both fulfilling the guideline presented by Vivian et al. (2015). Lastly, a set of mixtures are investigated to show that the already presented guidelines are shown to be applicable for mixtures as well.

D.2 Modelling Approach

D.2.1 System and parameter overview

The basic Rankine cycle consisting of a pump, pre-heater, evaporator, super-heater, turbine, and a condenser illustrated in figure D.1 is considered. The working fluid leaves the condenser as saturated liquid (point 1), is pumped to a higher pressure (point 2), is heated at constant pressure in the boiler to a given temperature to either saturated vapour or superheated vapour (point 3), is expanded in a turbine (point 4), and is condensed before entering the pump again (point 1). Depending on the fluid and hot source temperature considered, the cycles are either sub-critical or trans-critical depending on how the maximum net power output can be obtained.

The parameter of interest in this study is mainly the net work output defined by:

$$W_{\mathrm{net}} = \dot{m}_{\mathrm{wf}} \left(h_3 - h_4 - h_2 + h_1 \right), \tag{D.1}$$

This parameter describes how much power the given Rankine cycle is able to produce under the given conditions. Table D.1 lists the conditions and parameters used in the study and if they are independent, dependent, or constant values throughout the analysis. The parameters are chosen to resemble the conditions in waste heat recovery systems. To be able to compare the results to other systems using different hot sources than dry flue gas, the heat capacity rate $\dot{c}_{\mathrm{p}} = \dot{m} \cdot c_{\mathrm{p}}$ is used as a unique parameter. This parameter

Table D.1: Modelling parameters in the analysis.

Parameter	Symbol	Value
Hot source		
Hot fluid		Dry air
Hot source inlet temperature	$T_{hf,in}$	[50;280] °C
Hot source outlet temperature	$T_{hf,out}$	indep.
Hot source pressure	P_{hf}	1.5 bar
Pinch point temperature in boiler	$T_{pp,boil}$	10 K
Hot source mass flow rate	$\dot{m}_{hf}$	150 kg/s
Cold source		
Cold fluid		Water
Cold source inlet temperature	$T_{cf,in}$	15 °C
Cold source outlet temperature	$T_{cf,out}$	20 °C
Cold source pressure	P_{cf}	1.5 bar
Pinch temperature in condenser	$T_{pp,cond}$	5 K
Cold source mass flow rate	$\dot{m}_{cf}$	depen.
Cycle parameters		
Turbine inlet temperature	$T_{turb,in}$	indep.
Working fluid mass flow rate	$\dot{m}_{wf}$	depen.
Boiling pressure	P_{boil}	indep.
Condensation pressure	P_{cond}	indep.
Working fluid composition	χ	indep.
Pump isentropic efficiency	η_{pump}	0.8
Turbine isentropic efficiency	η_{turb}	0.8
Number of boil. discretisations	n_{boil}	40
Number of cond. discretisations	n_{cond}	40

defines the rate at which temperature changes as energy is transferred. Estimating $\dot{c}_p$ based on the hot source mass flow of 150 kg/s, the heat capacity rate is almost constant at values between 151 kJ/(K·s) and 156 kJ/(K·s) for inlet temperatures in the range between 50 °C and 280 °C.

As shown in table D.1, a constant mass flow rate of 150 kg/s is used in this study. It is however important to note that it does not affect the guidelines presented in this study. That is, a unit mass flow rate could have been used as well, resulting in the exact same guidelines. The mass flow rates of the working fluid and cold source and the net power output are simply scaled accordingly.

D.2.2 Heat transfer modelling

The energy transferred in the heat exchangers can be estimated by the overall heat transfer coefficient U, the heat transfer area A, and the mean temperature difference at which energy is transferred:

$$\dot{Q} = UA\Delta T_{\text{lm}}, \tag{D.2}$$

where details on how the temperature difference is evaluated are given in subsection D.2.3. Instead of applying partly validated correlations for U to cover all the different fluids, conditions, and mixtures considered in this study, UA values are reported. The UA value for a heat exchanger is a measure of the required heat exchanger size. For this study, where the hot source is flue gas with a low Prandtl number, the heat transfer in the boiler is limited by the flue gas side heat transfer as stated by Roetzel and Spang (2010). When mixtures are considered, the boiling and condensing heat transfer coefficients differ significantly as described by Cheng and Mewes (2006). For this study transient effects due to fouling and start-up of the system are not considered. As UA values are reported, the reader can use their own heat exchangers with known UA values to get the results reported.

D.2.3 Heat exchanger discretisation

As already pointed out by Maraver et al. (2014), the heat exchanger discretisation is important to resolve the heat transfer process. For this study, where fixed pinch points in the boiler and condenser are used, the pinch point location is unknown before modelling the process. Furthermore, as the additional computational time is proportional to the number of discretisations, it is a important in order to keep the overall computational time of the optimisations as low as possible low. Therefore, a discretisation analysis is carried out in the present study to find a reasonable number of discretisation for a typical heat exchanger process. The trans-critical process having almost parallel T-Q profiles for the hot source and working fluid does not require a high number of discretisations to resolve the process. Therefore, focus is on the sub-critical boiling and condensation processes. Figure D.2(a) and (b) show examples of a sub-critical boiling process and condensation process using ammonia as the working fluid being heated by hot source at 100 °C. The pressure levels and turbine inlet temperature, and hot source outlet temperature are found by the optimisation process presented in this study. Each process is discretised with $n = 5$ and $n = 10,000$ to illustrate the difference between a coarse and very fine discretisation.

As the figure shows, the discretisation used influences the amount of energy extracted from the hot source. To quantify the effect of discretisation, figure D.3 shows the mean temperature difference with different number of
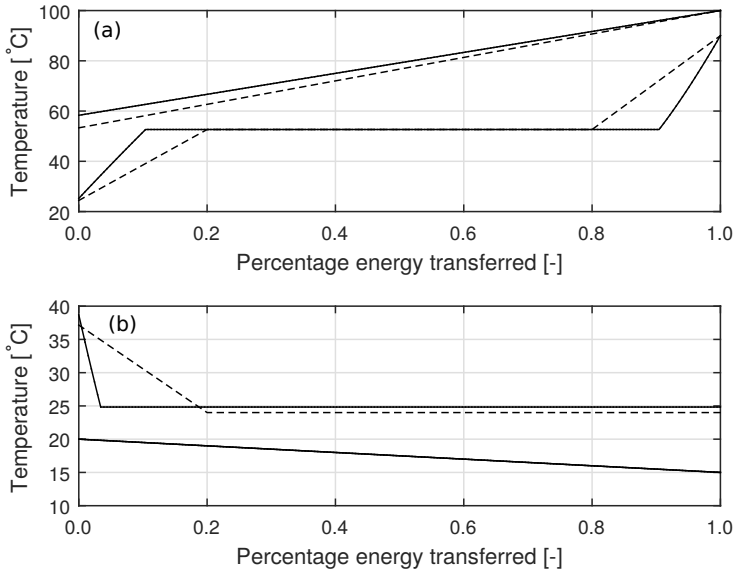
Figure D.2: Comparison of *T-Q* profiles for ammonia being heated by a hot source at 100°C with different number of discretisations *n* in: (a) Boiler with $n = 5$, - - -, $n = 10,000$, ——; (b) Condenser with $n = 5$, - - -, $n = 10,000$, ——.
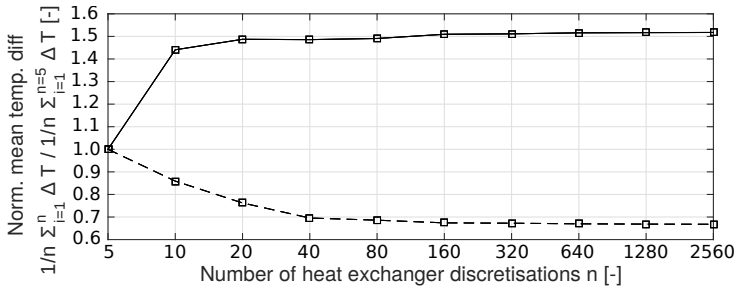
Figure D.3: The influence of number of discretisations on the mean temperature difference between hot/cold source and the working fluid being ammonia and hot source at 100 °C in this example: Boiler, ——, condenser, - - -.

discretisations in the range [5;2560] normalised by the mean temperature difference with 5 discretisations.

Based on the results in figure D.3, the heat exchangers are discretised into 40 sections. These discretisations are both used when evaluating the pinch point location using *T-Q* profiles and when calculating the mean temperature difference ΔT_{lm} by:

$$\Delta T_{lm} = \frac{1}{n} \sum_{i=1}^{n} \Delta T_i \tag{D.3}$$

Table D.2: Working fluids considered in this study along with their critical point, inverse slope of vapour saturation line, and chemical name and listed by their ASHRAE number.

| Number	Chemical name	T_{crit} [°C]	P_{crit} [bar]	ξ [J/(kg K^2)]	Equation of state
R22	chlorodifluoromethane	96.2	5.0	-1.32	Kamei et al. (1995)
R23	trifluoromethane	26.1	4.8	-8.87	Penoncello et al. (1995)
R32	difluoromethane	78.1	57.8	-3.55	Tillner-Roth and Yokozeki (1997)
R41	fluoromethane	44.1	59.0	-8.05	Lemmon and Span (2006)
R123	2,2-dichloro-1,1,1-trifluoroethane	183.7	36.6	0.41	Younglove and McLinden (1994)
R124	2-chloro-1,1,1,2-tetrafluoroethane	122.3	36.2	0.24	de Vries et al. (1995)
R125	pentafluoroethane	66.0	36.2	-0.23	Lemmon and Jacobsen (2005)
R134a	1,1,1,2-tetrafluoroethane	101.1	40.6	-0.37	Tillner-Roth and Baehr (1994b)
R141b	1,1-dichloro-1-fluoroethane	204.4	42.1	0.35	Lemmon and Span (2006)
R142b	1-chloro-1,1-difluoroethane	137.1	40.6	0.03	Lemmon and Span (2006)
R143a	1,1,1-trifluoroethane	72.7	37.6	-0.75	Lemmon and Jacobsen (2000)
R152a	1,1-difluoroethane	113.3	45.2	-1.29	Outcalt and McLinden (1996)
R170	ethane	32.2	48.7	-9.86	Buecker and Wagner (2006b)
R218	octafluoropropane	71.9	26.4	0.89	Lemmon and Span (2006)
R227ea	1,1,1,2,3,3,3-heptafluoropropan	101.8	30.0	0.79	Lemmon and Span (2006)
R236ea	1,1,1,2,3,3-hexafluoropropane	139.3	35.0	0.78	Huber and Ely (1994)
R245ca	1,1,2,2,3-pentafluoropropane	174.4	39.3	0.77	Huber and Ely (1994)
R245fa	1,1,1,3,3-pentafluoropropane	154.0	36.5	0.61	Lemmon and Span (2006)
R290	propane	96.7	42.5	-0.76	Lemmon et al. (2009)
R600	butane	152.0	38.0	1.19	Buecker and Wagner (2006a)
R600a	isobutane	134.7	36.3	1.07	Buecker and Wagner (2006a)
R601	pentane	196.6	33.7	2.07	Jaeschke and Schley (1995)
R601a	ipentane	187.2	33.8	2.09	Lemmon and Span (2006)
R717	ammonia	132.3	113.3	-11.52	Tillner-Roth and Baehr (1994a)
R744	carbon dioxide	31.0	73.8	-9.58	Span and Wagner (1996)
R7146	sulfur Hexaflouride (SF6)	45.6	37.6	-0.41	Guder and Wagner (2009)

D.2.4 Working fluids and their thermodynamic properties

A list containing the 26 fluids candidates considered in this study is given in table D.2. These fluids investigated are fluids commonly reported in literature.

Along with the critical temperature and pressure, the inverse of the slope of vapour saturation line $\xi = ds/dT$ on the T-s diagram is given. This parameter, first proposed by Liu et al. (2004) has been suggested in other studies along with the critical point to be key parameters when determining the maximum potential of a given fluid at a given hot source temperature. In this study, ξ is evaluated at $ds^2/dT^2 = 0$ for dry fluids and at 20°C for wet fluids corresponding to approximately the condensing temperature. If $ds^2/dT^2 = 0$ does not exist between 20°C and T_{crit}, then it is evaluated at 20°C for dry fluids as well. This approach has been used for all the fluid candidates investigated in this study and is found to give representative values of xi for the cycles considered. Examples are given in figure D.4 with pentane and propane as dry and wet fluids respectively. The figure shows both the pure fluids and how the saturation dome is altered by different mixture compositions.

As research still goes on to improve the equation of states for the different fluids, the references for the equations of states used in this study are given
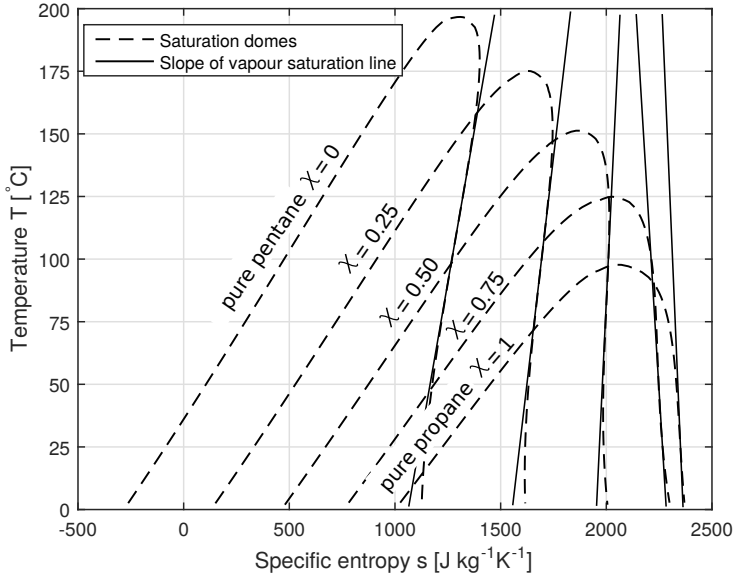
Figure D.4: Saturation domes for a propane-pentane mixture of compositions 0/1 (pure pentane), 0.25/0.75, 0.50/0.50, 0.75/0.25, and 1/0 (pure propane). The slope of vapour saturation lines ζ evaluated at the evaluation criterion used in this study are shown as well. Note that the lines shown correspond to $\zeta^{-1} = \mathrm{d}T/\mathrm{d}s$.

in the last column in table D.2.

To visualise the slope of vapour saturation line and critical temperatures of the fluids considered, figure D.5 is used. To evaluate thermodynamic properties for the fluids the extensive REFPROP library by Lemmon et al. (2013) is used, as reviews of thermodynamic databases such as Ziviani et al. (2014) suggests the REFPROP library to be the most complete in terms of available fluids and accuracy. Typical accuracies are 0.1 % in densities, 1 % in heat capacities, 1 % in speed of sound, and 0.2 % in vapour pressure. The uncertainties do however vary by small amounts for the different fluids and for some fluids the exact uncertainty remains undocumented. Transport properties are not modelled as neither the heat exchangers nor the pressure loss is modelled.

To model exact *T-s* profiles, temperature dependent heat capacities are taken into account for both sources. The hot source is modelled as a combination of 21 % oxygen, 78 % nitrogen, and 1 % argon on mole basis, which corresponds to atmospheric air, as atmospheric air and flue gas contains almost the same thermodynamic properties (within 2-3 %). The cold source is modelled as pure water according to the equation of state presented by Wagner and Pruss (2002) and implemented in the REFPROP library.
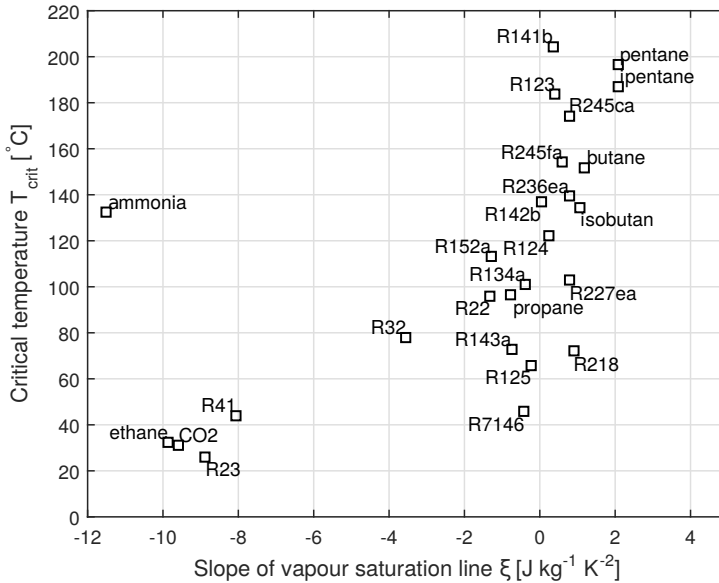
Figure D.5: Critical temperature as function of slope of vapour saturation line for the pure fluid candidates considered in this study.

D.3 Optimisation

D.3.1 Definition of optimisation problems

The optimisation problem considered will be to maximise the net work output by optimal combination of turbine inlet temperature and pressure, hot source outlet temperature, and condensing pressure. For mixtures, the mixture composition χ is optimised as well. A set of constraints is set up to allow only thermodynamically feasible designs that do not violate the specific minimum pinch point temperatures given in table D.1. As the optimisation is carried out for different fluid candidates and different hot source temperatures, the constraints vary for every optimisation. For example the minimum condenser pressure depends on the saturation pressure, which is fluid de-

Table D.3: Mesh parameters for the different meshes.

cells	Value
Maximum number of generations	300
Maximum number of stalled generations	50
Maximum tolerance within stalled generations	10^{-10}
Population size	50
Crossover fraction	0.8
Elite count	2

pendent. The following expresses the optimisation in a general manner:

$$
\begin{aligned}
\text{maximise:} \quad & W_{\text{net}} = f\left(T_{\text{turb,in}}, P_{\text{turb,in}}, T_{\text{hf,out}}, P_{\text{cond}}, \chi\right), \\
\text{subject to:} \quad & T_{\text{cf,in}} + T_{\text{pp,cond}} \leq T_{\text{turb,in}} \leq T_{\text{hf,in}} - T_{\text{pp,boil}}, \\
& T_{\text{cf,in}} + T_{\text{pp,cond}} + T_{\text{pp,boil}} \leq T_{\text{hf,out}} \leq T_{\text{hf,in}}, \\
& P_{\text{sat}@T=T_{\text{cf,in}}} \leq P_{\text{cond}} \leq P_{\text{turb,in}}, \\
& P_{\text{cond}} \leq P_{\text{turb,in}} \leq 200 \text{ bar}, \\
& 0 \leq \chi \leq 1, \\
& 1 \leq x_{\text{turb,out}},
\end{aligned}
\tag{D.4}
$$

where χ denotes the mass fraction of the first-mentioned substance for a given mixture and $x_{\text{turb,out}}$ is the quality of the fluid at the outlet of the turbine. This optimisation process described by (D.4) is carried out of every fluid in table D.2 at hot source temperatures ranging from 50°C to 280°C at intervals of 5 K.

D.3.2 Considerations on convergence

For the optimisations carried out in this study, the MATLAB implementation of the genetic algorithm first presented by Holland (1992) is used. By using the genetic algorithm, the global optimum is found by a successive series of cross-over and mutation operations. For this study, convergence is assumed when the average relative change in net power output is 10^{-10} over 50 stalled generations. This criterion is chosen to ensure the true optimum is found. Table D.3 gives an overview of the settings used for genetic algorithm.

Running the same optimisation multiple times with the settings in table D.3 is found to give consistent results. This suggests that the optimisation algorithm has successfully found the true optimum.

D.3.3 Validation of results obtained

To make sure that the results obtained by the thermodynamic models are accurate, and that the optimisation process convergences to the optimum with reasonable accuracy, the results are compared to results reported in literature. To ensure sufficient convergence is obtained for both optimisation algorithms, the modelling parameters in table D.1 are changed to fit those in other studies and the results are compared. Andreasen et al. (2014) presents results for $T_{hf,in} = 120$ °C and $T_{hf,in} = 90$ °C for the simple ORC for both pure fluids and mixtures. The results obtained by the model in this study deviate less than 3 % when comparing quantities such as boiler and condenser pressure, and turbine inlet temperature. Other studies used for comparison include Walraven et al. (2013), Dai et al. (2009), and Chys et al. (2012).

D.3.4 Visualisation of parameters and objective function

As multiple parameters are considered in this optimisation, a way to visualise the results of the optimisations is required. Figure D.6 visualises the results of the optimisation by relating the different parameters and the objective at a hot source temperature of 200 °C. For most fluid candidates, the almost parallel lines between the hot source outlet temperature, turbine inlet temperature, boiling pressure, and condensation pressure suggests these to be directly related. Four fluid candidates, namely R141b, R123, R245ca, and ammonia, the relation between hot source outlet temperature and turbine inlet temperature differs significantly. Inspection of the cycles for R141b, R123, and R245ca shows that these are all operated sub-critically with a distinct evaporation process. The more dry fluids fluids having high critical temperatures like pentane and ipentane are expanded directly through the saturation dome after pre-heating resulting in the tri-lateral cycle, which is discussed in details by Fischer (2011) and Ajimotokan and Sher (2015).
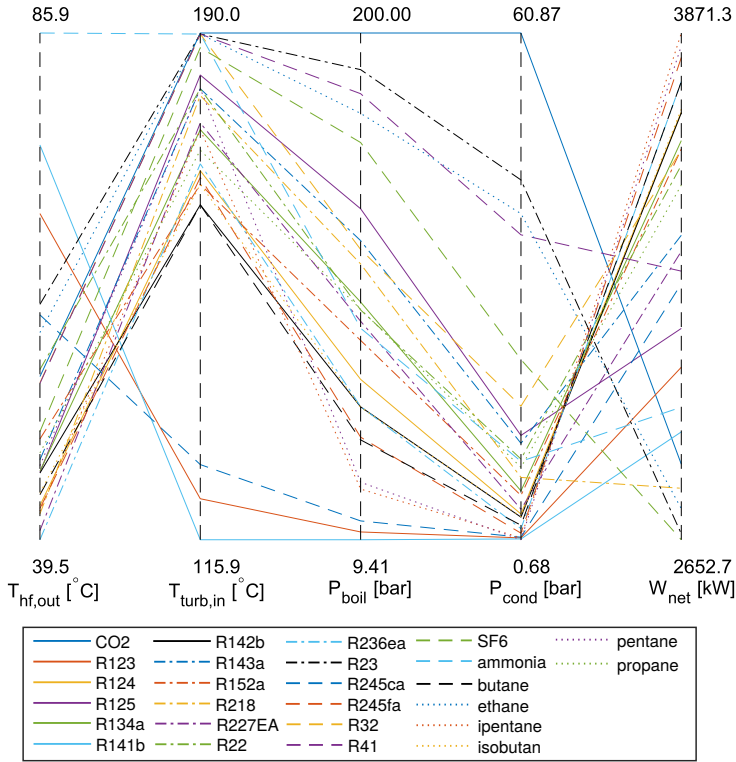
D.4 General Considerations on Optimal Fluids Based on Optimisation

D.4.1 Pure fluid candidates

Figure D.7 shows the maximum potential in terms of net power output W_{net} for some of the pure working fluid candidates at a varying hot source temperature $T_{hf,in}$ in the range [50;280] °C with 5 K intervals. That is, each point in the figure corresponds to an optimal solution found by the genetic algorithm.

The results in the figure D.7 shows how the maximum net power output in general increases with higher hot source temperatures. The maximum

Figure D.6: Parallel coordinates showing the how the parameters are linked to the objective function for the optimised cycles using the different fluid candidates at a hot source temperature of 200 °C.

net power output that can be obtained for a given fluid increases exponentially at low hot source temperatures. At a certain transition point, the net power output begins to increase linearly with increasing hot source temperature. This critical point is observed to be fluid dependent and is found to occur when the optimal cycle changes from being sub-critical to trans-critical. When comparing the different fluids, the figure suggests that each fluid only has a single and limited range in which it is optimal. That is, a fluid resulting in high net power output at low temperatures will not perform as good at high temperatures when compared to other fluids. To better compare the results in figure D.7, the optimised net power output is normalised by the optimised net power output for ammonia at the same hot source temperature. The normalised results are shown in figure D.8. Using this approach, the different fluids have a certain hot source temperature at which the ratio $W_{\mathrm{net}}/W_{\mathrm{net,ammonia}}$ is maximum. Ammonia is chosen for comparison because it is a commonly used fluid in various cycles.
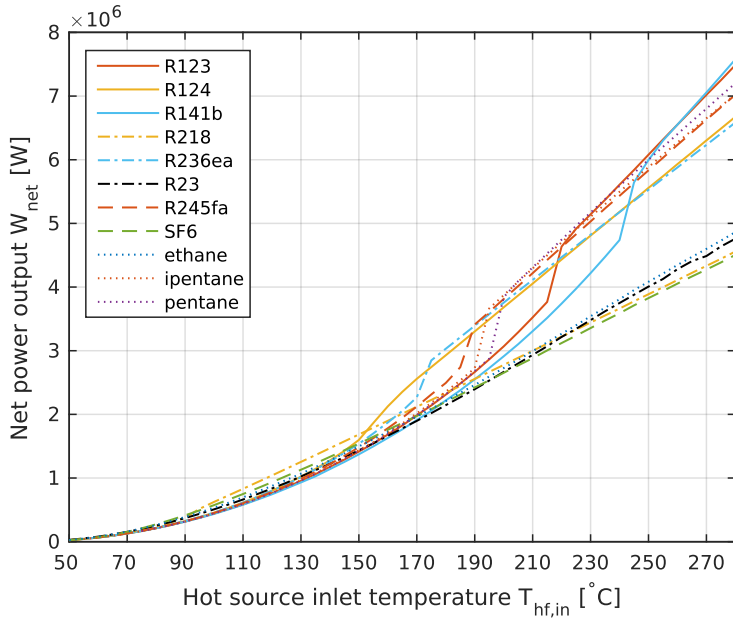
Figure D.7: Optimal designs in terms otransferedf net power output for different working fluid at a varying hot source temperature in the range [50;280] °C.
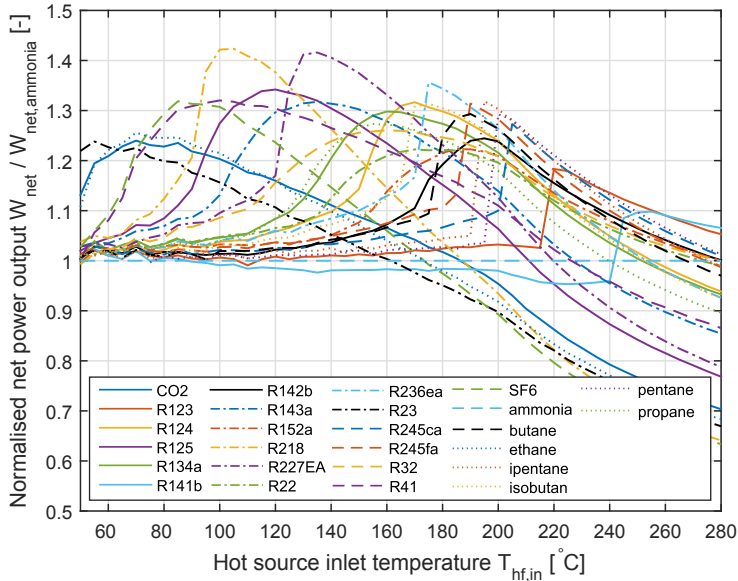
Figure D.8: Optimal designs visualised by the net power output normalised by ammonia for different working fluids at a varying hot source temperature in the range [50;280]°C.

Table D.4: The optimal working fluids in terms of net power output in different hot source temperature ranges.

| Hot source temp. range [°C]	Fluid candidate	Critical temperature [°C]
[50;60]	R23	26.1
[65;70]	ethane	32.2
[75;90]	R7146	45.6
[95;120]	R218	71.9
[125;160]	R227ea	101.8
[165;170]	R124	122.3
[175;185]	R236ea	139.3
[190;190]	R245fa	154.0
[195;200]	ipentane	187.2
[205;235]	pentane	196.6
[240;255]	R123	183.7
[260;280]	R141b	204.4

The figure shows how ammonia is outperformed or outperforms the different fluid candidates in terms of net power output at different hot source temperatures in the range [50;280]°C. If another fluid was used for comparison, this figure would look different, but the relative difference between the working fluid candidates would still be same. To investigate whether there is a correlation between the optimal fluid in the different hot source temperature intervals and their critical temperature, table D.4 is used. This table lists the optimal working fluid candidates in terms of net power output in different hot source temperature ranges along with their critical temperature.

Table D.4 shows how the best fluid candidates all should be operated at hot source temperatures above their critical temperature, which can be explained by a better thermal match with hot source temperature allowing for a better hot source utilisation. As an example, figure D.9 shows the optimal cycles for R218 when the hot source temperature is varied between 75°C and 140°C. The figure shows that when the $T_{hf,in} = 95°C$ (approximately 25 K above the critical point) the optimal cycle is trans-critical resulting in a significantly better thermal match between the hot source temperature and working fluid. The result is a high net work output and consequently a low mean temperature difference. As heat is transferred at a lower mean temperature difference, the required heat exchanger size will be significantly higher. Figure D.10 and D.11 show the net power output to heat exchanger UA-value for the boiler in D.10 and condenser in D.11 for the designs in figure D.7. The results in figure D.10 suggest the net power to boiler heat exchanger UA-value to increase with hot source temperature, until a certain hot source temperature where the ratio drops drastically. This sudden drop in net power
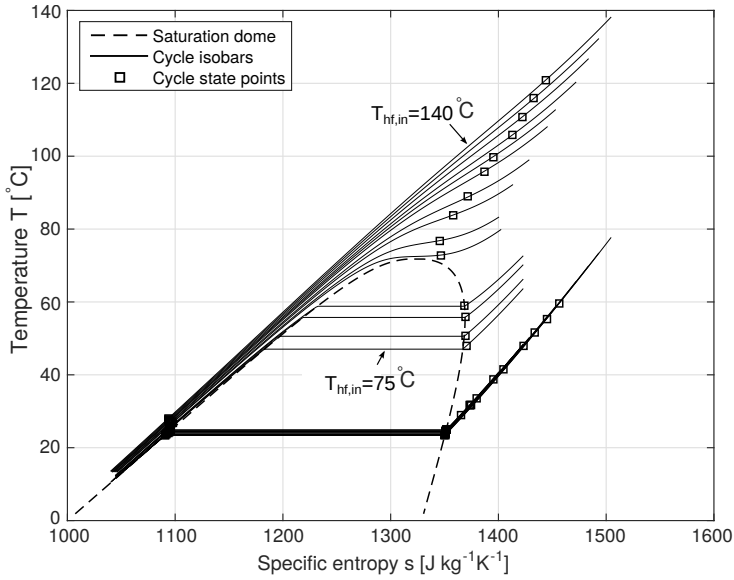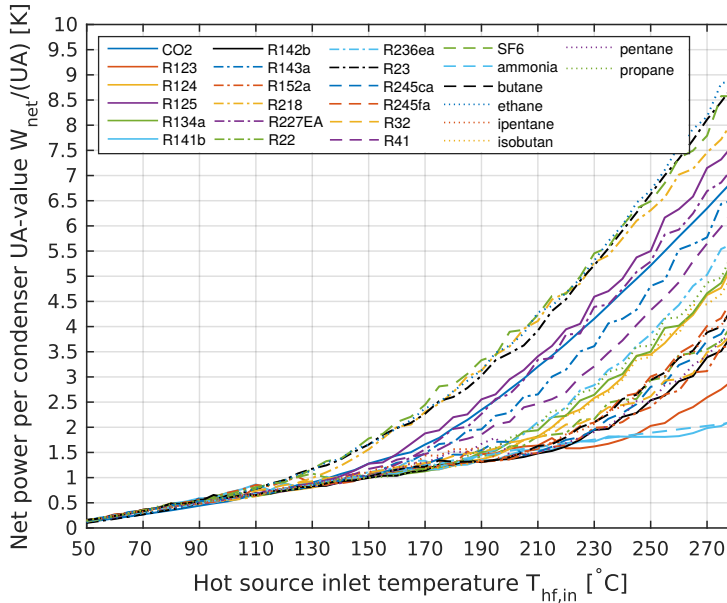
Figure D.9: Optimal cycles for R218 with hot source temperatures in the range [75;140]°C with intervals of 5 K.
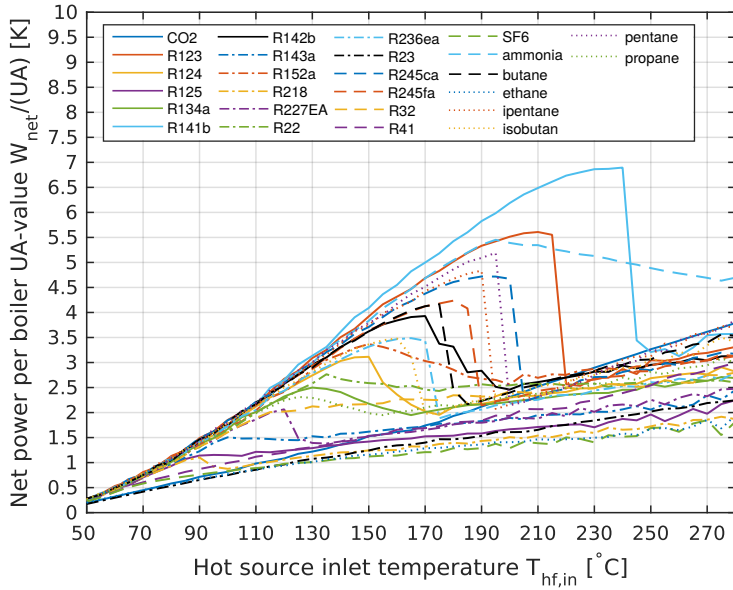
Figure D.10: Optimal designs by net work output shown with net power output per heat exchanger UA-value for the condenser and boiler at a varying hot source temperature in the range [50;280]°C.

Figure D.11: Optimal designs by net work output shown with net power output per heat exchanger UA-value for the condenser and boiler at a varying hot source temperature in the range [50;280]°C.

to heat exchanger UA-value ratio can be explained by the optimal cycles going from sub-critical to trans-critical. Furthermore, the results suggest this sudden drop to be more evident for dry fluids having $\xi < 0$. On the other hand, fluids having $\xi \ll 0$ such as ammonia, ethane, CO_2, R23, and R41 do not show this behaviour. The results in figure D.11 suggest the net power to condenser heat exchanger UA-value to increase throughout the hot source temperature range. This can be explained by the increasing net power output and the condenser UA-value being almost constant due to fixed conditions for the cold source.

The results in table D.4 suggest that an optimal pure working fluid should have a critical temperature 30-50 K below the hot source temperature. As figure D.8 suggested, all the working fluids have a temperature range in which they are significantly better than ammonia. For fluids having low critical temperatures such as R23, CO2, and Ethane, they outperform ammonia at low hot source temperatures. Likewise do the fluids having high critical temperatures such as R141b, pentane, ipentane, and R123 outperform ammonia and high hot source temperatures. This statement is in fact valid for all the working fluid candidates investigated in this study. Figure D.12 shows the normalised net power output as function of temperature difference between the hot source inlet temperature and the critical temperature. As the figure sug-

215
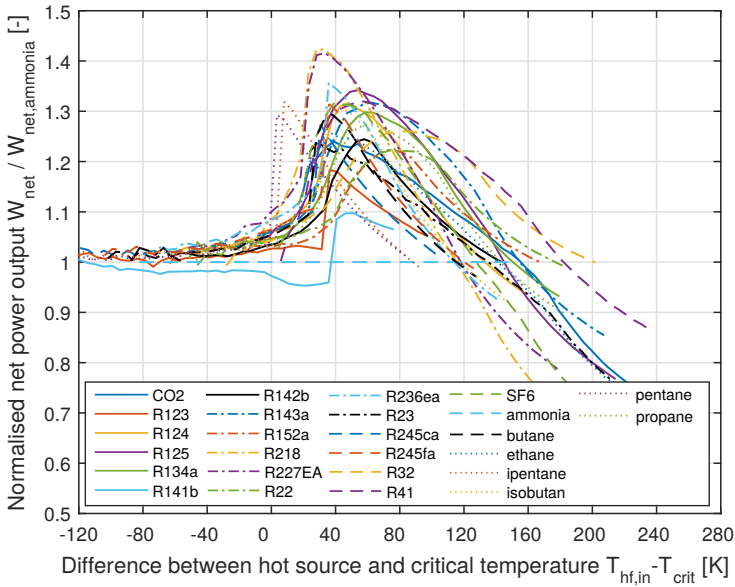
Figure D.12: Normalised net power output as function of temperature difference between the hot source and critical temperature of the fluid candidates.

gests, all the candidates outperform ammonia when operated at a hot source temperature approximately 30-50 K above their critical temperature, that is $T_{hf,in} - T_{crit} = [30; 50]$ K. For fluids having $\xi \gg 0$ such as pentane and ipentane, $T_{hf,in} - T_{crit}$ should be slightly lower around $T_{hf,in} - T_{crit} = [0; 15]$ K but still operated at $T_{hf,in} > T_{crit}$. The results of this study therefore suggests that there is not a single $T_{hf,in}/T_{crit}$ parameter resulting in optimal performance. Instead, a optimal difference $(T_{hf,in} - T_{crit})$ exists, such that the performance is optimal for a given hot source temperature.

Two fluids candidates can however have the almost same critical temperature. Therefore, a criteria is set up to choose between two fluids having the approximately same critical temperature in order to obtain the maximum net work output. Studies from literature have suggested the the slope of vapour saturation line to play a major role as super heating can be avoided for fluids with $\xi > 0$. Figure D.13 shows the optimal fluids from table D.4 listed by their critical temperature and slope of vapour saturation line. Ethane and R23 being the optimal fluids for hot source temperatures in the range [50;70] have both $\xi \ll 0$. An alternative could have been R7146 (SF6) which only has a slightly higher critical temperature but $\xi \approx 0$. This result suggests the critical temperature to be more important than the slope of vapour saturation line, when looking for a working fluid for a given hot source temperature to obtain the maximum net power output. If fluids having critical temperatures
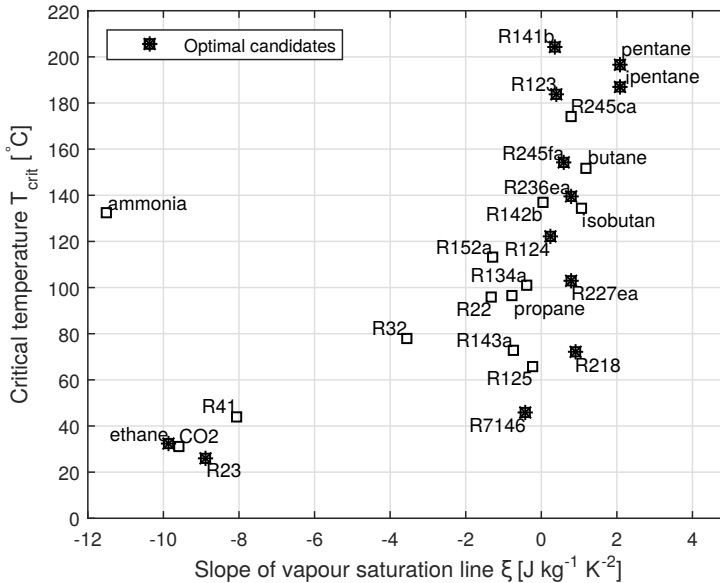
Figure D.13: Optimal working fluid candidates shown in a critical temperature as function of slope of vapour saturation line chart.

similar to R23 and Ethane and slope of vapour saturation line close to zero were included, these are expected to perform better than R23 and Ethane. At hot source temperatures in the range [95;190]°C, fluids having $\xi > 0$ are favoured when more fluid candidates have almost the same critical temperature, an example being R218 and R143a where R218 has $\xi > 0$ and R143a has $\xi < 0$. For mixtures, the critical temperature and slope of vapour saturation line depends on the mixture composition. In the following, considerations on the optimal mixture are given.

D.4.2 Mixture candidates

By considering mixtures with the mixture composition as a design variable, the mixture composition χ can be used to alter the two parameters discussed until now. That is the critical temperature T_{crit} and slope of vapour saturation line ξ. How the position in the $T_{\mathrm{crit}} - \xi$ chart is altered when the composition is shifted by 0.1 for the mixtures is shown in figure D.14. Furthermore, the mixtures do as well introduce a temperature glide, which allows for a better thermal match with the hot and cold sources. This is especially important for the iso-thermal condensation and sub-critical boiling processes, which would otherwise introduce large irreversibilities. Figure D.15 shows the temperature glide for the three mixtures as function of mixture composition for condensation processes where the mixtures leave the condenser at
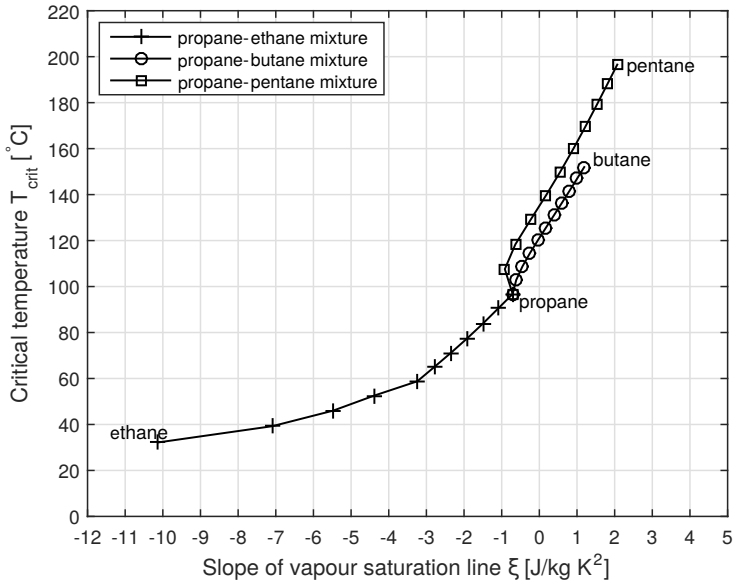
Figure D.14: Critical temperature as function of slope of vapour saturation line for the mixtures considered in this study. Marks are placed at changes in mixture composition of 0.1.
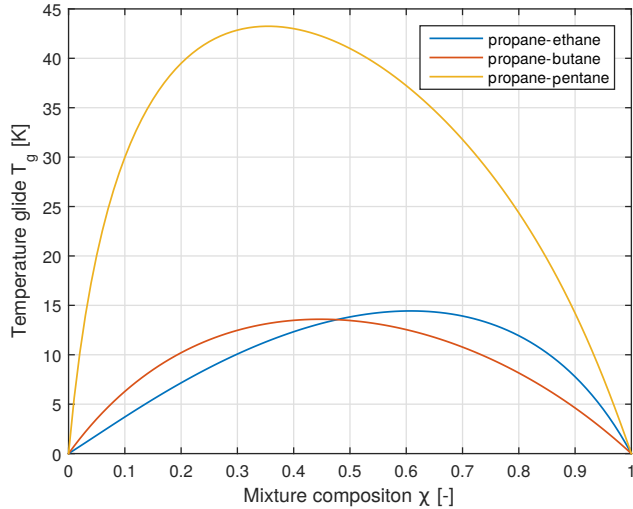
Figure D.15: Temperature glide of the mixtures during condensation as function of the mixture composition when mixture leaves the condenser at saturated liquid at 20 °C.

saturated liquid at 20 °C. Performing the optimisations for the mixtures with the mixture composition as an additional design variable, the results in figure
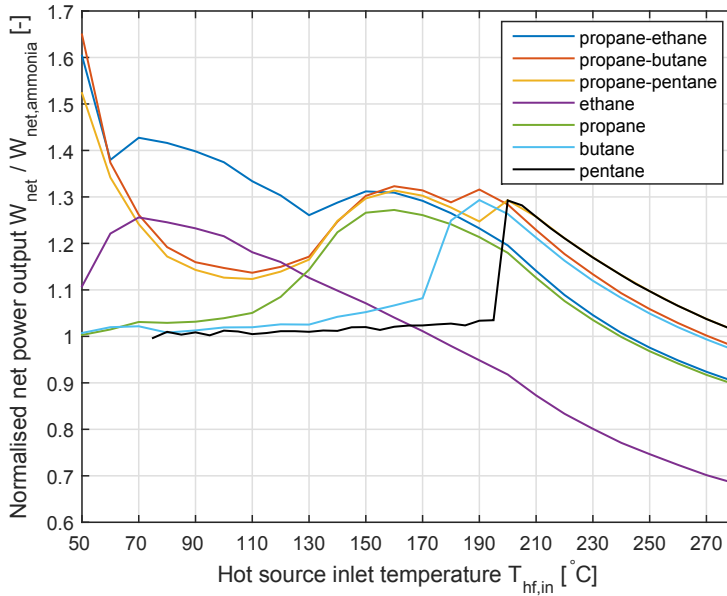
**Figure D.16:** Optimal designs visualised by the net power output normalised by ammonia for different working fluid mixtures at a varying hot source temperature in the range [50;280] °C with intervals of 10 K. The pure fluid candidates from figure D.8 are shown for reference.

D.16 are obtained with the mixture compositions shown in figure D.17.

As the mixture composition is found by optimisation, the mixtures should at least perform as good as the pure fluids used in the mixture. Figure D.16 shows that this is actually the case. Furthermore, the figure shows that the mixtures in most cases perform better than the pure fluids with the exception of the propane-pentane mixture, which at hot source temperature above 200°C perform similar to pure pentane. Figure D.17 shows that the optimal mixture composition for the propane-pentane mixture is indeed 0 (corresponding to pure pentane) for $T_{hf,in} > 200°C$. That is, even though the condensation process can be improved by a better thermal match by adding propane to pentane, the lower critical temperature introduced by adding Propane results in lower net power output.

For the propane-butane mixture, the net power output is increased at all hot source temperatures, suggesting a temperature glide to increase the net power output even though the critical temperature is decreased slightly by the addition of propane. At lower hot source temperatures ($T_{th,in} < 190°C$), the optimal mixtures contain Propane fractions in the order of 0.8-0.9. At higher hot source temperatures ($T_{th,in} > 190°C$) the optimal mixture composition changes radically to consist of mostly butane. In all the hot source temperature interval, the mixture composition results in a temperature glide

219
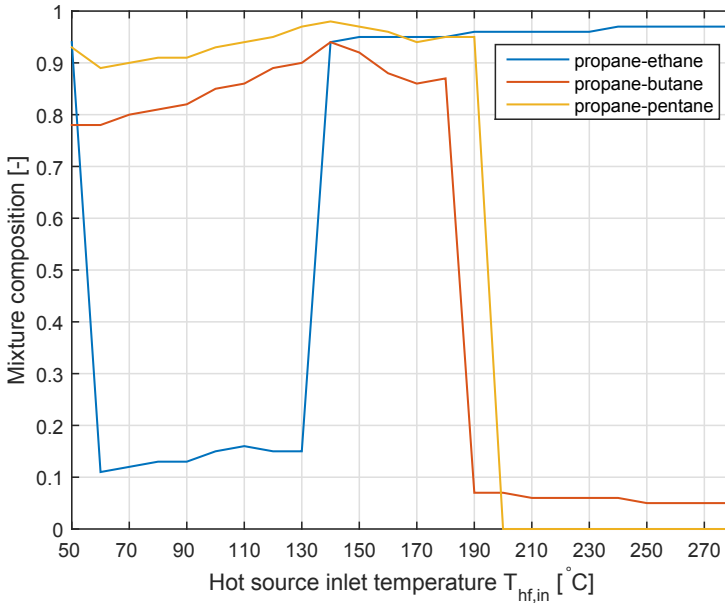
Figure D.17: Optimal mixture composition at varying hot source temperatures in the range [50;280]°C with intervals of 10 K.

of approximately 5 K resulting in a good thermal match with the cold source.

For the propane-ethane mixture, the net power output is again increased in all the hot source temperature interval compared to the pure propane and ethane. Again a radical change in mixture composition is observed. For the propane-ethane mixture this transition occurs at 140°C, where the optimal mixture composition changes from approximately 0.15/0.85 to 0.95/0.05. Both these mixture compositions result in a temperature glide of 5 K as seen in figure D.15. As opposed to the other two mixtures, the propane-ethane mixture favours propane at higher temperatures ($T_{hf,in} > 140$°C). This can be explained by the fact that propane has a higher critical temperature than ethane.

To sum up, all three mixtures show that the net power output can be increased by a mixture compared to the corresponding pure fluids alternatives. The optimisations furthermore suggest that the mixture composition should results in a temperature glide approximately equal to the temperature rise of the cold source. If two mixture compositions fulfil this criteria, the mixture composition should be chosen to comply with the guideline for pure fluids. That is the mixture composition should be changed from consisting of mostly the low critical temperature fluid to the higher critical temperature fluid, when the guideline of $T_{hf,in} - T_{crit} = [30;50]$ K can be obtained using the higher critical temperature fluid. In that case a small amount of the

lower temperature fluid should be added to make the temperature glide in the condenser match the cold source temperature rise.

D.5 Conclusion

In this study, the performance of an ORC system in its simplest configuration is optimised with 26 pure fluids and 3 mixtures at hot source temperatures ranging from 50°C to 280°C. By optimising the ORC at different hot source temperature for a wide range of different fluid candidates with different saturation curves, generals correlations have been identified and described. By comparing the different working fluids candidates to ammonia in terms of net power output, each fluid candidate has an optimal hot source inlet temperature. By correlating this optimal hot source temperature and the critical temperature of the different fluid candidates, it is found that for a given hot source temperature $T_{hf,in}$ the optimal fluid has a critical temperature in the range [30;50] K below $T_{hf,in}$. When more fluids have almost the same critical temperature such as R218 ($T_{crit} = 71.9$°C) and R143a ($T_{crit} = 72.7$°C) the fluid the the lowest ξ has a higher net work output but is more limited to the hot source temperature being [30;50] K above the critical temperature.

This optimal hot source temperature for each fluid can be explained by a better thermal match to the working fluid as the working cycles changes from sub-critical to trans-critical. The hot source temperature where the optimal cycles change from sub-critical to trans-critical will however require significantly higher heat transfer areas resulting in a lower W_{net}/A ratio. This statement is especially valid for fluids having slope of vapour saturation lines $\xi > 0$. On the other hand, fluids having $\xi \ll 0$ do not show a sudden decrease in W_{net}/A ratio.

Furthermore, working fluid suggestions are given for different hot source temperature ranges. From a hot source temperature of 50°C to 280°C, the optimal working fluids in terms of net power output are R23, ethane, R7146 (SF6), R218, R227ea, R124, R236ea, R245fa, isopentane, Pentane, R123, and R141b.

When mixtures are considered as potential working fluids, the optimal mixtures all have compositions resulting in a temperature glide approximating the cold source temperature rise. Such a temperature rise is possible by either low or high mass fractions, resulting in two possible solutions. The solution giving the required temperature glide and a critical temperature 30-50 K below the hot source temperature should be chosen. When such critical temperature cannot be obtained, the mass fraction of the mixture should be changed radically to obtain a similar temperature glide and a critical temperature.

Acknowledgement

Bibliography

H. A. Ajimotokan and I. Sher. Thermodynamic performance simulation and design optimisation of trilateral-cycle engines for waste heat recovery-to-power generation. *Applied Energy*, 154:26–34, 2015. URL `http://dx.doi.org/10.1016/j.apenergy.2015.04.095`.

J.G Andreasen, U. Larsen, T. Knudsen, L. Pierobon, and F. Haglind. Selection and optimization of pure and mixed working fluids for low grade heat utilization using organic rankine cycles. *Energy*, 73:204–213, 2014. URL `http://dx.doi.org/10.1016/j.energy.2014.06.012`.

J. Bao and L. Zhao. A review of working fluid and expander selections for organic rankine cycle. *Renewable and Sustainable Energy Reviews*, 24:325–342, 2013. URL `http://dx.doi.org/10.1016/j.rser.2013.03.040`.

Konstantinos Braimakis, Markus Preißinger, Dieter Brüggemann, Sotirios Karellas, and Kyriakos Panopoulos. Low grade waste heat recovery with subcritical and supercritical organic rankine cycle based on natural refrigerants and their binary mixtures. *Energy*, :, 2015. URL `http://dx.doi.org/10.1016/j.energy.2015.03.092`.

D. Buecker and W. Wagner. Reference equations of state for the thermodynamic properties of fluid phase n-butane and isobutane. *Journal of Physical and Chemical Reference Data*, 35:929–1019, 2006a.

D. Buecker and W. Wagner. A reference equation of state for the thermodynamic properties of ethane for temperatures from the melting line to 675 k and pressures up to 900 mpa. *Journal of Physical and Chemical Reference Data*, 35:205–266, 2006b.

Lixin Cheng and Dieter Mewes. Review of two-phase flow and flow boiling of mixtures in small and mini channels. *International Journal of Multiphase Flow*, 32:183–207, 2006. URL `http://dx.doi.org/10.1016/j.ijmultiphaseflow.2005.10.001`.

M. Chys, M. van den Broek, B. Vanslambrouck, and M. De. Paepe. Potential of zeotropic mixtures as working fluids in organic rankine cycles. *Energy*,

44:623–632, 2012. URL `http://dx.doi.org/10.1016/j.energy.2012.05.030`.

Yiping Dai, Jiangfeng Wang, and Lin Gao. Parametric optimization and comparative study of organic rankine cycle (orc) for low grade waste heat recovery. *Energy Conversion and Management*, 50:576–582, 2009. URL `http://dx.doi.org/10.1016/j.enconman.2008.10.018`.

B. de Vries, R. Tillner-Roth, and H.D. Baehr. Thermodynamic properties of hcfc 124. *19th International Congress of Refrigeration, The Hague, The Netherlands, International Institute of Refrigeration*, IVa:582–589, 1995.

J. Fischer. Comparison of trilateral cycles and organic rankine cycles. *Energy*, 36:6208–6219, 2011. URL `http://dx.doi.org/10.1016/j.energy.2011.07.041`.

C. Guder and W. Wagner. A reference equation of state for the thermodynamic properties of sulfur hexafluoride (sf6) for temperatures from the melting line to 625 k and pressures up to 150 mpa. *Journal of Physical and Chemical Reference Data*, 38:33–94, 2009.

Florian Heberle, Markus Preißinger, and Dieter Grüggemann. Zeotropic mixtures as working fluids in organic rankine cycles for low-enthalpy geothermal resources. *Renewable Energy*, 37:364–370, 2012. URL `http://dx.doi.org/10.1016/j.renene.2011.06.044`.

J. H. Holland. *Adaption in Natural and Artificial Systems - An Introductory Analysis with Applications to Biology, Control, and Artificial Intelligence*. MIT Press, 1992. ISBN: 978-0262581110.

M. L. Huber and J. F. Ely. A predictive extended corresponding states model for pure and mixed refrigerants including an equation of state for r134a. *International Journal of Refrigeration*, 17:18–31, 1994.

M. Jaeschke and P. Schley. Ideal-gas thermodynamic properties for natural-gas applications. *International Journal of Thermophysics*, 16:1381–1392, 1995.

A. Kamei, S. W. Beyerlein, and R. R. Jacobsen. Application of nonlinear regression in the development of a wide range formulation for hcfc-22. *International Journal of Thermophysics*, 16:1155–1164, 1995.

Steven Lecompte, Henk Huisseune, Martijn van den Broek, Bruno Vanslambrouck, and Michel De Paepe. Review of organic rankine cycle (orc) architectures for waste heat recovery. *Renewable and Sustainable Energy Reviews*, 47:448–461, 2015. URL `http://dx.doi.org/10.1016/j.rser.2015.03.089`.

E. W. Lemmon and R. T. Jacobsen. An international standard formulation for the thermodynamic properties of 1,1,1-trifluoroethane (hfc-143a) for temperatures from 161 to 450 k and pressures to 50 mpa. *Journal of Physical and Chemical Reference Data*, 29:521–552, 2000.

E. W. Lemmon and R. T. Jacobsen. A new functional form and new fitting techniques for equations of state with application to pentafluoroethane (hfc-125). *Journal of Physical and Chemical Reference Data*, 34:69–108, 2005.

E. W. Lemmon and R. Span. Short fundamental equations of state for 20 industrial fluids. *Journal of Physical and Chemical Reference Data*, 51:785–850, 2006.

E. W. Lemmon, M. O. McLinden, and W. Wagner. Thermodynamic properties of propane. iii. a reference equation of state for temperatures from the melting line to 650 k and pressures up to 1000 mpa. *Journal of Chemical Engineering Data*, 54:3141–3180, 2009.

E.W. Lemmon, M.L. Huber, and M.O. McLinden. *NIST Standard Reference Database 23: Reference Fluid Thermodynamic and Transport Properties-REFPROP, Version 9.1, National Institute of Standards and Technology, Standard Reference Data Program, Gaithersburg*, 2013.

You-Rong Li, Mei-Tang Du, Chun-Mei Wu, Shuang-Ying Wu, and Chao Liu. Potential of organic rankine cycle using zeotropic mixtures as working fluids for waste heat recovery. *Energy*, 77:509–519, 2014. URL http://dx.doi.org/10.1016/j.energy.2014.09.035.

Bo-Tau Liu, Kuo-Hsiang Chien, and Chi-Chuan Wang. Effect of working fluids on organic rankine cycle for waste heat recovery. *Energy*, 29:1207–1217, 2004. URL http://dx.doi.org/10.1016/j.energy.2004.01.004.

Daniel Maraver, Javier Royo, Vincent Lemont, and Sylvain Quoilin. Systematic optimization of subcritical and transcritical organic rankine cycles (orcs) constrained by technical parameters in multiple. *Applied Energy*, Applied Energy:11–29, 2014. URL http://dx.doi.org/10.1016/j.apenergy.2013.11.076.

S. L. Outcalt and M. O. McLinden. A modified benedict-webb-rubin equation of state for the thermodynamic properties of r152a (1,1-difluoroethane). *Journal of Physical and Chemical Reference Data*, 25:605–636, 1996.

Athanasios I. Papadopoulos, Mirko Stijepovic, and Patrick Linke. On the systematic design and selection of optimal working fluids for organic rankine cycles. *Applied Thermal Engineering*, 30:760–769, 2010. URL http://dx.doi.org/10.1016/j.applthermaleng.2009.12.006.

S. G. Penoncello, E. W. Lemmon, R. T. Jacobsen, and Z. Shan. A fundamental equation for trifluoromethane (r-23). *Journal of Physical and Chemical Reference Data*, 32:1473–1499, 1995.

G.S. Chaianya Prasad, c. Suresh Kumar, S. Srinivasa Murthy, and G. VenKatarathnam. Performance of an organic rankine cycle with multicomponent mixtures. *Energy*, :, 2015. URL `http://dx.doi.org/10.1016/j.energy.2015.05.102`.

Jovana Radulovic and Nadia I. Beleno Castaneda. On the potential of zeotropic mixtures in supercritical orc powered by geothermal energy source. *Energy Conversion and Management*, 88:365–371, 2014. URL `http://dx.doi.org/10.1016/j.enconman.2014.08.048`.

Wilfried Roetzel and Bernhard Spang. C3 typical values of overall heat transfer coefficients. In *VDI Heat Atlas*, pages 75–78. VDI-Verlag GmbH, Düsseldorf, 2010. ISBN: 978-3-540-77876-9.

Bahaa Saleh, Gerald Koglbauer, Martin Wendland, and Johann Fischer. Working fluids for low-temperature organic rankine cycles. *Energy*, 32:1210–1221, 2007. URL `http://dx.doi.org/10.1016/j.energy.2006.07.001`.

R. Span and W. Wagner. A new equation of state for carbon dioxide covering the fluid region from the triple-point temperature to 1100 k at pressures up to 800 mpa. *Journal of Physical and Chemical Reference Data*, 25:1509–1596, 1996.

Bertrand F. Tchanche, Gr. Lambrinos, A. Frangoudakis, and G. Papadakis. Low-grade heat conversion into power using organic rankine cycles – a review of various applications. *Renewable and Sustainable Energy Reviews*, 15: 3963–3979, 2011. URL `http://dx.doi.org/10.1016/j.rser.2011.07.024`.

R. Tillner-Roth and H. D. Baehr. *Thermodynamic Properties of Environmentally Acceptable Refrigerants: Equations of State and Tables for Ammonia, R22, R134a, R152a, and R123*. Springer-Verlag Berlin, 1994a. ISBN 978-3540586937.

R. Tillner-Roth and H.D. Baehr. An international standard formulation of the thermodynamic properties of 1,1,1,2-tetrafluoroethane (hfc-134a) for temperatures from 170 k to 455 k and pressures up to 70 mpa. *Journal of Physical and Chemical Reference Data*, 23:657–729, 1994b.

R. Tillner-Roth and A. Yokozeki. An international standard equation of state for difluoromethane (r-32) for temperatures from the triple point at 136.34 k to 435 k and pressures up to 70 mpa. *Journal of Physical and Chemical Reference Data*, 26:1273–1328, 1997.

Christian Vetter, Hans-Joachim Wiemer, and Dietmar Kuhn. Comparison of sub- and supercritical organic rankine cycles for power generation from low-temperature/low-enthalpy geothermal wells, considering specific net power output and efficiency. *Applied Thermal Engineering*, 51:871–879, 2013. URL `http://dx.doi.org/10.1016/j.applthermaleng.2012.10.042`.

Jacopo Vivian, Giovanni Manente, and Andrea Lazzaretto. A general framework to select working fluid and configuration of orcs for low-to-medium temperature heat sources. *Applied Energy*, 156:727–746, 2015. URL `http://dx.doi.org/10.1016/j.apenergy.2015.07.005`.

W. Wagner and A. Pruss. The iapws formulation 1995 for the thermodynamic properties of ordinary water substance for general and scientific use. *Journal of Physical and Chemical Reference Data*, 31:387–535, 2002.

Daniël Walraven, Ben Laenen, and William D'haeseleer. Comparison of thermodynamic cycles for power production from low-temperature geothermal heat sources. *Energy Conversion and Management*, 66:220–233, 2013. URL `http://dx.doi.org/10.1016/j.enconman.2012.10.003`.

Jinliang Xu and Chao Yu. Critical temperature criterion for selection of working fluids for subcritical pressure organic rankine cycles. *Energy*, 74:719–733, 2014. URL `http://dx.doi.org/10.1016/j.energy.2014.07.038`.

B. A. Younglove and M. O. McLinden. An international standard equation of state for the thermodynamic properties of refrigerant 123 (2,2-dichloro-1,1,1-trifluoroethane). *Journal of Physical and Chemical Reference Data*, 23:731–779, 1994.

Davide Ziviani, Asfaw Beyene, and Mauro Venturini. Advances and challenges in orc systems modeling for low grade thermal energy recovery. *Applied Energy*, 121:79–95, 2014. URL `http://dx.doi.org/10.1016/j.apenergy.2014.01.074`.

Nomenclature

A	Heat exchanger area, [m^2]
c_p	Specific heat capacity, [J/K kg]
h	Heat transfer coefficient, [W/m^{2}K]
$\dot{m}$	Mass flow rate, [kg/s]
n	Number of discretisations, [$-$]
P	Pressure, [Pa]
$\dot{Q}$	Heat transfer rate, [W]
R	Thermal resistance, [K/W]
s	Specific entropy, [J/K kg]
T	Temperature, [°C]
U	Overall heat transfer coefficient, [W/m^{2}K]
x	Quality, [$-$]

Greek letters

η	Efficiency, [$-$]
χ	Mass fraction of first-mentioned fluid, [$-$]
ξ	Slope of vapour saturation line, [J/K^{2}kg]

Subscripts

1,2,3,4	State points
cf	Cold fluid
crit	Critical state
g	Glide
hf	Hot fluid
i	index
in	Inlet
lm	Mean temperature difference
out	Outlet
pp	Pinch point
sat	Saturation state
wf	Working fluid

Acronyms

ASHRAE	American Society of Heating, Refrigerating and Air-Conditioning Engineers
CAMD	Computer Aided Molecular Design
ORC	Organic Rankine Cycle
REFPROP	Reference Fluid Thermodynamic and Transport Properties Data